CHARGE STRIPES AND LOCAL STRUCTURAL INHOMOGENEITIES IN $La_{2-x}(Sr,Ba)_xCuO_4$ HIGH TEMPERATURE SUPERCONDUCTORS

By

Emil S. Bozin

A DISSERTATION

Submitted to

Michigan State University

in partial fulfillment of the requirements

for the Degree of

DOCTOR OF PHILOSOPHY

Department of Physics and Astronomy

2003

CHARGE ST

$La_{2-x}(Sr.$

We have investig

planes of the hi

mogeneous. poss

the properties o

No long-range o

which means th

ordered and no

Atomic pair

investigate the

$La_{2-x}(Sr.Ba)_xC$

tained by time-

for temperatur

ture in the und

ABSTRACT

CHARGE STRIPES AND LOCAL STRUCTURAL INHOMOGENEITIES IN $La_{2-x}(Sr,Ba)_xCuO_4$ HIGH TEMPERATURE SUPERCONDUCTORS

By

Emil S. Bozin

We have investigated the possibility that the doped charge distribution in the CuO_2 planes of the high temperature superconducting cuprates is microscopically inhomogeneous, possibly with a striped morphology. The existence and importance to the properties of charge stripes in superconducting samples is not fully established. No long-range ordered static stripes have been observed in superconducting samples which means that either such formations are not present, or they are short range ordered and not observable crystallographically.

Atomic pair distribution function *local* structural study has been carried out to investigate the nature of the doped-charge distribution within the CuO_2 planes of $La_{2-x}(Sr,Ba)_xCuO_4$ as a function of doping and temperature. The data were obtained by time-of-flight neutron powder diffraction experiments. Evidence is found for temperature dependent atomic-scale structural inhomogeneities at low temperature in the underdoped and optimally doped regions of the phase diagram, compatible

with the presenc

geneities are see

nificant degree o

inhomogeneities

They also disap

spin and charge

measurements.

Recent theor

system has pred

contrast to the

new way of under

in the understan

LSCO system has

results. in contra

planar-doping pic

that a small amo

doping.

with the presence of inhomogeneous charge distribution in the CuO_2 planes. Inhomogeneities are seen as a planar Cu-O bondlength distribution, accompanied by a significant degree of the CuO_2-octahedral tilt magnitude and directional disorder. The inhomogeneities disappear on crossing into the overdoped region at low temperature. They also disappear in underdoped samples at temperatures which correlate with spin and charge freezing in this system inferred from transport, NQR, and XANES measurements.

Recent theoretical calculations suggested that the doping in the $La_{2-x}Sr_xCuO_4$ system has predominantly apical character, perpendicular to the CuO_2 planes, in contrast to the established understanding that doping has planar character. This new way of understanding the doping, if it is right, would result in a paradigm shift in the understanding of cuprate physics. The orbital character of doped holes in the LSCO system has been reexamined from the structural perspective. The structural results, in contrast to the above theoretical prediction, are in agreement with the planar-doping picture in the underdoped and optimally doped regime, and indicate that a small amount of doped charge may have apical character above the optimal doping.

To my family

"There

moment.

If one fully

to do, and

(Tsuneto

"There is surely nothing other than the single purpose of the present moment. A man's whole life is a succession of moment after moment. If one fully understands the present moment, there will be nothing else to do, and nothing left to pursue."

(Tsunetomo Yamamoto, September 10, 1716)

In all de
constantly g
this is possib
trusted in my
I would li
S. D. Mahant
my studies an
Significant
segments of th
P. M. Duxbury
for all her help
as well as to R.
A samurai w
DiFrancesco for
mann is greatly
terson, and X. C
all of them.
If one were t
lies in one being
most gratefulness
guidance, unlimit
port throughout
Grants No. DMR-
Foundation.
Finally, I than
support, knowing

Acknowledgments

In all dealings with people, it is essential to have a fresh approach. One should constantly give the impression that he is doing something exceptional. It is said that this is possible with but a little understanding. I thank Professor J. S. Kovacs who trusted in my abilities despite modest TOEFL scores.

I would like to express unreserved gratitude to my thesis committee members, S. D. Mahanti, S. Tessmer, C.-P. Yuan and S. Pratt for their enthusiastic help during my studies and for their time and effort while being on the committee.

Significant contributions of H. Takagi, G. H. Kwei, and M. Gutmann in various segments of the project presented here are acknowledged. Occasional discussions with P. M. Duxbury and M. F. Thorpe are greatly appreciated. Special thanks to S. Short for all her help and patience during the experiments at SEPD at IPNS, ANL Argonne, as well as to R. Loloee for the help with SQUID characterizations.

A samurai with no group and no horse is not a samurai at all. I thank R. G. DiFrancesco for all his help and patience when I joined the group. Help from M. Gutmann is greatly appreciated. Thanks to Th. Proffen, V. Petkov, I-K. Jeong, P. F. Peterson, and X. Qiu for their help and support, it was an honor to be surrounded by all of them.

If one were to say in a word what the condition of being a samurai is, its basis lies in one being seriously devoted to his master. I would like to express my utmost gratefulness to my thesis adviser, S. J. L. Billinge, for his unselfish help, kind guidance, unlimited patience and understanding in hardships, and for financial support throughout my graduate studies. This work was supported by NSF through Grants No. DMR-0075149 and No. DMR-9700966, and also supported by the Sloan Foundation.

Finally, I thank my family for all the sacrifice, patience, continuous love and support, knowing that time spent away from them cannot be replaced.

Conter

Contents

List of

List of Tables

4.1 Einstei
were ex
for LSC
and th
to the
param
LBCO

6.1 Ampli
octahe
ampli
erage
ramet
denot

6.2 R_w-fa
to fu

6.3 R_w-f

6.4 R_w-f

6.5 Tem
the a
Rep
lar t

6.6 The
LSC
565
apia

6.7 The
samp
bond
and
6.8 The
LBC
LCO
at HI
in th
multi
6.9 Atom
as ob
Å^2).
6.10 Severa
consid
earth
Shann
deviati
7.1 Standa
results
weighte

List of

List of Figures

1.9 The Ja
of the
generat
Furthe
onal di
Ideal C
atoms
distort
arrows.
1.10 Univers
1.11 Schema
1.12 (a) and
at 10 K
in inten
Gaussia
1.13 The sup
of temp
magneti
solid lin
LTT pha
1.14 Phase di
supercon
charge-or

2.1 Effect of
values of
2.2 Experime
ing $N(r)$

2.3 Struc

Singl

scatte

atomi

the di

2.4 Comp

PDFs

using

(solid

the sa

CuO_6

2.5 X-ray

ature:

corresp

first tw

2.6 Ewald

Details

matic b

2.7 Left: sc

Empty

detector

L_0 is th

of the se

sample, a

2.8 Exam
spectr
IPNS.
are evi
over in
short w
2.9 Examp
intensi
sity as
2.10 Blendi
togethe
limits a
range in
mining
applies
2.11 Bond va
two ato
another
getting
3.1 Sample
tion (sa
perature
quenchi
of °C. a

3.2 Possib
sis: (a
circles
while g
able ca
occur i
other r
3.3 A segm
pattern
tained b
ing from
of T'-ph
peaks a
the sam
T-phase
3.4 XRD pa
with stro
tural ph
perature
ing depe
composit
structura
differenc
member
room tem
XRD pat
ment, all

3.10 Ortho
charac
diffrac
(see te
ted as
the sa
main c
per Kα
1.5443
intensi

3.11 (a) Ort
superla
phase t
tical ax
tempera
UK.

3.12 $La_{2-x}Sr$
for x=0.
tical axi
tempera
UK.

3.13 The st
tural p
Sr/Ba
bols d
spond
circles
line de
in LBC
structu
transiti
Dotted

4.1 Examin
view of
Filled c
two dim
radii: lo
4.2 The firs
formatio
the first
Cu-O1 a
4.3 PDF pe
levels (s
lines: int
their cen

4.4 Peak v
obtain
as σ^2 v
height-
line up
4.5 (a) PD
$r = 0.$
dashed
PDF fr
the PD
the PD
4.6 (a) Rec
$La_{1.875}S$
cles). T
with th
$r = 1.9$
4.7 Mean-sq
function
and (c)
dicted b
peak hei
(d) Tem
$La_{1.875}Sr$
diamond
dependen

4.8 Comp
σ^2, of
ture fo
and (2
squares
fitting
Einstei
reporte
dashed

4.9 (a) Ty
$La_{1.47}$
erage
10 K
bars
tained
neares
for th

4.10 Invers
LSC
ples
rescal
perat

4.11 Phase
gap op
port u
ments
$x > 0$.
joined
temper

5.1 Schem

5.2 (a) Co
symme
(dash-d
mately
in pane
tilt), an
clearly
these q

5.3 (a) Full
imentall
The diff
shows t
Fully co
x=0.30

5.4 Deper
$|\theta|$, on
obtai
(see te
increas
tilts di

5.5 Differ
5° cas
solid
Diffe

5.6 (a) F
line)
Diffa
line
(b)

5.7 (a)
con
diff
line
(b)

5.8 (a)
co
dif
lin
(b

5.9 (a) Fu
comp
differ
line sh
(b) Th
5.10 Schem
in the
denote
the ap
with s
and a
at the
plane
5.11 Scher
plane
are d
of th
with
and
at th
plan
the

5.12 (a) C
tilt a
line is
the x
of a c
open
$x = 0$
large
repro
The
5.13 Com
5.14 Mixi
prod
from
mix
in t
tilts
0.12
tota
is p
repr
win
tran
5.15 (a)
tal
agre

6.4 Temp
plitud
and O
Temp
cles) i
octah
6.5 Temp
plitud
and O
Temp
cles) is
octah
6.6 Energy
LBCO
plot of
along t
et al.).
6.7 The lan
atoms, f
bonds, t
and four

6.8 Schem
in the
shared
inside
octahe
the co
(not sh
to flip
the de

6.9 Schem
in the
share
inside
octah
at th
tilts
defe
requ

6.10 Tilt
dop
stra
don

7.1 Sch
in
ab

7.2 Cryst
(A-JT
the JT
7.3 Repres
data fo
model
solid li
level. I
to $Q_{M,}$
7.4 Evoluti
lengths
PDF re
electro
PTG r
phase t
7.5 Sum of
strontia
guide t
displac
PTG r
7.6 (a) Par
tributio
using R
planar
measure

8.1 CuO_6
dashe
slopin
doping
8.2 CuO_6
cates a
change
Solid a
of zero
8.3 CuO_6
bols).
indica
slope
denot
the p
8.4 CuO_6
squar
HTT
guide
apica
optim
pende
8.5 Evolu
300 K
distar
and o

Chapt

Introd

"According to

hawk taking a b

no attention to

1.1 Intr

The discovery

A=(Sr,Ba). (L

and later other

interest in the

fields in conten

the mechanism

properties of th

this type of mat

quantum compu

trains. However

of these systems

Superconduc

Chapter 1

Introduction and Motivation

"*According to what one of the elders said, taking an enemy on the battlefield is like a hawk taking a bird. Even though it enters into the midst of a thousand of them, it gives no attention to any bird other than the one that it has first marked.*" (T. Yamamoto)

1.1 Introduction

The discovery of the high temperature superconductivity (HTS) in $La_{2-x}A_xCuO_4$, A=(Sr,Ba), (LSCO and LBCO respectively, also known as the '214' family) [1] in 1986, and later other layered copper oxides with perovskite-like structure [2, 3], renewed interest in the superconductivity and opened one of the most complex and exciting fields in contemporary condensed matter physics. The importance of understanding the mechanism behind the HTS phenomenon, as well as being able to utilize the properties of the HTS materials, is enormous. Potential technological applications of this type of materials span a wide spectrum from the field of microelectronics such as quantum computing to the more macroscopic applications such as levitated maglev trains. However, in order to facilitate the engineering stage, fundamental properties of these systems have to be understood in detail.

Superconductivity in the conventional low temperature superconductors is well

understood w
ing opposite n
through an eff
carriers for the
is known as a
integer net spi
ficiently low te
do "communic
transition tem
transition fro
resistivity dro
diamagnetism
of the key issu
mechanism in

While the
conventional
ducting state,
structure, the
many unusual
herence lengt
the normal st
the normal st
HTS systems.
normal state,
are relatively

One of the
crystal structu

understood within the framework of the BCS theory [4]. Pairs of electrons having opposite momenta and opposite spins form Cooper pairs [5] in reciprocal space, through an effectively attractive phonon-mediated interaction. The resulting charge carriers for the superconductivity are these pairs with a charge magnitude of $2e$. This is known as a phonon-mediated pairing mechanism. Such pairs of electrons have integer net spin, and since they are bosons, are subject to Bose condensation at sufficiently low temperature. Despite their spatial separation, electrons forming a pair do "communicate" to each other via the crystal lattice. Below the superconducting transition temperature, T_c, the pairs condense resulting in superconductivity. The transition from the normal to the superconducting state is second order. At T_c the resistivity drops to zero, and the material exhibits perfect conductivity *and* perfect diamagnetism, in contrast to perfect conductors that exhibit the former only [6]. One of the key issues in the HTS field that has remained unresolved to date is the pairing mechanism in these novel superconducting systems.

While the HTS systems have many common features to those observed in the conventional superconductors, such as paired carriers, energy gap in the superconducting state, repulsion of the external magnetic field (Meissner effect) and a vortex structure, there are remarkable differences as well [6, 7]. The HTS systems possess many unusual properties, the extremely high values of T_c [3] and extremely short coherence lengths [8, 9] being merely the most obvious of them. Unusual properties of the normal state of HTS materials, such as a linear with temperature dc-resistivity in the normal state [10], highlight another important aspect of interest in studies of the HTS systems. Unlike the conventional BCS superconductors that are metallic in their normal state, the HTS copper oxides are *doped* antiferromagnetic (AF) insulators and are relatively poor conductors in the normal state [6].

One of the most remarkable features of the HTS materials is a highly anisotropic crystal structure [3]. An anisotropic superconducting gap [11, 12, 13, 14], anisotropy

Figure 1.1: Ex

separated by t

T-structure in

families the C

of the superc

large ratio of

in the HTS sy

of the HTS m

The HTS c

is shown in Fig

by the rare-ea

layers. The nu

214 family co

successive pla

be very weak.

represent the

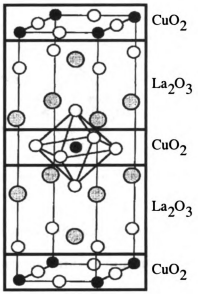

Figure 1.1: Example of the layered HTS structure: 214 family. The CuO_2 layers are separated by the insulating $(La/Sr)_2O_3$ blocks, as schematically presented. So-called T-structure in the LSCO system is shown for illustration. In some HTS cuprate families the CuO_2 planes come in blocks of several consecutive planes (up to 3).

of the superconducting coherence length [6, 7, 15], and anisotropic resistivity with large ratio of the in-plane resistivity to the perpendicular resistivity [16] are observed in the HTS systems. The extent to which the lattice may be relevant for the physics of the HTS materials is addressed in more detail below.

The HTS cuprates have layered structures [3], and an example of the LSCO system is shown in Figure 1.1. The structure contains copper-oxygen (CuO_2) planes separated by the rare-earth oxide insulating layers frequently referred to as the charge reservoir layers. The number of successive CuO_2 planes varies from one family to another. The 214 family contains only one CuO_2 plane, while other families have up to 3 or more successive planes. The electronic coupling between separated planes is considered to be very weak, giving rise to a huge anisotropy in resistivity [17]. The CuO_2 planes represent the most prominent structural link between all the HTS cuprates. The three

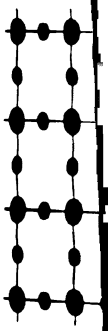

Figure 1.2: Sch
of the planes th

typical buildin
shown in Figu

The HTS i
like or electron
appropriate ch
understood tha
20, 21, 22, 23,
charge distribu
microscopically
this has a bea
existance of ch
long-range orde
are not present

The primar
charge distribu
information ab
structural prop
benefits from t

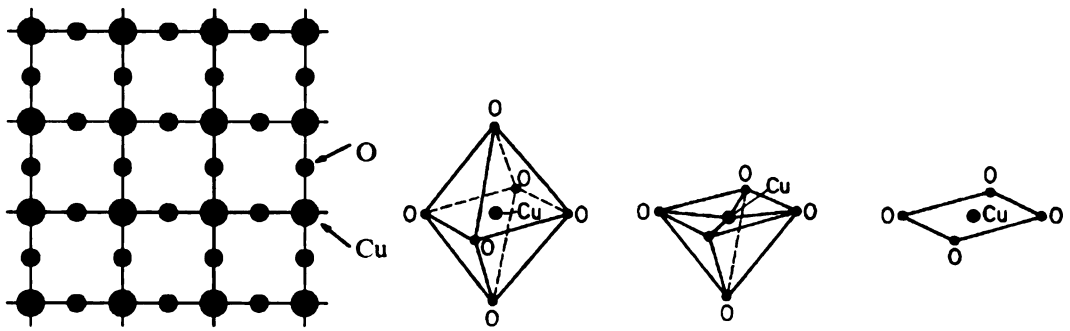

Figure 1.2: Schematics of the CuO_2 plane structure, and three typical building blocks of the planes that occur in various cuprate families [17].

typical building blocks that form the planes, as well as the structure of the plane, are shown in Figure 1.2 [17].

The HTS is achieved by a doping process, where an excess charge, either hole-like or electron-like, is introduced into the system at the synthesis stage by either appropriate chemical substitution or by varying the oxygen content. It is widely understood that the CuO_2 planes are the hosts for the doped charges [10, 16, 18, 19, 20, 21, 22, 23, 24]. There has been mounting interest in the possibility that the doped charge distribution in the CuO_2 planes of the high-temperature superconductors is microscopically inhomogeneous, possibly with a striped morphology [25, 26], and that this has a bearing on the high temperature superconductivity itself. However, the existance of charge stripes in superconducting samples is not fully established. No long-range ordered static stripes are observed which means that either such formations are not present, or they are short range ordered and not observable.

The primary interest of this study is to investigate *the local nature* of the doped charge distribution in the LSCO and LBCO systems. The method used to access the information about the charge distribution is indirect, and involves a study of the local structural properties as a function of doping and temperature. This type of study benefits from the strong charge-lattice coupling evidenced in variety of experiments

on these syste

In what fo

magnetic, supe

served in the p

by a review of

followed by the

1.2 Pha

Soon after the

class of coppe

they share a

is frequently

cuprates, prin

that has been

of LSCO [35]

such as magn

temperature-

$La_{2-x}Sr_xCuO$

doping issue,

anomalous fe

1.2.1 Do

Properties of

interpreted in

classify the n

undoped, un

on these systems [18, 26, 27, 28, 29, 30, 31].

In what follows in this chapter, we first review the 214 phase diagram, addressing magnetic, superconducting and structural properties, as well as certain anomalies observed in the phase diagram. The stripe phase concepts are introduced next, followed by a review of the experimental results. Motivation for the current study is given, followed by the thesis outline that closes the chapter.

1.2 Phase diagram of 214 HTS cuprates

Soon after the discovery of superconductivity in the LBCO and LSCO systems, a wide class of copper oxides was found to exhibit HTS properties, and it was realized that they share a quite universal electronic phase diagram [32, 33, 34]. The 214 system is frequently used as a prototype for constructing the universal diagram of the HTS cuprates, primarily because it could be doped over a wide range and is a system that has been extensively studied and characterized. The very rich phase diagram of LSCO [35] is presented schematically in Figure 1.3, highlighting various aspects such as magnetism, superconductivity, and structure. The phase diagram is in the temperature-doping phase space, with the doping axis featuring the Sr-content, x, in $La_{2-x}Sr_xCuO_4$, rather than the charge concentration. After a short digression on the doping issue, we review a variety of properties of the HTS cuprates, as well as certain anomalous features that were observed.

1.2.1 Doping

Properties of the 214 family, as well as of various other layered cuprates, can be interpreted in terms of the charge doping into the CuO_2 planes. It is common to classify the materials of any given family of HTS cuprates with respect to doping as undoped, underdoped, optimally doped, and overdoped. This jargon relates to the

Figure 1.3: S
system [35].
are addresse

amount of d
is a maximu
parent comp

The dopi
compound o
as $La_2^{3-}Cu^{2-}$
partially fill
particular st
further in th

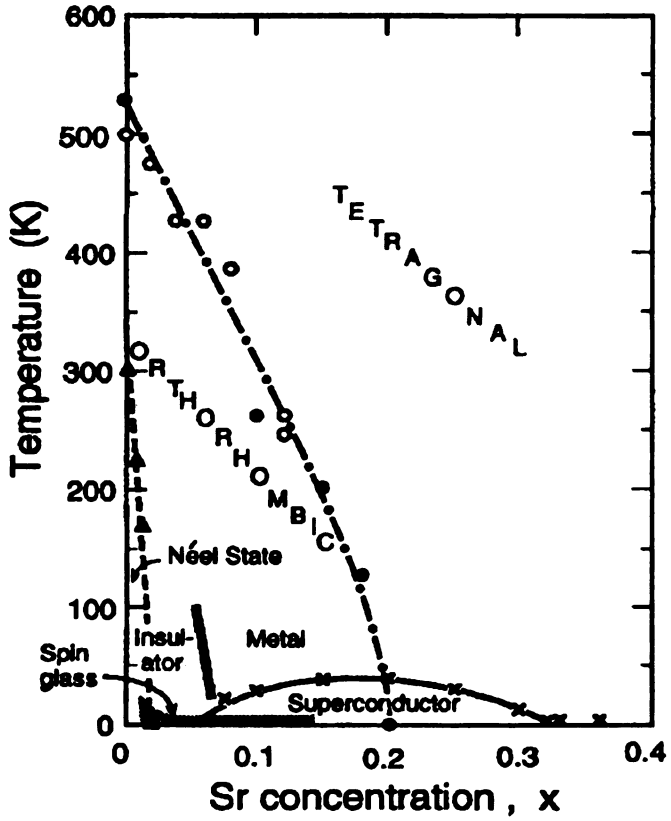

Figure 1.3: Schematic phase diagram of the 214 HTS cuprates featuring the LSCO system [35]. Note that this diagram does not show several anomalous features which are addressed in the text.

amount of doped charge relative to the concentration for which T_c of the material is a maximum. The undoped endmember of a series is commonly referred to as the parent compound.

The doping process can be illustrated by exploring the 214 case. The parent compound of this system is La_2CuO_4 (LCO), whose valence states are identified as $La_2^{3+}Cu^{2+}O_4^{2-}$. We note that the Cu-ion has the configuration $3d^9$, having one partially filled shell. This is important both for the magnetism of the system and a particular structural distortion that occurs in the 214 family, which will be addressed further in this Chapter. In this sense the Cu-ion could be considered to have one d-

hole. The dop

or Ba^{2+} for ex

(A=Sr.Ba). T

and hence nor

for La and O

to introduce c

the sample eit

deficient and

summarized u

When evo

tion has to be

tion of the ch

proper synthe

in Chapter 3

the concentra

the 214 mate

holes per cop

parameter. V

Through

tems only, a

doped La_2C

1.2.2 M

The parent

lators [16, 3

induce a gap

the CuO_2 pl

hole. The doping in 214 could be achieved by chemical substitution of La^{3+} with Sr^{2+} or Ba^{2+} for example, and this is described using the chemical formula $La_{2-x}A_xCuO_4$ (A=Sr,Ba). The dopant ions contribute one electron less to the system than La does, and hence nominally act as acceptors. Keeping the formal ionic charges of +3 and -2 for La and O respectively, the formal ionic charge of Cu is $2+x$. Another possibility to introduce charge into the 214 system is to vary the O-content of the sample, when the sample either contains excess oxygen that occupies interstitial sites, or is oxygen-deficient and vacancies are present on some oxygen sites. Both doping routes are summarized using the chemical formula $La_{2-x}A_xCuO_{4-\delta}$.

When evolution with doping of various HTS properties is investigated, a distinction has to be made between the concentration of the doped charge and the concentration of the chemical species used for doping. The knowledge of the later is ensured by proper synthesis of the sample and its careful characterization, as discussed in detail in Chapter 3. For every HTS cuprate family there is a unique relationship between the concentration of the doped holes and the concentration of the dopant ions. For the 214 materials this relationship is $p = x - 2\delta$ [20], where p is the concentration of holes per copper, x is the dopant ion concentration, and δ is the oxygen deficiency parameter. When δ is zero, the sample is said to be stoichiometric.

Throughout this thesis the '214' label refers to $La_{2-x}A_xCuO_4$ (A=Sr,Ba,Nd) systems only, and not the entire 214 family, which in addition includes excess-oxygen doped $La_2CuO_{4-\delta}$ and electron-doped $Nd_{2-x}Ce_xCuO_{4-\delta}$, for example.

1.2.2 Magnetism

The parent cuprate compounds, such as La_2CuO_4 and $YBa_2Cu_3O_6$, are Mott insulators [16, 36], due to the strong electron-electron correlations. These correlations induce a gap of $\sim$2 eV in a half-filled band. The spins of the unpaired electrons in the CuO_2 planes exhibit an antiferromagnetic (AF) order [35]. This AF state occurs

Figure 1.4: In-

obtained for si

in the parent c

temperature a

is labeled as th

and with solid

at very low te

The magnetic

temperatures, a

phase transitio

at around $x =$

1.2.3 Supe

Superconductiv

at low tempera

diagram in Fig

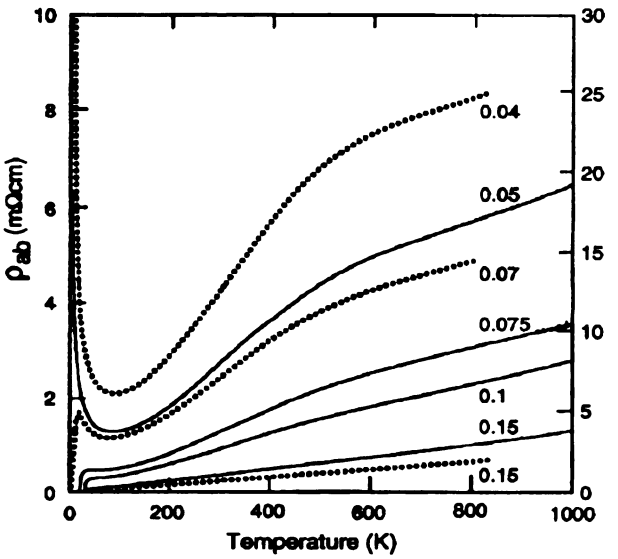

Figure 1.4: In-plane resistivity of LSCO as a function of temperature and doping, as obtained for single crystal samples [10].

in the parent compound at lower temperatures and persists in a very narrow range of temperature and doping [37, 38]. In the phase diagram in Figure 1.3 this AF phase is labeled as the 'Néel state', and the corresponding phase line is presented as dashed and with solid triangles. In the limited underdoped regime, above $x = 0.02$ and at very low temperatures, as indicated, there is also a spin-glass phase [39, 40, 41]. The magnetic correlation strength is weakened as doping progresses [42]. At higher temperatures, and outside the AF phase, the system is in a paramagnetic state. The phase transition from an insulating to a metallic phase [36] at low temperature occurs at around $x = 0.06$ [16, 35], as denoted by the thick solid line.

1.2.3 Superconductivity

Superconductivity in the LSCO [43, 44] and LBCO [45, 46] occurs for $0.06 \leq x \leq 0.26$ at low temperatures. The HTS transition temperature, T_c, is denoted on the phase diagram in Figure 1.3 by the solid line with cross-symbols. This bell-shaped curve

has a maxim

Within any g

referred to as

The optimal c

The region of

while the ove

where the su

heavily overd

superconduc

that $T_c(x)$ c

reflecting su

observed in

In the super

that shows l

range, as ol

shown) is a

with the st

planes.

1.2.4 S

The crysta

still not ful

tural phase

example, r

tem exhibi

family, exh

ing $0 \leq x$

has a maximum at around $x = 0.15$ for stoichiometric LSCO and LBCO samples. Within any given HTS cuprate family the doping at which $T_c = T_c^{max}$ occurs is referred to as the optimal doping. Above and below optimal doping T_c decreases. The optimal doping in the LSCO family of stoichiometric samples occurs at $x = 0.15$. The region of the phase diagram with $x < 0.15$ corresponds to the underdoped regime, while the overdoped regime is when $x > 0.15$. The portion of the overdoped region where the superconductivity is completely suppressed [20] is often referred to as the heavily overdoped region. Within the $0.06 \leq x \leq 0.26$ region and at $T > T_c$, as far as superconductivity is concerned, the material is in its normal state. It should be noted that T_c(x) curve exhibits an anomalous dip at $x = 1/8$ (not shown in Figure 1.3), reflecting suppressed superconductivity at this doping level. This and other anomalies observed in the phase diagram of the HTS cuprates will be addressed in Section 1.2.5. In the superconducting state the resistivity drops to zero, as illustrated in Figure 1.4 that shows LSCO in-plane resistivity for various dopings and over a wide temperature range, as observed in single crystal samples [10]. The out-of-plane resistivity (not shown) is an order of magnitude higher than the in-plane resistivity [16], in accord with the structural anisotropy and the notion of the doping being into the CuO_2 planes.

1.2.4 Structure

The crystal structure of high-T_c superconductors [48] plays an important [27] and still not fully understood [25] role in their interesting properties. The different structural phases of the first discovered [1] 214 superconductors $La_{2-x}(Sr,Ba)_xCuO_4$, for example, may have a direct impact on their physical properties [25]. The 214 system exhibits several structural phases [48]. The parent LCO, as well as its Sr-doped family, exhibit one structural phase transition [49, 50, 51, 52]. In the range of doping $0 \leq x \leq 0.2$, and at various transition temperatures, LSCO undergoes a second

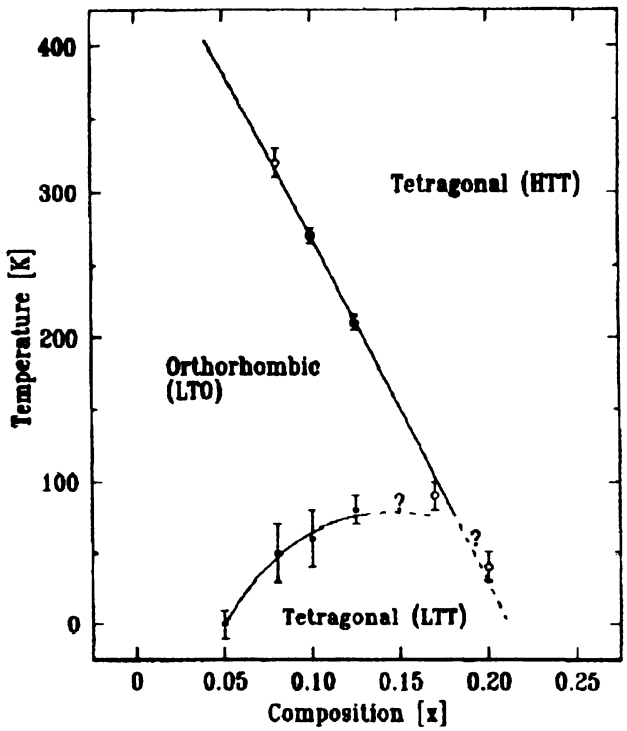

Figure 1.5: Structural phase diagram for the LBCO system [47].

order structural phase transition from a low temperature orthorhombic (LTO) phase to a high temperature tetragonal phase (HTT) [50], as indicated by the dash-dotted line in Figure 1.3. The LBCO system undergoes the same phase transition [53], and also features an additional low temperature tetragonal (LTT) structural phase [47] for doping in the approximate range of $0.05 \leq x \leq 0.15$ at lower temperature. This phase transition is first order. The corresponding structural phase diagram of the LBCO system [47] is shown in Figure 1.5. The LTT phase also appears in Nd co-doped LSCO samples [54, 55].

The structural phases in question can be visualized in a simple manner if the HTT structure is taken as the starting point [56]. The HTT structure (also known as T-phase structure, see Chapter 3 for more details) features corner-sharing CuO_6 octahedra and La atoms surrounding it, as shown in Figure 1.6. The structure has a

a
[10

body centered

per unit cell.

representation

merely a conve

of atoms that

structural para

octahedra are a

The LTO str

rotating the Cu

between nearest

hedra. The CuO

their basal plane

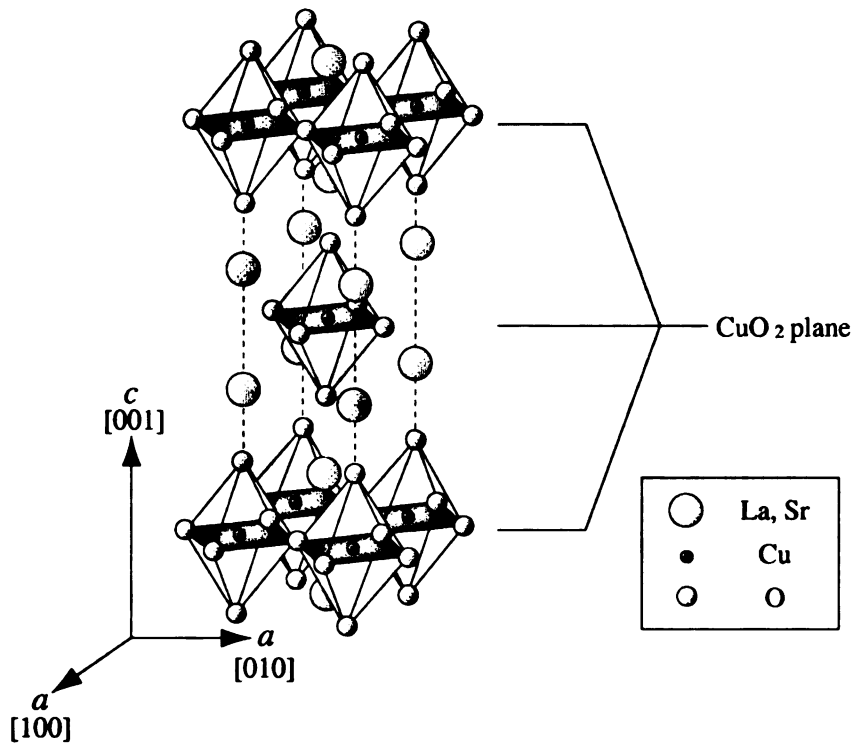

Figure 1.6: The HTT structure.

body centered tetragonal lattice, space group $I4/mmm$ [56], and two formula units per unit cell. It is common practice to present this structure using an equivalent representation [44], where the a and b axes are 45°-rotated about the c-axis. This is merely a convenience, since the HTT phase is then described using the same number of atoms that is necessary for description of the LTO and LTT phases, and the structural parameters obtained from the data are directly comparable. The CuO_6 octahedra are aligned along the c-axis.

The LTO structure, space group *Bmab* (or isomorphic *Cmca*) [44], is obtained by rotating the CuO_6 about the [010] axes such that the rotation direction alternates between nearest neighbors in the basal plane, as governed by the corner-shared octahedra. The CuO_6 planes are then buckled, with all planar O-atoms displaced out of their basal planes, as illustrated in Figure 1.7. The apical O and La sites are displaced

Figure 1.7: (

parallel to the

In the LTT

rotating the oc

bonds, in cont

about the c-ax

half of the pla

La sites are ag

is illustrated ir

compared.

The CuO_6 o

featuring 4 sho

is present in th

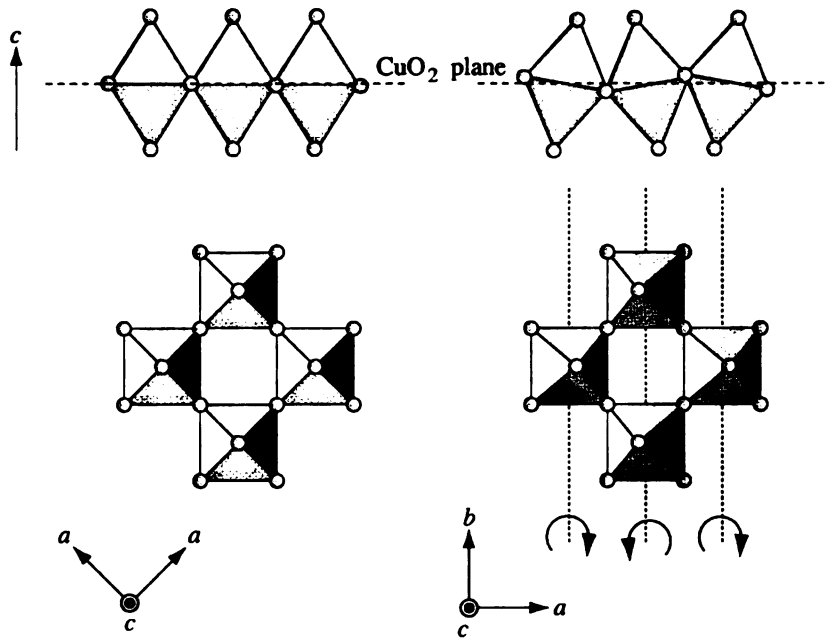

Figure 1.7: Comparison of the CuO_6 behavior in the HTT and LTO structures.

parallel to the a,b-planes since the octahedra are approximately rigid.

In the LTT phase, space group $P4_2/ncm$ [47], the displacements are obtained by rotating the octahedra about [110] directions. The tilt axis is along the planar Cu-O bonds, in contrast to the octahedral tilting in the LTO phase which is 45°-rotated about the c-axis with respect to the planar Cu-O bonds. Note that in the LTT phase half of the planar O atoms are undisplaced from the basal planes. The apical O and La sites are again displaced parallel to the a,b-planes, parallel to [110] directions. This is illustrated in Figure 1.8, where all three phases occurring in the LBCO system are compared.

The CuO_6 octahedra in all three structural phases are Jahn-Teller (JT) distorted, featuring 4 short in-plane bonds and 2 long apical bonds. The effect in 214 system is present in the parent compound, as well as in the doped variants. We briefly

Figure 1.8: Co

LTT. The top

denote the octa

highlight the o

the literature

environment, a

the Jahn-Teller

such a way as

such that origi

in Figure 1.9

1.2.5 An

The rich phase

of anomalies

universal phas

Early syste

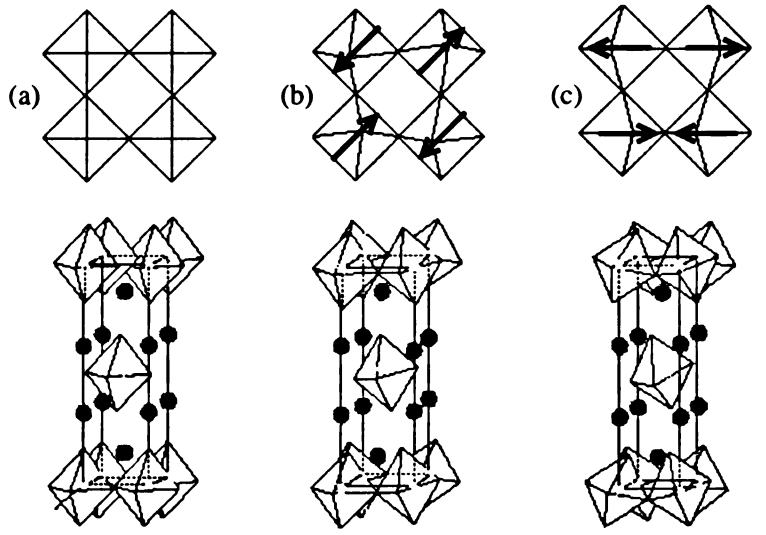

Figure 1.8: Comparison of the LBCO structural phases: (a) HTT, (b) LTO, and (c) LTT. The top portions show the c-axis perspective of the CuO_6 octahedra. Arrows denote the octahedral tilting patterns.

highlight the origin of this effect, and for greater details refer the interested reader to the literature [57]. The d-hole in the case of Cu^{2+} is in the E-state in the octahedral environment, and the possible orbital symmetries are $3z^2-r^2$ or x^2-y^2. According to the Jahn-Teller theorem, the system lowers its energy by distorting the octahedron in such a way as to lift the degeneracy of the orbitals. The structural distortion occurs such that originally regular octahedron is elongated. This is schematically presented in Figure 1.9 [57].

1.2.5 Anomalous features of the phase diagram

The rich phase diagram of HTS cuprates exhibits several peculiar features. A number of anomalies observed in the properties of the cuprates are reviewed in light of the universal phase diagram shown in Figure 1.10.

Early systematic studies of doping in HTS cuprates revealed the existence of an

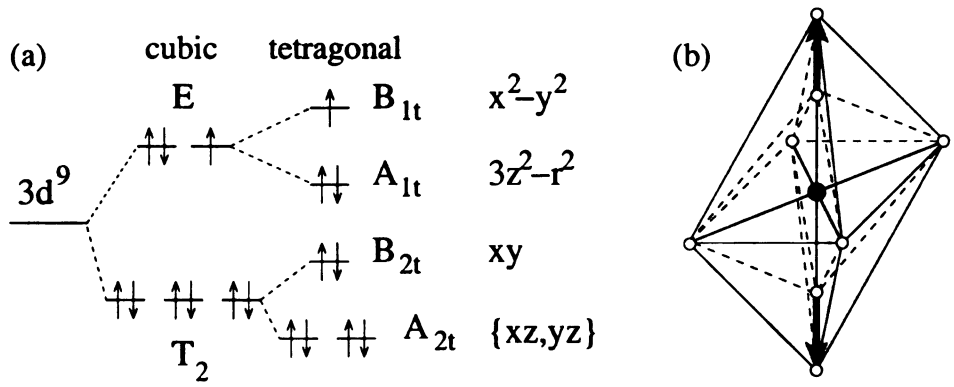

Figure 1.9: The Jahn-Teller distortion: (a) Rigid-band schematic representation of the Cu^{2+} level structure in octahedral environment. Orbitally degenerate E and T_2 levels are created in the large cubic crystal field. Further splitting of the levels occurs in the presence of a small tetragonal distortion. The Jahn-Teller distortion lifts the degeneracy [57]. (b) Ideal CuO_6 octahedron (dashed lines), with Cu in the middle and O atoms at the vertices, has six equal Cu-O bonds. When Jahn-Teller distorted, the octahedron elongates (solid lines), as indicated by the arrows, which results in two long and four short Cu-O bonds.

anomalous suppression of T_c in a narrow doping range around rational value of 1/8 holes per copper, as indicated by the arrow in Figure 1.10. This was first established in the LBCO system from magnetization and resistivity measurements [45], and is known as the 1/8-anomaly. Similar observations followed in LSCO [43] and other HTS cuprates. The suppression of T_c is most prominent in the LBCO system, and is incomplete in some HTS systems, where it typically appears as a shoulder in the T_c doping dependence. After the structural diagram of LBCO was established [47], it was proposed that the anomaly relates to the LTT structural phase [30, 54, 58], which was also blamed for the overall lower values of T_c in the LBCO system, as compared to the LSCO. A possible relationship between the anomaly and the LTT phase has been further considered for the LSCO system, but crystallographic studies

failed to evid

at very low t

for various th

Another s

in the *norma*

changes in th

doped region

temperature a

seen in ordina

metal", while

been argued th

when temperat

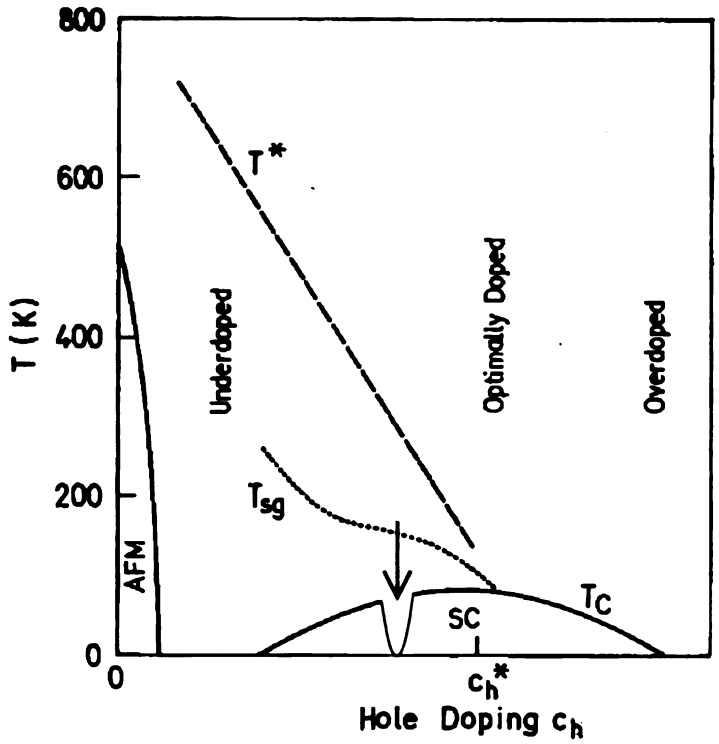

Figure 1.10: Universal phase diagram of the HTS cuprates.

failed to evidence the LTT phase, suggesting that the LSCO is in the LTO phase even at very low temperature [30]. The 1/8-anomaly established an important checkpoint for various theories of the HTS phenomenon in cuprates.

Another set of anomalies is seen in measurements of various physical properties in the *normal* state of the *underdoped* HTS cuprates. Different probes sensitive to changes in the electronic and magnetic channels all observe anomalies in the underdoped region and well above T_c. The anomalies disappear at some characteristic high temperature and also in the overdoped region, where the properties resemble those seen in ordinary metals. The anomalous normal state is often labeled as a "strange metal", while the state where anomalies disappear is referred to as "metallic". It has been argued that the system exhibits a crossover behavior from one state to the other when temperature or doping are changed [59].

For exam

ior up to ve

behavior, bu

derdoped sa

Hall coefficie

whereas tem

ture and in t

infrared spect

spectroscopy

magnetic reso

mental work i

Two crosso

temperature.

indicated in F

present on wh

suggest differe

lated to the p

one relates to

as the pseudo

features corre

to a complete

in the sense t

to be a univer

The new e

stood at prese

to the HTS ph

conditions hav

For example, dc-resistivity measurements revealed an anomalous linear behavior up to very high temperatures in the optimally doped case, and similar linear behavior, but with a change in slope at some characteristic temperature in the underdoped samples (see Figure 1.4) [10]. Also, temperature dependent normal state Hall coefficient was observed below certain temperature in the "strange metal" state, whereas temperature independent Hall coefficient was obtained for high temperature and in the overdoped regime [60]. Various anomalies were also observed by infrared spectroscopy [61, 62], electronic specific heat measurements [63], tunneling spectroscopy [64], angle resolved photoemission spectroscopy [65, 66], and nuclear magnetic resonance technique [59, 67, 68, 69, 70, 71]. A recent review of the experimental work is provided by Timusk and Statt [59].

Two crossover temperatures were suggested from the experiments, an upper crossover temperature, T^*, and a lower crossover temperature, T_{sg}. These crossover lines are indicated in Figure 1.10. However, in the HTS community there is no consensus at present on whether these two are indeed different, since different probes appear to suggest different temperature scales. It has been suggested that the upper one is related to the phenomenon affecting the electronic density of states, whereas the lower one relates to the magnetic AF excitations [59]. The upper scale, T^*, is also known as the pseudogap in the normal state of the cuprates, since the observed gap-like features correspond to an incomplete suppression of the density of states, rather than to a complete gap. The pseudogap appears to be related to the superconducting gap in the sense that it smoothly evolves into the superconducting gap, and is believed to be a universal feature of the HTS cuprates [59].

The new energy scale and its relevance to the HTS phenomenon is not fully understood at present. One possible and rather speculative interpretation of its relationship to the HTS phenomenon could be as follows. For superconductivity to take place two conditions have to be met: (i) the superconducting pairs have to be formed and (ii)

the pairs hav

energy scales

plified scenar

Bose conden

at temperatu

densation oc

preformed pa

model involve

place on a mi

characteristic

doped charge

doped charges

1.3 Cha

1.3.1 Th

Layered La_2C

attracted cons

systematic stu

properties, suc

These isostruc

two-dimension

parent compou

Although Cu a

exhibit differe

while Ni^{2+} is i

of these systen

the pairs have to Bose condense. These two events are associated with corresponding energy scales. For the BCS superconductors the two energy scales, in this oversimplified scenario, would be the same, leading to a *simultaneous* pair formation and Bose condensation. For the HTS cuprates the two energy scales could be different: at temperature $T > T_c$ the pairs are formed, and at lower temperature, T_c, the condensation occurs. Theories for the HTS cuprates exist which incorporate the idea of preformed pairs in the normal state as one of their key ingredients [59]. One such model involves charge stripes [72]. This model predicts that phase separation takes place on a microscopic scale, such that stripes of doped charge are formed at some characteristic temperature higher than T_c. Above the characteristic temperature the doped charge distribution is uniform, and below the characteristic temperature the doped charges are confined to linear stripes separated by undoped AF regions [59].

1.3 Charge stripes

1.3.1 Theoretical highlights

Layered La_2CuO_4 and La_2NiO_4 compounds, containing 3d-transition metals, have attracted considerable experimental and theoretical attention as suitable systems for systematic studies of the electron correlation effects and their influence on the physical properties, such as the metal-insulator transition, magnetism, and superconductivity. These isostructural compounds are controllably dopable and maintain their quasi two-dimensionality without significantly altering the K_2NiF_4-type structure. The parent compounds of both 214 cuprates and nickelates are AF insulators [43, 73]. Although Cu and Ni have the same nominal valence in the parent compounds, they exhibit different charge and spin states: Cu^{2+} is in the $3d^9$ state with spin 1/2, while Ni^{2+} is in the $3d^8$ state with spin 1. This results in quite different properties of these systems when they are doped. On Sr substitution for La in $La_{2-x}Sr_xMO_4$

(M=Cu,Ni)
the overdop
not supercon

The HTS
such a mann
the coexiste
volves segre
in the undo
compound
two-dimens
strong tend
suggested
eral theori
mechanism
and this
theories a
have to b
issue will

The c
taneously
ically rep
Within t
and the
circles de
order *wit*
and filled
within a

(M=Cu,Ni), the cuprates become superconducting at $x = 0.06$ and paramagnetic in the overdoped regime, while the nickelates become paramagnetic at $x = 1.0$ and are not superconducting at any doping [74].

The HTS in cuprates is achieved by introducing holes into an AF insulator in such a manner that *local* AF order survives the doping [75]. One way to understand the coexistence of holes doped into the CuO_2 planes and the local magnetism involves segregation of the doped holes in such a way that the AF order is preserved in the undoped regions [76]. Distribution of the doped holes within an AF parent compound has been considered in a large body of theoretical work, exploring quasi two-dimensional models featuring the MO_2 planes. These considerations predicted a strong tendency for phase separation with an inhomogeneous charge distribution and suggested their striped morphology [77, 78, 79, 80, 81, 82, 83, 84, 85, 86, 87, 88]. Several theories exist that incorporate stripe correlations to explain the superconducting mechanism in cuprates. Details of these theories are out of the scope of this thesis and this review, and we refer interested reader to the literature [89, 90, 91]. Some theories also predict that for the charge stripes to be energetically stabilized, they have to be insulating [77], and therefore competing with superconductivity [92]. This issue will be revisited after experimental evidence for the stripes is reviewed below.

The concept of a stripe phase, where the doped charges concentrate along spontaneously generated domain walls separating local AF insulating regions, is schematically represented in Figure 1.11. The figure shows a CuO_2 plane featuring stripes. Within the plane only the Cu-sites are shown as circles. The arrows indicate spins and the arrays of successively filled and open circles denote the stripes. The filled circles denote the dopant-induced holes as centered on Cu-sites, although the charge order *within* a single stripe is not suggested by the models. The distribution of empty and filled circles shown here only indicates that there is one hole per two copper sites within a stripe for the doping shown in Figure 1.11. The magnetic order within the

Figure

plane is AF

aries for the

within the s

cuprates is s

1.3.2 Ex

Charge stripe

iments [95].

onal" [96, 97

respect to the

temperature

is also tempo

dence for the

correlated m

105, 106]. Th

distributions

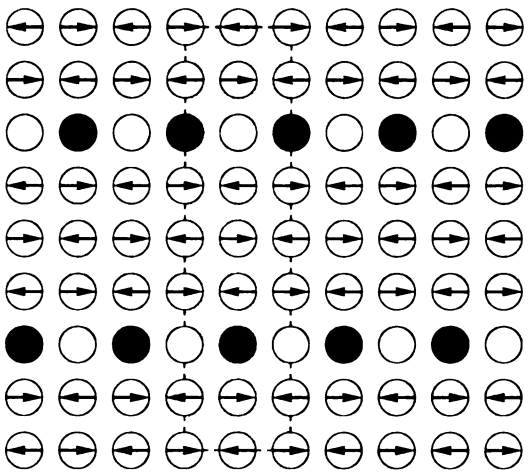

Figure 1.11: Schematics of the stripe phase model for $p = 1/8$ doping [26].

plane is AF between the stripes, and the stripes represent antiphase domain boundaries for the spin order. Theoretical models feature homogeneous charge distribution within the stripes [26]. The importance of the stripes to the HTS phenomenon in cuprates is subject of the intensive investigation [85, 89, 93, 94].

1.3.2 Experimental evidence

Charge stripes were first evidenced in $La_{2-x}Sr_xNiO_{4+\delta}$ from electron diffraction experiments [95]. Followup experiments indicated that the stripes in nickelates are "diagonal" [96, 97, 98, 99, 100, 101], referring to a stripe direction that is 45°-rotated with respect to the in-plane Ni-O bonds. The periodicity of the charge stripes is found to be temperature dependent, suggesting that the charge concentration along each stripe is also temperature dependent [102]. There is now considerable experimental evidence for the existence of striped charge distributions in two other classes of strongly correlated materials, $La_{2-x-y}Nd_ySr_xCuO_{4+\delta}$ [26, 31, 103] and $La_{1-x}Ca_xMnO_3$ [104, 105, 106]. There is also growing circumstantial evidence that similar striped charge distributions are present more widely in other HTS cuprates [107, 108, 109, 110].

The mos
geneities exi
in neutron d
strongly cou
are static an
also LRO an
patterns. H
on where to
peculiar cha
perlatice pe
Figure 1.12
collaborato
of the char
issues. Firs
LTT phase
family are s
rational 1/8
lower temp
is led by th
shown in F
peak intens
and probin
for rational
having perio
with the ma
"vertical", i

The most compelling experimental evidence that microscopic charge inhomogeneities exist in these systems comes from the observation of superlattice peaks in neutron diffraction patterns. The stripes of localized charge in these systems are strongly coupled to the lattice and induce structural distortions. When the stripes are static and long range ordered (LRO), the corresponding structural distortions are also LRO and observable in the form of structural superlattice peaks in the diffraction patterns. However, these peaks typically have weak intensities and a good intuition on where to look for them in the experimental data is crucial. In addition to this peculiar charge ordering, a spin modulation occurs and corresponding magnetic supperlatice peaks appear as well [26]. Charge-order supperlattice peaks are shown in Figure 1.12 for the $La_{2-x-y}Nd_ySr_xCuO_4$ sample, as first found by Tranquada and collaborators [26, 31]. Detailed studies of the temperature and Sr-doping dependence of the charge stripes in the Nd-codoped LSCO samples revealed several important issues. First, the long-range static charge stripe order seems to appear only in the LTT phase of the Nd-codoped LSCO system, suggesting that the stripes in the 214 family are strongly coupled to the LTT environment [111] and are most pronounced at rational 1/8 doping [112, 113, 114]. Second, on cooling the magnetic order sets in at lower temperature than the charge order, suggesting that the observed phenomenon is led by the charge rather than the spin degrees of freedom [26, 31, 75]. This is shown in Figure 1.13 where the temperature evolution of corresponding superlattice peak intensities is presented. The charge order and spin order appear to be coupled, and probing either of them may indicate the presence of the stripe phase. Third, for rational 1/8 doping the charge and spin order are periodic, with the spin order having periodicity twice as large as that of the charge order, as shown in Figure 1.11 with the magnetic unit cell indicated. The stripes observed in cuprate samples are "vertical", i.e. along the direction of the in-plane Cu-O bonds [26].

Figure 1.12:
at 10 K (soli
measured at
lines) [31].

1.3.3 Str

The direct ev
ing nickelates
pete with sup
samples appea
perconductivit
between the su

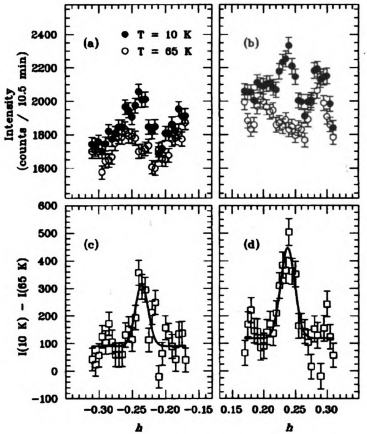

Figure 1.12: (a) and (b) Charge order superlattice peaks in $La_{1.48}Nd_{0.4}Sr_{0.12}CuO_4$ at 10 K (solid circles) and 65 K (empty circles). (c) and (d) Difference in intensity measured at 10 K and 65 K. The data have been fit using Gaussian profiles (solid lines) [31].

1.3.3 Stripes and superconductivity

The direct evidence for the LRO charge stripes has only been seen in the insulating nickelates and in selected cuprate samples where this ordering appears to compete with superconductivity [115]. The static LRO charge stripes in Nd co-doped samples appear to be pinned by the LTT structure, and in samples where the superconductivity is suppressed. This is shown in Figure 1.14, where the correlation between the suppression of superconductivity in $La_{1.6-x}Nd_{0.4}Sr_xCuO_4$ at $x = 1/8$ and

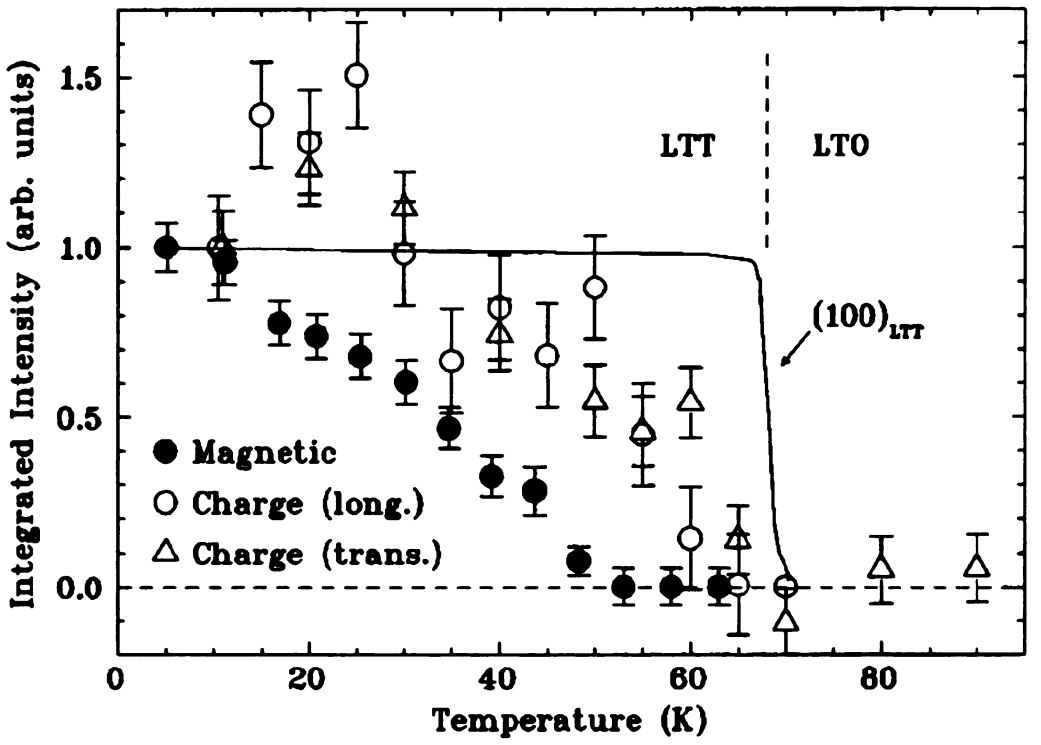

Figure 1.13: The superlattice peak intensities in $La_{1.48}Nd_{0.4}Sr_{0.12}CuO_4$ as a function of temperature, normalized to 10 K. Solid symbols correspond to the magnetic peak, open symbols correspond to the charge-order peak, and solid line shows the behavior of the structural superlattice peak of the LTT phase [31].

the maximum in the charge-ordering temperature for the long range ordered static stripes is brought to light. This observation could provide a natural explanation of the 1/8-anomaly observed in the HTS cuprates, since the formation of long-range charge stripes in this system appears to be stabilized at this rational doping fraction [26, 31, 113, 115, 116, 117].

The role that stripes play in the HTS is not fully understood at present, although there is a strong sense that these two phenomena are related. While the LRO stripes appear to suppress superconductivity, weak stripe order was evidenced in the vicinity of T_c in the excess-oxygen-doped $La_2CuO_{4+\delta}$ [118]. The superconducting

Figure 1.14:

perconductiv

T_c is suggest

ple. single cry

that the low-

$(1/2 \pm \alpha, 1/2$

linearly with

observed for t

linear relation

Based on thes

quires stripes

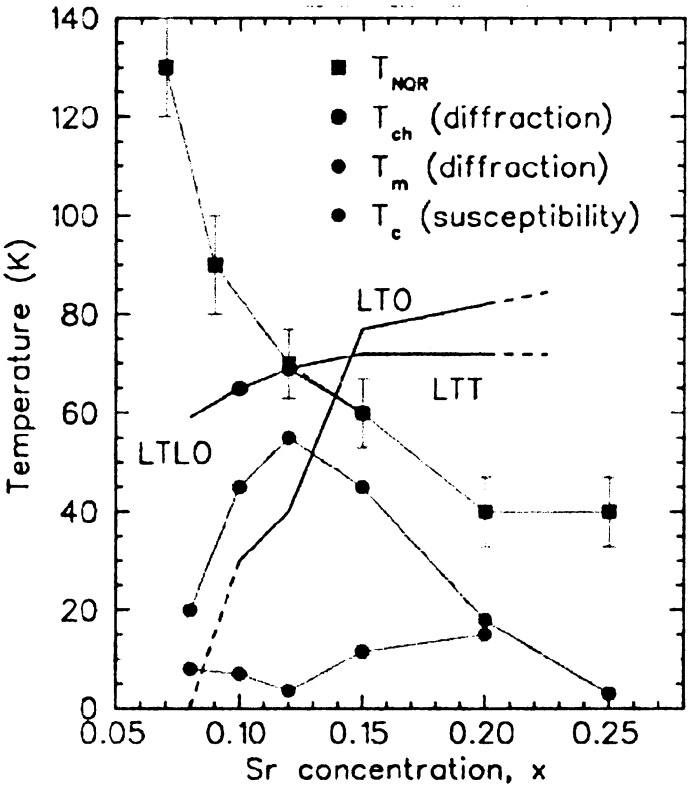

Figure 1.14: Phase diagram of $La_{1.6-x}Nd_{0.4}Sr_xCuO_4$. Note that the suppression of superconductivity at $x = 1/8$ correlates with the maximum in the charge-ordering [121].

T_c is suggested to be linearly dependent on the inverse stripe spacing. For example, single crystal $La_{2-x}Sr_xCuO_4$ low-energy neutron scattering studies [119] revealed that the low-energy spin-fluctuation peak position shifts on doping from $(1/2, 1/2)$ to $(1/2 \pm \alpha, 1/2)$ and $(1/2, 1/2 \pm \alpha)$, where α is the incommensurability. The T_c scales linearly with α up to the optimal doping. In $YBa_2Cu_3O_{6+x}$ similar behavior was observed for the width of the peak in the spin susceptibility [120], which also has a linear relationship with T_c. In the overdoped regime the stripe order disappears [75]. Based on these empirical observations it was suggested that superconductivity requires stripes that are neither static and LRO, nor too wildly fluctuating [75].

1.4 Motivation

As presented, two unusual phenomena are observed in the normal state in the underdoped cuprates: a pseudo-gap [59] in the electronic [33, 122, 123, 124] and magnetic [125, 126] densities of states, and the possibility that the doped charge in the CuO_2 planes of these materials is inhomogeneously distributed, possibly in a striped arrangement [26, 75, 85, 86, 87, 88, 90, 119, 127, 128, 129]. However, unlike the pseudogap phenomenon, the universal observation of stripes among different HTS systems has not been established.

The strongest evidence for stripes in the cuprates is the observation of *long range ordered* static charge stripes in $La_{2-x-y}Nd_ySr_xCuO_4$ compounds [26]. These have been seen in both insulating and superconducting compounds but they appear to compete with the superconductivity [121]. There is currently no direct evidence that the stripe phases exist in superconducting samples, although there has been an observation where stripes and superconductivity were observed in the same samples [115]. While static and long-range stripe order seems to suppress the superconductivity, *fluctuating short-range ordered* charge stripes may play an active role in the HTS phenomenon [75, 85, 86, 87, 88, 90, 129]. Such stripes would provide a natural explanation for incommensurate spin fluctuations [119, 130, 131, 132] observed in $La_{2-x}Sr_xCuO_4$ [119] and $YBa_2Cu_3O_{6+\delta}$ [133], as well as for various other experimental observations [121, 127, 133, 134, 135, 136].

Due to their possible role in the HTS phenomenon, it is clearly important to establish whether local charge-stripe ordered domains really exist in the superconducting regions of the phase diagram.

1.5 Approach

Various lattice effects in the high-temperature superconductors have been described in a number of recent reviews [25, 137, 138, 139, 140, 141]. The doped charges in the 214 system are coupled to the lattice, and produce a structural distortion [26, 44]. When the charges form LRO stripes, the structural modulation becomes periodic and a superlattice is observed in neutron, x-ray and electron diffraction [26, 31, 104, 105, 112, 115]. The absence of superlattice peaks can mean that the stripe order has disappeared. However, it is also possible that the stripes persist locally but are not long-range ordered and are fluctuating. In this latter case the *local* structural distortion due to the inhomogeneous charge distribution will persist even when the superlattice peaks have disappeared. A probe of the *local* structure can therefore give information about whether local stripe order exists even in the absence of the superlattice peaks.

In this study we use the atomic pair distribution function (PDF) analysis [142, 143, 144] of powder neutron diffraction data to look for evidence of local charge stripe order in $La_{2-x}Sr_xCuO_4$ and $La_{2-x}Ba_xCuO_4$. The aim is to explore the nature of the charge-distribution in these systems over a range of doping and temperature.

The atomic PDF technique is based on diffraction experiments, and it utilizes both the Bragg scattering that carries information on the average atomic positions and the diffuse scattering that carries local structural information. The PDF yields structure on various lengthscales, and is suitable for studies of the short range order, the intermediate range order, and the long range order in materials. The PDF can address the charge distribution issue only indirectly. By studying the local structure, that is expected to carry a fingerprint of the charge behavior, it is possible to infer information about the charge distribution. The rationale for our study came from the results of NMR studies, that indicated possible locally inhomogeneous doped charge distribution within the CuO_2 planes [107, 145, 146]. Also, detailed crystallographic

structural studies of $La_{2-x}Sr_xCuO_{4+\delta}$ showed that the average in-plane Cu-O bond rapidly contracts on doping [44]. The effect of the in-plane bond shortening on doping is accompanied with the reduction in the octahedral tilt angle [44]. Therefore, detailed PDF local structural study of the CuO_2 planes and the behavior of the CuO_6 octahedra have the potential of yielding important new information on the nature of the local charge distribution in this class of HTS cuprates.

1.6 Thesis outline

The material presented in this thesis is organized as follows. Chapter 2 represents a description of the PDF experimental technique, including explanations of several peculiar methods for extracting relevant information from the PDF, such as PDF peak height and width analysis. A detailed description of the sample preparation and characterization constitutes Chapter 3. Results on the structural response to local charge order in the CuO_2 planes of the LSCO and LBCO as a function of doping and temperature are presented in Chapter 4, which form the backbone of the thesis. Further local structural evidence that is supportive of the results presented in Chapter 4 is discussed in Chapter 5, where different tilt patterns are explored in more detail. The local structural aspects of the orthorhombic to tetragonal structural phase transition occurring in LSCO and LBCO are explored in Chapter 6. These results support the important relationship between the crystal structure and charge doping. Finally, motivated by recent *ab initio* theoretical results, in which the importance of the out-of-plane copper-oxygen bands has been emphasized, we searched for the experimental evidence in the structural data that would confirm (or otherwise) the theoretical findings. The results of this investigation are presented in Chapter 7. Concluding remarks and possible avenues for further work are given in Chapter 8.

Chapter 2

The Pair Distribution Function Technique

"It is bad when one thing becomes two. One should not look for anything else in the Way of the Samurai. It is the same for anything else that is called a Way. If one understands things in this manner, he should be able to hear about all ways and be more and more in accord with his own." (T. Yamamoto)

2.1 Introduction

The structure of materials often has profound consequences for their physical properties, and our understanding of these properties critically relies on the accurate structural determination. Various techniques have been developed over the time, focusing on different structural aspects. Diffraction based techniques have long been used to reveal microscopic structure of the materials [147, 148, 149, 150]. In a diffraction experiment the sample is exposed to a beam of x-rays, neutrons, or electrons, and scattered radiation is detected and recorded as a diffraction pattern. The structural information should be the same irrespective of the probe used. In practice, the choice of the probe is governed by the type of the interaction and the scattering properties of

the material. The structural information is obtained from the data, either via structural modeling, where applicable, or by other means. Structure is frequently studied under various conditions, such as pressure, temperature, electric and magnetic fields.

Conventional crystallographic structural studies of powders use diffraction information contained in the Bragg peaks only. The positions of the Bragg peaks provide information on the lattice constants and the underlying symmetry, while the intensities reveal details of the atomic arrangement within the unit cell. The structural information is routinely obtained using a least square Rietveld-type structural refinement method, where a model structure is proposed, its diffraction pattern is calculated and compared to the measured one [151]. The structure determined in this manner is known as the average crystallographic structure. This method is based on the assumption of the perfect three dimensional periodicity of the crystals. However, when dealing with nanocrystalline materials, or materials with significant degree of structural disorder, the average crystallographic description of the structure is no longer appropriate and does not provide information about local structural deviations which may be of key importance for understanding the physical properties of interest.

Structural disorder in a material, defined as any deviation from a strict long-range order, yields a diffuse scattering signal in the diffraction pattern. The signal is widely spread in reciprocal space, and of low intensity. Local structural information could be obtained by direct analysis of the diffuse scattering signal [152]. Obtaining local structural information in this manner is a subject of the single crystal diffuse scattering studies, that are both intensity-limited and require long data-collection times [153].

Alternative approach in studying the local structure and short range order in materials is found in the x-ray absorption experiments. The changes in the absorption spectrum are examined using x-rays tuned through the resonant energy of particular atomic species. Final state of the photoelectron is modified by the atoms surrounding

the excite

sorption s

electron s

in strong

are weake

trum is c

the higher

(EXAFS)

coefficient

provides st

the structu

to near nei

due to pha

Anothe

formation i

in a powder

possible to

structural s

pair distrib

ment [158],

The PDF m

amorphous

materials as

tural informa

and provides

damentals of

the PDF met

the excited atom, hence providing information on the local structure [154]. The absorption spectrum can be divided into two parts, distinguished by the strength of the electron scattering. At low electron energies the cross section is high, which results in strong modulations of the absorption spectrum. At higher energies modulations are weaker due to the weaker scattering. The low energy part of the absorption spectrum is considered in the x-ray absorption near edge spectroscopy (XANES), while the higher energy part is considered in the extended x-ray absorption fine structure (EXAFS) technique. In an EXAFS measurement, oscillations of the x-ray absorption coefficient on the high energy side of an absorption edge are studied [155, 156]. It provides structural information on the local environment of a specific atomic type in the structure. However, local structural information from EXAFS is typically limited to near neighbor distances. Furthermore, this information is problematic to analyze, due to phase shifts and multiple scattering effects of the photoelectron [157].

Another alternative way to study the local structure using diffuse scattering information is through a total scattering measurement on powder samples. Although in a powder diffraction measurement all directional information is sacrificed, it is still possible to obtain significant local structural information [144]. The total scattering structural study utilizes both Bragg and diffuse scattering information. The atomic pair distribution function (PDF) technique is based on a total scattering experiment [158], and is obtained by a sine Fourier transform of the scattering data [157]. The PDF method has been widely used to study the structure of glasses, liquids and amorphous materials [159], and more recently has been applied to study crystalline materials as well [143]. The advantages of the PDF method are that it provides structural information on various lengthscales (short, intermediate and long range scale), and provides information in direct rather than reciprocal space. In this chapter fundamentals of the total scattering experiment using neutron time-of-flight probe and the PDF method are presented.

2.2 The PDF method

The atomic PDF method is based on a total scattering experiment where both Bragg and diffuse scattering information are utilized to obtain structural information. The incident beam of neutrons of known state is scattered from a powder sample. The sample is seen by the beam as a collection of scattering centers characterized by a potential. The interaction of the incident beam particles with the potential affects their momentum and, in general, their energy. By experimentally determining the final states of the scattered particles and knowing the initial state the information on the scattering potential and the underlying sample structure can be determined. In a powder measurement the scattering intensity is obtained as a function of the scattering-vector magnitude, Q. The structural information is contained in the coherent part of the scattering intensity, that is extracted from the measured total intensity. The coherent intensity determines the total scattering structural function, S(Q), which is then reduced and Fourier transformed into real space yielding the PDF. Here we will show how this comes about, and what kind of structural information is contained in the PDF.

The PDF foundations are deeply rooted in scattering theory. An important component of the scattering process is the nature of the interaction between the probe and the sample. Both neutrons and x-rays are weakly scattered by matter. Neutron scattering involves a strong and short ranged interaction between the beam and the sample nuclei, and in principle, due to the spin of the neutron, dipolar scattering from any magnetic moments in the sample. The interaction between the neutron beam and the nuclear scattering centers has the effective range of the order of femtometers. The typical separation between the scattering centers is of the order of angstroms. Therefore most of the incident neutron beam with thermal energies will simply pass through the sample unchanged. More important consequences of the potential's short range are that (i) the scatterers as seen by the beam of neutrons are point-like, and that

(ii) the scattering from each scattering center is isotropic. The neutron scattering formalism starts with a consideration of the scattering of a neutron beam from a single isolated nucleus. Such a point-like scattering center will scatter the incident plane wave into a spherical scattered wave [160]. The Born approximation applies for weak perturbation potentials only, and therefore using it for a strong potential, such as the one we are dealing with, is strictly incorrect. Nevertheless, it has been used to *construct* the approximate potential that provides the scattered s-wave. This constructed potential is known as the Fermi pseudo-potential. The consideration then extends to a spatially distributed set of point-like scattering centers that represent the sample.

The fingerprint of each scattering event is the scattering amplitude that measures the fraction of the incident wave scattered in a spatial angle element in a given direction, and that carries the structural information. The elastic scattering amplitude, $f_{\vec{k}i,\vec{k}f}(\theta,\phi)$, where $\vec{k}_i$ and $\vec{k}_f$ denote incident and scattered wave vectors respectively, is

$$f_{\vec{k}i,\vec{k}f}(\theta,\phi) = \int e^{i\vec{k}i\cdot\vec{r}} U(\vec{r}) e^{-i\vec{k}f\cdot\vec{r}} d^3r, \tag{2.1}$$

where $U(\vec{r})$ is the net scattering potential representing the sample, which is a sum of the individual scattering-center potentials over all the nuclei in the sample

$$U(\vec{r}) = \sum_{\alpha=1}^{N} U_\alpha(\vec{R}_\alpha), \tag{2.2}$$

where N denotes the total number of scatterers and

$$\vec{R}_\alpha = \vec{r} - \vec{r}_\alpha, \tag{2.3}$$

where $\vec{r}$ denotes the observation-point position with respect to the origin, $\vec{R}_\alpha$ corresponds to the scatterer to observation-point relative separation, and $\vec{r}_\alpha$ defines the scatterer position with respect to the origin. In scattering theory it is common to define the scattering vector as a difference between the wave vectors of the initial and final beam

$$\vec{Q} = \vec{k}_i - \vec{k}_f. \tag{2.4}$$

For the elastic scattering simple application of the cosine theorem yields

$$Q = |\vec{Q}| = \frac{4\pi}{\lambda} sin\theta, \tag{2.5}$$

where λ is the wavelength of the radiation used, and 2θ is the scattering angle. This further yields

$$\begin{aligned} f_{\vec{k}i,\vec{k}f}(\theta,\phi) &= \int \sum_{\alpha} e^{i(\vec{k}i-\vec{k}f)\cdot(\vec{r}\alpha+\vec{R}\alpha)} U_{\alpha}(\vec{R}_{\alpha}) d^3R_{\alpha} \\ &= \sum_{\alpha} e^{i\vec{Q}\cdot\vec{r}\alpha} \int e^{i\vec{Q}\cdot\vec{R}\alpha} U_{\alpha}(\vec{R}_{\alpha}) d^3R_{\alpha}. \end{aligned} \tag{2.6}$$

When a neutron probe is used the scattering potential is the Fermi pseudo-potential

$$U_{\alpha}(\vec{R}_{\alpha}) = b_{\alpha}\delta(\vec{R}_{\alpha}), \tag{2.7}$$

where b_{α} is the neutron scattering length. One of the sound differences between the neutron and x-ray probes is that while the neutron scattering length is Q-independent, the corresponding x-ray quantity depends on Q. Furthermore, x-ray scattering lengths across the periodic table depend on the atomic number of the element in question, making light atoms weak x-ray scatterers and heavy atoms good x-ray scatterers. In contrast to this, neutron scattering lengths are 'randomly' distributed across the periodic table, and this fact makes neutrons an important complementary probe when studying the structure of materials containing light atoms. Substituting the pseudopotential into Equation 2.6 yields a simple expression for the scattering amplitude

$$f_{\vec{Q}}(\theta,\phi) = \sum_{\alpha} b_{\alpha} e^{i\vec{Q}\cdot\vec{r}\alpha}. \tag{2.8}$$

The structural information is contained in the single scattering coherent differential cross-section, which is related to the measured intensity and is defined as a square modulus of the scattering amplitude

$$\begin{aligned} \frac{d\sigma_{coh}}{d\Omega} &= |f_{\vec{Q}}(\theta,\phi)|^2 = f_{\vec{Q}}(\theta,\phi) f^*_{\vec{Q}}(\theta,\phi) \\ &= \sum_{\alpha} b_{\alpha} e^{i\vec{Q}\cdot\vec{r}\alpha} \sum_{\beta} b^*_{\beta} e^{-i\vec{Q}\cdot\vec{r}\beta} \\ &= \sum_{\alpha,\beta} b_{\alpha} b^*_{\beta} e^{i\vec{Q}\cdot(\vec{r}\alpha-\vec{r}\beta)}. \end{aligned} \tag{2.9}$$

This equat

gle. The p

the phase s

is readily s

eres rather

Equation 2

states of th

However, it

For a multi-

average sam

The scatteri

and a deviat

Since

$$b_\alpha b_\beta^* =$$

it is easily s

denoted with

and

It is convenie

This equation is the essence of all diffraction experiments. Ω denotes the solid angle. The positions of the scatterers are contained in the exponentials representing the phase shifts involved in the interference and observable intensity fluctuations. It is readily seen that the phase shifts depend on the relative positions of the scatterers rather than their absolute positions. The coherent differential cross-section in Equation 2.9 is assumed to be already averaged over all the isotopes and the spin states of the nuclei. The scattering lengths are then reflecting this type of averaging. However, it has to be further averaged over the chemical composition of the sample. For a multi-component sample (i.e. not a single element material) we can define the average sample scattering length as

$$\langle b \rangle = \sum_{\alpha} c_{\alpha} b_{\alpha}, \quad \sum_{\alpha} c_{\alpha} = 1. \tag{2.10}$$

The scattering length of each scatterer can then be represented as a sum of the average and a deviation

$$b_{\alpha} = \langle b \rangle + \delta b_{\alpha}. \tag{2.11}$$

Since

$$b_{\alpha} b_{\beta}^{*} = (\langle b \rangle + \delta b_{\alpha})(\langle b \rangle^{*} + \delta b_{\beta}^{*}) = |\langle b \rangle|^2 + \langle b \rangle \delta b_{\beta}^{*} + \langle b \rangle^{*} \delta b_{\alpha} + \delta b_{\alpha} \delta b_{\beta}^{*}, \tag{2.12}$$

it is easily seen that the averaging over the chemical composition of the sample, denoted with $\langle ... \rangle$, yields

$$\begin{aligned} \langle b_{\alpha} b_{\beta}^{*} \rangle &= |\langle b \rangle|^2, \ \alpha \neq \beta \\ \langle b_{\alpha} b_{\beta}^{*} \rangle &= |\langle b \rangle|^2 + \langle |\delta b|^2 \rangle, \ \alpha = \beta \end{aligned} \tag{2.13}$$

and

$$\langle |\delta b|^2 \rangle = \langle |b|^2 \rangle - |\langle b \rangle|^2. \tag{2.14}$$

It is convenient to define the atomic separation vector as

$$\vec{r}_{\alpha\beta} = \vec{r}_{\alpha} - \vec{r}_{\beta}. \tag{2.15}$$

To comp

the doub

$$\frac{d\sigma}{d}$$

and then

$$\langle\frac{d\sigma}{d}$$

The sum

and is ty

Simple a

lights an

transforn

The cons

preted as

The qua

correlatio

son funct

To compositionally average the differential cross-section in Equation 2.9, we first split the double sum into two parts as

$$\frac{d\sigma_{coh}}{d\Omega} = \sum_{\alpha}\sum_{\beta} b_\alpha b_\beta^* e^{i\vec{Q}\cdot\vec{r}\alpha\beta} = \sum_{\alpha}\sum_{\beta\neq\alpha} b_\alpha b_\beta^* e^{i\vec{Q}\cdot\vec{r}\alpha\beta} + \sum_{\alpha}\sum_{\beta=\alpha} b_\alpha b_\beta^* e^{i\vec{Q}\cdot\vec{r}\alpha\beta}, \tag{2.16}$$

and then perform the compositional averaging as follows

$$\begin{aligned}
\langle\frac{d\sigma_{coh}}{d\Omega}\rangle &= \sum_{\alpha}\sum_{\beta\neq\alpha}\langle b_\alpha b_\beta^*\rangle e^{i\vec{Q}\cdot\vec{r}\alpha\beta} + \sum_{\alpha}\sum_{\beta=\alpha}\langle b_\alpha b_\beta^*\rangle e^{i\vec{Q}\cdot\vec{r}\alpha\beta} \\
&= |\langle b\rangle|^2\sum_{\alpha}\sum_{\beta\neq\alpha} e^{i\vec{Q}\cdot\vec{r}\alpha\beta} + |\langle b\rangle|^2\sum_{\alpha}\sum_{\beta=\alpha} e^{i\vec{Q}\cdot\vec{r}\alpha\beta} + \sum_{\alpha}\sum_{\beta=\alpha}\langle|\delta b_\alpha|^2\rangle e^{i\vec{Q}\cdot\vec{r}\alpha\beta} \\
&= |\langle b\rangle|^2\sum_{\alpha}\sum_{\beta} e^{i\vec{Q}\cdot\vec{r}\alpha\beta} + (\langle|b|^2\rangle - |\langle b\rangle|^2)\sum_{\alpha}\sum_{\beta=\alpha} e^{i\vec{Q}\cdot\vec{r}\alpha\beta} \\
&= |\langle b\rangle|^2\sum_{\alpha}\sum_{\beta} e^{i\vec{Q}\cdot\vec{r}\alpha\beta} + N(\langle|b|^2\rangle - |\langle b\rangle|^2).
\end{aligned} \tag{2.17}$$

The sum-free term represents the Laue monotonic scattering term, that is incoherent and is typically removed. The total scattering structural function is then defined as

$$S(\vec{Q}) = \frac{1}{N|\langle b\rangle|^2}\langle\frac{d\sigma_{coh}}{d\Omega}\rangle - \frac{\langle|b|^2\rangle - |\langle b\rangle|^2}{|\langle b\rangle|^2}. \tag{2.18}$$

Simple analysis of the expression for the scattering amplitude in Equation 2.8 highlights an important point - the scattering amplitude is proportional to the Fourier transform of the nuclear density function, $\rho_N(\vec{r})$

$$\begin{aligned}
\rho_N(\vec{Q}) &= \int d^3r\ e^{i\vec{Q}\cdot\vec{r}}\ \rho_N(\vec{r}) = \int d^3r\ e^{i\vec{Q}\cdot\vec{r}}\frac{1}{\langle b\rangle\sqrt{N}}\sum_{\alpha} b_\alpha\ \delta(\vec{r}-\vec{r}_\alpha) \\
&= \frac{1}{\langle b\rangle\sqrt{N}}\sum_{\alpha} b_\alpha\ e^{i\vec{Q}\cdot\vec{r}\alpha}.
\end{aligned} \tag{2.19}$$

The consequence of this is that the total scattering structure function can be interpreted as a thermodynamic average of the square of the nuclear density function

$$S(\vec{Q}) = \langle|\rho_N(\vec{Q})|^2\rangle = \int\int d^3r_1\ d^3r_2 e^{i\vec{Q}\cdot(\vec{r}1-\vec{r}2)}\ \langle\rho_N(\vec{r}_1)\rho_N(\vec{r}_2)\rangle. \tag{2.20}$$

The quantity representing the kernel of the double integral is then a two-particle correlation function, or density-density correlation function. The generalized Patterson function is then defined as a Fourier transform of the total scattering structural

functio

The Pa
average
latter g
to any
since

It is co
term

which a
venientl
number

The sec
term, a

function

$$
\begin{aligned}
P(\vec{r}) &= \frac{1}{(2\pi)^3}\int d^3Q\; e^{i\vec{Q}\cdot\vec{r}}\; S(\vec{Q}) \\
&= \frac{1}{(2\pi)^3}\int\int\int d^3r_1\; d^3r_2\; d^3Q\; e^{i\vec{Q}\cdot\vec{r}}\; e^{i\vec{Q}\cdot(\vec{r}1-\vec{r}2)}\; \langle\rho_N(\vec{r}_1)\rho_N(\vec{r}_2)\rangle \\
&= \int\int d^3r_1\; d^3r_2\; \langle\rho_N(\vec{r}_1)\rho_N(\vec{r}_2)\rangle\; \frac{1}{(2\pi)^3}\int d^3Q e^{i\vec{Q}\cdot(\vec{r}1-\vec{r}2+\vec{r})} \\
&= \int\int d^3r_1\; d^3r_2\; \langle\rho_N(\vec{r}_1)\rho_N(\vec{r}_2)\rangle\; \delta(\vec{r}_1+\vec{r}-\vec{r}_2) \\
&= \int d^3r_1\; \langle\rho_N(\vec{r}_1)\rho_N(\vec{r}_1+\vec{r})\rangle \\
&= \rho_0 g_\circ(\vec{r}). \qquad (2.21)
\end{aligned}
$$

The Patterson function represents a pair density correlation function, where ρ_0 is the average number density of the material, and $g_\circ(\vec{r})$ is the pair correlation function. The latter gives the probability density of finding any particle at position $\vec{r}$ with respect to any particle taken as the origin. Then $S(\vec{Q})$ and $\rho_0 g_\circ(\vec{r})$ represent a Fourier pair, since

$$
\begin{aligned}
\rho_0 g_\circ(\vec{r}) &= \frac{1}{(2\pi)^3}\int S(\vec{Q})e^{i\vec{Q}\cdot\vec{r}}d^3Q \\
S(\vec{Q}) &= \int \rho_0 g_\circ(\vec{r})e^{i\vec{Q}\cdot\vec{r}}d^3r \qquad (2.22)
\end{aligned}
$$

It is convenient to separate the self-correlation term from the true pair-correlation term

$$\rho_0 g_\circ(\vec{r}) = \rho_0[g(\vec{r}) + \frac{1}{\rho_0}\delta(\vec{r})], \qquad (2.23)$$

which after integration in the expression for $S(\vec{Q})$ generates unity that is then conveniently subtracted from $S(\vec{Q})$. It is of interest to add and subtract the average number density as follows

$$S(\vec{Q}) - 1 = \int[\rho_0 g(\vec{r}) - \rho_0]e^{i\vec{Q}\cdot\vec{r}}d^3r + \int \rho_0 e^{i\vec{Q}\cdot\vec{r}}d^3r. \qquad (2.24)$$

The second term on the right hand side of Equation 2.24 is known as the self-scattering term, and is essentially a δ-function centered at $\vec{Q} = 0$. This is reflecting the fact

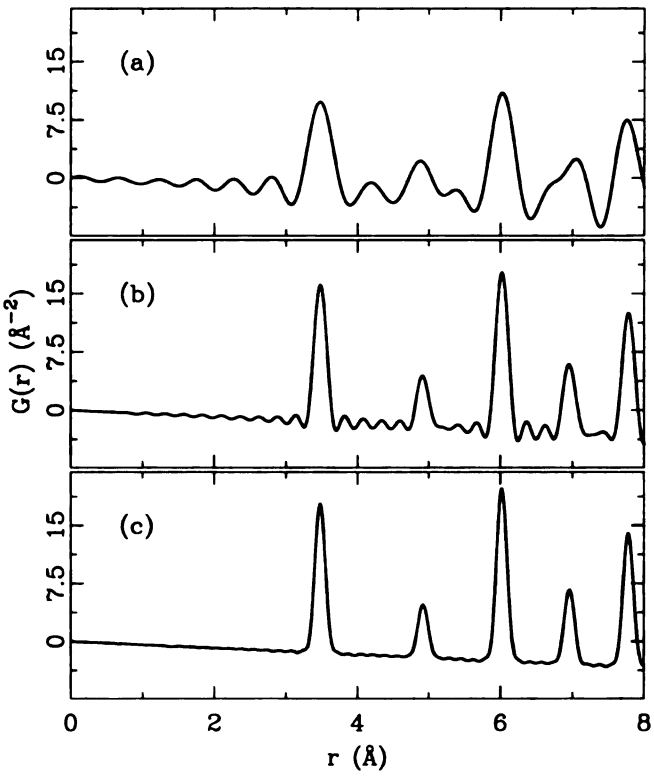

Figure 2.1: Effect of the termination ripples: simulated PDF of lead using Q_{max} values of (a) 12 Å^{-1}, (b) 24 Å^{-1}, and (c) 36 Å^{-1}.

that the self-scattering in the experiment is confined to a narrow range around the primary beam direction at small scattering angles. Therefore, it is not a measurable quantity since the scattered signal cannot be separated from the direct beam that passed through the sample.

In the diffraction experiments on fine powders the scattering is isotropic and the directional information is lost. This comes about due to the powder-averaging effect

$$\begin{aligned} \langle e^{i\vec{Q}\cdot\vec{x}}\rangle_\Omega &= \frac{1}{4\pi}\int_0^{2\pi} d\phi \int_0^{\pi} d\theta \, \sin\theta \, e^{iQx\cos\theta} \\ &= \frac{1}{2}\int_{-1}^{1} e^{iQxz} dz = \frac{\sin Qx}{Qx}. \end{aligned} \tag{2.25}$$

As a consequence of the powder averaging one obtains

$$\rho_0[g(r)-1] = \frac{1}{2\pi^2 r}\int_0^{\infty} Q(S(Q)-1)\sin(Qr)dQ, \tag{2.26}$$

where r represents the relative distance between the atoms, and Q is the magnitude of the momentum transfer vector. The kernel of the integral, $F(Q) = Q(S(Q) - 1)$, is known as the reduced total scattering structural function. By defining the microscopic number density of the sample as

$$\rho(r) = \rho_0 g(r), \tag{2.27}$$

the reduced atomic pair distribution function (PDF), $G(r)$, is obtained as

$$G(r) = 4\pi r[\rho(r) - \rho_0] = \frac{2}{\pi}\int_0^\infty Q(S(Q) - 1)\sin(Qr)dQ. \tag{2.28}$$

Although it is not the only pair distribution function that carries the 'PDF' label, this function is what throughout this thesis we call the atomic PDF. This function has several advantages. It is the one directly obtainable from the experimentally determined $S(Q)$, therefore most directly related to the data. While determination of the other distribution functions ($\rho(r)$, $g(r)$, and $R(r)$ which is defined below) from the data requires prior knowledge of ρ_0, and therefore the structure, determination of $G(r)$ does not. Another advantage is that the random uncertainties of the data propagated to $G(r)$ are r-independent [157].

Integration in Equation 2.28 goes up to ∞, while the experimental data are obtained for a finite Q-range only, and the integration is terminated at some finite value $Q = Q_{max}$. This is a source of termination ripples that appear in the experimental PDF, coming from the convolution of the true G(r) with the sinc function [144], given by

$$G_{exp}(r) = \frac{1}{\pi}\int_0^\infty G(r')[\frac{\sin Q_{max}(r - r')}{r - r'} - \frac{\sin Q_{max}(r + r')}{r + r'}]dr'. \tag{2.29}$$

This effect is illustrated in Figure 2.1 where the simulated PDF of lead is shown calculated using various values of Q_{max}.

Another commonly used representation is the radial distribution function (RDF), $R(r)$, which is related to $G(r)$ through

$$R(r) = rG(r) + 4\pi r^2\rho_0 = 4\pi r^2\rho_0 g(r), \tag{2.30}$$

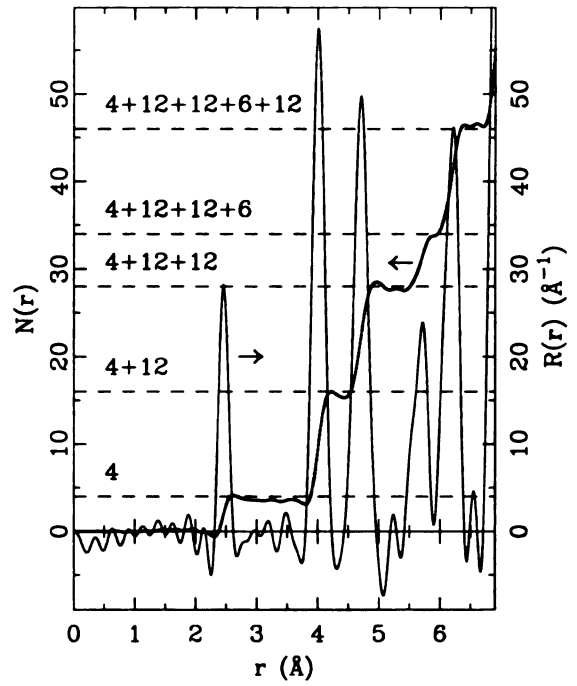

Figure 2.2: Experimentally obtained radial distribution function and corresponding $N(r)$ for elemental germanium with face centered cubic structure.

and has a useful property that $R(r)dr$ gives the number of atoms in a spherical shell of thickness dr at a distance r from another atom. When integrated over r, it gives a cumulative function, $N(r)$, defined as

$$N(r) = \int_0^r R(r')dr', \tag{2.31}$$

which, for a monoatomic material, represents the cumulative coordination number function. This is illustrated in Figure 2.2 where the experimentally determined $R(r)$ and corresponding $N(r)$ are shown for pure germanium at 300 K. If the integration in Equation 2.31 is carried out over a narrow range $r \in \{r_1, r_2\}$ describing a coordination shell, it results in the coordination number of that shell. For polyatomic materials the function $R(r)$ is weighted by the scattering lengths of contributing atoms, and the interpretation of $N(r)$ becomes more complicated. The function $R(r)$ diverges as r^2 at large values of r.

Generally, $R(r)$ is defined as

$$R(r) = 4\pi r^2 \rho(r) = \sum_i \sum_{j \neq i} \frac{b_i b_j}{\langle b \rangle^2} \delta(r - r_{ij}), \tag{2.32}$$

where sums rum over all atoms in a large sample. In practice, peaks in $R(r)$ coming from well defined atom-atom pairs reflect the precise shape of the pair-distribution probability, and within the harmonic approximation have Gaussian shape [157], such that

$$R(r) = \sum_i \sum_{j \neq i} \frac{b_i b_j}{\langle b \rangle^2 \sqrt{2\pi\sigma_{ij}^2}} exp(-\frac{(r - r_{ij})^2}{2\sigma_{ij}^2}). \tag{2.33}$$

The atomic PDF provides structural information on different lengthscales, depending on the range of r in the PDF that is studied [157]. If the sample has a domain structure with some characteristic domain size ξ, then the PDF at a lengthscale $\ll \xi$ provides the intra-domain structure, as most of the sampled pairs of atoms that give rise to features in the PDF lie within the same domain. However, if the same PDF is explored at distances $r > \xi/2$, then the sampling will be predominantly over the pairs of atoms that lie in different domains, and the PDF at these distances reflects the coherent average of the different local structures [157].

One of the most elegant examples of this is found in the structure of solid C_{60}. The structure is a face centered cubic arrangement of carbon molecules, C_{60}, which are spinning around their centers. The diameter of each molecule is 7.1 Å, while the nearest neighbor molecule centers are separated by approximately 10 Å. This is illustrated in Figure 2.3, where a single molecule and the bulk C_{60} are shown, together with the measured reduced total scattering structural function, $F(Q) = Q[S(Q) - 1]$, and the corresponding PDF. The sharp peaks observed in the PDF below 7.1 Å distance correspond to the characteristic $C - C$ pairs within a molecule. Beyond 7.1 Å the structural coherence is lost, apparently due to the spinning of the molecules, and the sharp features are lacking. However, broad peaks at approximately 10 Å, 14.1 Å, and 17.3 Å are observed, and these correspond to the nearest neighbor molecule-to-

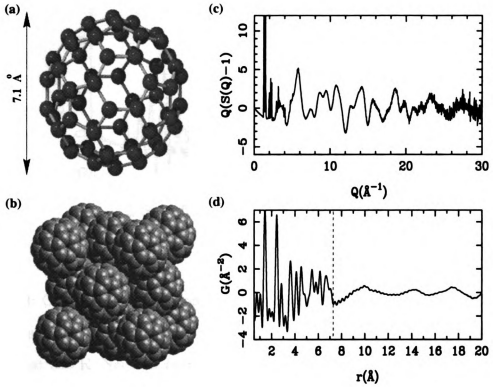

Figure 2.3: Structure on different length-scales from the PDF: the case of C_{60}. (a) Single C_{60} molecule, (b) bulk solid C_{60}, (c) corresponding reduced total scattering structural function, $F(Q)$, and (d) its Fourier transform, the atomic PDF, $G(r)$, are shown. The dashed line in (d) at 7.1 Å denotes the diameter of C_{60} molecule. See text for details.

molecule (center to center) distance $r_\circ$, $\sqrt{2}r_\circ$, and $\sqrt{3}r_\circ$. The structure is than seen as a domain-separated structure, domains being the C_{60} molecules themselves. The sharp features represent the intra-domain structure (correlations within a molecule), while the broad features represent the inter-domain structure (molecule-molecule correlations).

Figure 2
are calc
structur
circles)
describi

2.3

The ch
the stru
propert
element
scatteri
content
chosen,
compler
the Cu-
nation o
both in

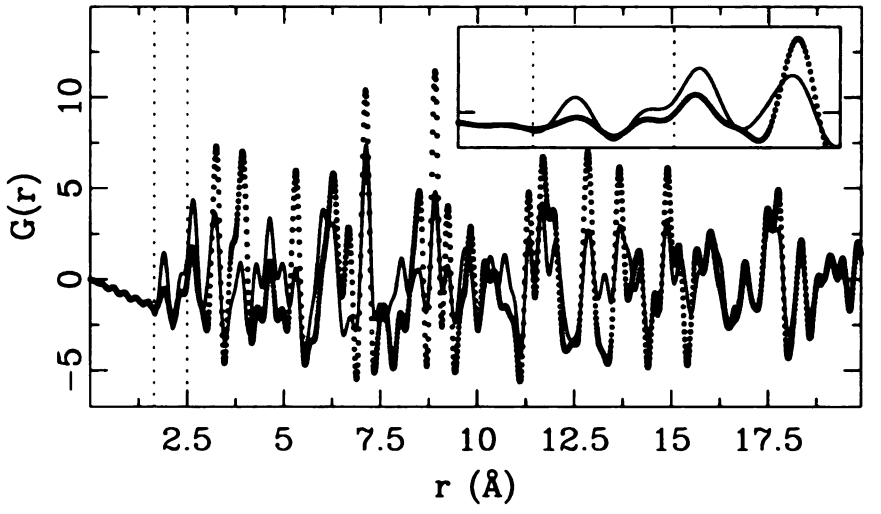

Figure 2.4: Comparison of neutron and x-ray based simulated PDFs for LSCO. PDFs are calculated for the two types of radiation for x=0.125 LSCO using crystallographic structure at 300 K. Neutron radiation based (solid line), and the x-ray based (open circles) PDFs originate from the same structure. The dotted lines mark the r-region describing the CuO_6 octahedron. The inset is the low-r portion of the main figure.

2.3 Probe choice

The choice of the appropriate probe for the scattering experiment is governed by the structural information of interest, and is essentially dictated by the scattering properties of the sample such as the individual scattering properties of the ingredient elements, or the element-to-element relative scattering properties, also known as the scattering contrast. This choice is sometimes easy to make, since the sample chemical content is experimenter-friendly. More often, however, the probe has to be carefully chosen, and sometimes it is desirable to use more than one type of probe yielding complementary information, if all the structural secrets are to be revealed. Studying the Cu-O distances in LSCO and LBCO critically depends on the accurate determination of the Cu and O atomic positions. Light oxygen scatters x-rays rather gently, both in the absolute sense and when contrasted to the other atoms in these materials.

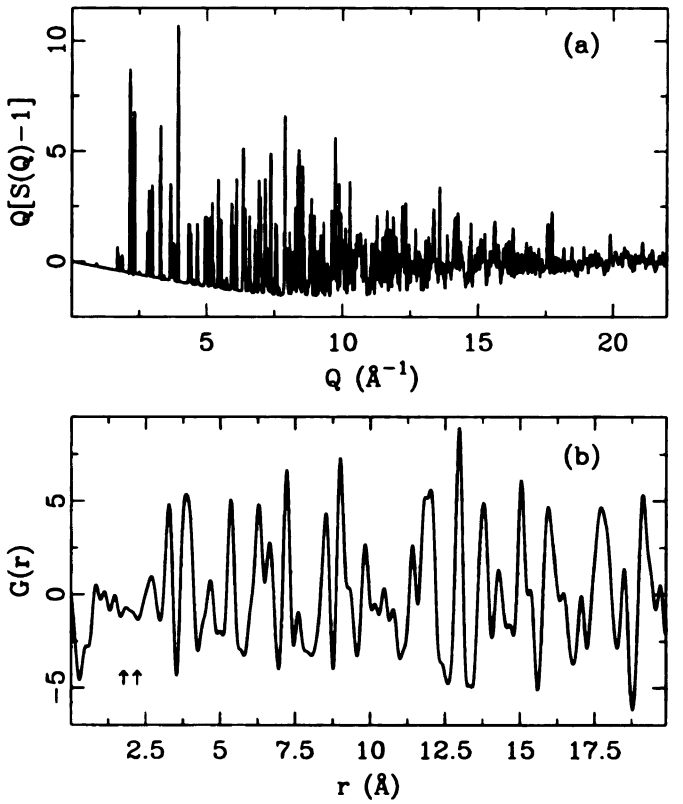

Figure 2.5: X-ray experimental data for x=0.125 LSCO sample at room temperature: (a) the reduced total scattering structural function, and (b) corresponding PDF are shown. Arrows in (b) denote positions of the first two PDF peaks related to the in-plane and apical Cu-O distances.

X-rays are therefore not a suitable probe for this type of study, and neutron probe represents a better choice.

To illustrate this, we provide a brief comparison of the scattering properties for the constituent elements, and ignoring the exact content of the samples. For example, using 30 keV x-rays, the real part of the atomic scattering factor, in electron units, for oxygen is 8.002, while for lanthanum, strontium, barium, and copper are 55.86, 38.25, 54.73, and 29.26 respectively. In addition, we see that the scattering contrast of La and Ba, that share the same crystallographic site, is not favorable. On the other hand, if a neutron probe is used, the coherent scattering length of oxygen is

5.80 fm, while for lanthanum, strontium, barium, and copper it is 8.24 fm, 7.02 fm, 5.07 fm, and 7.72 fm respectively. The oxygen has greater chance to be detected using neutrons. It is worth to note that in the measured intensities scattering lengths are squared, which, if x-rays are used, makes O-O intensities almost two orders of magnitude weaker than La-La intensities, for example.

PDFs have been calculated using the PDFFIT program [161], for x=0.125 LSCO sample, using the known crystallographic structure at 300 K temperature [44], for both neutron and x-ray radiation. These are compared in Figure 2.4, where the vertical dotted lines denote the r-region providing structural information on the CuO_6 octahedron. The advantage of using the neutron probe is apparent. Data from a test-experiment using a synchrotron-based x-ray source is shown in Figure 2.5, further emphasizing that the x-ray probe is inappropriate for the intended study. The arrows in Figure 2.5(b) denote positions of the two nearest neighbor PDF peaks corresponding to the planar and apical Cu-O distances. By inspection one sees that these peaks cannot be observed at all in the experimental PDF. The experiment was performed at 6ID-B μ-cat beam line of the Advanced Photon Source at the Argonne National Laboratory using 38.05 keV (λ=0.326Å) radiation. The PDF is obtained using the PDFgetX data analysis package [162].

2.4 Neutron scattering at a pulsed source

2.4.1 Introduction

The goal of each scattering experiment on powder samples is to obtain the scattering intensity as a function of the magnitude of the scattering vector, the momentum transfer variable Q. This is achieved by employing one of the two general experimental settings, defined by the means of scanning the Q-variable. In the first setting the wavelength of the radiation is constant and the data is collected as a function of

the scattering angle by repositioning the detector, therefore scanning the Q-axis by changing the scattering angle. This is known as the angle-dispersive setting, and is commonly used in experiments using conventional constant wavelength x-ray sources, or synchrotron x-ray radiation with a monochromator, for example. In the second setting, the detector position, and therefore the scattering angle, is kept fixed, and the energy of the probe, and therefore the wavelength, is continuously varied. In this method scanning of the Q-axis originates from the wavelength changes. This is known as the energy-dispersive setting, and is used when having a polychromatic (or white) beam of radiation. It is easily recognized that both the scattering angle, 2θ, and the wavelength, λ, are not the variables of essence for the structural study. They are merely different representations of the momentum transfer, and reflect different experimental conditions. The importance of the momentum transfer comes from the unique relationship between the reciprocal and the direct lattices. For elastic scattering relationship between Q, λ, and 2θ is given by Equation 2.5. In a single crystal experiment, the Bragg peaks in the diffraction pattern occur whenever scattering vector $\vec{Q}$ matches a reciprocal lattice vector $\vec{T}$. This is illustrated in Figure 2.6(a), where the well known Ewald-construction representation of the Laue condition for diffraction is shown. A two-dimensional cut of an arbitrary reciprocal lattice (represented by dots) is shown. The incident radiation with wave vector $\vec{k}_i$, scattered wave with wave vector $\vec{k}_f$, scattering vector $\vec{Q}$, and a reciprocal lattice vector $\vec{T}$ are shown as arrows. O denotes the origin. The solid circle represents the corresponding Ewald sphere, whose radius, κ, is inversely proportional to the wavelength of the radiation. Reciprocal lattice points that lie on the Ewald sphere surface satisfy the Laue condition. In order to scan reciprocal space for the Bragg reflections, the crystal is rotated (rocked) about the origin, as indicated by the double arrow. This changes the relative position of the reciprocal lattice and the Ewald sphere, bringing different reciprocal lattice points onto the sphere. The limiting sphere, shown in Figure 2.6(b)

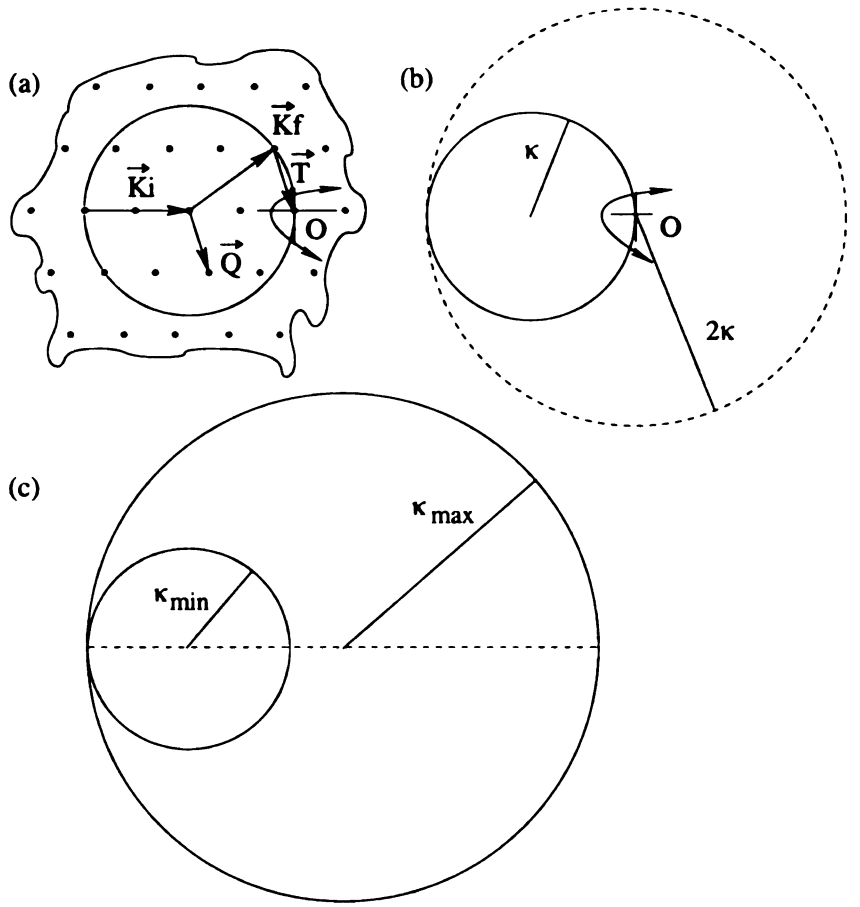

Figure 2.6: Ewald construction for monochromatic and polychromatic beam. (a) Details of the construction. (b) Limiting sphere concept. (c) Polychromatic beam case. See text for details.

as a dashed circle with radius 2κ, limits how many reciprocal lattice points can be brought onto the Ewald sphere by rocking the sample, hence satisfying the Laue condition and being observable in the experiment. If a polychromatic beam having all the wavelengths within some range $\lambda_{min} \leq \lambda \leq \lambda_{max}$ is used, a continuum of Ewald spheres $\kappa_{min} \leq \kappa \leq \kappa_{max}$ is obtained for a fixed scattering geometry. This is shown in Figure 2.6(c): the Ewald-continuum is enclosed by the two extremal Ewald spheres. Reciprocal lattice points of an entire section of the reciprocal lattice will then simultaneously satisfy the Laue condition. However, for true white beam radiation this hardly represents a technical advantage. The problem occurs when many of the

observed Bragg peaks overlap, making the structural determination nearly impossible.

Fortunately, a remedy for this frustrating experimental condition is found in so-called time-of-flight (TOF) techniques. Neutron scattering at a pulsed source is based on the TOF methodology. Pulses of neutrons with a wide spectrum of energies in the thermal and epithermal ranges are incident on a sample, and are scattered. The neutrons having different energies (wavelengths) have different velocities, and therefore are scattered from the sample at different times. For the same reason scattered neutrons with different wavelengths are detected at different times. This new parameter, time, allows such a scattering experiment to be seen as a continuous (in time) set of monochromatic scattering experiments, where all the monochromatic components from the white spectrum are used, but at different times. If a tidy book-keeping of the time parameter is performed, the full advantage of the above energy-dispersive setting can be utilized. The diffraction pattern is then easily reconstructed from the intensity vs. TOF histogram, and the problem of the overlapping reflections is avoided.

2.4.2 Neutron time-of-flight experiment

For the PDF study described in this thesis, the neutron time-of-flight scattering method is exploited, using pulses of neutrons with energies in the thermal and epithermal ranges. In the experiment the detectors have fixed geometry. The intensity is collected at each detector as a function of TOF.

The neutron pulses are produced in a spallation process. Accelerated proton pulses impinge on a heavy metal target producing a large number of highly energized neutrons. These are then slowed down by a moderator, made of a substance that encourages inelastic collisions such as methane or water, that is kept at constant temperature. This results in a neutron pulse with spectrum of energies in the thermal range, which also contains short wavelength undermoderated neutrons constituting

Figur
Empt
TOF
neutr
mode

the e
mode
samp
Neut
mom
expre
and t

Sche
of th
dent
quen

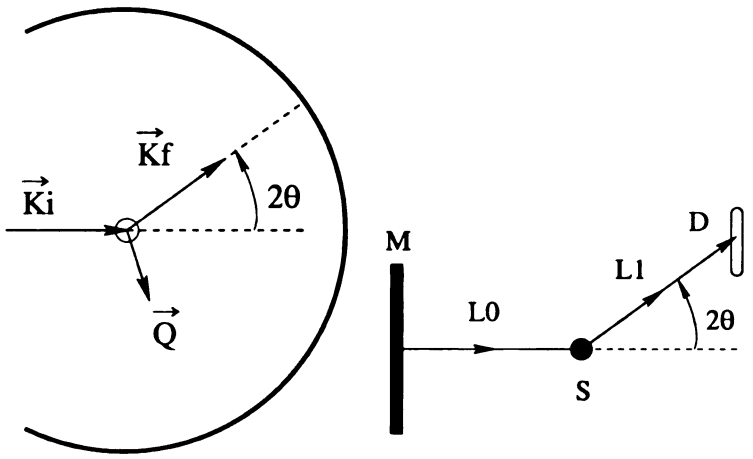

Figure 2.7: Left: scattering experiment schematics. Labels are defined in the text. Empty circle denotes sample position. Partial circle denotes locus of detectors. Right: TOF experiment schematics. Labels are as follows: L_0 is the length of the primary neutron flight path, L_1 is the length of the secondary neutron flight path, M denotes moderator, S denotes sample, and D denotes detector.

the epithermal tail of the spectrum. The neutrons of the incident beam leaving the moderator fly down an evacuated primary flightpath of length L_0, scatter off the sample, and fly towards the detectors along the secondary flight path of length L_1. Neutrons have the deBroglie wavelength $\lambda = h/p$, where $p = m_N v$ is the neutron momentum, m_N is the neutron mass, and the neutron speed is given by classical expression $v = L/t$, where $L = L_0 + L_1$ is the total flight path length of neutrons, and t is the time of flight. The TOF to Q conversion is then achieved by

$$Q = \frac{2m_N}{\hbar}\frac{L\sin\theta}{t} \tag{2.34}$$

Schematics of a typical TOF experimental setup is given in Figure 2.7. The shape of the neutron spectrum in the TOF experiments is characterized by an independent scattering experiment using a material that incoherently scatters neutrons. Frequently this is either pure vanadium, which scatters neutrons almost completely in-

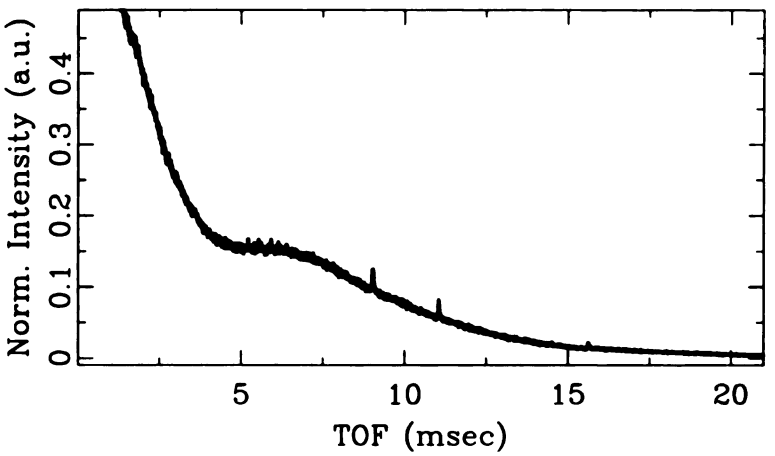

Figure 2.8: Example of a source spectrum from a neutron spallation source. The spectrum shown as a function of TOF corresponds to the SEPD at IPNS, and is obtained using vanadium standard. Residual Bragg peaks are evident in the profile. Maxwellian peak at around 7 msec crosses over into a quickly rising epithermal tail at short times (high energies, short wavelengths). See text for more details.

coherently, or a so-called null-scattering alloy like VNb, where the coherent part of the scattering is completely suppressed. A typical shape of the neutron spectrum is shown in Figure 2.8. The TOF and neutron wavelength are related via $\lambda = ht/m_N L$, and the Maxwellian peak maximum occurs when

$$\lambda = \frac{h}{\sqrt{2m_N k_b T_m}} \tag{2.35}$$

where k_b is the Boltzmann constant, and T_m is the moderator temperature. The Maxwellian part of the neutron spectrum is composed of neutrons that are in thermal equilibrium with the moderator. The epithermal tail, as mentioned, is constituted of the undermoderated neutrons. This part of the spectrum is of great importance for the PDF study since it allows for the high-Q part of the total scattering structural function to be obtained in the experiment. An example of the TOF data from a real crystalline sample is shown in Figure 2.9, where the intensity obtained from $Rb_3D(SeO_4)_2$ sample at SEPD at IPNS is shown both as a function of TOF, and as

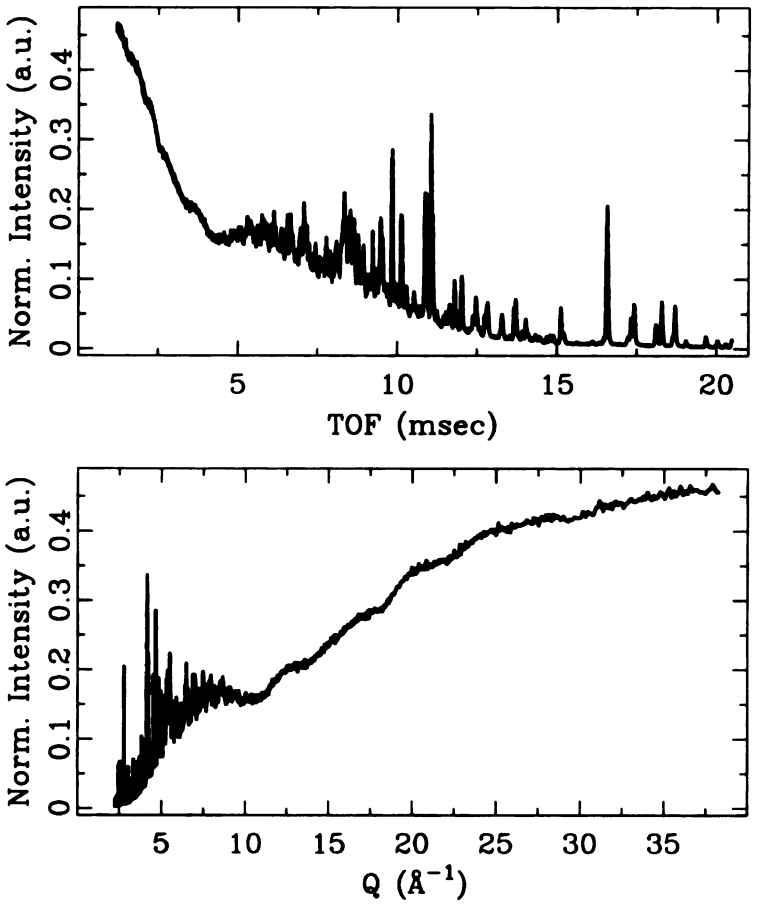

Figure 2.9: Example of real TOF data from crystalline $Rb_3D(SeO_4)_2$ sample. Top: intensity vs. TOF from a crystalline sample. Bottom: the same intensity as a function of Q, converted from TOF variable using Equation 2.34.

a function of Q.

2.5 Data collection

The data investigated in this thesis were collected at various diffractometers. These are the Special Environment Powder Diffractometer (SEPD) and the Glass, Liquid and Amorphous Diffractometer (GLAD) at the Intense Pulsed Neutron Source (IPNS) at Argonne National Laboratory (ANL), High Intensity Powder Diffractometer (HIPD) at the Manuel Lujan Jr. Neutron Scattering Center (MLNSC) at Los

Alamos National Laboratory (LANL), and the General Materials (GEM) diffractometer, at ISIS Pulsed Neutron and Muon Source at Rutherford Appleton Laboratory in UK. Most of the data presented in this work are obtained at SEPD at IPNS, therefore this instrument will be described in some detail, having in mind that, apart from fine details, the general description holds for the other instruments as well.

At IPNS, protons are accelerated to about 450 MeV energy in bunches. The proton current is $\sim$14 μA, and the proton-pulse frequency is 30 Hz. These proton bundles collide with a tungsten target and about 20 neutrons per proton are obtained in the spallation process. Neutron pulses of high energy enter a moderator of liquid methane kept at 100 K. The neutron spectrum contains wavelengths of approximate range from 0.25 Å to 8 Å. The neutrons then travel down the evacuated primary flight path, which is 14 m long in the case of SEPD, before scattering off the sample that is in the center of the diffractometer. The powder samples of $\sim$10 grams are carefully packed in cylindrical extruded vanadium holders that are $\sim$5 cm high and $\sim$1 cm in diameter. The sample temperature is controlled with an accuracy of 1/10 of a degree from $\sim$8 K to above 300 K, using a Lake Shore temperature controller. The cooling of the sample is achieved using a closed cycle displex refrigerator. The packing of the samples is done under helium atmosphere, and the sample holders are sealed with indium wire afterwards. Maintaining the helium atmosphere within the vanadium container is crucial since helium acts as an exchange gas and provides good thermal contact between the powder sample and the cold stage of the displex. Another important aspect of having the sample under helium is that the space between the powder grains is then not filled with the air that produces ice at temperatures below liquid nitrogen temperature (77 K). Air would be a significant source of background signal in the low temperature experiments. After being scattered by the sample, the neutrons travel along the secondary flightpath, which is 1.5 m long in the case of SEPD, and are detected by a series of detectors located on a circular locus surrounding

Figu
toge
typic
Cons
bank

the s

neut
energ
press

where
photo
mainr
by the
that is

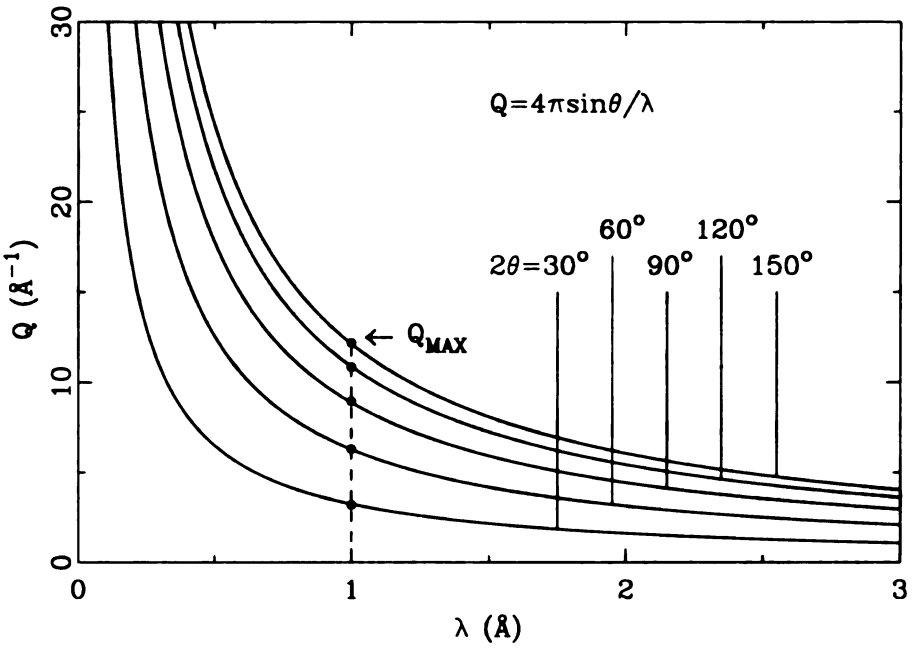

Figure 2.10: Blending limit determination: data from various banks are blended together to obtainin the total scattering structural function. Blending limits are typically chosen such to maintain the constant wavelength range in each of the banks. Constant wavelength cut is shown for determining the blending Q_{max} for different banks. The same methodology applies when Q_{min} values are chosen.

the sample.

Neutrons are typically detected using ionization-chamber type detectors, where neutrons are easily captured, followed by some strong ionizing radiation such as high energy protons. The detectors are made of tubes filled with ^{3}He gas at ~10 atm pressure. The detection process is described by

$$^3He + n \longrightarrow p + \tau + \gamma, \tag{2.36}$$

where n denotes neutron, p denotes proton, τ denotes triton, and γ denotes gamma photon. The tube is a proportional counter with a wire along the tube-axis, which is maintained at high voltage. The gas in the vicinity of the nuclear reaction is ionized by the high energy product particles of the reaction. This results in a charge pulse that is then swept out of the detector due to the applied voltage. The analog signal

obtained in the detector is then amplified, converted into a digital pulse, and then counted in a computer. The detecting system is electronically synchronized with the neutron source, and the start-time of the pulse is known. The TOF is recorded upon neutron arrival at a detector.

Although a single detector located at a suitable angle is theoretically sufficient to obtain the diffraction pattern, in practice multiple detectors are used. The main reason for having multiple detectors is to increase the count rate by filling the solid angle with detectors. Furthermore, since the neutron spectrum used is finite, various positions of the detectors provide different Q-space coverage and with different Q-space resolution. At SEPD there is total of 158 detectors, distributed along a circular locus (see Figure 2.7), that are grouped in 8 individual banks. These banks are time focused onto nominal 2θ angles of $\pm$ 22°, 44°, 90°, and 150°. The data from positive and negative angles of the same magnitude are summed together, so the total number of banks is four. It is readily seen that 2θ angles corresponding to the individual detectors in a bank are different. This issue is dealt with within the time focusing process, where the TOF of the data from a detector located at $2\theta + \delta\theta$ is modified to reflect the arrival as if it have happened at position 2θ. This way, without loss of resolution, the data obtained in multiple detectors is mapped onto a single effective detector located at the 2θ position. The data from various banks is then corrected for various experimental artifacts, as briefly described in the next section, and then blended together to obtain the total scattering structure function and the PDF. The data from various banks is typically terminated in such a way as to maintain the same neutron wavelength range in each bank. This is illustrated in Figure 2.10

The total scattering experiment contains the main measurement on the sample, as well as several additional measurements that are used to characterize the experimental conditions. These additional measurements are on vanadium rod, empty sample container with all the heat shields used, as well as background measurements

which
charac
suppo
the sa
Da
availa
at SE
On o

2.6

In or
func
how
on t
colle
neu
tim
arti
teri
be p
cess
info

tion
The

which contain scattering from the displex environment. The vanadium run is used to characterize the source spectrum and the efficiency of the detectors. The other two supporting measurements are used to remove all the scattering not originating from the sample.

Data-collection time depends on several parameters, such as the amount of sample available, the neutron flux, and the number of detectors used. Data-collection time at SEPD for ~10 gr LSCO sample, for example, is between 6 and 8 hours per run. On other instruments this time can be significantly different.

2.6 Data reduction

In order to obtain the PDF from the experimental data, the total scattering structural function of the sample alone is needed. The convenience of the scattering experiment, however, has its price: the measured intensity profile contains information not only on the sample, but also on the sample environment, on the source spectrum, on the collection time, as well as on the amount of sample being irradiated. In addition, the neutron pulses may overlap, such that the slowest neutrons from one pulse overlap in time with the fastest neutrons from the next pulse. Apart from that, experimental artifacts contribute their share to the complication through absorption, multiple scattering, inelastic and incoherent scattering processes. The raw data therefore has to be processed to account and correct for these artifacts. The final product of this process is the single-particle total scattering structure function, that carries the sample information of interest.

The purpose of the characterization measurements mentioned in the previous section is to allow for the structure function to be accurately recovered from the data. The total intensity obtained in the experiment, and the sample intensity containing

the coherent part relevant for the structural study are given by

$$\begin{aligned} I_{tot} &= I_{sam} + I_{bgrd} \\ I_{sam} &= A \cdot P \cdot [C \cdot I_{coh} + I_{inc} + I_{mul}] \end{aligned} \tag{2.37}$$

where I_{tot}, I_{sam}, I_{bgrd}, I_{coh}, I_{inc}, and I_{mul} are the total, sample, background, coherent, incoherent and multiple scattering intensities respectively. The sample intensity is further affected by the absorption and polarization effects, denoted by A and P, and C is a normalization constant related to the number of scatterers within the irradiated sample volume.

The data reduction procedure contains a sequence of corrections, some of which are measured while the other are calculated. These are described in detail in chapter 5 of Reference [157], for example. Each collected data set is normalized by the total integrated intensity, to account for the length of the measurement and the fluctuations in neutron spectrum. The background scattering intensity coming from the sample holder and the sample environment, as well as the fraction of delayed neutrons are corrected for. Theoretical corrections for the multiple scattering, absorption, polarization, incoherent and inelastic scattering are calculated and accounted for, based on the sample content and the cylindrical experimental geometry. Known parameters in these corrections, apart from the tabulated values for relevant cross-sections, are the beam size and shape, and sample container size, shape, and wall thickness. The corrected intensities from the sample are then divided by the intensity of the vanadium standard, to correct for the incident spectrum and detector efficiency effects. After the corrections are performed, the structure function of the sample is converted into the single particle structure function by normalizing it to the total number of scatterers, which yields $S(Q)$ that asymptotes to unity at large Q-values. In practice the total number of scatterers in the sample is unknown, and a suitable parameter representing the effective sample density is varied until the normalization condition is

met. This is the only variable parameter used in the data reduction procedure. The data was processed using the program PDFgetN, and the interested reader is referred to the existing software documentation for more information [163].

2.7 Extracting the structural information

This section briefly reviews several methods used for extracting the structural information from the experimentally obtained PDF. This can be achieved by modeling the experimental PDF using a structural model, calculating the corresponding model PDF, and comparing it to the data. Another approach is to analyze the PDF profiles directly using the PDF peak height and width analysis.

2.7.1 Structural modeling

Structural modeling represents an important step in determining the local structural information from the experimental PDFs. The average structure of the studied materials is usually well known, typically from a Rietveld-type structural refinement. The starting point to calculate the model-PDF is then based on the structural parameters describing the average structure, such as lattice parameters, atomic fractional coordinates, displacement parameters and occupancies of the crystallographic sites. These parameters are then varied, observing the constraints of the underlying crystal symmetry, to determine how well the average crystallographic model, describing the long-range ordered structure, agrees with the local structural information contained in the experimental PDF. The advantage of the PDF modeling is that the average symmetry constraints can be intentionally violated, when necessary, in an attempt to incorporate local distortions into the model that could explain the local structure when it deviates from the average structure. However, this often represents a difficult task, since deviations from the average structure may be either small or localized to

the nearest neighbor distances only.

In the modeling procedure a small unit cell is defined that satisfies periodic boundary conditions in order to obtain the pattern of delta-functions that are centered to atomic positions. The delta-functions are convoluted with Gaussian functions to simulate the distribution of the correlations due to thermal motion and other harmonic disorder. The PDF refinement procedure is analogous with and complementary to the Rietveld refinement of diffraction data [144]. These two approaches can be used together for refining both the local *and* the long-range structures from the same data and based on the same structural model.

The real space full profile refinement technique is performed using the PDFFIT modeling program [161], and represents a convenient way for extracting the structural information related to the *local* atomic order from the PDF. The experimental PDF, extracted from the data, is fitted with the calculated PDF, based on the theoretical model of the structure. The model PDF can be calculated as

$$G_{mod}(r) = \frac{1}{r}\sum_{i=1}^{N}\sum_{j=1}^{N}\frac{b_i b_j}{\langle b\rangle^2}\delta(r_{ij}-r) - 4\pi r\rho_0 \tag{2.38}$$

where summations are over all the pairs of atoms in the sample, the b's represent neutron scattering lengths and the $\langle ...\rangle$ denotes averaging over all the atoms in the sample. Each contribution given by $\delta(r_{ij}-r)$ is then convoluted with a Gaussian accounting for the displacements [161].

The fitting uses a minimization procedure based on a least-squares approach. The lattice parameters, fractional coordinates, anisotropic displacement parameters, occupancies, and a scale factor represent modeling parameters that are allowed to vary until a residuals function, R_w, is minimized. Within the PDFFIT program the R_w factor is defined as

$$R_w = \sqrt{\frac{\sum_{i=1}^{N} w(r_i)[G_{exp}(r_i) - G_{mod}(r_i)]^2}{\sum_{i=1}^{N} w(r_i)G_{exp}^2(r_i)}} \tag{2.39}$$

where G_{exp} is the experimental PDF, G_{exp} is the model PDF, and $w(r_i) = 1/\Delta G_{exp}^2(r_i)$

represent the weights coming from the statistical uncertainties of the measurement that are properly propagated to the PDF [157]. As a sum of squares of residuals, the R_w factor is a residual function similar to the R factor used in crystal structure refinements.

2.7.2 PDF peak height and width analysis

An alternative way to learn about the disorder from a PDF is to investigate the features in the PDF by a direct analysis of the PDF peak heights and widths. The peaks in the PDF are providing information on the atomic pairs separated by a given distance. While in the ideal perfect crystal the PDF peaks would be delta-functions, in real crystals these peaks have finite widths that originate from thermal and static disorder within a solid, as well as from the convolution effects coming from the finite Q-range of the measurement. The relationship between the peak height and width can be seen from the Equations 2.30-2.33. The integrated area of the peaks is conserved since it is proportional to the number of contributing atoms, that is constant. The peak height is then inversely proportional to the peak width. In typical PDF studies external parameters that are varied are the sample composition and/or the sample temperature. By extracting the PDF peak height and width, important information on the presence or absence of local structural disorder can be obtained. This type of analysis alone does not provide information on the nature of the underlying distortions. However, it does tell us which atoms are involved and also provides qualitative information on disorder as a function of the external parameters. This model-independent method can be utilized to study particular bond length distributions in a material, that may exhibit local changes even when such changes are averaged out and not observable in studies of the long-range order. The analysis is carried out by fitting a Gaussian profile to the experimental RDF peak of interest, or appropriately calculated PDF-type peak to the experimental PDF-peak.

As an outcome of the fitting process the peak height and width are extracted. This method requires either prior knowledge of the average number density, ρ_0, or this can be set as a fitting parameter when fitting a PDF-like profile to the experimental PDF. In practice, as it turns out, the issue of ρ_0 does not represent a major obstacle. This method, as presented further in the thesis, is applied to study the nearest neighbor Cu-O bondlength distribution in LSCO and LBCO both as a function of chemical content and temperature. For this type of analysis it is important to use the identical termination criteria in the Fourier transform of $F(Q)$, maintaining the convolution effects the same throughout the series of PDFs under investigation. The termination effects, observable as a convolution of the true PDF with the convolution function, are incorporated into the fitting procedure.

2.8 Bond valence analysis

The relationship between bond length and the atomic valence and coordination number has been quantified in the theory of bond-valence [164]. This theory is quite useful in complicated systems such as we are dealing with where ions have a number of bonds of differing length. The idea is that the valence of an ion is divided between all the bonds it has with its neighbors, and the amount of charge assigned to each bond, the bond-valence, s, depends on the bond length, r, according to

$$s(r) = \exp -\frac{(r - r_0)}{B}, \tag{2.40}$$

where B=0.37Å is a universal empirical parameter and r_0 is a parameter which depends on the ionic species involved. By summing over all of the bonds associated with an ion, one recovers the valence of the ion:

$$V_i = \sum_j s_{ij}. \tag{2.41}$$

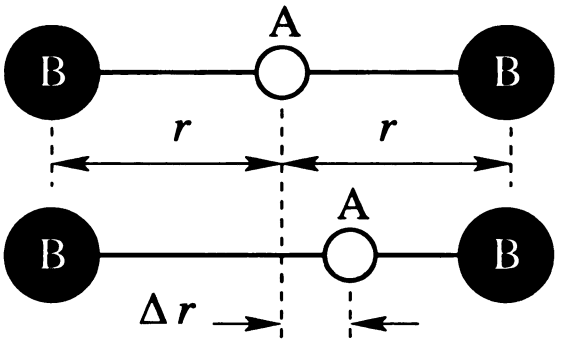

Figure 2.11: Bond valence archetype: linear molecule AB_2. Atom A is bonded to two atoms B. Initially two A-B bonds are of the same length, r. In another case, atom A displaces away from the high symmetry position, getting closer to one of the B-atoms. The displacement is Δr.

Bond valence sum (BVS) phenomenological theory is useful in a number of respects. First, if V_i does not add up to the nominal valence, V_n, of the ion in question, we know that this ion's bonds are not fully relaxed. The bond valence increases with decreasing bond-length; thus, if $V_i > V_n$ we know that on average the bonds are too short and the site is in compression, and if $V_i < V_n$ the bonds are too long and the site is in tension. Second, the non-linearity of the expression for $s(r)$ means that an ion can increase V_i by lowering its site symmetry. This can be illustrated using a simplistic example of a linear molecule AB_2 shown in Figure 2.11. If atom A sitting equally between two neighbors B displaces to the side for Δr, one bond lengthens $(r + \Delta r)$ and the other equally shortens $(r - \Delta r)$. In the symmetric case the two bonds have equal bond valences of $s(r) = \exp(\frac{r_0 - r}{B})$, and the BVS is $V = 2s$. It is readily seen that when atom A displaces as described, the bond valence of the longer bond becomes $s_l(r) = s(r)\exp(-\frac{\Delta r}{B})$, while the valence of the shorter bond equals $s_s(r) = s(r)\exp(\frac{\Delta r}{B})$. For a displacement of 0.05 Å, the bond valence of the longer bond changes by $\sim$0.87, while bond valence of the shorter bond changes by $\sim$1.15 in comparison with the starting valence, s. Therefore, for the longer bond s_l decreases

and it in

decrease

BVS as

the BVS

where Δ

to lower

symmetr

see whic

are mak

is preser

distortio

experime

in questi

Thro

their cha

ture dep

practical

material

and it increases for the shorter bond, s_s; however, the increase in s_s is greater than the decrease in s_l and the overall BVS, V_i, therefore increases. In this particular example BVS as a function of displacement takes the form $V_i = V_n \ cosh(\frac{\Delta r}{B})$. Notice that the BVS then has the smallest value if atom A is in the highest symmetry position where $\Delta r = 0$. We thus see that ionic sites which are in tension will tend to distort to lower their symmetry, and conversely sites in compression will maintain as high a symmetry as possible. Third, by looking at the bond-valence of each bond we can see which bonds are more relaxed than others. This allows us to predict which bonds are making the largest contributions to changing the bond-valence when a distortion is present in the structure; we can infer that these bonds are therefore driving the distortion. Fourth, by applying the BVS methodology using bondlengths obtained experimentally, we can investigate the nature of the charge distribution around ions in question.

Throughout the structural study presented in this thesis various bondlengths and their changes are investigated in great detail, such as their doping and temperature dependencies across the phase diagrams. Hence, the BVS method represents a practical tool helpful in addressing various aspects of properties of the investigated materials.

Chapter 3

Sample Preparation and Characterization

"Among the maxims on Lord Naoshige's wall there was this one: 'Matters of great concern should be treated lightly'. Master Ittei commented: 'Matters of small concern should be treated seriously'." (T. Yamamoto)

3.1 Introduction

In this study we explore the issue of the possible presence of rather subtle structural effects arising from coupling of the doped charges with the crystal lattice. In an indirect way, this is aimed to address the nature of the distribution of the doped charges and implications to other observed properties. However, there may be other competing structural effects, such as structural artifacts caused by phase impurities or macroscopic sample inhomogeneities, by stoichiometry problems, and similar. Such a scenario would make the data analysis and interpretation very hard, if not impossible, and it should be prevented. It is therefore of the greatest importance for this investigation to use bulk samples of exceptional quality. The quality of the samples depends on the preparation process, as well as on the purity of the ingredient substances used

in the synthesis. For this reason it is of the utmost importance to follow well established sample preparation routes, and to perform a thorough characterization of the samples.

Sample synthesis and characterization is a complex scientific field, and our intention is not to cover all the peculiar details. However, we provide a report on the fundamental steps necessary for obtaining $La_{2-x}A_xCuO_4$ (A=Sr,Ba) samples of reliable quality and in sufficient amounts for a neutron powder diffraction study and PDF analysis. The procedure is described more extensively for LSCO samples, with LBCO-specific synthesis details mentioned afterwards, although the process is essentially the same for both. Samples investigated in this work were synthesized following the recipe reported by M. Breuer et al. [165]. In this chapter, we elaborate on the preparation procedure, followed by characterization methods used to determine phase purity of the HTSC powders, verification of their oxygen content, δ, determination of the critical temperature for superconductivity, T_c, and finally determination of the structural phase transitions. A summary of all the characterizations performed on the samples used in this study concludes the chapter.

3.2 Preparation of powder samples

Various samples of $La_{2-x}Sr_xCuO_4$ ($0 \leq x \leq 0.30$), about 15 grams of each, were prepared using standard solid state reactions. [165] Ingredients used for the sample preparation process were commercially available powders of La_2O_3 (99.999%), $SrCO_3$ (99.995%) and CuO (99.9999%) obtained from Sigma-Aldrich. The initial step in the sample preparation is performed by weighing the starting powder materials in appropriate amounts to get the desired stoichiometry, and mixing them for 30 minutes in an eccentric electric mill with agate walls and crunch-balls. It was reported earlier that the powder treated in this way exhibits superior homogeneity, as compared to powder

Table 3.1: Typical synthesis starting information used to obtain LSCO samples.

Element	mass (amu)
La	138.9055
Sr	87.62
Cu	63.546
O	15.9994
C	12.011

that is mixed manually [165]. We mention that the ingredient powders mixed in this way also undergo thermomechanical reactions. It is very important to perform weighing and initial mixing in a *dry* atmosphere, since some of the ingredients are quite hygroscopic and any moisture that is absorbed by the ingredients will change the effective Sr-content of the samples by influencing the effective weighing accuracy. For illustration purposes, information on the mixture calculations for obtaining optimally doped LSCO is given in more detail. In order to obtain 15 grams of $La_{1.85}Sr_{0.15}CuO_4$ sample, one has to calculate the amounts of necessary ingredients, La_2O_3, $SrCO_3$, and CuO. A simplistic calculation, whose result is summarized in Table 3.2, contains two steps. In the first step one calculates the molecular masses of the ingredients and of the final product, expressed in amu, based on their composition and the atomic masses given in Table 3.1. The molecular mass of the LSCO sample with Sr content x, in atomic mass units (amu), is

$$M(LSCO)(x) = (2-x) \times M(La) + x \times M(Sr) + M(Cu) + 4 \times M(O). \qquad (3.1)$$

One finds that M(LSCO)(0.15)=397.6618 amu. Using an identical procedure molecular masses of the ingredient compounds are found to be $M(La_2O_3)$=325.8092 amu, $M(SrCO_3)$=147.6292 amu, and M(CuO)=79.5454 amu. Knowing this, one proceeds to the second step, which is to calculate the real masses (in grams) of the ingredient

Table

optima

powde

At t

denc

unit

is 1,

of o

mas

of t

3.2.

Initia

cruci

Prere

conce

Table 3.2: Typical synthesis mixture information used for obtaining 15 grams of optimally doped LSCO sample with strontium content of 0.15.

Ingredient	mass (g)
La_2O_3	11.3680
$SrCO_3$	0.8353
CuO	3.0005

powders necessary to obtain 15 grams of $La_{2-x}Sr_xCuO_4$ sample. This is as follows:

$$m(La_2O_3) = 15g \times \frac{M(La_2O_3)}{M(LSCO)(x)} \times \frac{2-x}{2}, \tag{3.2}$$

$$m(SrCO_3) = 15g \times \frac{M(SrCO_3)}{M(LSCO)(x)} \times x, \tag{3.3}$$

$$m(CuO) = 15g \times \frac{M(CuO)}{M(LSCO)(x)}. \tag{3.4}$$

At this point a remark should be made: in $m(La_2O_3)$ there is a factor of 2 in the denominator, and this is reflecting the fact that there are two La atoms per formula unit in this ingredient. For the other two ingredients the corresponding contribution is 1, which is then omitted in the calculation. The calculated masses in the case of optimally doped LSCO (x=0.15) are summarized in Table 3.2, and represent the masses of the ingredient powders that should be mixed in order to obtain 15 grams of the sample.

3.2.1 Prereaction

Initial mixtures of powders, prepared as described, are placed in aluminum-oxide crucibles and prereacted to achieve calcination and homogenization of the samples. Prereaction conditions are adjusted to the sample compositions. Samples with Sr concentrations $x \leq 0.15$ (i.e. underdoped and optimally doped samples) are heated to

1000°C at a rate of 10°C/min, and held at this temperature for about 25 h, followed by cooling to room temperature within 6-8 hours. Overdoped samples ($x \geq 0.15$) are prereacted at a higher temperature, 1100°C, for about 25 h, and quenched in air afterwards. A higher prereaction temperature is used for overdoped samples in order to prevent the formation of the so-called T" phase [165]. Prereactions were repeated for each sample three times, with intermediate grinding to provide sample homogeneity, in order to obtain single phase samples. Performing more than two prereactions is also known to be a key parameter to obtain desirable superconducting properties: a larger number of prereactions provides better homogeneity of the oxygen and cation distributions [165].

3.2.2 Sintering

The main reaction and oxygenation steps are summarized in Figure 3.1. The main reaction consists of sintering cylindrical pellets of powder at 1150°C. Pellets were created using a 31 mm radius die and exposing it to a 28 ton load, prior the reaction. Two sintering steps are typically performed, for 100 hours and 50 hours respectively, with intermediate grindings and re-pelleting. The heating rate used was 18°C/min. Pellets were quenched in air afterwards.

3.2.3 Oxygen annealing

As a final step in sample preparation, oxygenation of the samples is performed. Samples are first heated up to 800°C at a rate of 2°C/min, and held at this temperature for 50 hours. The second step of oxygenation takes place at a 500°C temperature, to which the samples are cooled down at a rate of 0.6°C/min, and at which samples are held for 30 hours. The process of oxygenation ends by cooling down the samples to room temperature at a rate of 0.6°C/min. The entire oxygenation process is performed in a tube-furnace and in a constant oxygen flow. During this part of the

Figu

(sar

timi

phase

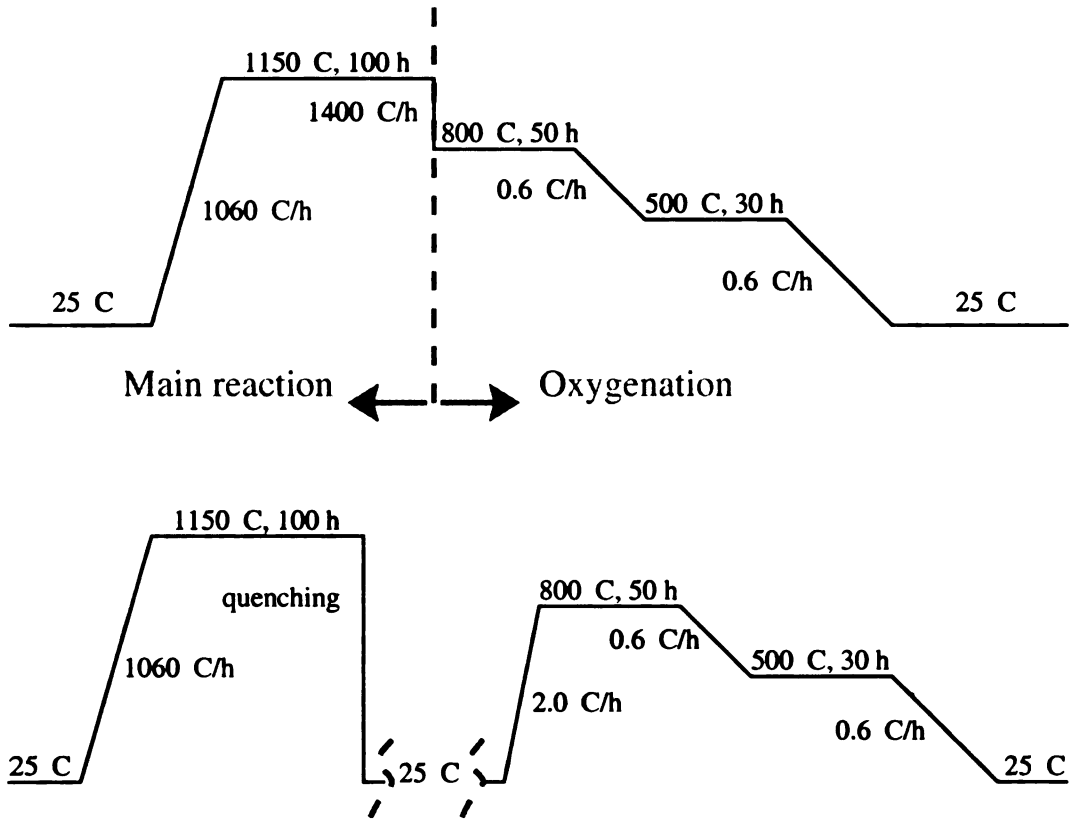

Figure 3.1: Sample preparation summary: main reaction (sintering) and oxygenation (sample relaxation in the oxygen flow). Top panel shows full temperature cycle with timing for each step. Bottom panel emphasizes quenching in air and the oxygenation phase. Temperature is in units of $^{\circ}C$, and timing is in hours.

synthe

proces

compos

3.2.4

Polycry

solid st

availab

tempera

product

hours [

3.3

The key

how clo

the sam

stoichio

study.

The

the oxy

are typi

hole co

sample.

are gene

where δ

the doped

synthesis oxygen enters the pellet and re-occupies oxygen deficient sites through a process of diffusion. It is through this process that the samples with an appropriate composition become superconducting.

3.2.4 Synthesis of Ba-doped samples

Polycrystalline samples of $La_{2-x}Ba_xCuO_4$ (x=0.15), were prepared using conventional solid state reaction described above. Ingredients used in the mixture are commercially available powders of La_2O_3, $BaCO_3$ and CuO. The mixture was calcined at various temperatures between 900°C and 1050°C, with several intermediate grindings. The product was sintered at 1000°C for 100 hours, and oxygen annealed at 800°C for 100 hours [166].

3.3 Stoichiometry and phase purity verification

The key part of what is considered the sample-quality characterization is to establish how close a sample is to its nominal chemical formula (stoichiometry), and whether the sample is single-phased. The sample is considered to be of good quality if it is stoichiometric, and if it is single phase. Both issues are equally important for this study.

The primary interest in the stoichiometry of $La_{2-x}A_xCuO_4$ (A=Sr,Ba) is related to the oxygen content of the samples. Vacancies on oxygen sites and oxygen interstitials are typical synthesis-embedded defects that, if significantly present, affect the doped hole concentration, HTS transition temperature, and structural properties of the sample. This matter is therefore of great concern, and non-stoichiometric samples are generally considered to be of poor quality. The notation used is $La_{2-x}A_xCuO_{4-\delta}$, where δ refers to the oxygen deficiency of the sample. The true concentration of the doped holes is given by $p = x - 2\delta$. If stoichiometry is achieved ($\delta \approx 0$), then

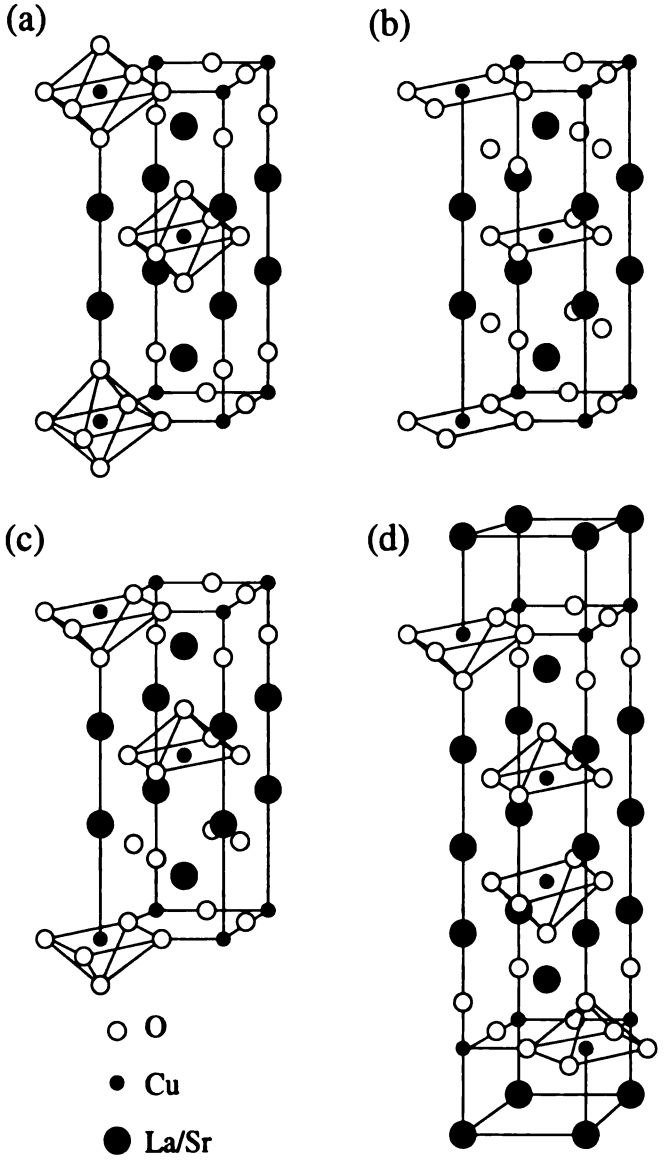

Figure 3.2: Possible alternative structures that may result from LSCO-type synthesis: (a) T-phase, (b) T'-phase, (c) T*-phase, and (d) T"-phase. Black circles represent copper atoms, white circles represent oxygen atoms, while gray circles represent lanthanum/strontium atoms. The favorable case for this study is the T-phase. However, not all the phases occur in the synthesis of pure LSCO, some of them appear when another rare earth element is co-doped *in addition* to strontium [165].

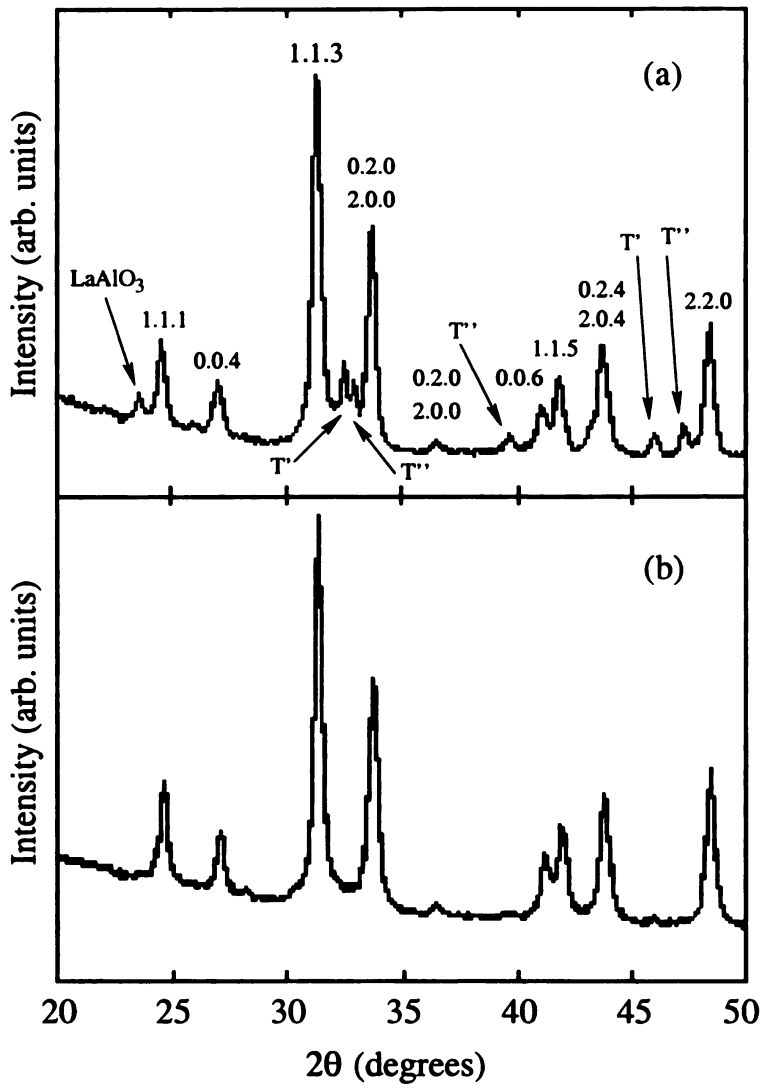

Figure 3.3: A segment of typical XRD patterns for Nd-codoped LSCO. (a) XRD pattern of low-quality sample, containing impurity peaks: sample obtained by only one prereaction, with an additional impurity peak coming from the reaction between the sample and the crucible. Positions of T'-phase and T"-phase impurity peaks, as well as $LaAlO_3$ impurity peaks are marked. (b) After two prereactions and with the absence of the sample-crucible reaction: a clean XRD pattern corresponding to T-phase is obtained [165].

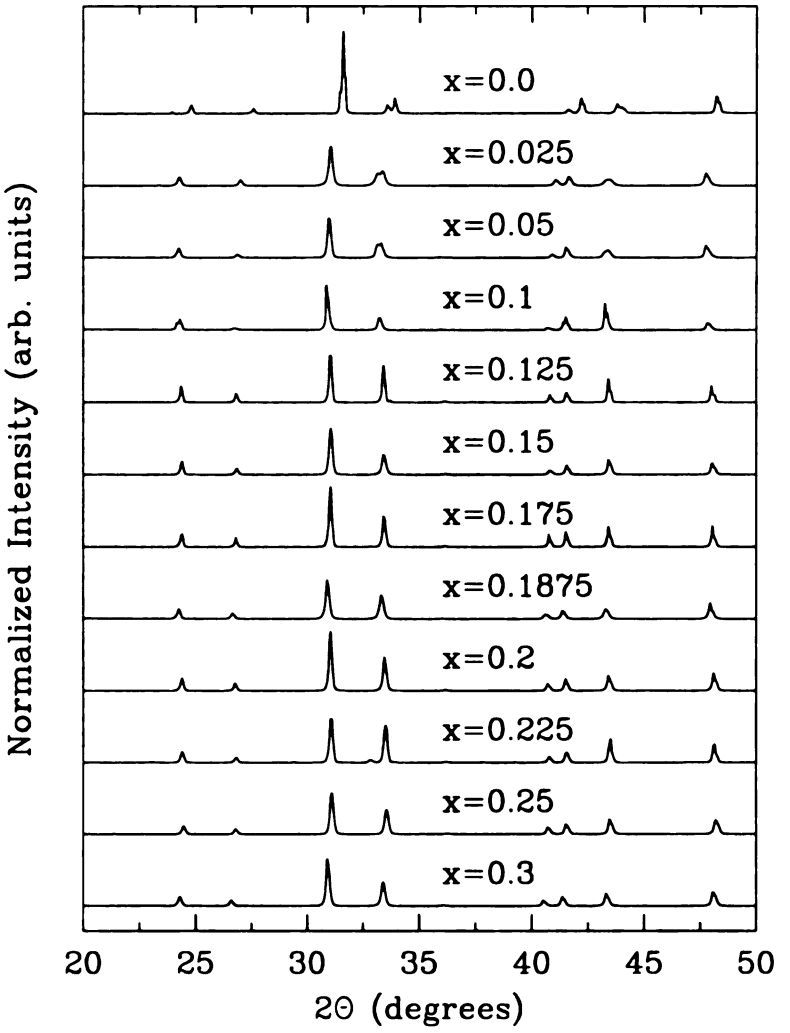

Figure 3.4: XRD patterns of LSCO samples characterized at room temperature, with strontium content specified. Note: LSCO samples exhibit a structural phase transition from high temperature tetragonal to low temperature orthorhombic phase, with transition temperature being doping dependent. Depending on strontium content samples of various compositions at room temperature will therefore be in one of the two structural phases, hence having slightly different XRD patterns. This difference is recognized by direct comparison of the patterns for end-member samples (x=0.0 and x=0.3). Heavily underdoped samples at room temperature have a lower symmetry structure, and therefore their XRD patterns contain more Bragg peaks. In terms of oxygen arrangement, all the samples still have the T-type structure.

$p = x$ is assumed. However, if δ is inappropriately neglected when nonzero, the hole concentration is overestimated. When phase diagrams are considered, lack of this correction is effectively shifting the doped-hole axis in the regions where contributions of δ are appreciable.

Samples that contain a significant amount of impurities structurally appear as multiphase. In extremal cases fundamental physical properties of the original sample are affected, irrespective of whether the impurities are related to stoichiometry or not. Depending on the synthesis route employed, and for the stoichiometric case, it is possible to obtain samples with alternative atomic arrangements that exhibit quite different physical properties. In the case of LSCO samples this means both structural and superconducting properties are altered. Samples containing impurity phase are considered to be of poor quality.

In the synthesis of rare earth (RE) doped samples $(La_{2-x-y}RE_ySr_x)CuO_4$, where RE can for example be Pr, Nd, Sm, Eu, Gd, Dy, Ho, or Er, three phases may typically occur (depending on the RE used): T, T', and T* phases [23], Figure 3.2 (a), (b) and (c). The arrangement of oxygen atoms represents the main difference between these phases: while CuO_6-octahedra and two parallel layers (CuO_2 and LaO) are distinct characteristics of the T-phase, T'-phase has fourfold oxygen-coordinated copper atoms, and T*-phase essentially represents a mixture of T and T' phases [165]. Another phase occurs in RE co-doped samples, and that is double-layered T"-phase (Figure 3.2 (d)). This phase typically occurs for Sr concentrations of about 1 (i.e. $x = 1$), and usually at reaction temperatures close to 950°C. While this phase is unlikely to occur in underdoped samples, it is of some concern to avoid its formation in overdoped samples. However, this phase is easily avoided if reaction temperatures for Sr-rich samples are kept well above 950°C with subsequent quenching.

During the sample preparation process, and afterwards, samples were characterized for structural phase purity by means of x-ray diffraction (XRD). High resolu-

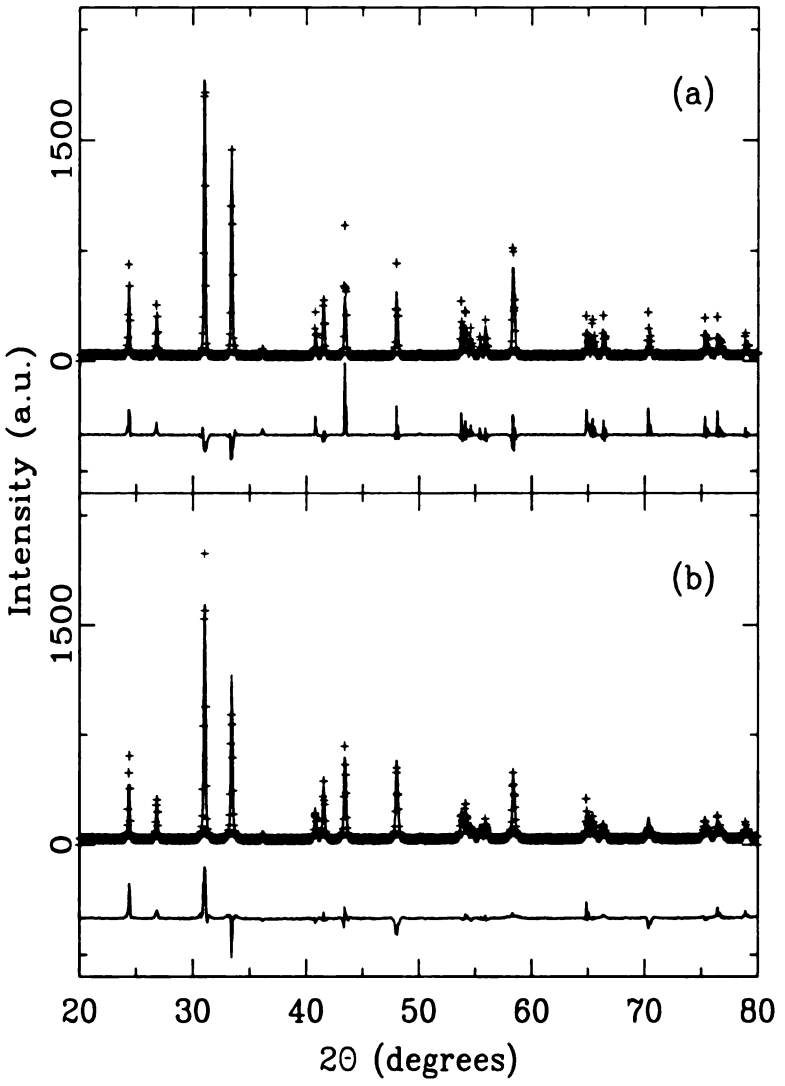

Figure 3.5: Rietveld fits of selected XRD patterns for LSCO samples: (a) x=0.125 and (b) x=0.15. Solid lines denote structural models, crosses are the data. Difference curves are shown below the data.

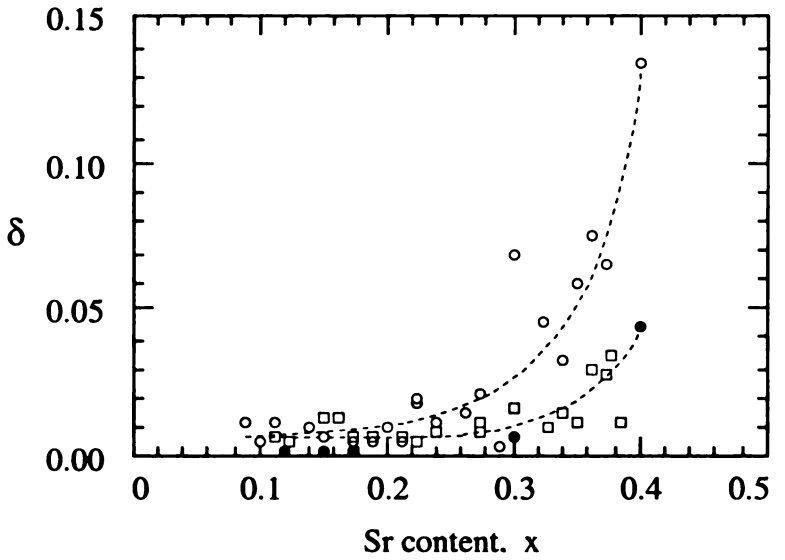

Figure 3.6: Oxygen deficiency per formula unit, δ, versus strontium content for LSCO samples obtained using various synthesis routes (after Radaelli *et. al.* [44]. The lines are guides to the eye. The reported accuracy of the measurement is about 0.01.

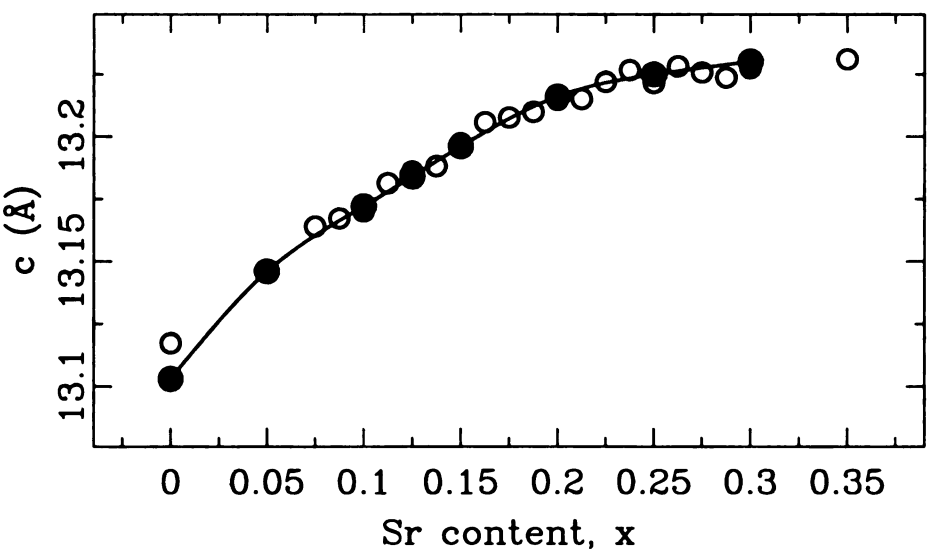

Figure 3.7: The c-axis parameter versus strontium content for stoichiometric LSCO samples of Radaelli and collaborators [44] (open circles), and for our samples (solid circles), from Rietveld refinement of neutron powder diffraction data at 10 K. Solid line is a guide to the eye.

tion XRD patterns in the angular range of 10°-100° were obtained using an inhouse RIGAKU 200B rotating anode diffractometer with a wide angle goniometer. This system has access to 1°-140° 2θ range, and with its maximum voltage of 60 kV and current of 200 mA provides a high-intensity x-ray beam. Typical features of the impurity phases in the XRD patterns are shown in the top panel of Figure 3.3, while the XRD pattern from a good sample is presented in the bottom panel of the same figure. The set of XRD characterization patterns for the LSCO samples considered for this study are shown in Figure 3.4, with strontium content as labeled. Phase-purity of all the samples is checked by structural modeling of the obtained XRD patterns using the FULLPROF Rietveld code [167, 168]. Rietveld structural refinement is a traditional reciprocal-space based method for extracting average structural information from the diffraction data [151]. Representative fits are shown in Figure 3.5. All the samples that were used for this study showed the absence of known impurity phases. Another concern is that for reaction temperatures larger than 1050°C there is the possibility of reaction of LaO_2 with the aluminum oxide crucible. However, no evidence of extra Bragg reflections is found in the XRD patterns of the samples we used for this study.

The oxygen content, as mentioned earlier, influences the properties of HTS samples. There are several ways to verify the stoichiometry. The technique that is typically used by chemists is iodometric titration [169, 170, 171, 172]. However, another possibility is based on diffraction experiments. Through a process of modeling, where oxygen content could be set as one of the variables, one addresses the stoichiometry issue. It is also known that the c-axis lattice parameter is very sensitive to the oxygen content [44], and therefore stoichiometry can be monitored through the value of this parameter as well. The oxygen deficiency parameter, δ, depends on the strontium content of the sample, x. This dependence is shown in Figure 3.6. As can be seen, δ weakly depends on x in the region of interest for this study. It is only in the heavily overdoped region ($x \geq 0.35$) where more dramatic deviations from stoichiometric δ=0

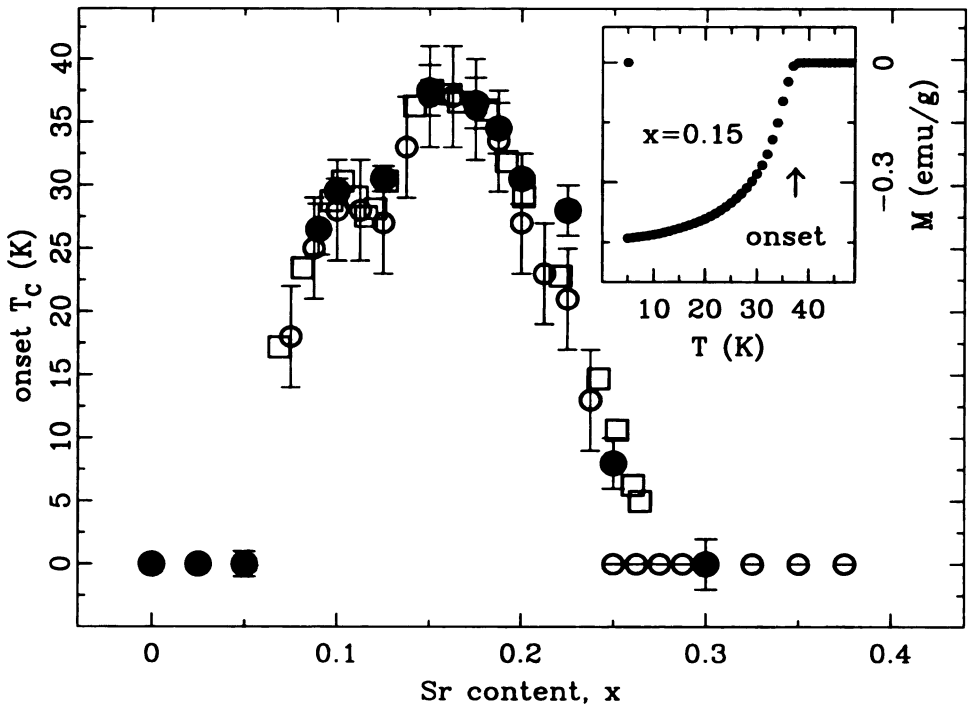

Figure 3.8: Superconducting transition temperature (onset T_c) as a function of Sr content for LSCO samples: literature values are given as open circles [44] and open squares [119], and values for the samples considered for this study are represented by solid circles. Inset: dc magnetization (per unit mass) as a function of temperature, for x=0.15 LSCO sample. The arrow denotes onset of superconductivity.

is expected. Stoichiometry verification for the samples used in this study is done by comparing the c-axis parameters for our samples, obtained from Rietveld refinements of neutron powder diffraction data for 10 K temperature, with appropriate c-axis parameters that correspond to stoichiometric samples [44]. Parameters obtained for samples used in this study lie along those for stoichiometric samples of Radaelli and coworkers, within the scatter of their data, as shown in Figure 3.7.

3.4 Determination of T_c

The superconducting properties of the samples in question are characterized through magnetometric measurements using a Quantum Design sample property measurement system, which is a standard superconducting quantum interferometric device (SQUID). The onset temperature for superconductivity, T_c, is determined for the samples as a function of doping, and compared to the literature values. Superconducting fractions of the samples are estimated as well.

Magnetometric characterization using the SQUID is well established. Magnetic properties of materials are studied by applying an external magnetic field and observing their response through the induced magnetization [173]. This is expressed through:

$$\mathbf{B} = \mathbf{H} + 4\pi\mathbf{M}, \tag{3.5}$$

where $\mathbf{B}$ is the magnetic induction experienced by the sample, $\mathbf{H}$ is the applied external magnetic field, and $\mathbf{M}$ is the magnetization (magnetic moment per unit volume) of the sample. The volume susceptibility is defined as $\chi_v = d\mathbf{M}/d\mathbf{H}$. A diamagnetic response, observed in materials containing all paired electrons, consists of a current induced in the material whose associated magnetic field is oppositely directed to the applied field. As a result, diamagnetic susceptibility is small, negative relative to the applied field, and temperature independent. Superconducting materials, on the other hand, become diamagnetic only below the critical temperature, when they are in the superconducting state. The resultant susceptibility is very large ($\mathbf{B} = 0$, $\mathbf{H} = -4\pi\mathbf{M}$, $\chi_v = -1/4\pi$ in the limiting case), and is to some degree temperature dependent.

As mentioned, when samples become superconducting, and in the presence of low to moderate external magnetic fields, an internal magnetic field is induced such to create zero net magnetic field within the sample. This phenomenon, where external magnetic field is effectively *expelled* from the superconducting samples submerged

in it, is known as the Meissner effect. However, if the external field is sufficiently large, the sample exhibits a loss of superconductivity, as the strong external magnetic field tends to suppress superconductivity. The Meissner effect therefore provides a unique and reliable method for determining the superconducting properties and the superconducting transition temperature, T_c, of bulk samples. The magnetization of a superconducting sample exhibits a typical diamagnetic response. The characteristic negative signal in the magnetization versus temperature curve, observed in the superconducting phase, changes sign when superconductivity is suppressed at elevated temperatures, and hence enables one to determine superconducting transition temperature, T_c. This robust method is routinely performed by employing SQUID dc magnetization measurements on bulk samples. On the other hand, resistivity measurements on powder samples are less reliable, since the results depend on the quality of the electric contacts in typical four-probe measurements, and also such measurements often yield properties of the surface of the sample, or of the preferred directions within the sample, rather than properties of the bulk.

The superconducting transition temperatures for the samples considered for this study were determined from dc magnetization measurements using SQUID apparatus. Small amounts of the samples, with their masses noted, were first cooled from room temperature down to 5 K in the absence of the external magnetic field (zero-field cooled). At base temperature and in the absence of the field, magnetization of the sample was recorded to calibrate the system for eventual residual magnetic field in the apparatus. Afterwards, a relatively small external field of 100 Gauss was applied, and temperature increased in uniform steps, keeping a record of magnetization at each temperature. Low-field magnetization as a function of temperature, on warming, enabled us to determine the onset T_c for all the samples, when they undergo a second order phase transition from the superconducting to the normal state. The estimated transition temperatures as a function of Sr content are shown in Figure 3.8. In the

inset of the same figure we show a typical temperature dependence of the magnetization per unit mass, in this case for optimally doped LSCO sample (x=0.15) that exhibits the highest T_c (within the LSCO family) of about 38 K.

Typically, only a fraction of the sample volume exhibits superconductivity. Good bookkeeping in the characterization is important, as it allows one to estimate the superconducting (Meissner) volume fraction of a HTS sample. In Figure 3.9 we present an estimate of the Meissner fraction for the LSCO samples.

The Meissner fraction, f, can be estimated from susceptibility measurements using the following equation [174]:

$$f = \frac{4\pi\rho\Delta M}{m\Delta H}, \tag{3.6}$$

where ρ is the mass-density of the sample, calculated from the unit cell volume and known masses of the atoms constituting the unit cell, m is the mass of the sample being characterized, ΔH is the change in the external magnetic field, and ΔM is the corresponding change in the magnetization of the sample as obtained from the SQUID measurement. When calculating the Meissner fraction using the above equation, the following assumptions have been made: (i) the particles have spherical shape, (ii) no vortex lines and (iii) no grain boundaries that would pin these vortices are present in the sample at a given external magnetic field (this is the reason for cooling the sample without external field), as well as that (iv) the grains are not interconnected (i.e. do not form Josephson junctions). All the reasons listed above are source of rather large uncertainty, and the Meissner fraction parameter is rather difficult to determine accurately [175]. Meissner fraction for our samples is estimated using mass densities calculated from neutron diffraction structural data at 10 K temperature [44], and the results of the SQUID characterization experiments at 5 K. The average crystal structures of the samples do not change appreciably from 10 K to 5 K. Table 3.3 provides a summary of the values used in the Meissner fraction calculations for LSCO samples.

Table 3.3: Notes summarizing information relevant for characterization of the magnetic properties of LSCO samples. Table includes information on the following quantities: doping concentration, mass of the samples used in the measurements, mass density of these samples at 5 K temperature, and measured dc magnetization. External magnetic field applied was 100 Gauss.

doping	m (gr)	$\rho_m(gr/cm^3)$	ΔM (emu)	f (%)
0.00	0.892(1)	7.1060(5)	0.0000(1)	0
0.05	0.794(2)	7.0843(5)	0.0000(1)	0
0.10	0.627(1)	7.0592(5)	0.3095(2)	30(14)
0.125	0.401(5)	7.0441(5)	0.1280(1)	28(7)
0.15	0.675(5)	7.0276(5)	0.2973(5)	39(10)
0.175	0.439(5)	7.0199(5)	0.2189(5)	44(10)
0.1875	0.575(5)	7.0176(5)	0.23313(5)	36(10)
0.20	0.755(5)	7.0088(5)	0.19576(5)	22(7)
0.225	0.329(5)	6.9903(5)	0.06397(5)	17(7)
0.25	0.450(5)	6.9738(5)	0.04313(5)	8(5)
0.30	0.708(1)	6.9400(5)	0.00942(5)	1(1)

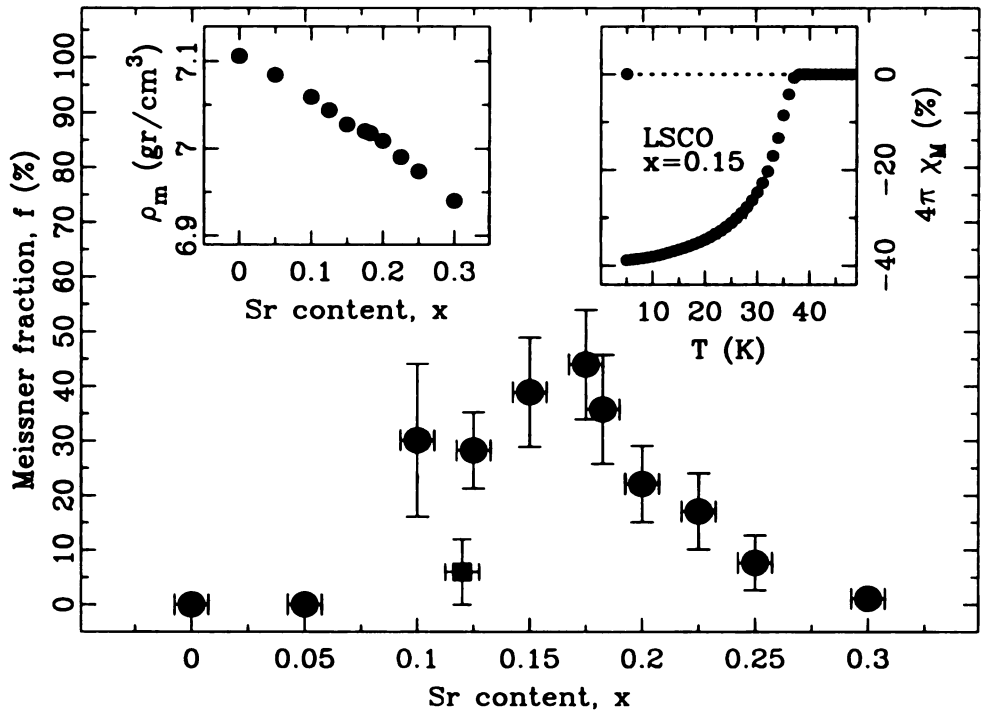

Figure 3.9: Meissner fraction as a function of doping at 5 K temperature as estimated from dc susceptibility measurements using external magnetic field of 100 Gauss (solid circles). The solid square symbol marks superconducting fraction for the Nd-codoped sample. Left inset: mass density of LSCO samples versus doping at 10 K temperature. Right inset: normalized magnetic dc susceptibility as a function of temperature, for x=0.15 LSCO sample. Dotted line denotes behavior within zero-field cooling cycle.

Optimally doped LBCO sample has been characterized elsewhere [166]. Diamagnetic response in this sample (not shown) appeared at approximately 27 K. The characterization consisted of standard zero-field cooling and field heating, with an applied magnetic field being 10 Gauss.

3.5 Structural phase transitions

To complete the characterization of the samples used, it is also of interest to determine the location of the structural phase transitions in the temperature-doping ($T-x$) phase space. Knowledge of this plays important role in discriminating whether observed structural effects are structural phase transition related, or whether they have some other origin.

In the LSCO case two structural phases occur, high temperature tetragonal (HTT) phase (space group $I4/mmm$, No. 139), and low temperature orthorhombic (LTO) phase (space group *Cmca*, No. 64). The structural phase transition from LTO to HTT is of the second order. In order to be able to use consistent set of axes throughout the phase diagram, however, it is more convenient to convert to the nonstandard (isomorphic) settings for both of the phases, and therefore we used *Bmab* setting for LTO, and $F4/mmm$ setting for the HTT phase [44]. Transformation from the original setting to the equivalent one is achieved by doubling the unit cell and rotating the a,b-axes by 45^o degrees about the c-axis.

On the other hand, the LBCO system undergoes the sequence of two structural phase transformations on cooling. At high enough temperature it is in HTT ($I4/mmm$) phase, and by lowering the temperature it reaches first LTO (*Bmab*) phase, and on further decline of temperature it enters the low temperature tetragonal (LTT) phase (space group $P4_2/ncm$, No. 138) [47]. The latter structural phase transition is of the first order, and has not been observed in the average structure of LSCO

samples. However, in samples that are double-doped with Nd and Sr the LTT phase occurs [31].

It is possible to determine the structural phase transition coordinates in $T - x$ phase space, and locate the structural phase transition using different methods. Here we mention two practical methods that are based on either inspection or simple considerations of structural parameters.

Firstly, in reciprocal space one can monitor superlattice peaks, that is Bragg peaks in the diffraction pattern that are sensitive to symmetry changes. It is a rule of thumb that the more symmetric the structure, the smaller the number of Bragg peaks its diffraction pattern contains (of course we have single sample in mind). Two types of superlattice peaks exist: (i) those that appear-disappear when the low-high symmetry boundary is crossed (lower-symmetry peaks), and (ii) those that exist in both low and high symmetry phases, but split into two peaks in the former case (splitting peaks). By monitoring the behavior of the superlattice peaks as a function of temperature and doping, the structural phase transition point can be determined. At the phase transition the low-symmetry peaks vanish, and therefore their intensity can be regarded as an order parameter. Alternatively, the separation between splitting peaks vanishes upon crossing into a high-symmetry phase, and hence the separation is an order parameter.

Secondly, and specifically for an orthorhombic-to-tetragonal phase transition, lattice parameters a and b can be monitored as a function of temperature and doping. This is usually quantified through a parameter known as orthorhombic strain, $\eta = (a-b)/(a+b)$, which is an order parameter and vanishes in the tetragonal phase, where $a = b$.

Both methods mentioned above were utilized to locate the structural phase transitions in LSCO and LBCO samples on the phase diagram. Typical 400/040 superlattice peak splitting is shown in Figure 3.10, where the LTO-HTT phase tran-

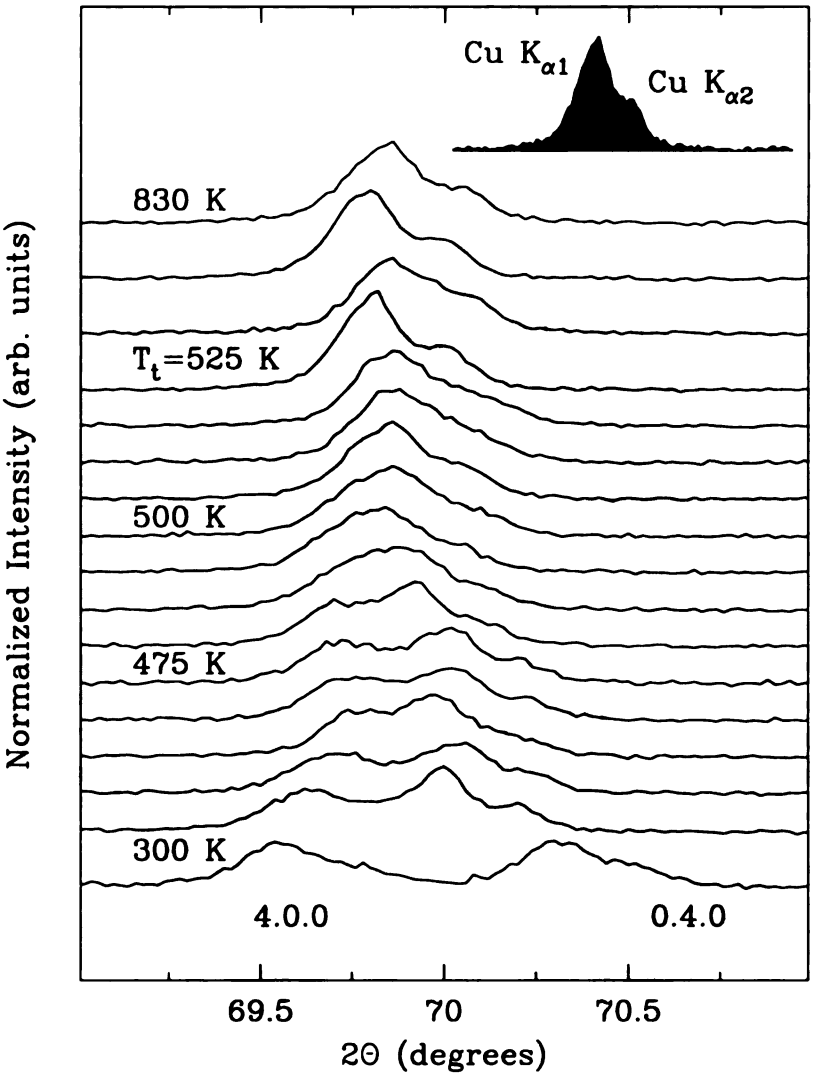

Figure 3.10: Orthorhombic to tetragonal structural phase transition in La_2CuO_4, characterized by splitting of the 400/040 superlattice peak. X-ray diffraction data has been collected with the in-house diffractometer (see text) using copper radiation. The normalized intensity is plotted as a function of the scattering angle, 2θ. Note the presence of the satellite shoulder-peak with the intensity of one half of that of the main contribution. It originates from the copper $K\alpha_2$ radiation. Copper $K\alpha_1$ and $K\alpha_2$ lines correspond to the wavelengths of 1.54056 Å and 1.54439 Å respectively, and are known to give Bragg peaks having 2:1 intensity ratio.

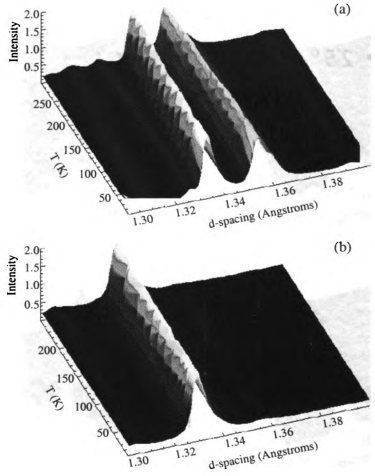

Figure 3.11: (a) Orthorhombic LTO phase is characterized by splitting of the 400/040 superlattice peak (La_2CuO_4 case shown). (b) In the tetragonal HTT phase these two peaks coincide ($La_{1.8}Sr_{0.2}CuO_4$ case shown). The vertical axis is the scattering intensity (arb. units), horizontal axes are temperature and d-spacing. Data were collected at GEM, ISIS facility, UK.

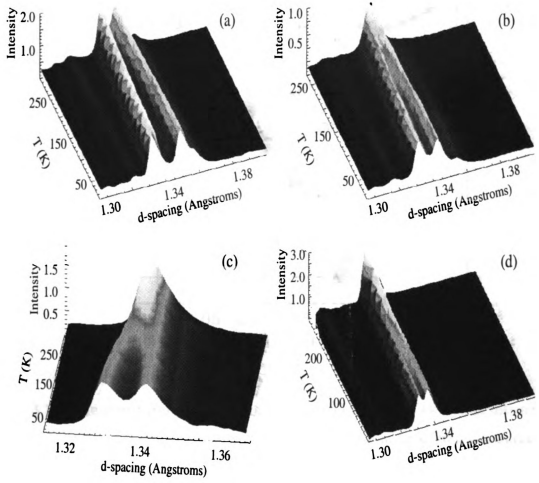

Figure 3.12: $La_{2-x}Sr_xCuO_4$ 400/040 superlattice peak evolution with temperature for x=0.05 (a), x=0.10 (b), x=0.125 (c), and x=0.15 (d). The vertical axis is the scattering intensity (arb. units), horizontal axes are temperature and d-spacing. Data were collected at GEM, ISIS facility, UK.

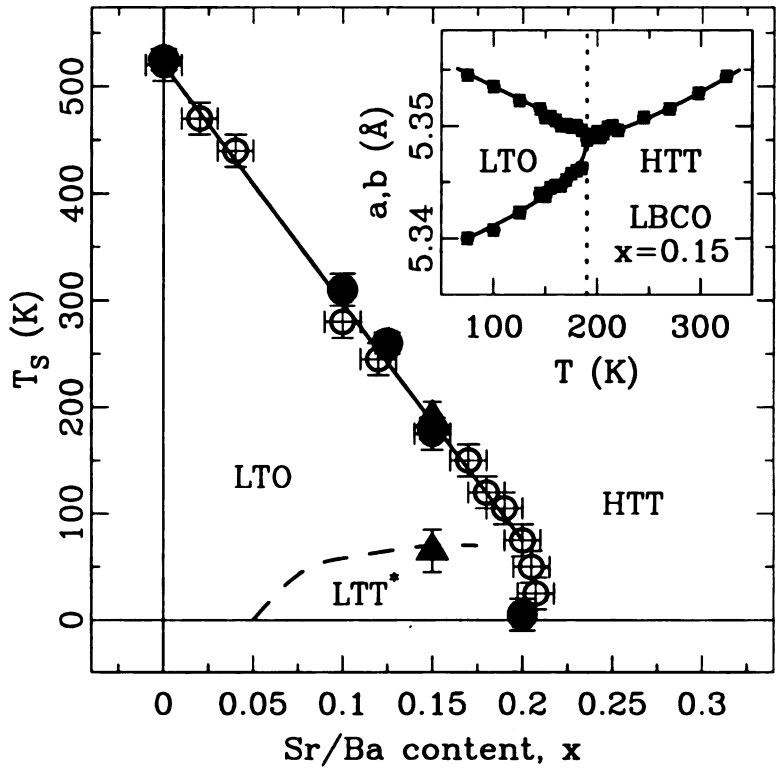

Figure 3.13: The structural phase diagram for LSCO and LBCO systems. Structural phase transition temperature, T_S, is plotted as a function of Sr/Ba concentration, based on Rietveld refinement results. Solid symbols denote values for the samples used in this study. Circles correspond to LSCO samples, while triangles mark the LBCO sample. Open circles are literature values [119]. Lines are guides for the eye. The dashed line denotes the LTO-LTT low temperature phase transition, occurring in LBCO samples. This transition has not been seen in the average structure of LSCO system*. Inset: T_S determination for the LTO-HTT transition in the LBCO sample from lattice parameter considerations. Dotted line denotes the phase transition.

sition temperature is searched for at high temperatures. A copper radiation based x-ray diffraction experiment was carried out in a furnace environment, using in-house diffractometer described earlier in this chapter. Evolution of 400/040 peaks with temperature in various LSCO samples is shown in Figures 3.11 and 3.12, as obtained from neutron powder diffraction experiments.

Results of the structural phase transition characterizations are summarized in Figure 3.13 and compared to the literature. The inset in Figure 3.13 shows the LTO to HTT phase transition in the optimally doped LBCO sample, as viewed from the lattice parameter perspective.

3.6 Summary

Samples used in this study were prepared in amounts sufficient for typical neutron powder diffraction based PDF study, following well established solid state preparation routes. The samples were characterized to determine their quality, phase purity, stoichiometry, superconducting properties, as well as to locate known structural phase transitions. All the characterizations were carried out using standard protocols. The summary of the characterizations is given in Table 3.4 and in Figure 3.13. Appropriate subset, with reliable properties, of all the samples addressed in this chapter was selected and studied, as we further present.

Table 3.4: Summary of relevant characterization results is presented. Information on dopant ion content, sample mass, T_c for superconductivity, phase purity from x-ray diffraction, and c-axis lattice parameter values obtained from Rietveld analysis of the x-ray diffraction (at room temperature) and neutron diffraction (at 10 K) data are given. Notation used in this table is as follows: single phase (s), multiphase (m), or identified impurity phase (where known) is specified. Overall, the samples are either labeled as good (g) or as bad (b), and were either used in the study (y), or not used (n).

sample	doping	m (g)	T_c (K)	XRD	c_N^{10K} (Å)	c_{XRD}^{293K} (Å)	note
LCO	0.00	11.7	-	s	13.1030(3)	13.1665(11)	g,y
LSCO	0.05	10.5	-	s	13.1460(3)	13.1748(10)	g,y
LSCO	0.10	6.1	29(1)	s	13.1720(3)	13.203(2)	g,y
LSCO	0.125	6.9	31(1)	s	13.1840(3)	13.2177(12)	g,y
LSCO	0.15	8.9	38(2)	s	13.1960(3)	13.219(2)	g,y
LSCO	0.175	11.5	37(2)	s	-	13.2261(9)	b,n
LSCO	0.1875	13.7	35(2)	s	-	-	g,n
LSCO	0.20	10.3	30(2)	s	13.2160(3)	13.2432(6)	g,y
LSCO	0.225	10.9	28(2)	T"	-	13.234(1)	b,n
LSCO	0.25	12.7	8(2)	s	13.2249(3)	13.2402(10)	g,y
LSCO	0.30	10.8	-	s	13.2301(3)	13.2518(8)	g,y
LBCO	0.15	12.5	27(2)	s	-	-	g,y
LNSCO	0.4,0.12	9.7	31(2)	Al_2O_3,T'	-	-	b,y

Chapter 4

Structural Response to Local Charge Order in Superconducting $La_{2-x}(Sr,Ba)_xCuO_4$

"When one has made a decision to kill a person, even if it will be very difficult to succeed by advancing straight ahead, it will not do to think about going at it in a long roundabout way. The Way of the Samurai is one of immediacy and it is best to dash in headlong." (T. Yamamoto)

4.1 Prelude

Here we present local structural evidence supporting the presence of charge inhomogeneities in the CuO_2 planes of LSCO and LBCO at low temperature. High-resolution atomic pair distribution functions of underdoped $La_{2-x}Sr_xCuO_4$ have been obtained from neutron powder diffraction data over the range of doping $0 \leq x \leq 0.30$ at 10 K. Despite the average structure getting less orthorhombic, a *broadening* is seen of the in-plane Cu-O bond distribution as a function of doping up to optimal doping. There-

after the distribution of the nearest neighbor distances abruptly sharpens. The nearest neighbor PDF peak broadening can be well explained by a local microscopic coexistence of doped and undoped material. The doping dependence of the distribution at low temperature suggests a crossover from a charge inhomogeneous state at and below optimal doping to a homogeneous charge state above optimal doping. The strong response of the local structure to the charge-state implies a strong electron-lattice coupling in these materials. The nearest neighbor PDF peak broadening observed in superconducting LSCO samples disappears at elevated temperature. Similar broadening has been observed in low temperature data of optimally doped LBCO and Nd co-doped LSCO samples as well. Atomic pair distribution function analysis of neutron powder diffraction data has been carried out on $La_{1.875}Sr_{0.125}CuO_4$, $La_{1.85}Ba_{0.15}CuO_4$, $La_{1.85}Sr_{0.15}CuO_4$, and $La_{1.475}Nd_{0.4}Sr_{0.125}CuO_4$ to obtain local structural information over 10 K $\leq T \leq$ 300 K temperature range. In this separate set of experiments we again observed an anomalous increase in the Cu-O bond length distribution at low temperature that may be associated with the presence of an inhomogeneous charge distribution. The increase at low temperature is found to have an *onset temperature* which correlates well with observations of charge and spin freezing seen by other probes.

4.2 Charge inhomogeneities in the CuO_2 plane at low temperature

4.2.1 Approach

The presence of charge inhomogeneities in the CuO_2 plane implies profound consequences for the local structure. It is well known that the average Cu-O bond length changes as the charge state of copper changes. Thus, the Cu-O bond in $La_{2-x}Sr_xCuO_4$

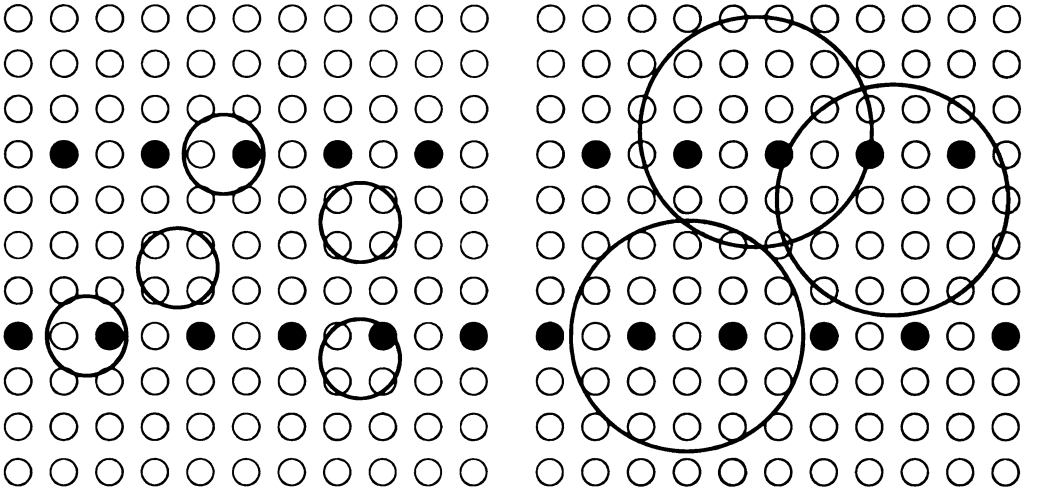

Figure 4.1: Examination of the CuO_2 plane using the PDF information: schematic view of the plane in 214 system. Small circles represent copper atoms. Filled circles represent sites with doped holes. Thick circles denote two dimensional cuts of the PDF probing sphere with various probing radii: low r (left panel) and intermediate r (right panel). See text for details.

shortens from 1.904 Å to 1.882 Å as x changes from 0 to 0.2 [44] and the average copper charge changes from +2 to $\sim$ +2.2. This is a generic feature of variably dopable HTS samples and comes about because the Cu-O bond is a covalent anti-bonding state which is stabilized by removing electron density from it [176]. Clearly, if the doped charge in the CuO_2 planes is inhomogeneously distributed, such that some copper sites have more charge than others, a distribution of in-plane Cu-O bond lengths will exist. A high resolution measurement of the in-plane Cu-O bond length *distribution* as a function of doping will therefore reveal the extent of charge inhomogeneities.

Details of how this would come about in the PDF are illustrated in Figure 4.1. In this Figure a schematic view of CuO_2 plane is given, and stripe-like distribution of holes is assumed, although our considerations would equally apply to other inhomogeneous distributions. When the radius of the PDF probing sphere is small (i.e. in the low-r PDF region), and in case of inhomogeneous distribution, one expects to see a

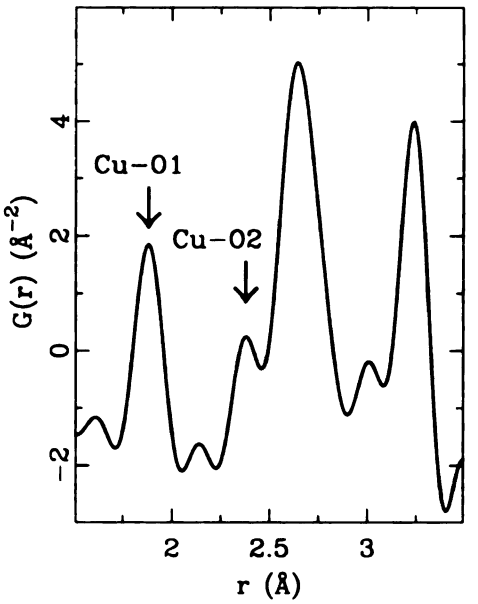

Figure 4.2: The first two peaks in the PDFs of 214 system. Local structural information on the in-plane and apical Cu-O distances is contained in the first two PDF peaks. These are marked by arrows, and labeled as Cu-O1 and Cu-O2 (in-plane and apical respectively).

mixture of undoped and heavily doped material. For intermediate size of the probing sphere (i.e. in the intermediate-r PDF region) and in presence of inhomogeneities that have striped morphology, one in principle expects to see evidence of stripe correlations. This can also be thought of using 'intra-domain' and 'inter-domain' terminology, as mentioned in Chapter 2. Investigation of the local structure of CuO_6 octahedra in 214 systems uses structural information contained in the first two peaks of the PDF profile, marked in Figure 4.2. The information related to the in-plane Cu-O bond (Cu-O1) can be assessed by studying the nearest-neighbor PDF peak. In the average structure the nearest neighbor PDF peak has a single contribution corresponding to four equal Cu-O1 distances. The PDF is sensitive to the nature of the atomic displacements, but is relatively insensitive to the symmetry of the ordering. Presence of any bond-length disorder would be observed as an anomalous broadening of the

nearest neighbor PDF peak. However, even if such disorder is observed and if it is indicative of the presence of charge inhomogeneities, it could not unambiguously discriminate between a striped arrangement of charges and any other arrangement. We note at this point that already the next-nearest-neighbor PDF peak, containing the information on the apical Cu-O distance (Cu-O2), is 'contaminated' in a sense that it has multiple contributions (i.e. includes short La-O-type distances). The analysis of possible Cu-O2 distance distribution directly from the PDF profile would therefore be more complicated. Since we are interested in the nature of the charge distribution in the CuO_2 planes, and therefore in the in-plane structural information, our attention in the analysis is confined to the nearest neighbor PDF peak. Certain aspects of the doping dependence of the apical distance are addressed in Chapters 7 and 8.

The ability of high-resolution PDF studies to reveal local bond-length inhomogeneities which are not apparent in the average structure has been clearly demonstrated [177]. The LSCO samples studied at low temperature cover the range from undoped, through underdoped and optimally doped ($x = 0.15$) to the overdoped regime. As it will be shown further in this chapter, we find that at 10 K the mean-square width of the in-plane Cu-O bond-length distribution, σ^2, increases approximately linearly with x until optimal doping above which it sharply decreases and returns to the value of the undoped material by $x = 0.25$. This is strong evidence for charge inhomogeneities in the under- and optimally-doped regimes of LSCO as we discuss below. This increase in bond-length distribution can be well explained by a linear superposition of the local structures of undoped and heavily doped material.

4.2.2 Experimental highlights

We have used the atomic PDF analysis of neutron powder diffraction data to measure accurate Cu-O bond length distributions with high resolution for a series of $La_{2-x}Sr_xCuO_4$ samples with ($0 \leq x \leq 0.3$). Samples of $La_{2-x}Sr_xCuO_4$ with $x = 0.0$,

0.05, 0.1, 0.125, 0.15, 0.2, 0.25, and 0.3 were made using standard solid state synthesis, as described in detail in Chapter 3. Neutron powder diffraction data were collected at 10 K on the SEPD at the IPNS at Argonne National Laboratory. Approximately 10 g of finely powdered sample was sealed in a cylindrical vanadium tube with He exchange gas. The samples were cooled using a closed-cycle He refrigerator. The PDFs were obtained from the measured total scattering functions according to the procedure described in Chapter 2. PDFs from these samples are shown in Chapter 5, as well as in Figures 5-8 of Reference [178] and in Figure 4.5 of this chapter. The PDFs examined here used total scattering data over a range 0.7 $\text{Å}^{-1} \leq Q \leq 28\ \text{Å}^{-1}$.

4.2.3 Nearest-neighbor Cu-O PDF peak width analysis

We are interested in extracting the width of the distribution of in-plane Cu-O bond-lengths. This information is contained in the width of the first PDF peak at ~ 1.9 Å. The peak-width comes from the thermal and zero-point motion of the atoms plus any bond-length distribution originating from other effects such as charge inhomogeneities. We can determine the latter by considering the PDF peak width of this peak as a function of doping at 10 K. Three independent measures of the peak width all show that the width increases significantly with doping up to $x = 0.15$, beyond which the peak quickly sharpens. First, this behavior is evident by simply looking at the data shown in Figure 4.3. This shows the low-r region of the PDF around the $r = 1.9$ Å peak as a function of x. Since we want to compare the relative peak widths (and heights), in this Figure the peaks have been shifted to line up the peak centroids and rescaled slightly to ensure that the integrated intensity of each peak is the same. It is clear that some of the peaks are significantly broader than others with lower peak heights and less steeply sloping sides. We have quantified this by fitting the peak with a single Gaussian. The Gaussian is first convoluted with the Fourier transform of the step function which was used to terminate the data [144]. This accounts

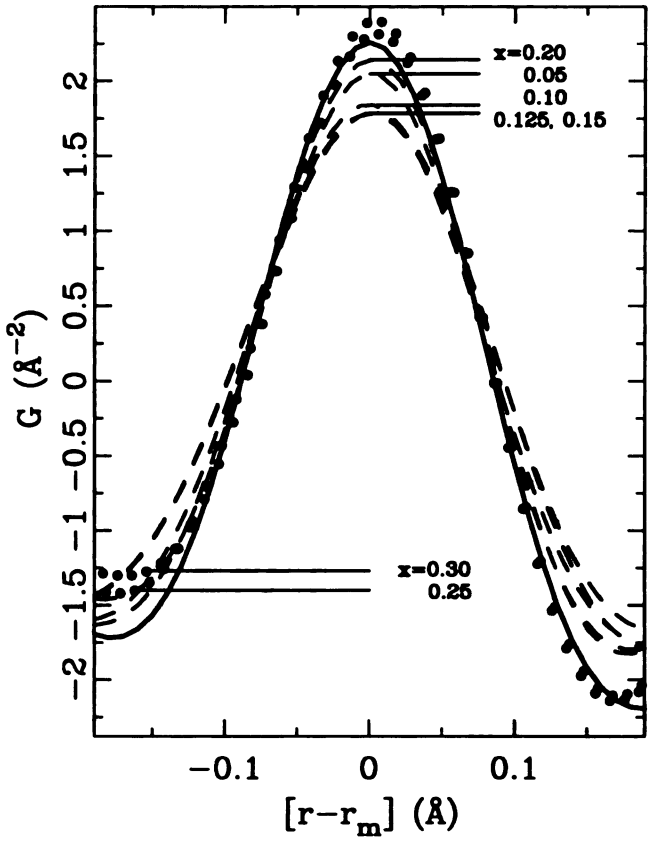

Figure 4.3: PDF peak coming from the in-plane Cu-O bond for various doping levels (solid line: undoped case; solid circles: overdoped cases; dashed lines: intermediate doping cases). The peaks have been shifted so that their centers line up at r_m = 1.91 Å.

for any termination ripples in the data introduced by the Fourier transform of the finite range data-set and does not introduce any additional parameters into the fit. The fitting parameters were peak position, scale-factor and width. The baseline is set by the average number density of the material and this was fixed at $\rho_0 = 0.07299$ Å^{-3}. The results are shown in Figure 4.4 as the solid circles. The mean-square width of the distribution increases monotonically (and almost linearly) with x until $x = 0.15$. Between 0.15 and 0.2 the peak abruptly sharpens and returns to the width of the undoped sample by $x = 0.25$. The same behavior can be obtained from the data in

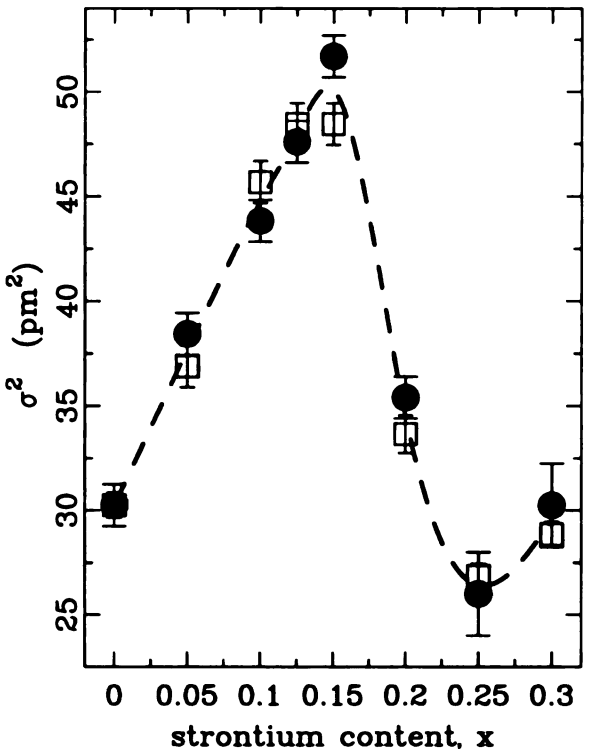

Figure 4.4: Peak width of the in-plane Cu-O PDF peak as a function of doping obtained by fitting a Gaussian (solid circles). The data are plotted as σ^2 where σ is the Gaussian standard deviation. The inverse peak-height-squared of the peaks in Figure 4.3 scaled so the $x = 0.0$ points line up is shown as open squares. The dashed line is a guide for the eye.

a totally model-independent way. If the integrated area of a Gaussian is constant the height is inversely proportional to the width. Thus, the peak height, h, of the rescaled data shown in Figure 4.3 should be inversely proportional to the width. The open squares in Figure 4.4 show C/h^2 where h was determined directly from the peak maximum in the data and the constant C was chosen to make the $x = 0.0$ points line up. There is excellent agreement lending confidence to the results from the fitting.

4.2.4 Discussion

We would like to discuss possible origins for these doping dependent changes in Cu-O bond-length distribution. First we rule out the possibility that it simply comes from changes in the orthorhombicity of the sample. The Cu-O PDF peak first broadens smoothly with increasing doping then dramatically sharpens at a composition close to the LTO-HTT structural phase boundary. This behavior does not reflect the monotonic decrease in orthorhombicity of the average structure. Indeed, in the overdoped region the PDF peak returns to the same narrow width it had in the undoped material which has the largest orthorhombic distortion of any of the samples. We also note that the in-plane Cu-O bonds are not expected to be sensitive to the orthorhombic distortion. They lie along the unit cell diagonals and not along the unit cell edges in the orthorhombic unit cell. In this case an orthorhombic distortion will change the bond-length but will not lead to two distinct bond-lengths. Next we show that the observed behavior cannot be explained by doping dependent changes in the octahedral tilts. The average [44] (and local [178]) tilt amplitude monotonically decreases with increasing doping which does not correlate with the behavior of the Cu-O bond length distribution. On the other hand, PDF peaks at higher-r do sharpen monotonically with increasing x reflecting the reduced octahedral tilt amplitude [178]. We also rule out the idea that the observed Cu-O peak broadening is an effect of size-effect disorder due to doping since the peak sharpens dramatically above $x = 0.2$ where the dopant induced disorder should be the greatest. We also note that size-effect dopant induced disorder is expected to have a large effect on octahedral tilts and a small effect on Cu-O bond lengths since the energy to change a Cu-O-Cu bond angle is much less than the energy to stretch the short Cu-O covalent bond. Furthermore, the extent of dopant induced tilt disorder is relatively small in $La_{2-x}Sr_xCuO_4$ as evidenced by the observation that higher-r PDF peaks sharpen on increased doping in this material. These peaks sharpen because of a decrease in

both the average orthorhombicity and octahedral tilt angle with increased doping. However, significant size-effect octahedral tilt disorder due to the chemical dopants tends to counter this effect, as seen in $La_{2-x}Ba_xCuO_4$ [179, 180]. We can also rule out structural fluctuations associated with the HTT-LTO transition. First, these fluctuations will affect primarily octahedral tilts and local orthorhombicity (the two order parameters of this structural transition) and as we have discussed, the Cu-O bond is expected to be quite insensitive to disorder in these parameters. However, in addition, we would expect these fluctuations to be largest when the structural phase transition temperature, T_s, is closest to our measurement temperature. These temperatures are closest for the $x = 0.2$ sample (T_s=60 K [181], T_{meas}=10 K) and this sample exhibits a narrow distribution of Cu-O bond-lengths. The largest distribution of Cu-O bond-lengths is seen for $x = 0.15$ where T_s=180 K. The observed behavior of the Cu-O bond-length distribution is best explained by the presence of charge inhomogeneities. As we have described, the charge-state of copper has a direct effect on the Cu-O bond length with the bond-length decreasing with increasing doping. Charge inhomogeneities will, thus, give rise to a distribution of Cu-O bond lengths. Increased doping will result in more Cu-O bonds being affected and therefore a larger measured effect in the PDF, as observed. Above optimal doping the PDF peak width abruptly sharpens to its value in the undoped material. This is consistent with the idea that in the overdoped region, the charge distribution in the Cu-O planes is becoming homogeneous.

We now discuss independent evidence from the data which supports this picture. In Figure 4.5(a) we show the low-r region of the PDF from the $x = 0.0$ and $x = 0.25$ samples. Referring to Figure 4.4 we see that these two data-sets have relatively *narrow* Cu-O bond-length distributions. Furthermore, in Figure 4.5(a) it is apparent that the peak position has shifted due to the change in the average Cu-O bond-length with doping, as expected. The difference curve below the data shows that the two data-sets

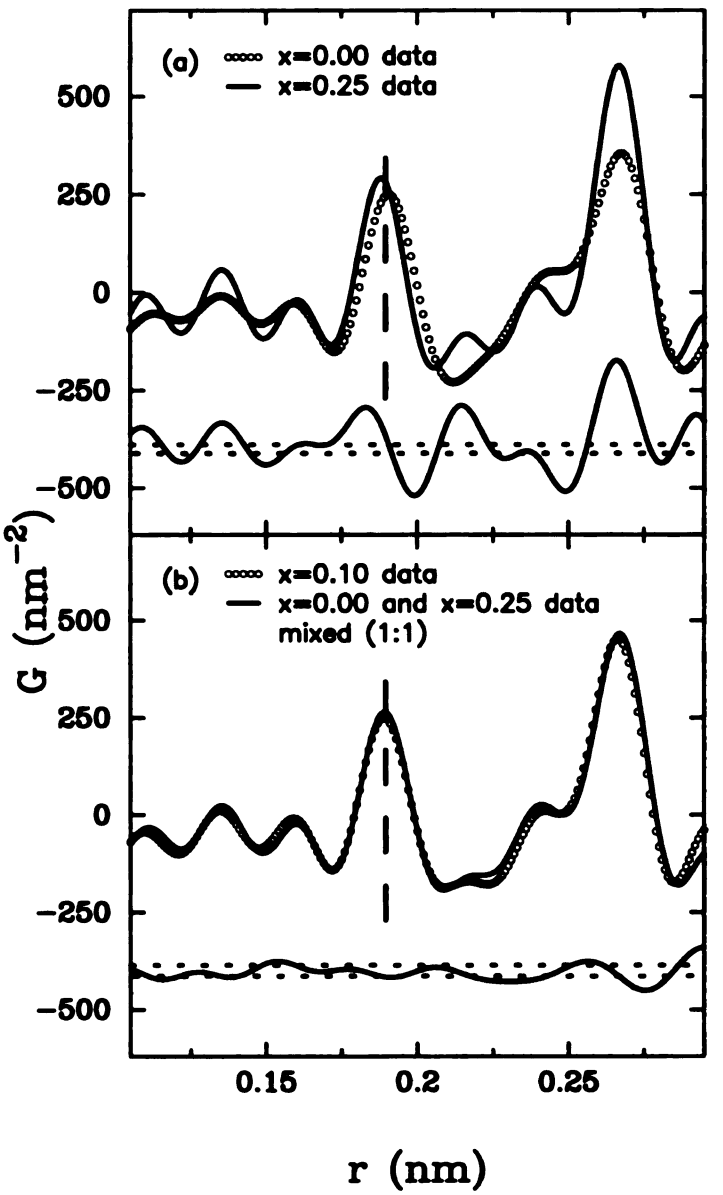

Figure 4.5: (a) PDFs from the 10 K data from the $x = 0.0$ (open circles) and $x = 0.25$ (solid line) samples. The difference is plotted below. The dashed lines indicate expected uncertainties due to random errors. (b) PDF from $x = 0.1$ data at 10 K (open circles). The solid line shows the PDF obtained by making a linear combination in a (1:1) ratio of the PDFs shown in (a). See the text for details.

are quite different due to the significant structural differences. In Figure 4.5(b) we show the intermediate $x = 0.1$ data-set plotted as open circles. This peak is centered at a position shown by the dashed line which is intermediate between the positions of the $x = 0.0$ and $x = 0.25$ data-sets. Referring to Figure 4.4 we see that the Cu-O bond-length distribution is relatively *broad* at this composition. Plotted on top of the $x = 0.1$ data-set in Figure 4.5(b) as the solid line is the PDF obtained by taking a linear combination of the $x = 0.0$ and $x = 0.25$ data-sets in the 1:1 ratio, without rescaling the data at all. The difference curve is shown below. The good agreement clearly demonstrates that the observed PDF peak position *and* broadening of the $x = 0.1$ data-set is entirely *consistent* with there being an underlying bimodal bond-length distribution consistent with heavily doped and undoped regions of the CuO_2 plane. We can infer from this analysis that the difference in the bond-lengths is ~ 0.024 Å which is the difference between the average bond-lengths of the $x = 0.0$ and $x = 0.25$ samples.

Finally, we note that the PDFs from underdoped $La_{2-x}Sr_xCuO_4$ are consistent with the presence of CuO_6 octahedral tilt disorder in the samples. The disorder has been seen both in tilt magnitudes and in tilt directions, as will be shown in Chapter 5, where this supporting evidence is discussed. We show that the measured PDFs could be well explained by a local structure which contains a mixture of large and small octahedral tilts. In addition, evidence from the PDFs is also presented for the presence of tilt-directional disorder in the sense that there is a mixture of $\langle 100 \rangle$ ("LTO") and $\langle 110 \rangle$ ("LTT") symmetry tilts existing in the local structure.

4.2.5 Summary

We have presented evidence from neutron diffraction data which strongly supports the idea that doped charge in the CuO_2 planes of superconducting $La_{2-x}Sr_xCuO_4$ for $0 < x \leq 0.15$ and at 10 K is inhomogeneous. For doping levels of $x = 0.2$ and above

the charge distribution in the CuO_2 plane becomes homogeneous.

4.3 Onset temperature determination

4.3.1 Approach

We used the atomic pair distribution function (PDF) analysis [182] of neutron powder diffraction data to study the local structure of $La_{2-x}(Sr,Ba)_xCuO_4$ as a function of temperature. Structural distortions coming from charge inhomogeneities appear in the PDF as an anomalous broadening of the nearest neighbor in-plane Cu-O bond length distribution, as shown in Section 4.2 [183]. Charge inhomogeneities imply a coexistence of heavily and lightly doped regions of the CuO_2 plane. The lattice responds if the charge inhomogeneities are fluctuating on phonon time-scales or slower. This results in a distribution of lengths for the in-plane Cu-O bond and correspondingly to a broadening of the atomic pair distribution at low temperature. Using the same approach applied in the study of the LSCO doping dependence at 10 K we evaluate the in-plane bond length distribution in several selected samples as a function of temperature. The 10 K behavior is reproduced in these independent measurements, and an onset temperature where the bondlength distribution appears is determined for these samples as well.

4.3.2 Experimental highlights

Samples with compositions $La_{1.875}Sr_{0.125}CuO_4$, $La_{1.85}Ba_{0.15}CuO_4$, $La_{1.85}Sr_{0.15}CuO_4$ and $La_{1.475}Nd_{0.4}Sr_{0.125}CuO_4$ of $\sim$ 10 g were synthesized using standard solid state techniques and characterized as described in detail in Chapter 3 [165, 166]. The oxygen content of the powdered samples was verified by measuring the c-axis parameter that was found to fall on the expected curve for stoichiometric samples [44]. Neutron powder diffraction measurements were carried out on the HIPD at the MLNSC at

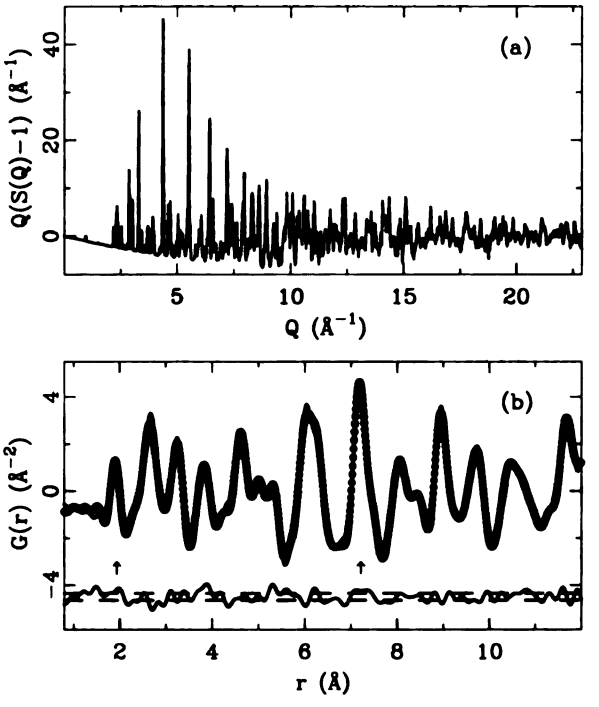

Figure 4.6: (a) Reduced total scattering structure function, $Q[S(Q) - 1]$, from $La_{1.875}Sr_{0.125}CuO_4$ at 300 K. (b) The resulting PDF, $G(r)$ (open circles). The solid line is a fit to the data of the crystallographic model with the difference curve below. Arrows indicate the PDF peaks at $r = 1.9$ Å and $r = 7.2$ Å whose widths are plotted in Figure 4.7.

Los Alamos National Laboratory and on the GLAD and the SEPD at the IPNS at Argonne National Laboratory. The samples were sealed in vanadium tubes with He exchange gas. Data were collected as a function of temperature from room temperature down to 10 K using a closed cycle He refrigerator. Standard corrections [184] were made to the raw data, to account for experimental effects such as sample absorption and multiple scattering, using the program PDFgetN [163], to obtain the total scattering structure function, $S(Q)$. This contains both Bragg and diffuse scattering and therefore information about atomic correlations on all length scales. Technical details are presented in Chapter 2.

The PDF from $La_{1.875}Sr_{0.125}CuO_4$ at 300 K is shown in Figure 4.6(b) with the

diffraction data in the form of $Q[S(Q) - 1]$ in Figure 4.6(a). Superimposed on the PDF is a fit to the data of the average structure model using the profile fitting least-squares regression program, PDFFIT [161]. This time the $S(Q)$ data were terminated at $Q_{max} = 24$ Å^{-1}. This is a *conservative* value for Q_{max} in typical PDF measurements and results in a *moderate resolution* in real-space. Since we are searching for the presence of small distortions, a higher Q_{max}, and therefore better real-space resolution, should be preferred. However, the data from high-Q has a poorer signal-to-noise ratio because of the effect of the Debye-Waller factor. By eliminating high-Q data from the Fourier transform we improve the signal-to-noise ratio of our data and the temperature to temperature reproducibility of the PDFs. This reduces our sensitivity to the changes, but also reduces the possibility that observed effects are noise artifacts. We can therefore have confidence that any effects that survive this conservative approach to Fourier transforming the data are real. The effects shown here have been observed for higher Q_{max} values as well.

4.3.3 Nearest-neighbor Cu-O PDF peak width analysis

In $La_{2-x}(Sr,Ba)_xCuO_4$, the first peak in the PDF at $r = 1.9$ Å originates from the in-plane Cu-O bond. The width of this peak comes from the relative motion of nearest neighbor in-plane Cu-O pairs, plus any static or quasistatic bond-length distribution, averaged over the whole sample. We have studied the mean square width, $\sigma^2 \propto \langle u^2 \rangle$, of this peak as a function of temperature for a series of underdoped $La_{2-x}(Sr,Ba)_xCuO_4$ compounds. Peak profiles in the PDF were again modeled using a Gaussian functionconvoluted with a Sinc function, $\sin Q_{max}r/Q_{max}r$ [144]. Since Q_{max} is a known experimental parameter it is possible to extract intrinsic peak widths for the underlying Gaussian distributions.

The results of the convoluted fitting process are shown in Figure 4.7(a)-(c). It is clear from the Figure that the peak width decreases with decreasing temperature as

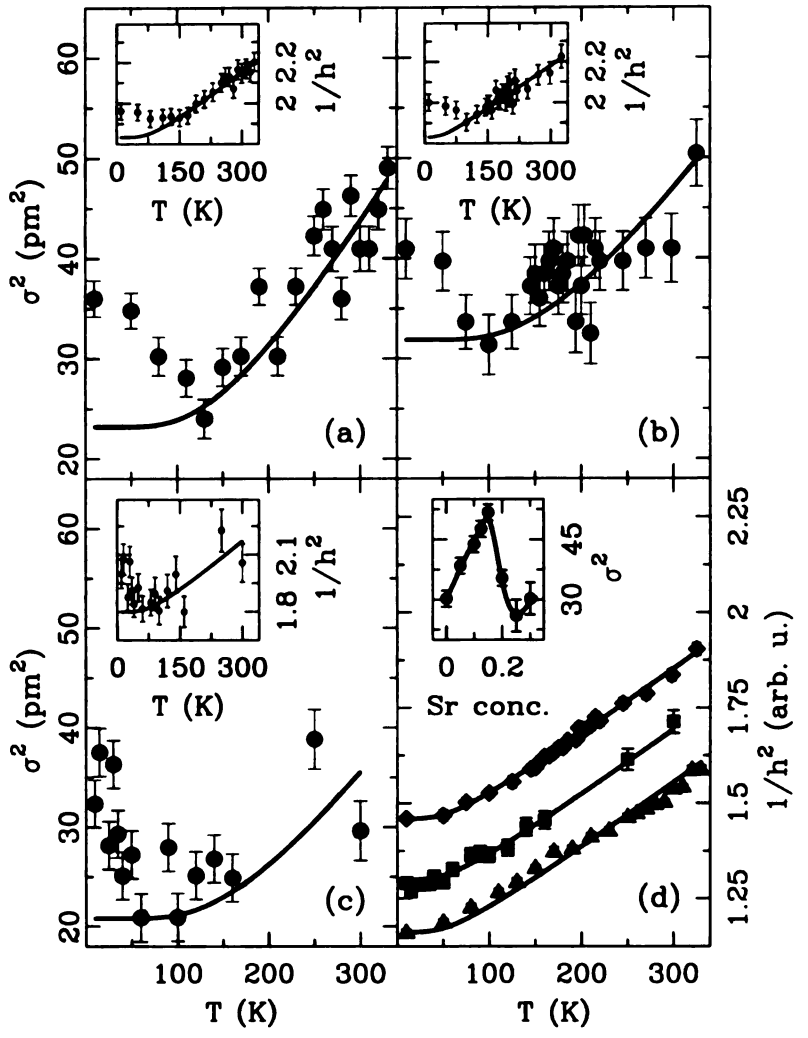

Figure 4.7: Mean-square width, σ^2, of the in-plane Cu-O PDF peak at 1.9 Å as a function of temperature for (a) $La_{1.875}Sr_{0.125}CuO_4$, (b) $La_{1.85}Ba_{0.15}CuO_4$, and (c) $La_{1.85}Sr_{0.15}CuO_4$. The solid line gives the T-dependence predicted by the Einstein model [185]. The insets show the inverse squared peak height for the same peak with an Einstein curve superimposed. (d) Temperature dependence of $1/h^2$ for the PDF peak at 7.2 Å for $La_{1.875}Sr_{0.125}CuO_4$ (triangles), $La_{1.85}Ba_{0.15}CuO_4$ (diamonds), and $La_{1.85}Sr_{0.15}CuO_4$ (squares). Inset shows the strontium-doping dependence of $\sigma^2(x)$ for $La_{2-x}Sr_xCuO_4$ at 10 K.

Table 4.1: Einstein model parameters: LBCO x=0.150 and LSCO x=0.125 data were explicitly fit over the high temperature region. Einstein-fit line for LSCO x=0.150 data has been estimated using offset parameter only and the Einstein temperature of optimally doped LBCO sample, due to the sparse datapoints in the high temperature region. Values of the parameters suggested in the literature from polarized XAFS study on LBCO is also given for comparison [179].

Sample	θ_E (K)	σ^2_{off} (Å^2)
LBCO x=0.150	535(30)	-0.0004(3)
LSCO x=0.125	475(35)	-0.0017(6)
LSCO x=0.150	535(30)	-0.0056(8)
LBCO x=0.125,0.150 ^{XAFS}	695(46)	0.0003(2)

expected. However, below a certain temperature the Cu-O bond length distribution *broadens* on further decrease of temperature. This effect cannot be explained by normal thermal behavior as indicated by the solid lines which have the expected Einstein form [185]. Also, no structural phase transitions occur at these temperatures (Chapter 3) [166, 183].

The parameters used for the Einstein model estimate, fitted to the high temperature parts of σ^2, are summarized in Table 4.1. The model has been calculated using the expression

$$\sigma^2(T) = \frac{\hbar^2}{2M_r k_B \Theta_E} coth(\frac{\Theta_E}{2T}) + \sigma^2_{off}, \tag{4.1}$$

where $\hbar$ is the Planck constant, k_B is the Boltzmann constant, M_r is reduced mass of the Cu-O atomic pair, Θ_E is the Einstein temperature parameter, T is temperature, and term σ^2_{off} denotes temperature independent static offset [185].

There is a danger that the magnitude of the observed effect obtained from the deconvolution process is amplified due to the limited real-space resolution coupled

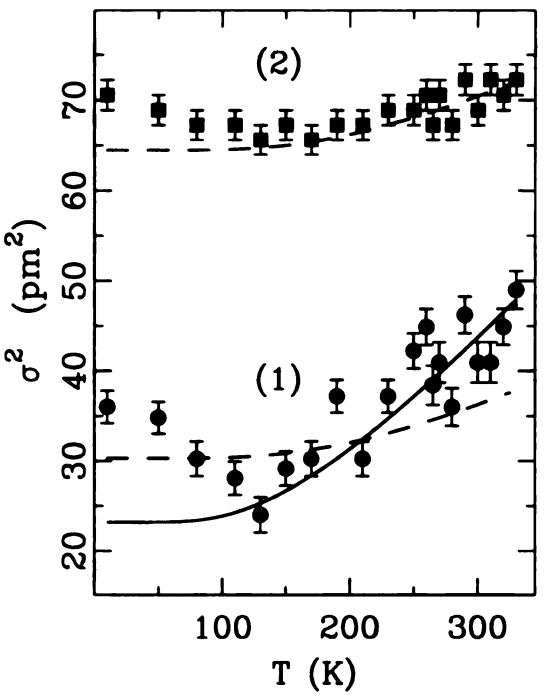

Figure 4.8: Comparison with non-convoluted fitting results: (1) Mean-square width, σ^2, of the in-plane Cu-O PDF peak at 1.9 Å as a function of temperature for $La_{1.875}Sr_{0.125}CuO_4$ from standard convoluted fit (solid circles) and (2) the same quantity obtained using fit with no convolution (solid squares). Solid line is the Einstein model prediction, as obtained from fitting of the high-T part of the data. Dashed line around (1) is the Einstein model line as obtained using parameters from polarized XAFS reported by Haskel *et. al.* [179]. Dashed line around (2) is the same as the dashed line for (1), with an additional static offset of 0.0034 Å^2.

with the deconvolution procedure that cannot easily distinguish termination ripples and noise ripples. It is therefore important to assess the robustness of the qualitative result. We therefore consider the same data analyzed in different ways without carrying out a convoluted fit. First, we simply plot the inverse-squared PDF peak height, $1/h^2$, obtained directly from the data. This is a model independent measure of σ^2 since the integrated area under the PDF peaks is conserved [144]. The inverse-squared peak heights are shown in the insets to Figure 4.7(a)-(c). We also fitted the 1.9 Å PDF peak with pure Gaussian functions that were not convoluted with Sinc functions, and the case of $La_{1.875}Sr_{0.125}CuO_4$ is shown in Figure 4.8.

Both these approaches reproduced *the qualitative* result shown in Figure 4.7(a)-(c) giving us confidence that it has a real origin and is not an artifact of the convoluted fitting procedure. All of these measures of the PDF peak width confirm the observation in the convoluted peak fits that the underlying in-plane Cu-O pair distribution is getting broader with decreasing temperature below some temperature, T_{si}.

Peaks not involving in-plane Cu-O pairs, at higher values of r, in the PDF behave canonically. This is shown in Figure 4.7(d) where $1/h^2(T)$ of the peak at $r = 7.2$ Å (indicated with an arrow in Figure 4.6) from each of the samples is plotted with an Einstein curve superimposed. As expected, no upturn is observed at low temperature.

Our study on effectively non-superconducting $La_{1.475}Nd_{0.4}Sr_{0.125}CuO_4$ sample revealed similar type of broadening at low temperature (Figure 4.9(b)), with an onset temperature in 50-60 K range. Unfortunately the sample used in this study had significant degree of impurity in it, and within the course of this study a verification-experiment with a sample of reliable quality had not been performed. Nevertheless, it is interesting to note that the effect appears to be present in the LNSCO sample as well, in which the presence of static long range ordered charge stripes is expected. Also, the onset temperature appears to be close to that observed by Tranquada *et*

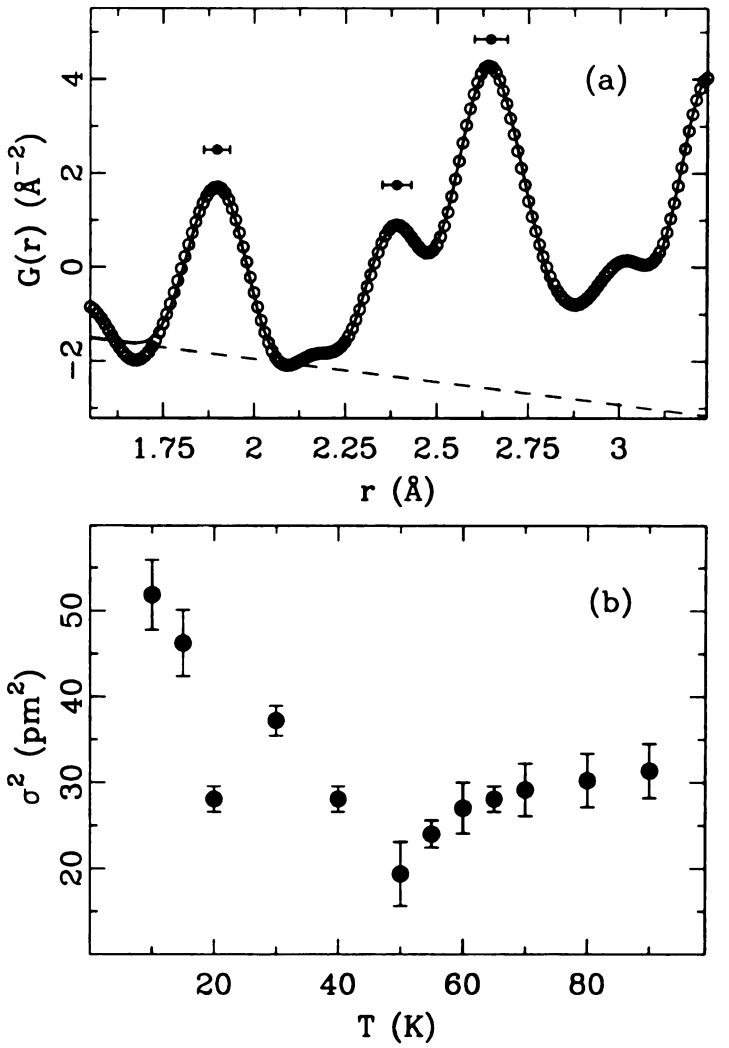

Figure 4.9: (a) Typical PWID fit of Gaussian profiles to the experimental PDF for $La_{1.475}Nd_{0.4}Sr_{0.125}CuO_4$: data (open circles), fit (solid line), and the average number-density slope (dashed line) with density of 0.0737 Å^{-3} at 10 K temperature. Solid circles denote peak positions, and horizontal bars denote peak σ values as obtained from the fit. The data is obtained using information up to $Q_{max} = 30$ Å^{-1}. (b) The square of the nearest neighbor distance distribution width, σ^2, versus temperature for the LNSCO sample.

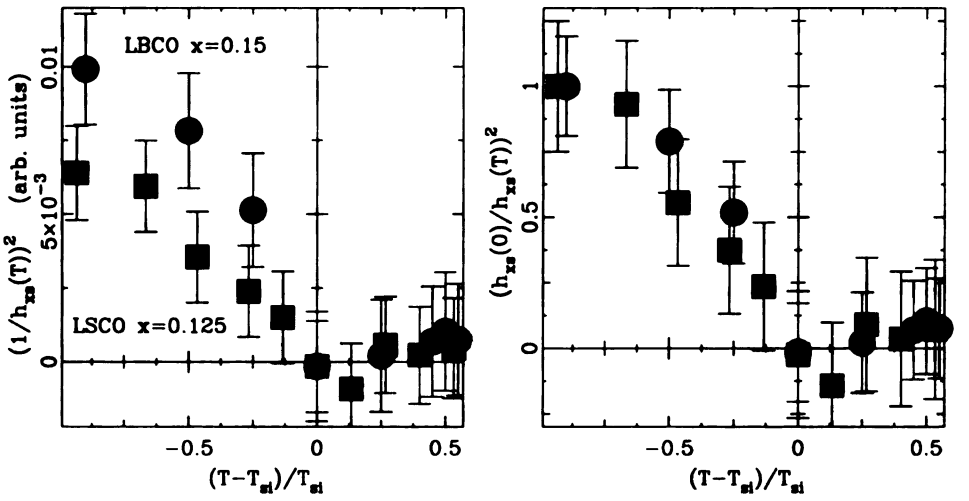

Figure 4.10: Inverse excess peak height as an order parameter: absolute values for LSCO x=0.125 (solid squares) and LBCO x=0.15 (solid circles) samples versus reduced temperature (left); relative values, obtained by rescaling the absolute values to the low-T points, versus reduced temperature (right).

al [26]. We note that an independent signature of charge stripes in this sample, in form of charge-order superlattice peaks, has *not* been seen. It is known that the charge order superlattice peaks have rather weak intensity, and are hidden by the background signal in a *powder* diffraction measurement, such as one we performed.

4.3.4 Discussion

The broadening of the r = 1.91 Å PDF peak at low temperature can be explained if charge inhomogeneities, such as charge stripes, are manifesting themselves in the structure at low temperature. This will occur both if the electronic correlations are appearing at low temperature or if preexisting correlations are slowing down and beginning to interact with the lattice. It was shown in an earlier PDF study [183] that a gradual broadening with increasing doping at 10 K of the r = 1.91 Å PDF peak in $La_{2-x}Sr_xCuO_4$ could be well explained as a microscopic coexistence of heavily

doped and undoped regions of the copper-oxygen plane. The x-dependence of this PDF peak width measured at 10 K is reproduced in the inset to Figure 4.7(d). This can be compared with the intrinsic peak widths at low temperature from this study.

The original x-dependent data were interpreted as follows. The relatively sharp peaks in the $x = 0$, 0.25, and 0.30 data were assumed to have a single valued bond length broadened by thermal and zero point motion resulting in a mean-square width of ~ 30 pm^2. The relatively broader peaks observed in the underdoped compounds ($x = 0.05$, 0.10, 0.125, 0.15) could be explained as a superposition of sharp peaks that are shifted in position originating, respectively, from less doped and more heavily doped regions of the copper oxide plane [183]. This simple model-independent analysis is likely to be an oversimplification of the real situation where local strains lead to broader distributions of the PDF peaks; however, it suggests that the observed effects in the PDF are consistent with structural distortions originating from charge inhomogeneities. Despite the current measurements being made on different materials at different times using different diffractometers it is clear that both the low-temperature thermal width of 25-31 pm^2 extrapolated from the Einstein model, as well as the excess peak height of $\sim 10 - 15$ pm^2, are in reasonably good agreement with our earlier observation of the x-dependence of $La_{2-x}Sr_xCuO_4$ [183]. This suggests that the underlying origin of the peak broadening is the same.

The in-plane Cu-O pair correlation has been studied in a number of XAFS measurements [179, 186, 187]. The data of Lanzara *et al.* [186] qualitatively suggest an upturn in the width of the distribution at low temperature, although later work suggests that uncertainties in unpolarized XAFS measurements are larger than the observed effects [187] and that polarized XAFS measurements are necessary to obtain higher precision [179]. In particular, this latter study puts an upper limit of 0.017 Å on possible non-thermal disorder amplitude present in the in-plane Cu-O bond distribution of $La_{1.875}Ba_{0.125}CuO_4$. This is similar to our suggestion of a ~ 0.02 Å splitting

observed in $La_{2-x}Sr_xCuO_4$ [183] and in the current work. This is larger than the ordered component of the distortion observed by neutron diffraction of ~ 0.004 Å [114]. It is possible that the entire sample is not long-range ordered in that case, leading to an underestimation of the distortion amplitude. Also, the PDF results are only semi-quantitative due to the moderate resolution of the measurement and the possible overestimate of the distortion from the fitting as we have discussed.

We have estimated a temperature, T_{si}, where the structural inhomogeneities set in by using the temperature where the observed width deviates from the Einstein curves plotted in Figure 4.7. The inverse excess PDF peak height (or excess PDF peak width) can then be regarded as an order parameter. The excess peak height is defined as $h_{measured}$-$h_{Einstein}$. For illustration, its inverse is plotted versus reduced temperature, $(T-T_{si})/T_{si}$, for $La_{1.85}Ba_{0.15}CuO_4$ and $La_{1.875}Sr_{0.125}CuO_4$ samples in Figure 4.10. In the left hand side panel absolute inverse excess peakheights are shown. The curve for x=0.125 LSCO sample is lower than the corresponding curve for the x=0.15 LBCO sample because of the fewer doped carriers in the former case. The excess heights in the right hand side panel of Figure 4.10 are scaled to the low-T points. The resulting values for T_{si} are 125 K for $La_{1.875}Sr_{0.125}CuO_4$ and 60 K and 100 K for $La_{1.85}Sr_{0.15}CuO_4$ and $La_{1.85}Ba_{0.15}CuO_4$, respectively. These are shown in Figure 4.11 as solid hexagons. The estimated error bars are rather large since the exact value of T_{si} depends on parameters used in the Einstein fits; also our data-sets are somewhat sparse. However, they give a temperature scale where the effects of charge inhomogeneities first appear in the local structure.

In Figure 4.11 we show a phase diagram for $La_{2-x}Sr_xCuO_4$ with T_{si} plotted along with T_c and T^* obtained from the literature [59]. Superimposed on this diagram are T_{sf}, the onset temperature for NQR signal "wipe-out" [134], T_u, the temperature where the deviation of the normalized resistivity, $\rho/\alpha T$, reaches a critical value [121], and T_x, the temperature where an anomaly is seen in XANES data [135]. All of these

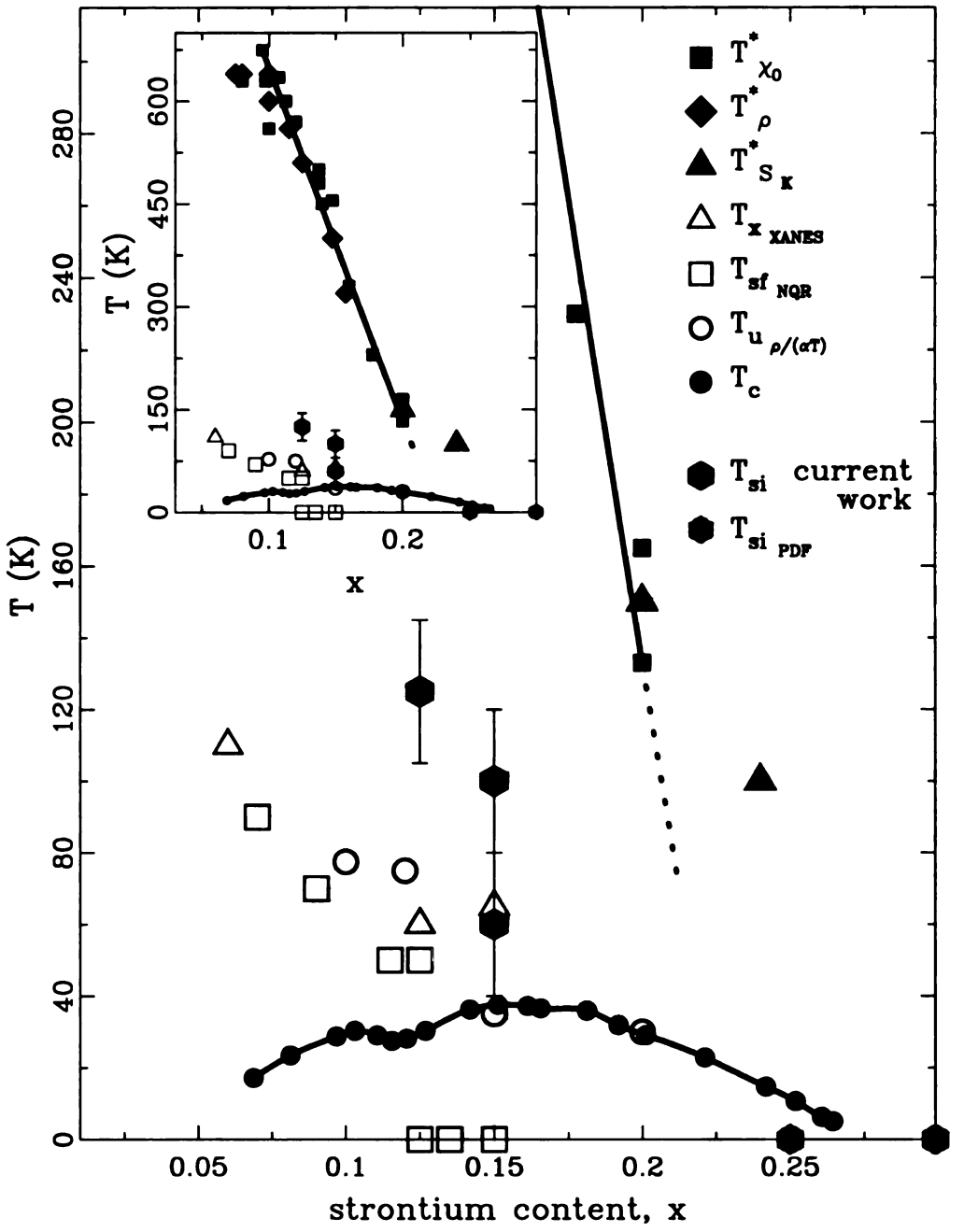

Figure 4.11: Phase diagram of $La_{2-x}Sr_xCuO_4$ showing the temperatures of pseudogap opening, T^* [59], XANES anomaly, T_x [135], NQR spin freezing, T_{sf} [134], transport upturn, T_u [121], and the T_{si}'s determined from the present measurements (black hexagons). T_{si} is known to be below 10 K for $La_{2-x}Sr_xCuO_4$ with $x > 0.2$ [183] as indicated (gray hexagons). T_c is shown as solid circles joined by a line. The inset is the same phase diagram on an expanded temperature scale.

characteristic temperatures have been associated with charge or spin freezing. It is clear that the T_{si}'s obtained from the present data correlate quite well with the other measures of spin and charge freezing.

4.3.5 Summary

Our results indicate that the charge inhomogeneities strongly couple to the lattice in $La_{2-x}(Sr,Ba)_xCuO_4$ compounds and become pinned by the lattice at low temperature. In the absence of Nd the pinning is not complete and the charges do not order over long range, even at x=0.125 in the Sr doped compound. Nonetheless, their strong coupling to the lattice will make them quite immobile. Our measurements yield the instantaneous structure and we cannot distinguish whether the inhomogeneities are static or fluctuating on phonon time scales or slower. It is possible that electronically driven stripes are important for superconductivity but a strong coupling to the lattice is destructive. However, phonon anomalies have been associated with charge stripe formation in $YBa_2Cu_3O_{6+\delta}$ [127, 136] and theories exist in which the charge stripes are stabilized by the lattice.

4.4 Summary

The PDF study indicates presence of local structural inhomogeneities in the CuO_2 planes in optimally doped and underdoped LSCO and LBCO samples at low temperature. The inhomogeneities are manifested as a distribution of the in-plane Cu-O distances. This effect abruptly disappears on crossing into the overdoped regime (LSCO), as well as at elevated temperature (LSCO, LBCO). The effect has an onset temperature which correlates well with the charge and spin freezing observed by other probes. The effect is best explained as a coexistence of undoped and heavily doped regions in the CuO_2 planes.

Chapter 5

Evidence Supporting Presence of Charge Inhomogeneities

"Our bodies are given life from the midst of nothingness. Existing where there is nothing is the meaning of the phrase 'Form is emptiness'. That all things are provided for by nothingness is the meaning of the phrase 'Emptiness is form'. One should not think that these are two separate things." (T. Yamamoto)

5.1 Prelude

The presence of microscopic charge inhomogeneities in the CuO_2 planes of underdoped and optimally doped LSCO and LBCO has been established in Chapter 4 through the nearest neighbor PDF peak analysis. Here we present further PDF evidence supporting an inhomogeneous local charge distribution in LSCO samples, compatible with a striped morphology. The local structure of $La_{2-x}Sr_xCuO_4$, for $0 \leq x \leq 0.30$ and at 10 K temperature, has been investigated using the atomic PDF analysis of neutron powder diffraction data. The local octahedral tilts are studied to look for evidence of [110] symmetry (i.e. LTT-symmetry) tilts locally, even though the average tilts have [010] symmetry (i.e. LTO-symmetry) in these compounds. We argue that

this observation is supportive of the presence of local charge inhomogeneities, and is consistent with local charge-stripe order. We show that the tilts are locally LTO in the undoped phase, in agreement with the average crystal structure. At non-zero doping the PDF data are consistent with the presence of local tilt disorder in the form of a mixture of LTO and LTT local tilt directions and a distribution of local tilt magnitudes. This represents strong additional PDF evidence for the inhomogeneous charge distribution in CuO_2 planes established in Chapter 4. We present topological tilt models which qualitatively explain the origin of tilt disorder in the presence of charge stripes and show that the PDF data are well explained by such a mixture of locally small and large amplitude tilts. Simplistic structural agreement analysis is performed to evaluate the spatial extent of such mixed local structure. From this a domain size is estimated which is compatible with the separation of the static charge stripes observed earlier in non-superconducting samples.

5.2 Approach

While PDF cannot unambiguously discriminate between the striped charge order and any other inhomogeneous charge distribution in CuO_2 planes, we investigate the local structure and look for indirect evidence and compatibility, at least in principle, of the obtained local structural information with the striped morphology of the charge distribution. An amenable system for this kind of study, as mentioned in Chapter 1, is the series of compounds based around $La_{2-x}(Sr,Ba)_xCuO_4$ (214 compounds) because in these compounds collective tilts of the CuO_6 octahedra exist which couple strongly to the electronic system [47, 54, 166, 188, 189] and the charge-stripes [26, 31]. In particular, it has been observed that long-range ordered charge-stripes are only seen in the cuprate system when the octahedra tilt collectively about axes along the Cu-O bonds, i.e., in the [110] crystallographic directions in the standard crystallographic setting

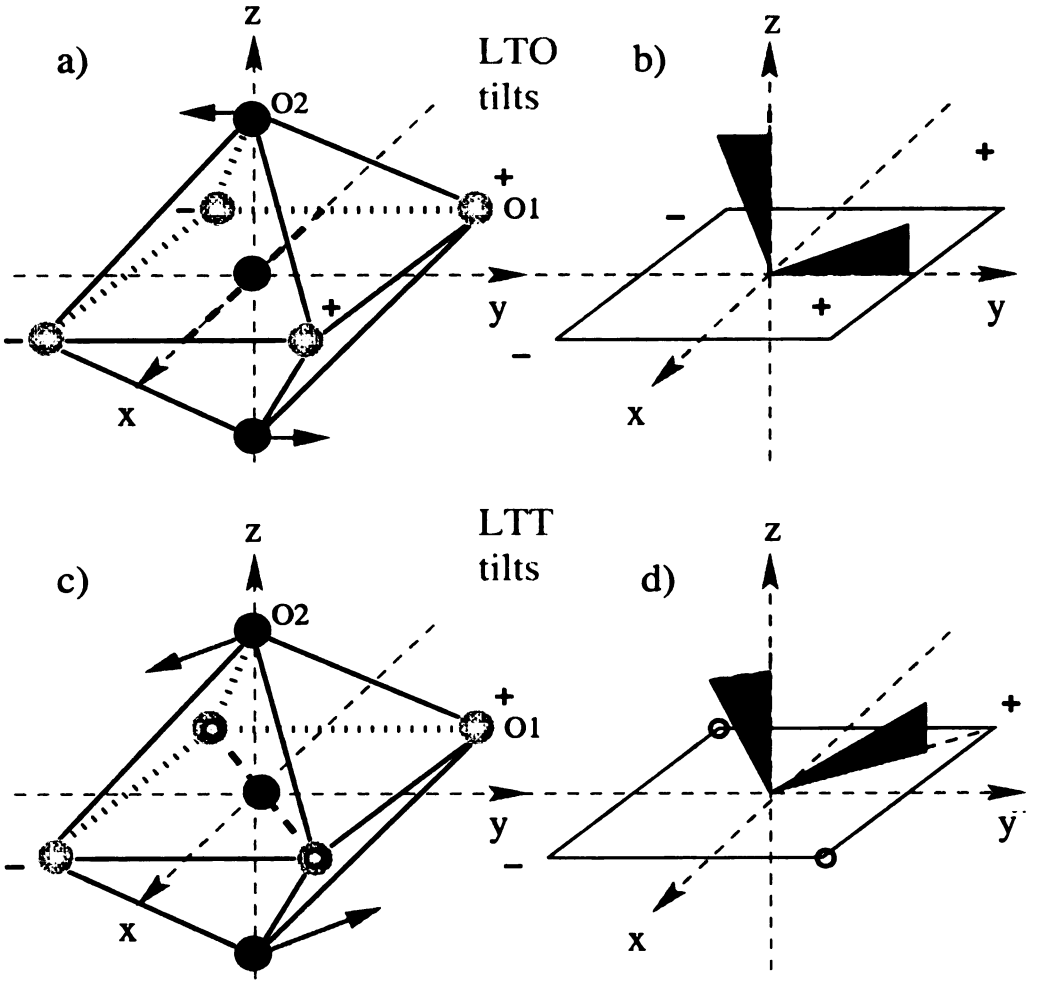

Figure 5.1: Schematics of the LTO and LTT octahedral tilt directions.

($P4_2/ncm$ for the LTT phase) [26, 31, 115]. This tilt pattern is the one observed in the low temperature tetragonal (LTT) phase [190]. Most of the superconducting compositions are in the alternative low temperature orthorhombic (LTO) phase [48] which has the octahedra tilting *on average* about axes parallel to the [100] crystallographic direction. It is thought that since the charge-stripes lie in [110] directions in the lattice (i.e. along Cu-O bonds), the [100] type LTO tilts prevent the stripes from ordering statically over long range. Because the charge-stripes are strongly coupled to the octahedral tilts [26, 31], we can use the octahedral tilts as a probe of the local stripe order. Schematics of the two different tilt directions are shown in Figure 5.1.

It was shown earlier [191] that in $La_{1.875}Ba_{0.125}CuO_4$ local regions of LTT-type octahedral tilt order persist in the LTO phase above the LTO-LTT phase transition. It was suggested that the LTO phase is made up of short-range ordered LTT-domains but that a linear combination of different LTT variants resulted in the average LTO tilt order observed in the crystallographic structure. There also are other observations that the local tilts in 214 materials are not always the same as those measured crystallographically [192, 193, 194, 195]. At the time of the earlier study [191], charge stripes had not been observed in the cuprates and there was no obvious explanation as to why the LTO phase should be made up of inhomogeneous domains of short-range LTT-order. However, the presence of dynamic or short range ordered charge-stripe domains provides a very natural explanation of this unexpected result.

In the present work we have studied the local octahedral tilts in $La_{2-x}Sr_xCuO_4$ to look for evidence of local LTT symmetry tilts. We chose to study the Sr doped, rather than the Ba doped, systems since ionic size effect disorder is less in this system. This is due to the fact that Sr^{2+} is closer in size to La^{3+} than is Ba^{2+}. This means that the disorder introduced into the structure due to ionic size effects is minimal and disorder in the local tilts will originate mainly from an inhomogeneous electronic charge distribution.

In this Chapter we show that the local octahedral tilt amplitude can be measured accurately using PDF techniques. If the tilt amplitude is large enough it is also possible to distinguish the tilt direction. We show that the local tilts are clearly LTO in nature in the undoped compound, as expected. However, away from zero doping ($x > 0$) the PDF is consistent with the presence of tilt disorder in the form of a mixture of tilt directions and a mixture of tilt amplitudes. As x increases at low temperature the local tilt amplitude decreases smoothly following the behavior of the average tilts. However, small but finite tilts persist locally when the sample goes into the high temperature tetragonal (HTT) phase above $x = 0.20$. In the discussion,

Section 5.5, we present topological tilt models which qualitatively explain the origin of tilt disorder in the presence of charge stripes and show that the PDF data are well explained by a mixture of locally small and large amplitude tilts.

5.3 Experimental highlights

Powder samples were prepared by conventional solid state reactions, as described in Chapter 3. Time-of-flight neutron diffraction measurements were carried out on LSCO powder samples (approximately 10 g of each) for the range of doping $0 \leq x \leq 0.30$ at 10 K temperature. This is the same set of experiments as one described in the first part of Chapter 4 where doping dependence of the charge distributions is investigated. Experiments were performed on the SEPD at the IPNS at Argonne National Laboratory.

The data were corrected for experimental effects and normalized (see Chapter 2 for details) to obtain the total scattering function, $S(Q)$, and further the PDF function, $G(r)$. The PDFs are then used to investigate features of the *local* structure of LSCO series at 10 K.

Local structural information discussed in this chapter is obtained from the data by a process of modeling. A model structure is proposed and the PDF calculated. Parameters in the model are then varied to optimize the agreement between the calculated and measured PDFs. From the refinements, different structural information can be extracted, such as lattice parameters, average atomic positions and amplitudes of their thermal motion, atomic displacements, and magnitudes of local octahedral tilts. The modeling procedure has been described in more detail in Chapter 2 and elsewhere in the literature [144, 161].

5.4 Results

5.4.1 Local tilt amplitudes as a function of doping

Initially we investigate the appearance in the PDF of the octahedral tilts and show the extent to which the PDF technique can detect their presence. In Figure 5.2(a), we compare three *model* PDFs to show qualitatively the effect of a change in the local octahedral tilt amplitude on $G(r)$. The PDFs are shown for the LTO structure with three different magnitudes of octahedral tilt: 0° (dash-dotted line), 3° (dashed line), and 5° (solid line). The initial parameters used in the models were obtained by converging the fit of the LTO model-PDF to the data-PDF from the $x = 0.125$ data-set at 10 K, using the RESPAR Real-Space Rietveld program [144]. The octahedral tilt angles were then calculated independently from the positions of the in-plane oxygen (O1) and the out-of-plane oxygen (O2). These tilt angles are denoted by $|\theta_{O1}|$ and $|\theta_{O2}|$ respectively. The tilt angle $|\theta_{O1}|$ was obtained from the z-displacement of O1 using

$$|\theta_{O1}| = \left|\arctan\left(\frac{c\,\delta O1_z}{b\,\delta O1_y}\right)\right|, \tag{5.1}$$

where $\delta O1_z$ and $\delta O1_y$ are the z and y fractional coordinates respectively of O1, and c and b are the corresponding lattice parameters. Similarly, the average tilt is obtained from displacements of O2 using

$$|\theta_{O2}| = \left|\arctan\left(\frac{b\,\delta O2_y}{c\,\delta O2_z}\right)\right|. \tag{5.2}$$

In the case where the octahedral tilts are rigid, $|\theta_{O1}| = |\theta_{O2}|$. The tilt angles were then artificially adjusted to 5°, 3°, and 0° in the model and the atomic positions for O1 and O2 determined from Equations 5.1 and 5.2. All other parameters in the model were held constant. In this way we could compare the effect of a change in tilt magnitude on the PDF neglecting other changes such as changes in bond-length or lattice parameter. As expected, the Cu-O nearest neighbor peak at 1.89 Å is

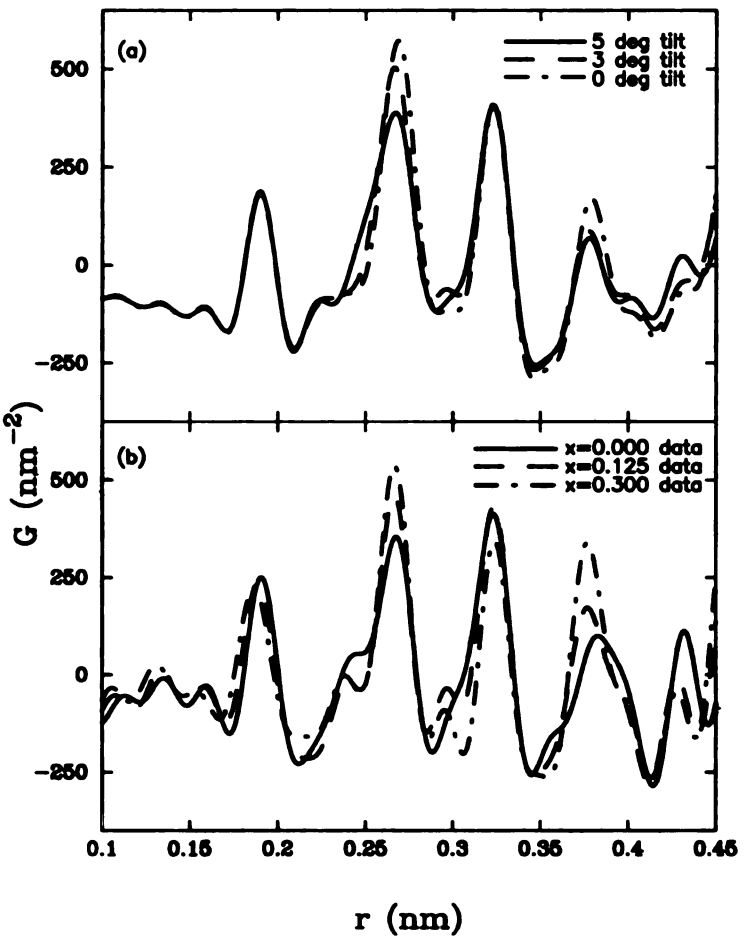

Figure 5.2: (a) Comparison between three *model* PDFs. The models have LTO symmetry with 5° tilts (solid line), 3° tilts (dashed line), and 0° tilts (dash-dotted line). **(b)** Three different 10 K *data* PDFs that approximately correspond to the same tilt magnitudes as shown in the models in panel (a): $x = 0$ (solid line, $\approx 5°$ tilt), $x = 0.125$ (dashed line, $\approx 3°$ tilt), and $x = 0.30$ (dash-dotted line, $\approx 1°$ tilt). The PDF technique clearly differentiates between the presence and absence of the tilts and these qualitative differences are evident in the data.

unaffected (the tilts are essentially rigid) but the peak at 2.7 Å, which contains the La-O1 and La-O2 correlations (as well as the O1-O1 correlations), shows a particularly large change.

The lower panel, Figure 5.2(b), presents PDFs obtained from the experimental data: $x = 0$ doping (solid line), where tilts of approximately 5° are present, $x = 0.125$ doping (dashed line) with tilts of approximately 3°, and $x = 0.30$ doping (dash-dotted line), with average tilts of zero. The changes in the data with doping are large and qualitatively similar to those expected for reductions in local tilt amplitude. In addition, a shortening of the average Cu-O bond is evident by a shift to the left of the nearest neighbor Cu-O peak, as expected from the average structure. This also gives an indication of the sensitivity of $G(r)$ to small structural changes such as this lattice contraction.

We have determined quantitatively the amplitudes of the local octahedral tilts as a function of doping using the LTO model and the Real-Space Rietveld modeling program. Characteristic fits are shown in Figure 5.3 for the undoped material (average tilts are large) and the overdoped material (average tilts are zero). Difference curves are plotted below the PDFs. The agreement of the HTT model to the $x = 0.3$ data is significantly poorer than the fit of the LTO model to the undoped material. As we discuss later, this is because small but finite local tilts are still present in the structure even in the HTT phase.

The local tilt angles obtained from the fits are shown in Figure 5.4 plotted as a function of doping, shown as filled circles. For comparison, average tilt angles obtained from a crystallographic analysis [44] are also plotted (shown as open circles). There is excellent agreement for lower dopings. The agreement is less good for compositions above $x = 0.15$. In this region the long-range average tilt angle is constrained to be zero because of the change in the average symmetry accompanying the phase change from LTO to HTT. However, in the PDF a better fit to the data is obtained when

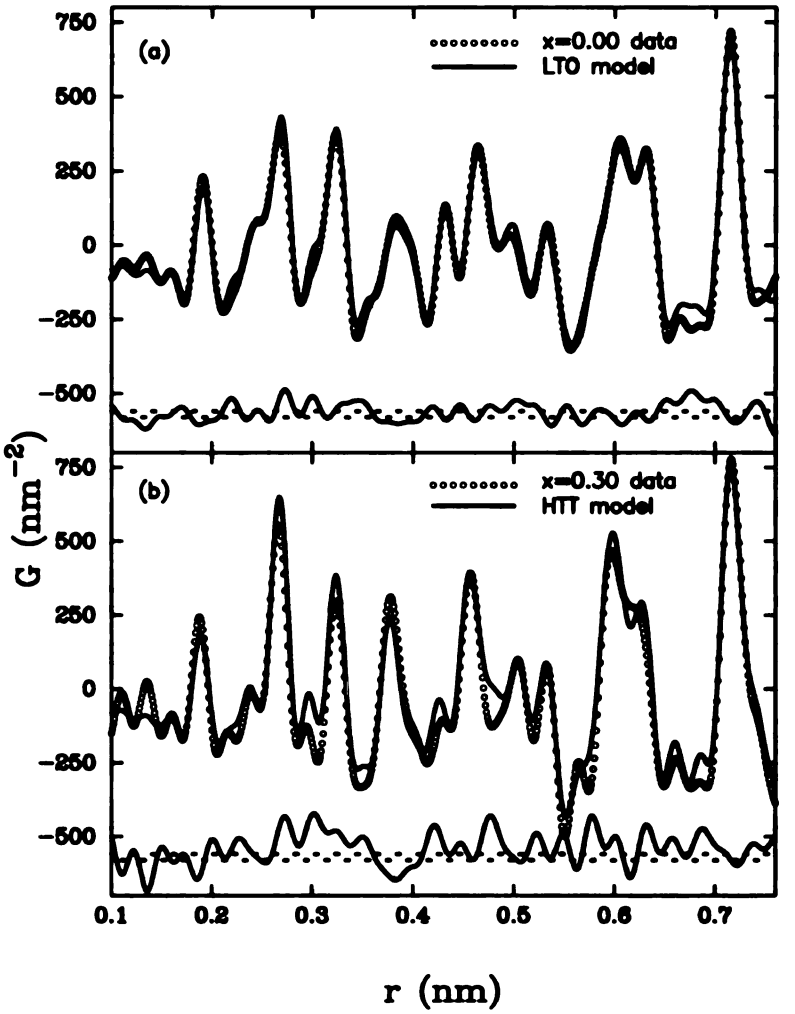

Figure 5.3: (a) Fully converged PDF for the LTO model (solid line), and experimentally obtained PDF for LSCO with x=0 at 10 K (open circles). The difference curve is plotted below as a solid line. The dotted line shows the expected errors at the level of two standard deviations. (b) Fully converged PDF for the HTT model (solid line), and LSCO with x=0.30 at 10 K (open circles).

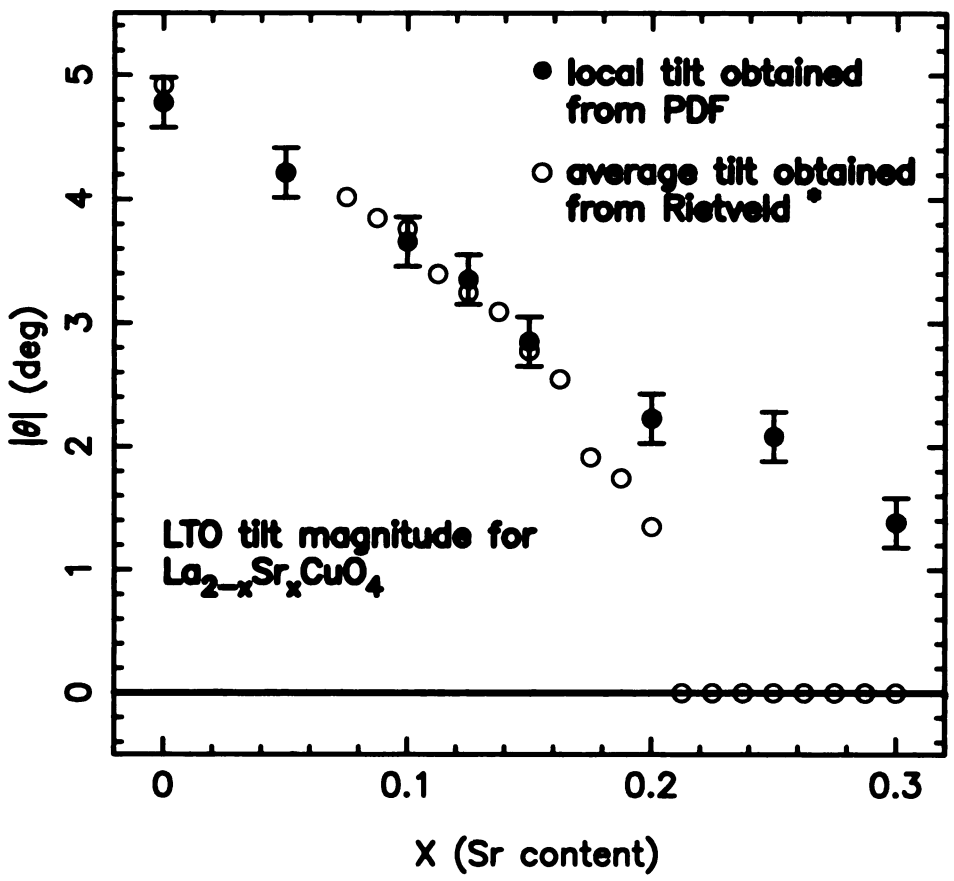

Figure 5.4: Dependence of the local octahedral tilt angle magnitude (black circles), $|\theta|$, on Sr content, x. Open circles present average tilt angle magnitude obtained from Rietveld refinement done by Radaelli and collaborators (see text). The result shows that $|\theta|$ smoothly decreases when x is increased. However, significant local tilts persist even when the average tilts disappear. The data were collected at 10 K.

the LTO model is used, rather than the HTT model, and a small but finite ($\approx 1-2°$) local tilt is refined [196]. The use of the LTO model to describe the local structure, even when the global structure is clearly HTT, is justified since the broken symmetry phase may persist locally. However, this analysis does not imply that, in our samples, the global structure is LTO in this region of doping.

5.4.2 Local tilt directions as a function of doping

We would like to use the PDF technique to differentiate between local tilts with the [010] (LTO: tilt axis 45° rotated with respect to planar Cu-O bond) and [110] (LTT: tilt axis is parallel to the Cu-O bond) tilt symmetries (Figure 5.1) since evidence for local LTT-like tilts might suggest the presence of charge stripes.

In Figure 5.5 we show a comparison of two model PDFs, one where the tilts belong to the LTO type, and the other that is of LTT type. In Figure 5.5(a) we show the difference for the case of a 5° tilt magnitude and in Figure 5.5(b) for a smaller 3° tilt. It is important to emphasize that the only difference between our models is in the tilt symmetry (or directions of the tilts), keeping all other parameters constant, including tilt amplitude. Therefore, the difference in the PDFs that is shown is *only* due to the change in the tilt symmetry.

As is usual with the PDF, some regions of the function are much more strongly affected by the change than others. A change in tilt direction affects the peaks around 2.67 Å and 2.95 Å, that correspond to (La/Sr)-O1 and (La/Sr)-O2 bonds respectively. There is also a large effect on the peak located close to 6.0 Å. Elsewhere in the PDF the changes are small. Notice that the peaks at $\approx$ 2.8 Å give a characteristic "W-shaped" feature in the difference curve, while the peak at $\approx$ 6 Å gives a characteristic "M-shaped" feature. The changes are similar, but much smaller, as the local tilt amplitude diminishes.

In Figure 5.6 we present fully converged fits of the LTO and LTT models to the

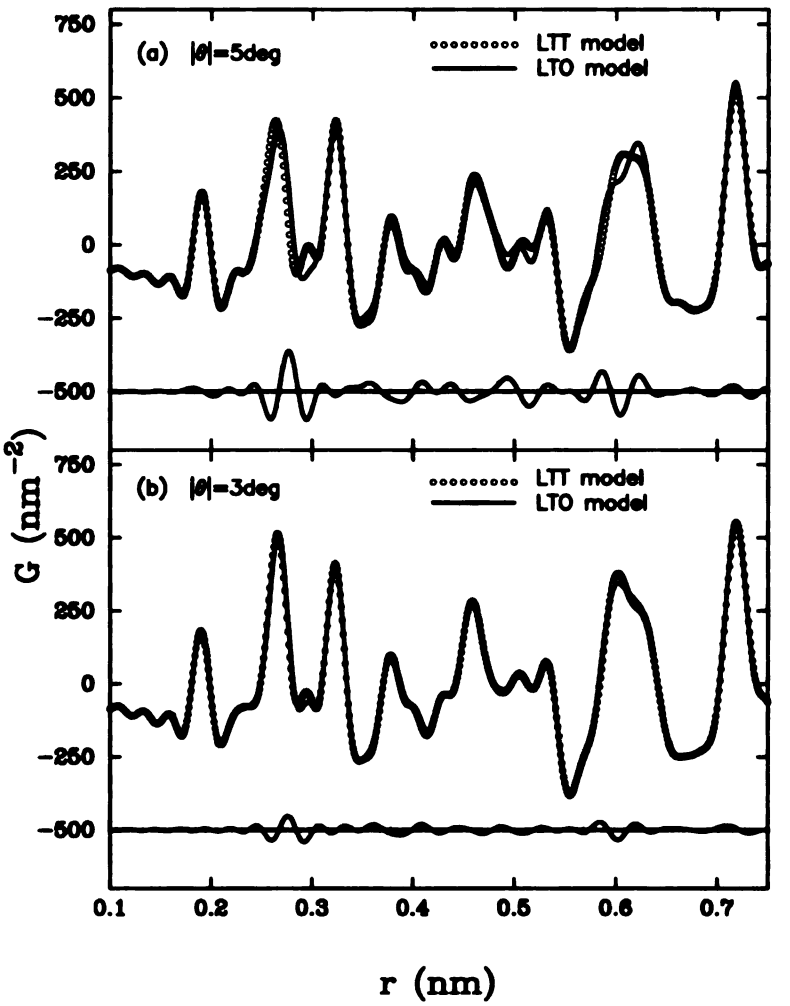

Figure 5.5: Difference in model PDFs for the LTT and LTO tilt symmetry: (a) 5° case, and (b) 3° case. The PDF for the LTT model is given as a solid line, while that for the LTO model is presented with open circles. Difference curve is given below PDFs for both cases.

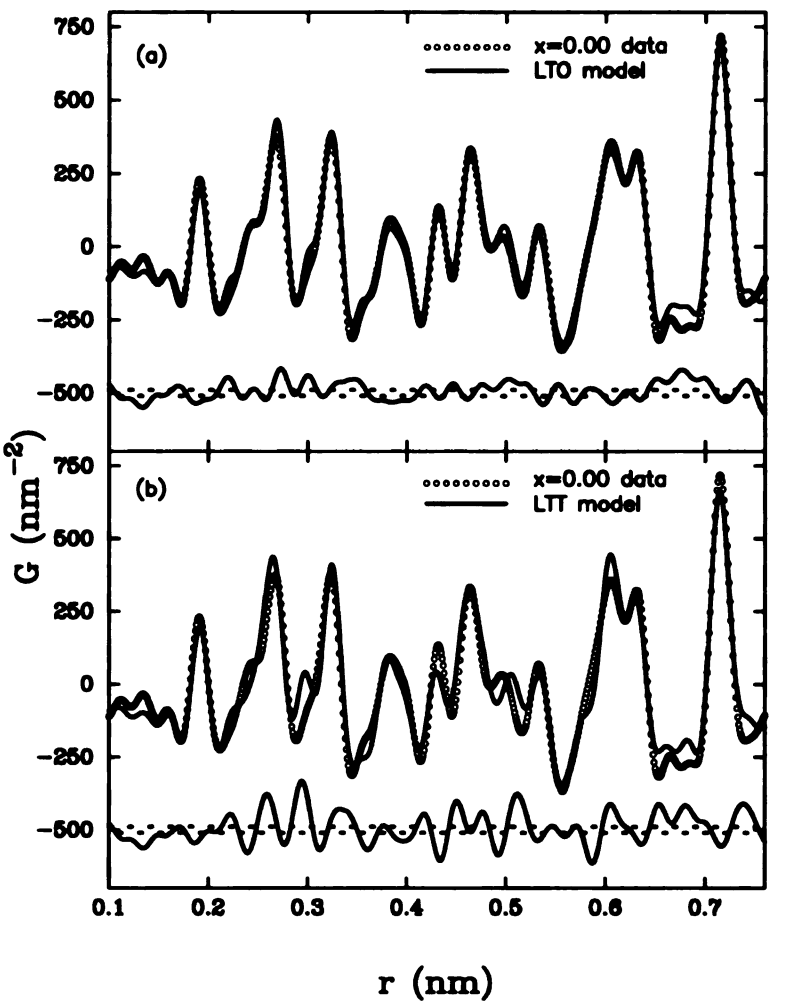

Figure 5.6: (a) Fully converged model PDF with the LTO tilt symmetry (solid line) compared to experimental PDF for x=0 at 10 K (open circles). Difference curve is shown below the PDFs as a solid line. The dotted line shows the expected errors at the level of two standard deviations. (b) The same for the case of LTT tilt symmetry.

undoped material. It is clear that the undoped material has *local* octahedral tilts that have the LTO symmetry: the fit is much better everywhere with the LTO model, and particularly large fluctuations are observed around $r = 2.8$ Å in the LTT model. This agrees also with average structure that has LTO-symmetry tilts.

We are interested if evidence for local LTT-like tilts appears as the CuO_2 planes are doped. In the set of Figures 5.7–5.9 we show the PDFs for the doped samples: again, upper panels show the PDF for fully converged LTO models (solid line) and experimental PDFs (open circles) with corresponding difference curves; lower panels compare PDFs for fully converged LTT models (solid line) with the PDFs obtained from the data (open circles), and give corresponding difference curves.

In Figure 5.7, for $x = 0.05$ we again see that the LTO fit is better than the LTT one overall, and the characteristic M-feature is evident in panel (b). The underlying local tilts are still predominantly LTO-like.

For $x = 0.10$ the situation is less clear. The tilt amplitude is now down to $3.6°$ making differentiation between LTO and LTT harder. Both models fit quite well. However, we note that in the critical region around $r = 2.8$ Å the LTT model actually has a *better* agreement with the data than the LTO model and in this case the difference curve from the LTO model has an M-shaped fluctuation centered at $r = 2.8$ Å consistent with some local LTT-like tilts.

As doping is raised beyond it becomes difficult to differentiate between the LTO and LTT models. Both models fit quite well as evidenced, for example, by the $x = 0.20$ data set shown in Figure 5.9.

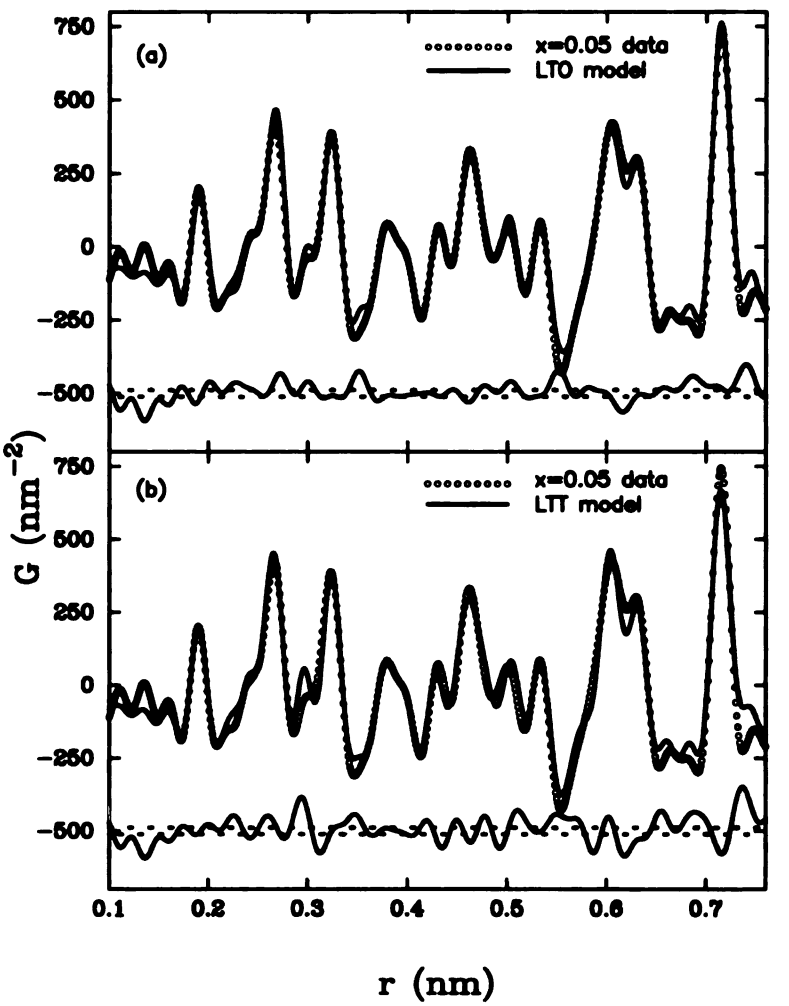

Figure 5.7: (a) Fully converged model PDF with the LTO tilt symmetry (solid line) compared to experimental PDF for x=0.05 at 10 K (open circles). The difference curve is shown below the PDFs as a solid line. The dotted line shows the expected errors at the level of two standard deviations. (b) The same for the case of LTT tilt symmetry.

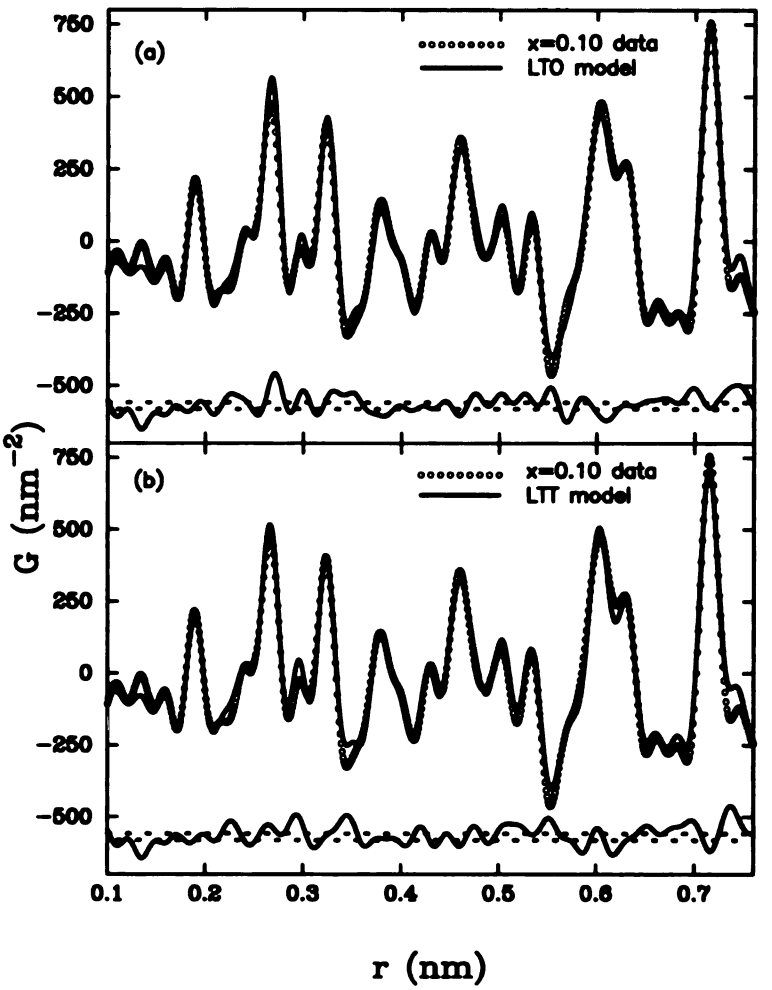

Figure 5.8: (a) Fully converged model PDF with the LTO tilt symmetry (solid line) **compared** to experimental PDF for x=0.10 at 10 K (open circles). The difference **curve** is shown below the PDFs as a solid line. The dotted line shows the expected **errors** at the level of two standard deviations. (b) The same for the case of LTT tilt **symmetry**.

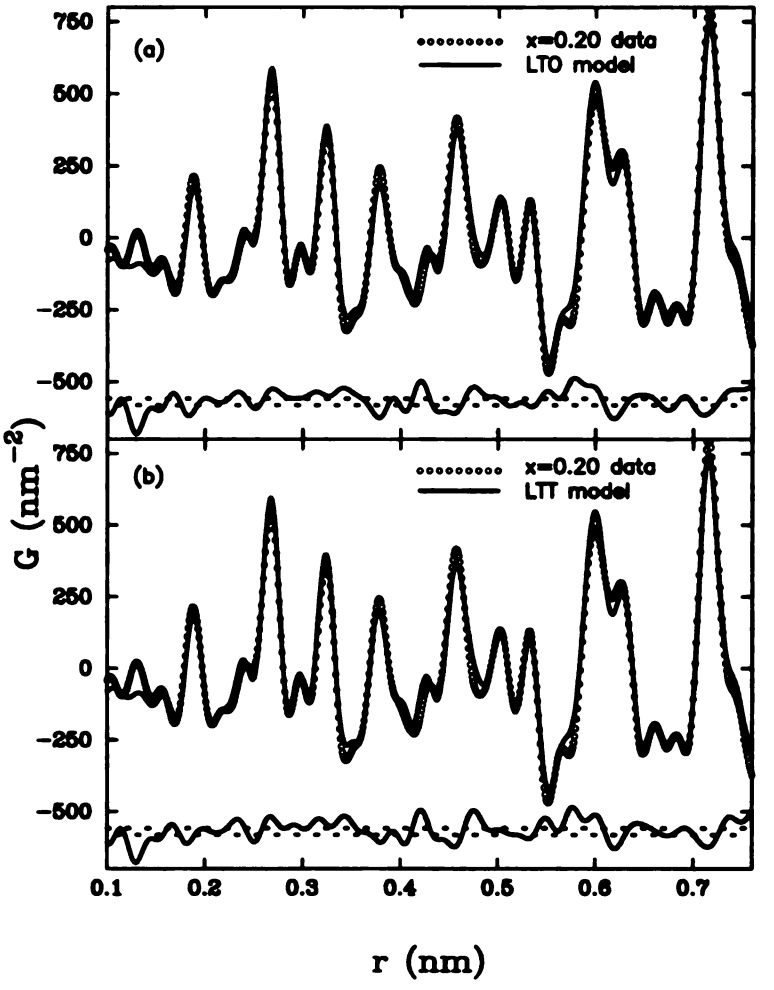

Figure 5.9: (a) Fully converged model PDF with the LTO tilt symmetry (solid line) compared to experimental PDF for x=0.20 at 10 K (open circles). The difference curve is shown below the PDFs as a solid line. The dotted line shows the expected errors at the level of two standard deviations. (b) The same for the case of LTT tilt symmetry.

5.5 Discussion

5.5.1 Tilt magnitude vs. doping

The evolution of the *local* tilt magnitude, determined by fitting the LTO model to the PDFs from the data, decreases smoothly with increasing doping. This is consistent with crystallographic studies which show a smoothly decreasing *average* tilt amplitude with doping [44, 197]. Furthermore, it is clear from Figure 5.4 that the average *local* tilt amplitude is quantitatively the same as the long-range ordered average tilt. Although this may not seem surprising, it is widely observed in these materials that the average *local* tilt amplitude can deviate significantly from the long-range ordered value. This occurs when finite local tilts exist but the tilt directions become disordered and the long-range tilt order is not preserved. This is very similar to a ferromagnetic-paramagnetic transition where the local moment survives but the long-range ordered moments average to zero. This behavior is seen in the temperature dependence of the tilts in these systems [193, 194, 195]. The present result shows that the real, local, tilt is decreasing as x increases: in these materials the tilts are not just becoming disordered at low temperature by the action of doping but are smoothly decreasing.

This is easy to understand by the argument that the copper-oxygen bond is shortening as holes are doped and this anti-bonding band is stabilized. The plane buckling occurs because the CuO_2 planes are constrained to fit continuously with the rare-earth oxide charge reservoir layers [113]. The buckling allows them to maintain a continuous structure with the charge reservoir layers while relieving stress introduced because the Cu-O bonds are just too long to fit perfectly. As the Cu-O bonds are shortened by doping the amplitude of tilt needed to relieve this stress is reduced and the tilts smoothly decrease.

In the high-doped region there is not perfect agreement between the local and long-range ordered tilt amplitudes. The crystallographic result is constrained to be

zero above $x = 0.2$ where the global structure goes to the HTT phase. There is a remnant amount of tilting of around 1-2° which persists even into the HTT phase. This is not completely unexpected because of the presence of Sr impurities in the structure which would be expected to modify the octahedral tilting in their immediate vicinity [107, 195]. It does not necessarily imply any significance with respect to the charge doping in the planes themselves.

5.5.2 Tilt direction vs. doping

If charge is doped into the material, it can be either distributed uniformly or it can be localized and over some doping range it can form charge stripes. Localized charge would cause local polaronic distortions, forcing the octahedra to change their shape, and affecting the magnitude of the tilts in the vicinity of the polaron. In addition, the presence of charge stripes should affect the direction of the octahedral tilting since it has been observed that long-range ordered charge stripes in the 214 materials have only been seen in samples in the LTT phase. Thus, the observation of *local* LTT-like tilts would be evidence for the presence of *local* charge-stripe order.

Local LTT-like tilts have been seen in the LTO phase of $La_{1.875}Ba_{0.125}CuO_4$ [191]. In this case tilt amplitude is larger than it is in the Sr doped case reported here (3.8° for Ba [180], x=0.15, vs 2.9° for Sr, x=0.15, both at 10 K) which explains why it was more clearly evident in the Ba doped case. At the time, there was no obvious physical justification for the presence of local LTT-domains which were globally disordered. However, it could be explained if the local LTT-like tilts are stabilized by the presence of local charge stripe order and if the charges are fluctuating dynamically. Long-range LTT tilt order would also be inhibited at doping fractions away from rational numbers where the holes can order commensurately with the lattice, even if the tilts were locally LTT-like. Models proposed in the earlier work showed that global LTO symmetry can be recovered by a linear superposition of two degenerate local LTT

variants. Thus, spatially or temporally fluctuating LTT domains can yield a global LTO tilt symmetry.

The picture of local, fluctuating, LTT-like domains is also consistent with recent thermal conductivity measurements [110] where the apparently contradictory result was obtained that the thermal conductivity (κ) of insulating samples of rare-earth doped $La_{2-x}Sr_xCuO_4$ was *higher* than that of similar samples which were conducting. Clearly the contribution of the charge carriers to the thermal transport is negligible, which is not surprising because of the low carrier density; but also implied by this result is that the inelastic phonon scattering is significantly greater in metallic samples than in insulating ones. The authors proposed that scattering was occurring off local domains of stripes. We would like to add that, in the present picture, this phonon scattering would be greatly enhanced if there were fluctuating domains of *tilt* disorder associated with these striped domains.

The first result we have demonstrated here is that the local tilt direction in undoped La_2CuO_4 is [010] (LTO), and that the PDF is clearly sensitive to the tilt direction for tilts of magnitude $\approx 5°$. The local tilt direction and magnitude is the same as the average crystallographic tilt direction and magnitude for the undoped material at low temperature and there is no tilt disorder [44, 197].

For doping levels greater than zero the PDF results are suggestive of the presence of local LTT-like tilts. The tilt directions and magnitudes are disordered, and also could be fluctuating and could originate from an inhomogeneous charge distribution in the CuO_2 planes. As we discuss below, we expect that charge localization in a background of octahedral tilts will give rise to complex patterns of tilt disorder which our simplistic modeling using pure LTO and LTT models cannot hope to reproduce. Below we describe qualitatively different models of tilt defects which give insight as to when LTO and LTT tilts, respectively, are stabilized.

5.5.3 Tilt defect models

We introduce here several different models for the tilt distortions which might be expected as a result of the presence of localized charges in the tilt background. Our starting point is based on the two following observations: (a) Buckling appears because Cu-O bonds are too long to match the bonding in the La-O intergrowth layers [113], and (b) Cu-O bonds become shorter on doping.

In the absence of holes the equilibrium tilt amplitude is 5°. On average, the tilts disappear for $x \approx 0.2$ which corresponds to a nominal copper charge-state of +2.2. If charges completely localize on a CuO_6 octahedron, the charge state of this copper is +3 which is easily high enough to remove the local tilt. However, between the localized charges the material is essentially undoped and large tilts are expected. Because the CuO_2 planes are a continuous network of corner shared octahedra, these untilted defects will introduce strains and there is expected to be a distribution of tilt amplitudes. However, it is possible to show geometrically that local LTT tilted octahedra (LTT-defects) can help reduce the strains.

We make the following assumptions in our models. First, the undistorted tilt pattern is LTO-like. Second, that the localized doped holes form into stripes with one hole associated with every second CuO_6 octahedron along the stripe [26]. The nominal doping then determines the average separation of neighboring stripes. We then considered two possibilities. The first is that the charge essentially delocalizes along the chain making the Cu-O bonds along the chain short, but not shortening the Cu-O bonds perpendicular to the stripe. The second is that each charge localizes on a single CuO_6 octahedron, similar to a Zhang-Rice singlet [198], sharing charge density equally between each of the four in-plane Cu-O bonds. We introduce these defects into the background of LTO tilts with the constraint that the octahedra are corner shared and displacements of an oxygen ion must be the same for neighboring octahedra. This gives rise to extended defects which we can identify using only these

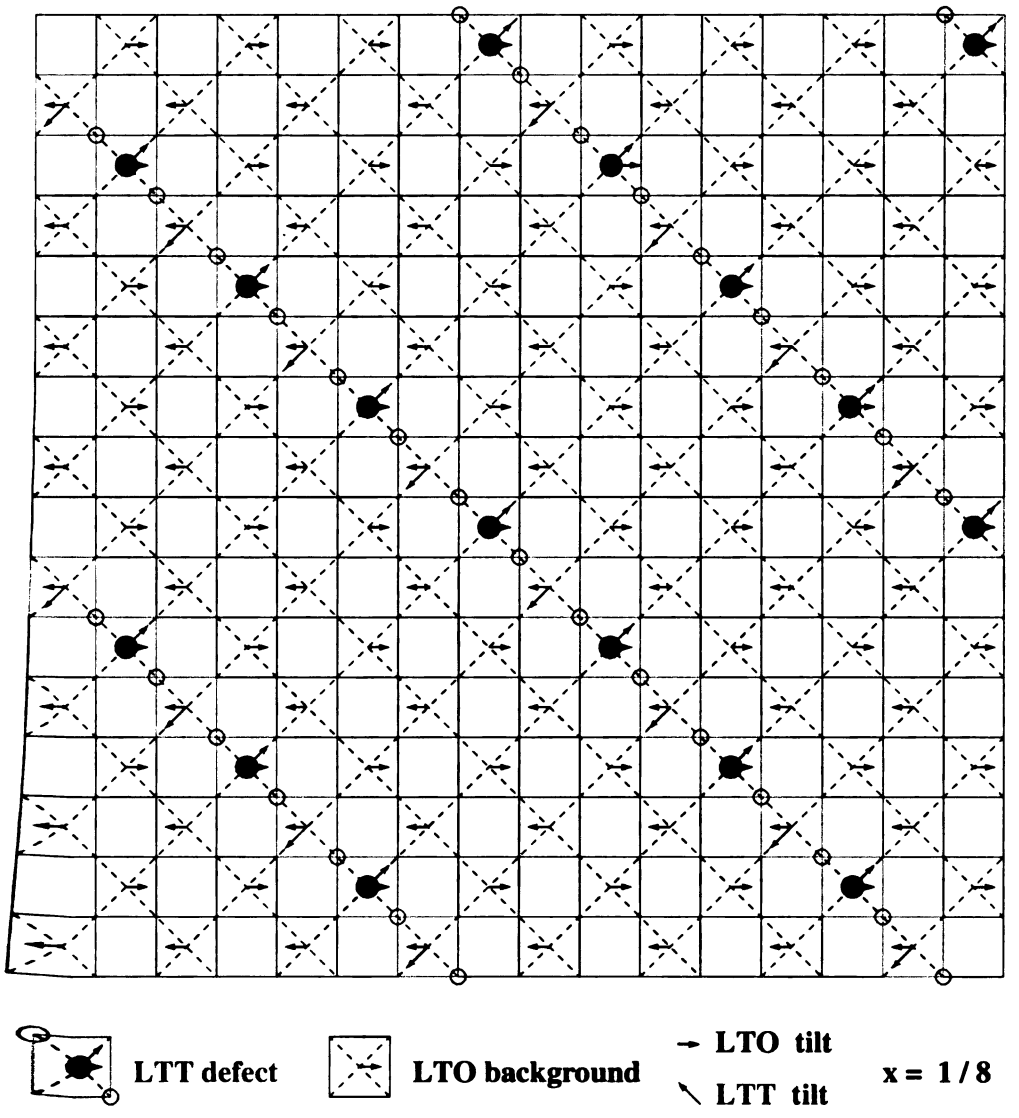

Figure 5.10: Schematic view of the Model I (see text) tilt pattern in the CuO_2 plane in the presence of charge stripes. Corner shared CuO_6 octahedra are denoted by squares with dashed crosses inside. The displacement of the apical oxygen above the plane due to octahedral tilting is shown with small arrows. In-plane O1 ions lie at the corners of the octahedra and are displaced up or down by the tilts (not shown). Open circles at the corners indicates an O1 ion which is undisplaced and lies in the plane. The presence of a localized hole is indicated by a black circle.

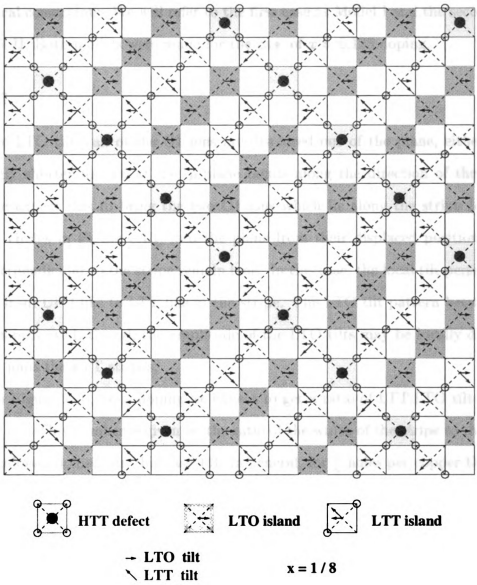

Figure 5.11: Schematic view of the Model II (see text) tilt pattern in the CuO_2 plane in the presence of charge stripes. Corner shared CuO_6 octahedra are denoted by squares with dashed crosses inside. The displacement of the apical oxygen above the plane due to octahedral tilting is shown with small arrows. In-plane O1 ions lie at the corners of the octahedra and are displaced up or down by the tilts (not shown). Open circles at the corners indicates an O1 ion which is undisplaced and lies in the plane. The presence of a localized hole is indicated by a black circle at the center of the octahedron.

topological constraints. We will refer to the first case as Model I and the second case as Model II. Both models were made for the case of $x = 0.125$ doping.

Model I

With the LTO tilts, all of the O1 ions are displaced out of the plane, either up or down. By shortening two of the in-plane bonds along the direction of the charge stripe we expect this to bring the two O1 ions which lie along the stripe (denoted by open circles in Figure 5.10) into the plane from their displaced positions. The bonds perpendicular to the stripe remain long. In this case, the local tilt persists, but changes from LTO-like to LTT-like in the stripe. The LTO tilt pattern between the stripes is preserved, though the amplitude of the LTO tilts may be locally distorted where it joins the LTT-stripes.

From Figure 5.10, for $\frac{1}{8}$ doping we expect to get a ratio of LTT:LTO tilted octahedra of 2:6. This number is given by the ratio of the width of the stripe to the width of the undoped domain; in this case 1:3. In general, for $\frac{1}{n}$ holes per copper this ratio is given by $1{:}\frac{n-2}{2}$.

This model predicts that in the presence of charge stripes the local tilt distribution should be a mixture of LTO and LTT tilts with a majority of LTO tilts in the doping range up to $x = 0.25$.

Model II

In this model the localized holes on every second site along the stripe produce octahedra which are completely untilted. This is equivalent to placing an HTT defect in the LTO background. Because the out-of-plane displacements of the O1 ions are removed, neighboring octahedra both along the direction of the stripe, and perpendicular to the stripe, take on an LTT-like tilt, as shown in Figure 5.11. The tilt axes of the LTT-like tilts propagating parallel and perpendicular to the stripes are rotated

by 90° with respect to each other. As it was pointed out in the earlier study [191], the linear superposition of these two degenerate LTT-variants yields the LTO symmetry of tilts on average.

As is clear from Figure 5.11, patches of LTO-like tilts also persist in this model; however, the extent of the LTT-like tilting is greater than in Model I. In the case of $x = \frac{1}{8}$ the ratio of HTT:LTT:LTO is 1:4:3. In general, for $\frac{1}{n}$ holes the ratio will be

$$1 : \frac{n}{2} : \frac{n-2}{2}. \tag{5.3}$$

One assumption inherent in this model is that the LTT-stripes propagating perpendicular to the charge-stripes persist all the way to the neighboring stripe. This is an approximation since the Cu-O bonds are long along this stripe and O1 ion displacements may not completely disappear along the stripe (even though these ions are depicted as open circles in Figure 5.11). Thus, when the charge-stripes are well separated at low doping we might expect that the ratio of LTT:LTO is smaller than predicted by Equation 5.3.

Discussion

These tilt models show that, if charge stripes are present, the real situation will be a mixture of LTO and LTT; or LTO, LTT and HTT tilts, and not purely LTO or LTT as we have modeled. The presence of charged stripes, and regions between the stripes with no holes present, implies that there coexists in the local structure regions with strongly diminished tilts, and regions with large tilts (as much as 5°) even in the doped materials whose average tilt is 3° or less. We would like to see whether this picture is consistent with our PDF data. We have made a simple test of this idea, and the results are shown in Figure 5.12. In this figure we compare PDFs which mimic the situation we would have if there were a coexistence of 5° tilts and $\approx 2°$ tilts, with the data from the $x = 0.10$ sample whose average tilt is 3.6°. We did this by averaging the data-PDFs from the $x = 0$ and $x = 0.25$ samples.

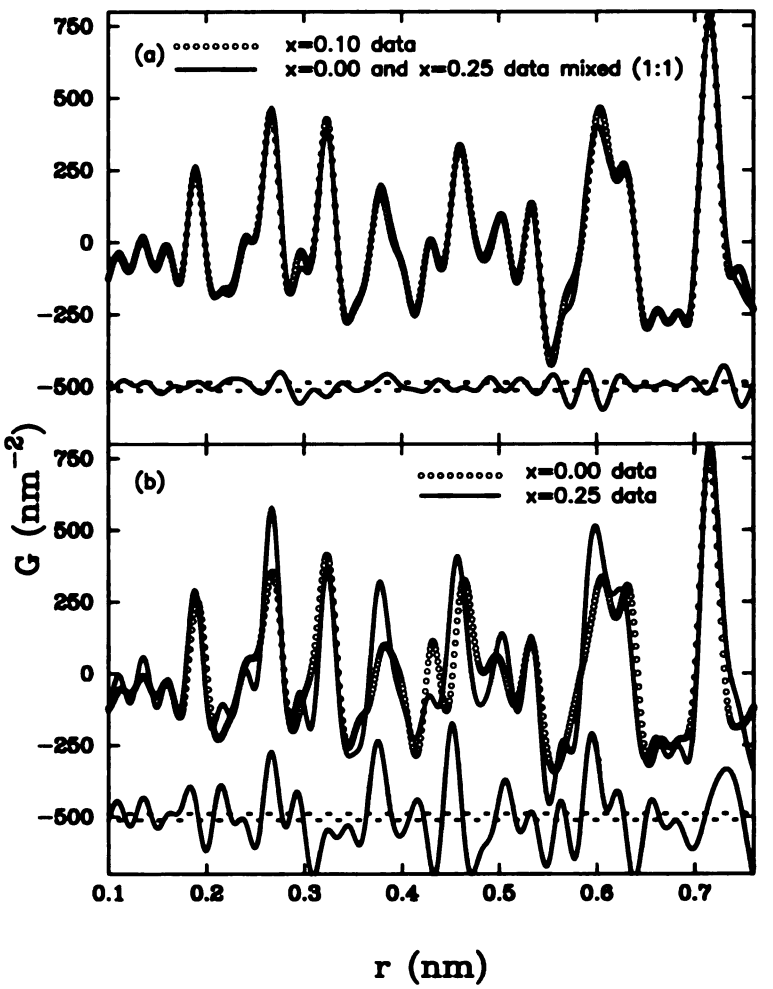

Figure 5.12: (a) Comparison of PDFs produced by a mixture of large and small tilt amplitudes and the data from the $x = 0.10$ sample. The solid line is the PDF obtained by mixing the $x = 0$ data set (5° tilts) with the $x = 0.25$ (< 2° tilts) data set in the ratio 1:1 to mimic the effect of a coexistence of large and small tilts in the local structure. The open circles show the PDF from the the $x = 0.10$ sample. (b) The $x = 0$ and $x = 0.25$ data-PDFs are plotted for comparison. There are large differences between these PDFs, yet when they are mixed they reproduce the PDF of the intermediate composition extremely well. The data were collected at 10 K.

The former has 5° LTO tilts and the latter sample has tilts with less than 2° of tilt amplitude. It is clear from the figure that the incoherent mixture of large and small tilts reproduces the data from the $x = 0.10$ sample excellently. For comparison, the data-PDFs from the $x = 0$ and $x = 0.25$ data are reproduced in the lower panel of this figure. There are large differences between them, yet when they are mixed together they give an excellent account of the $x = 0.10$ data. This shows that the data-PDFs for intermediate dopings are consistent with the presence of a distribution of local tilt magnitudes. Interestingly, the largest fluctuations in the difference curve between the $x = 0.10$ data and the mixture occur at $r \approx 2.8$ Å and $r \approx 6$ Å which is exactly where fluctuations are expected if local LTT-like tilts are present, as shown in Figure 5.13. This is also consistent with the fact that an inhomogeneous local tilt distribution exists in this material.

5.6 Domain size estimate

If charge inhomogeneities are organized in a stripe-like fashion, as schematically shown in Figure 5.11, then such doped hole clusters would separate undoped portions of the CuO_2 plane, which could be thought of as undoped micro-domains. If this is the case, it is reasonable to expect that the nature of the structural correlations observed in the PDF may change as a function of r. In principle this could yield information about the nano-scale domain size, ξ. Below $\sim \xi/2$ the PDF will resemble an incoherent mixture of the different local structures of the doped stripes and undoped regions between. On length-scales longer than $\sim \xi/2$ the structure in the PDF will start to resemble the average structure. Having in mind a simple-mined mixing "model" such as the one presented above, the issue of quantitative local agreement between the PDFs (Figure 5.12(a)) is investigated.

When comparing the mixture of two *data* PDFs corresponding to $x = 0$ and

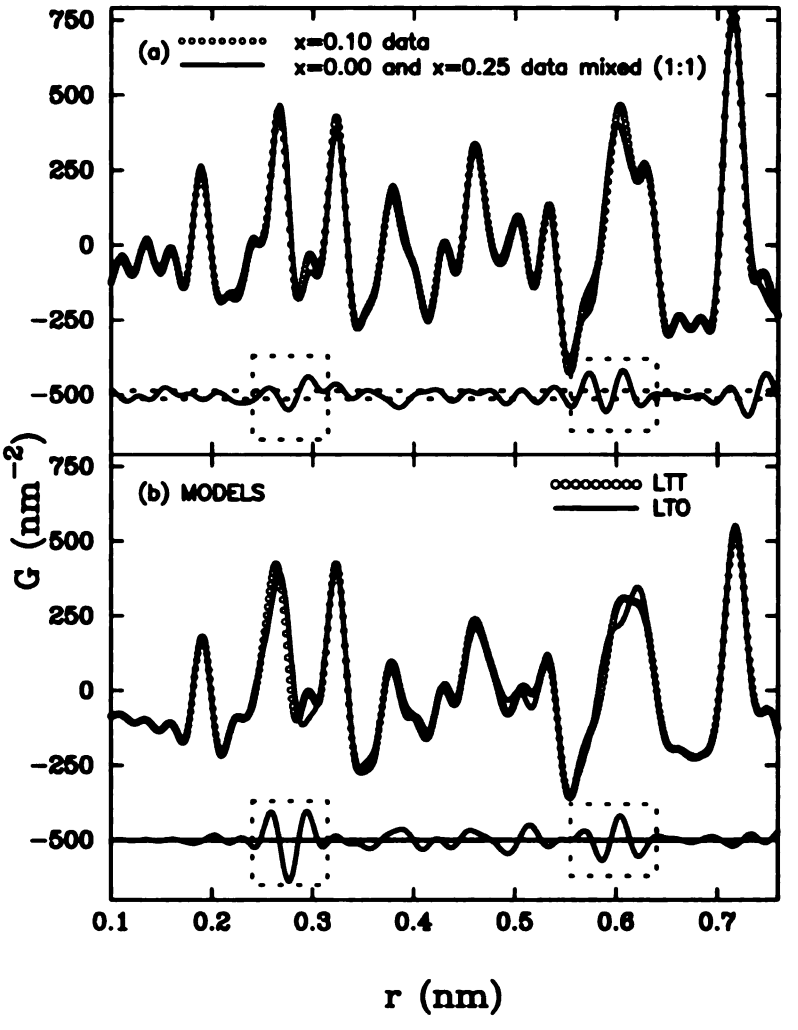

Figure 5.13: Comparison of the fluctuations in the PDF difference curve at low-r.

$x = 0.25$ samples ("the mixture") with the PDF of $x = 0.1$ sample ("the data") at 10 K, excellent agreement between the mixture and the data in the low-r region is observed. This is evident by inspecting the difference curve in Figure 5.12(a). However, the agreement between the PDFs corresponding to the mixture and the data gets systematically worse at high-r. In order to quantify the agreement between the mixture and the data, as well as to verify earlier results, we used recent data collected at 10 K at the GEM diffractometer at the ISIS facility, on a less extensive set of LSCO samples. Due to the decreased sensitivity of the PDF for discriminating between the LTO and LTT tilt symmetries for more heavily doped samples where tilt amplitude is smaller, as demonstrated in Figure 5.5, and due to the experimental restrictions (limited set of samples), the procedure was repeated using the 10 K PDFs of x=0.0, x=0.125, and x=0.2 samples. These PDFs we label as undoped, $G_0(r)$, underdoped, $G_{ud}(r)$, and overdoped, $G_{od}(r)$, respectively. The mixture PDF is then generally defined as a linear combination

$$G_{mix}(r) = x\ G_0(r) + (1 - x)\ G_{od}(r), \tag{5.4}$$

where x refers to the mixing fraction. The mixture PDF, $G_{mix}(r)$, is then compared to the underdoped PDF, $G_{ud}(r)$. To quantify the local agreement between the two, a weighted agreement is determined from the standard definition used in PDFFIT [161],

$$R_w = \sqrt{\frac{\sum_{i=1}^{N} w_i\ [G_{mix}(r_i) - G_{ud}(r_i)]^2}{\sum_{i=1}^{N} w_i\ G_{ud}^2(r_i)}}, \tag{5.5}$$

where the continuous variable r is replaced with its discrete variant, r_i, N represents the number of datapoints, and the weight of each data point, w_i, is given by

$$w_i = \frac{1}{\Delta G_{ud}^2(r_i)}. \tag{5.6}$$

The agreement factor is then calculated over a limited range of r according to Equation 5.5. This is a measure of the average agreement over this narrow range. The

centroid of this range is then shifted by one point and recalculated and this is repeated. This is shown in Figure 5.14. In this way the r-dependence of the agreement is determined. The optimal mixing fraction, x, which is defined as the one that minimizes the weighted agreement, evaluated over the whole range, was determined first. The agreement window position was fixed at the low-r side of the difference curve in this treatment. The typical dependence of the weighted agreement on the mixing fraction is shown in Figure 5.15(a), using an agreement window that is 4 Å wide. The mixing fraction is varied in steps of 0.01 from 0 to 1. Various widths of the agreement window in the range 1 Å - 17 Å were used (not shown). While the shape of the dependence changed for various window sizes, the position of the minimum remained the same. For the PDFs involved in this test optimal mixing is achieved for $x = 0.41$, as indicated by the dashed line in Figure 5.15(a). The comparison for the optimized mixture is shown in Figure 5.14.

Second, we evaluate the weighted agreement as a function of the agreement window center position for the *optimized* mixture. While this method is rather crude, it can be an important indicator of changes of structural correlations as r changes. The agreement window in this evaluation is operated from the low-r region of the difference curve to the high-r side in Figure 5.14, and the weighted agreement is evaluated and recorded as a function of the window center position. Due to the finite portion of the difference curve evaluated (20 Å) the operation-range of the agreement window has been adjusted according to the window-width so as to avoid end-effects. Various window-widths were used, and both the qualitative and the quantitative findings were essentially the same. The result is shown in Figure 5.15(b), for a 4 Å wide agreement window. The extent of variations due to the difference in the window-width are expressed through the errorbars shown in this figure.

The results of this test are as follows. First, large fluctuations argued to originate from the underlying LTT-symmetry tilts in the underdoped sample at $\sim$ 3 Å and

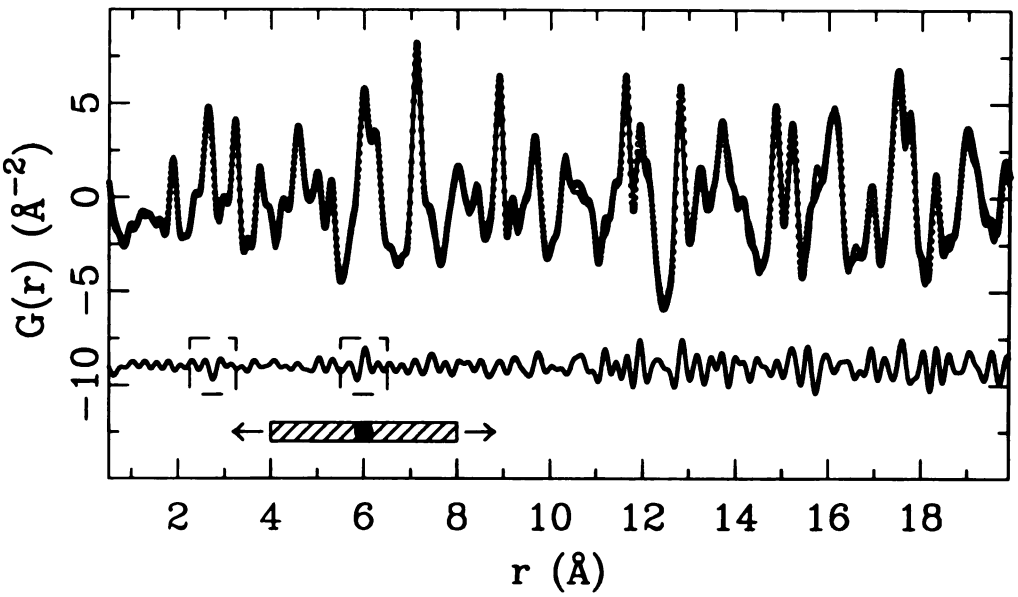

Figure 5.14: Mixing test comparison over a wide r-range. Comparison of PDFs produced by a mixture of large and small tilt amplitudes and the data from the $x = 0.125$ sample. The solid line is the PDF obtained by mixing the $x = 0$ data set (5° tilts) with the $x = 0.2$ (< 2° tilts) data set in the ratio 41:59 to mimic the effect of a coexistence of large and small tilts in the local structure. The points show the PDF from the $x = 0.125$ sample. Data shown are from GEM at ISIS at 10 K, and use the total scattering information up to Q_{max}=28 Å^{-1}. The difference curve is plotted below the data and is offset for clarity. Shaded rectangle represents an agreement window, and the solid circle is the agreement-window center. The arrows indicate how the agreement window is translated to extract an r-dependent measure of agreement.

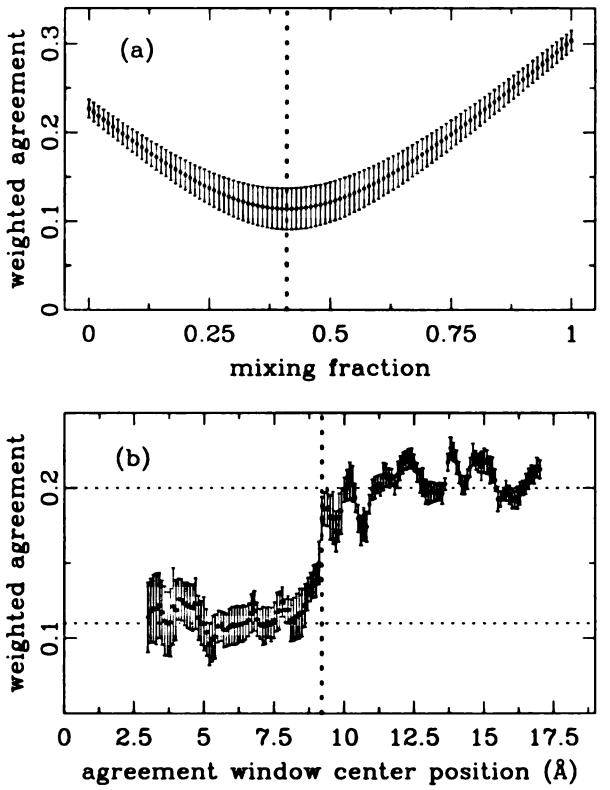

Figure 5.15: (a) Weighted agreement as a function of the mixing fraction. Horizontal dashed line indicates the optimal mixing fraction. (b) Weighted agreement as a function of r. The dashed lines are guides for the eye.

$\sim$ 6 Å are observed again. This can be seen by comparing the difference curves in the dashed boxes of Figures 5.13 and 5.14. Since these were independent measurements on different samples made at different diffractometers, this gives us some confidence that the fluctuations are real in origin. Second, a quantitative measure of the agreement between the mixture of undoped and overdoped structures and the underdoped structure is obtained which clearly shows a discrete jump in weighted agreement factor at around 8 Å. This is indicated by a vertical dashed line in Figure 5.15(b). The levels of the weighted agreement factor in the low-r and the high-r region are indicated with horizontal dotted lines. Small fluctuating features observed in the agreement factor come from the shape of the difference curve and propagate through due to the small window size used (4 Å). When a wider agreement window is used these features tend to be smaller. However, the step position observed in weighted agreement versus agreement window center curve remained essentially the same irrespective of the window width employed.

This sudden jump in the weighted agreement dependence on interatomic distance, as well as the fact that it has almost a step-like rather than continuous functional form, are supportive of the idea of having structural domains in the underdoped LSCO, whose *radial* extent is of the order of 8 Å.

While we cannot obtain directional information from this type of study, it is interesting to note that the static stripe separation observed in LNSCO [26] is of the order of 4 HTT lattice constants, or measured in Cu-O1 distances (assuming HTT symmetry and no tilts) about 8 nearest neighbor distances, half of which is $\sim$7.5 Å in overdoped LSCO at 10 K (Figure 5.16) [44].

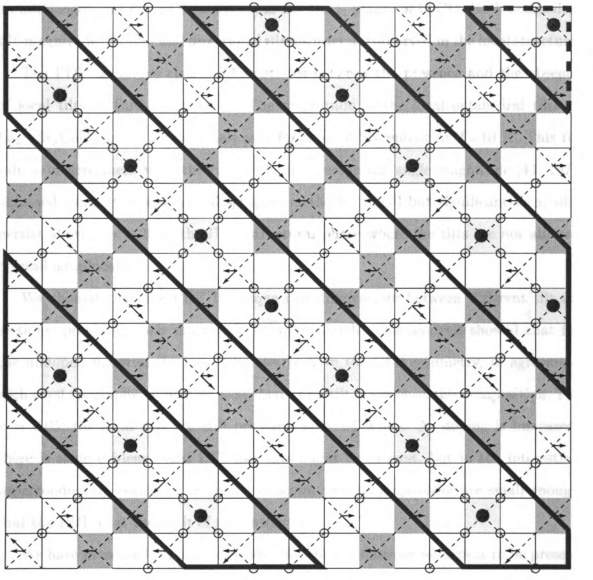

Figure 5.16: Schematics of the spatial extent of inhomogeneous domains within the Model II. From the PDF-based analysis summarized in Figure 5.15, the radial extent of the domains is about 8 Å.

5.7 Summary

In summary, we have presented additional PDF evidence supporting the presence of an inhomogeneous charge distribution in the CuO_2 planes of LSCO. Both octahedral tilt-magnitude disorder and directional tilt disorder are observed in the local structure.

The PDF technique clearly differentiates between the presence and the absence of local tilts of CuO_6 octahedra. The magnitude of the local octahedral tilts in $La_{2-x}Sr_xCuO_4$ smoothly decreases as a function of Sr-content at T=10 K. This result is in agreement with the result for the average tilt angle magnitude [44, 197], obtained using standard crystallographic methods. Small but significant local tilts persist above $x = 0.20$ in the HTT structural phase where the tilts are not allowed crystallographically.

We showed that the PDF technique can differentiate between different tilt directions, providing their magnitude is large enough. Our analysis showed that for the undoped material the local tilts clearly have the LTO symmetry, in agreement with crystallography, indicating that there is no tilt disorder at this composition. For $x = 0.05$, the local tilts are still predominantly LTO-like. As doping is increased, there is some evidence that LTT-like tilts might be present, but in the interesting superconducting region of the phase diagram the tilt amplitudes are small enough that the PDF is at the limit of its sensitivity.

We have presented topological models for the tilt disorder we expect to be present in these materials in the presence of charge-stripes. These imply that if charge stripe domains exist locally there should be a coexistence of large and small tilts, and LTO and LTT-like tilts locally. A simple test using PDF data shows that this is consistent with our measured PDFs. A more quantitative study of the weighted agreement in this test suggests the presence of micro-domains with radial extent of ~ 8 Å. A single crystal diffuse scattering, or electron diffraction measurement may be useful for elucidating this point.

Chapter 6

The Role of the Local Structure in the LTO-HTT Second Order Structural Phase Transition

"It is said that what is called 'the spirit of an age' is something to which one cannot return. That this spirit gradually dissipates is due to the world's coming to an end. For this reason, although one would like to change today's world back to the spirit of one hundred years or more ago, it cannot be done. Thus it is important to make the best out of every generation." (T. Yamamoto)

6.1 Prelude

The local atomic structure of undoped La_2CuO_4 and doped $La_{2-x}A_xCuO_4$ (A=Ba, Sr and x=0.15, 0.125 respectively) has been studied across the orthorhombic to tetragonal structural phase transition line using the atomic PDF analysis of neutron powder diffraction data. We find that standard low temperature orthorhombic (LTO) and high temperature tetragonal (HTT) models, that describe structure on the long range

scale, provide an inadequate description of the structure on the short range scale. The *local* tilts of CuO_6 octahedra persist at all temperatures, opposite to the prediction of the "displacive" models. Several "order-disorder" tilt models are introduced that may account for the observed presence of finite tilts in the HTT phase, and yet provide good agreement with the crystallographic results. The microscopic origin of the tilts is addressed within the framework of the bond valence sum calculations. Different topological models for Sr and Ba substitutional defects are proposed.

6.2 Octahedral tilts and structural phases

From the crystallographic perspective [48] that yields the average structure, La_2CuO_4 and $La_{2-x}A_xCuO_4$ (A=Sr,Ba) systems undergo a second order structural phase transition. On heating they transform from the LTO phase (s. g. *Cmca*) to the HTT phase (s. g. $I4/mmm$) when the transition temperature, T_t, is approached. The average tilts of the CuO_6 octahedra, that lie along [010] crystallographic directions in the LTO phase, disappear at high temperature, as illustrated in Figure 6.1. The square of the octahedral tilt angle magnitude represents an order parameter for this phase transition that in this view has "displacive" character. The phenomenology of the average long-range structure is quite well understood. There have been a number of detailed crystallographic studies. The most detailed to date are a single crystal study by Braden *et al.* [197] and a powder study by Radaelli *et al.* [44] which contain extensive references to the earlier crystallographic work. In addition to the HTT-LTO transition, a further transition to a new low temperature tetragonal (LTT) phase (s. g. $P4_2/ncm$) has been observed in LBCO [47] and in samples double doped with Sr and Nd [54, 55], which also exhibit a second kind of orthorhombic phase (LTO2) in a certain range of doping. The octahedral tilts in the LTT phase are along [110] directions. The transition from LTT to LTO phase is first order. All of this rich

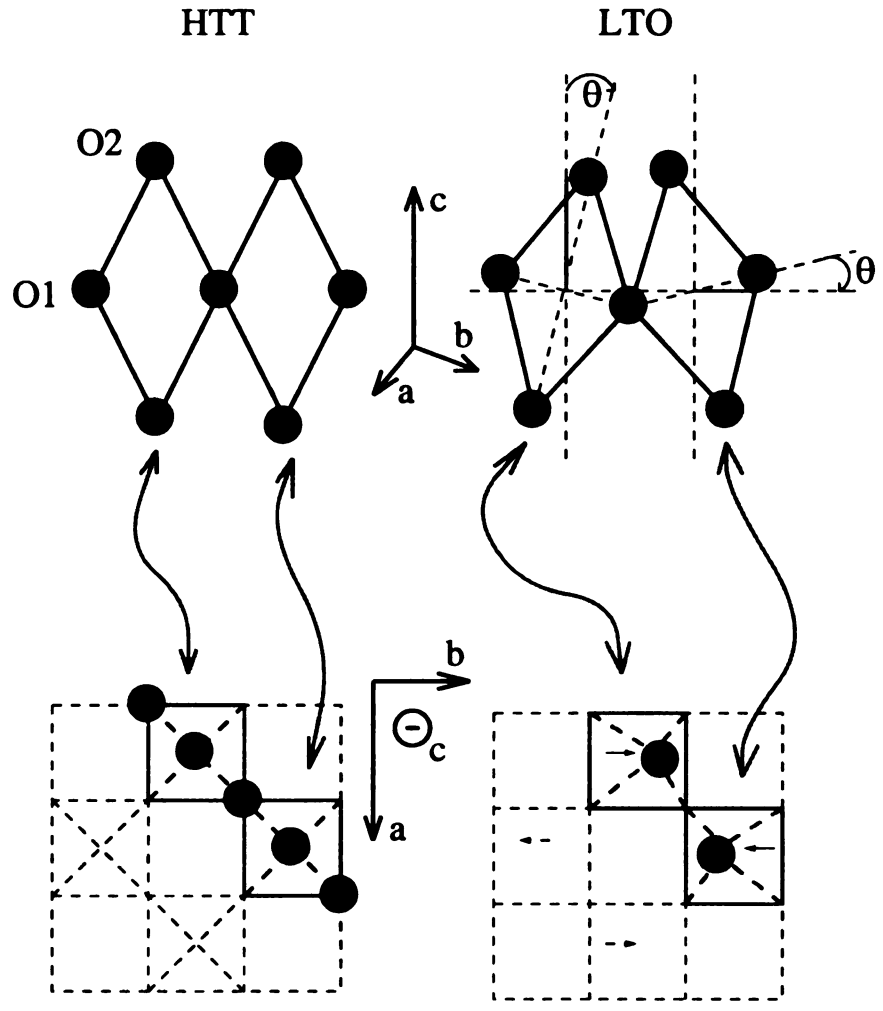

Figure 6.1: Schematic view of the tilt distortions. The top part of the scheme gives a side view of the CuO_6 octahedra in the HTT and LTO phases, showing the local tilt angle. The shaded circles are in-plane oxygen atoms (O1) and the black circles are the apical oxygens (O2). The top-view of the same tilts is shown schematically below. Note that the structure in the top view is 45° rotated with respect to the side view.

phenomenology is very well described in the framework of Landau theory [47, 199].

In contrast, early local structural studies of these systems indicated that disordered tilts may persist in the HTT phase. The first suggestions are based on a qualitative examination of the PDF data by Egami [192]. This effect was examined in more detail in subsequent PDF [191, 193] and XAFS [194] studies which concur that significant finite CuO_6 tilts persist into the HTT phase on a local scale even though the average tilts have gone to zero. In addition, measurements of elastic constants in these materials suggest that the "displacive" picture is not fully correct [200]. There is one conflicting result from ^{151}Eu Mössbauer spectroscopy of $La_{1.83-x}Eu_{0.17}Sr_xCuO_4$ [201] which suggests that the local tilts are disappearing in this strontium doped sample in the HTT phase.

The remedy for this apparent contradiction between average and local probes could be found, since the order parameter of the LTO-HTT phase transition is the square of the *long range ordered*, or average, octahedral tilt angle, $\langle\theta\rangle$, which does not necessarily reflect the actual *local* tilt angle, $|\theta|$. Local structural results do suggest that the simple picture that the HTT-LTO transition is a straightforward soft-mode "displacive" phase transition has to be reexamined. The crystallographic and local structural results can easily be reconciled if the transition is "order-disorder" in character: the tilts persist at high-temperature, but the direction of tilting becomes disordered. The local structural studies suggest that the HTT phase in LSCO and LBCO consists of disordered, and possibly dynamically fluctuating, finite octahedral tilts. The real situation may lie between these extremes of behavior with tilt amplitudes decreasing, but not going to zero on approach to T_t.

Inelastic neutron scattering experiments indicate the presence of modes which go soft at the HTT-LTO transition [29, 202] in the undoped La_2CuO_4 and in low-doped Sr doped samples. These results suggested that these transitions were canonical displacive soft-mode transitions. However, the observation of a soft mode does not

rule out the possibility that the tilts persist at high temperature. An octahedral tilting phonon mode with the symmetry of the LTO tilts softens to zero frequency when the static tilts set in. However, the microscopic nature of the soft phonon could be one in which finite tilts precess around the c-axis at high temperature rather than oscillate harmonically about the average untilted position. The precessional and vibrational modes would have the same **k**-vector and could not be distinguished from a measurement of phonon dispersion curves.

To study the *local* tilts directly it is necessary to use a local probe such as the PDF analysis of powder diffraction data or XAFS [154]. Such studies indicate that even at low temperature, away from T_t, significant disorder exists in the tilts [191, 192, 193, 194], and that the local tilts may even be along different direction than the average tilts [191], as we discussed in Chapter 5. It is clearly important to fully characterize the nature of the local tilts. Here we use the PDF method to study the behavior of the *local* tilts as the samples go through the transition from the LTO phase at low temperature to the HTT phase at high temperature.

Our study represents a more detailed and quantitative analysis. We find that, despite the fact that the average tilts disappear at this phase transition, significant local tilts remain within the HTT phase. This agrees with earlier qualitative observations from the PDF [192, 193] and XAFS data [194]. In the LCO and LBCO samples the temperature variation of the local tilt amplitude is negligible. The disappearance of the average tilts in these systems is presumably due to a loss in the long range order of the tilts. However, in the LSCO sample the residual tilts in the HTT phase are small, suggesting that the transition in this system has significant "displacive" component. As discussed in Chapter 5, the *local* tilts in doped samples appear to have a significant [110] character. Further evidence is presented in support of this conclusion. We consider a family of several "order-disorder" tilt models to describe the HTT phase, that may provide reconciliation of the short and long range order in these systems. The

bond valence sum calculations are performed to address the microscopic origin of the tilts. The issue of Sr and Ba substitutional defects is considered, and two topological models for these defects are proposed. Finally, certain aspects of the tilt symmetry in the presence of broken charge stripes are touched upon.

6.3 Experimental highlights

The PDF analysis of neutron powder diffraction data was used to study the local structure and the second order structural phase transition in undoped La_2CuO_4 and its doped variants $La_{1.85}Ba_{0.15}CuO_4$ and $La_{1.875}Sr_{0.125}CuO_4$. These specific samples are in this Chapter referred to as LCO, LBCO, and LSCO respectively, unless otherwise specified.

Preparation and characterization of the polycrystalline powder samples is described in detail in Chapter 3. The powder samples were characterized using standard x-ray diffracton methods. The transition temperatures, T_t, were obtained for LCO, LBCO, and LSCO, at approximately 525 K, 250 K, and 205 K respectively, by observing the [400]/[040] peak-splitting characteristic for the transition.

Neutron powder diffraction measurements were performed on several occasions on the HIPD at the MLNSC at Los Alamos National Laboratory, and on the GLAD at the IPNS at Argonne National Laboratory. The data were obtained for different temperature ranges encompassing the T_t's of the samples: from 10 K to 565 K for the LCO sample, from 10 K to 325 K for LBCO sample, and from 10 K to 330 K for LSCO sample. Real space structural refinements of the atomic PDFs obtained from neutron powder diffraction data were then carried out to examine the local structure of $La_{2-x}(Ba,Sr)_xCuO_4$. The RESPAR program [144] was used to perform refinements over a wide range in r-space, as described in Chapter 2.

The LTO-HTT structural phase transition in the average structure is clearly ev-

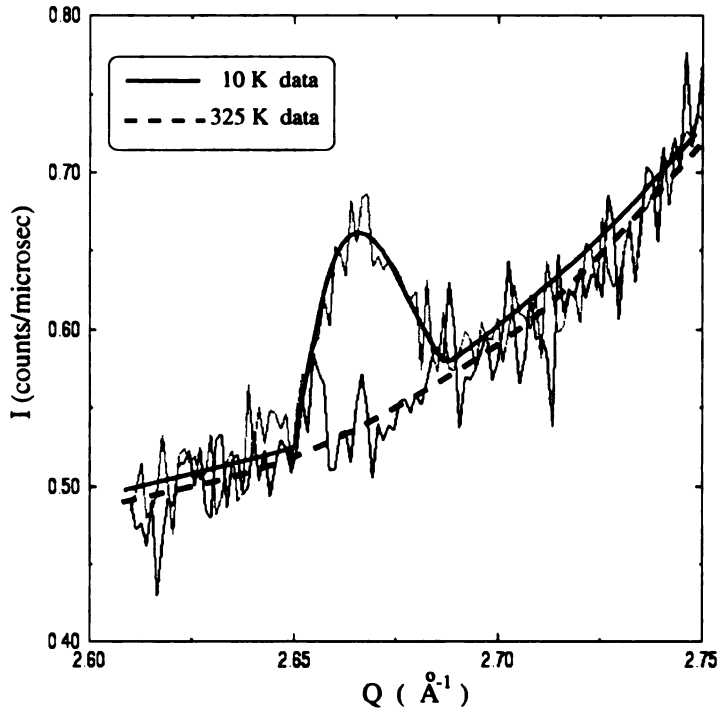

Figure 6.2: The [023] superlattice peak for $La_{1.85}Ba_{0.15}CuO_4$ sample, compared for 10 K (solid line) and 325 K (dashed line) data. The peak clearly disappears in the high temperature phase of the material. Lines are guides to the eye. The background slopes as a result of the incident spectrum. Neutron data collected at MLNSC at Los Alamos National Laboratory.

ident in our data from the disappearance of the [023] superlattice peak, shown in Figure 6.2. As pointed out by a number of authors [29, 202, 203], this superlattice peak is an order parameter for the CuO_6 octahedral tilting, and reflects the behavior of the square of the *long range ordered*, or average, octahedral tilt amplitude, $\langle\theta\rangle$, as mentioned earlier. Temperature dependence of the intensity of this superlattice peak for the LBCO and LSCO samples are shown in Section 6.5 where the local structural results are presented and compared to the average structure.

6.4 Structural models

6.4.1 Conventional displacive models

The crystal structures of the LTO and HTT phases are well understood [48]. The Cu atoms reside at the centers of oxygen octahedra that form a 2-D plane by corner sharing oxygen atoms which lie on the equatorial planes of the octahedra (O1). The apical oxygen atoms (O2) are at the top and the bottom position of each octahedron, and they are not shared by neighboring octahedra.

For the case of the LTO model, octahedra rotate by 3.5°-5° about the [100] axis, causing displacements of the apical oxygens in [010] directions. In the HTT model the octahedral rotations disappear. In this picture the HTT-LTO transition can be thought of as being a "displacive" transition. This is shown schematically in Figure 6.3(a),(e).

6.4.2 Order-disorder models

The above behavior describes the *average* long range order well, but does not necessarily agree with the local structure. We introduce a family of "order-disorder" models which may reconcile the local and long-range structural results. They are High Temperature Tetragonal Linear Superposition (HTTLS) model, Low Temperature Orthorhombic Linear Superposition (LTOLS) model, and Four Sites (FSITE) model. The main idea of the "order-disorder" family of models is rather simple. While in the "displacive" representation certain single fully occupied atomic positions are continuously displaced, in the "order-disorder" representation these atomic positions are replaced with two (or more) atomic positions that are *partially* occupied, and whose occupancies add up to one. The occupancies of the new atomic positions, as well as their spatial coordinates, can be varied and their linear superposition should be considered in order to obtain the average atomic position of a given site.

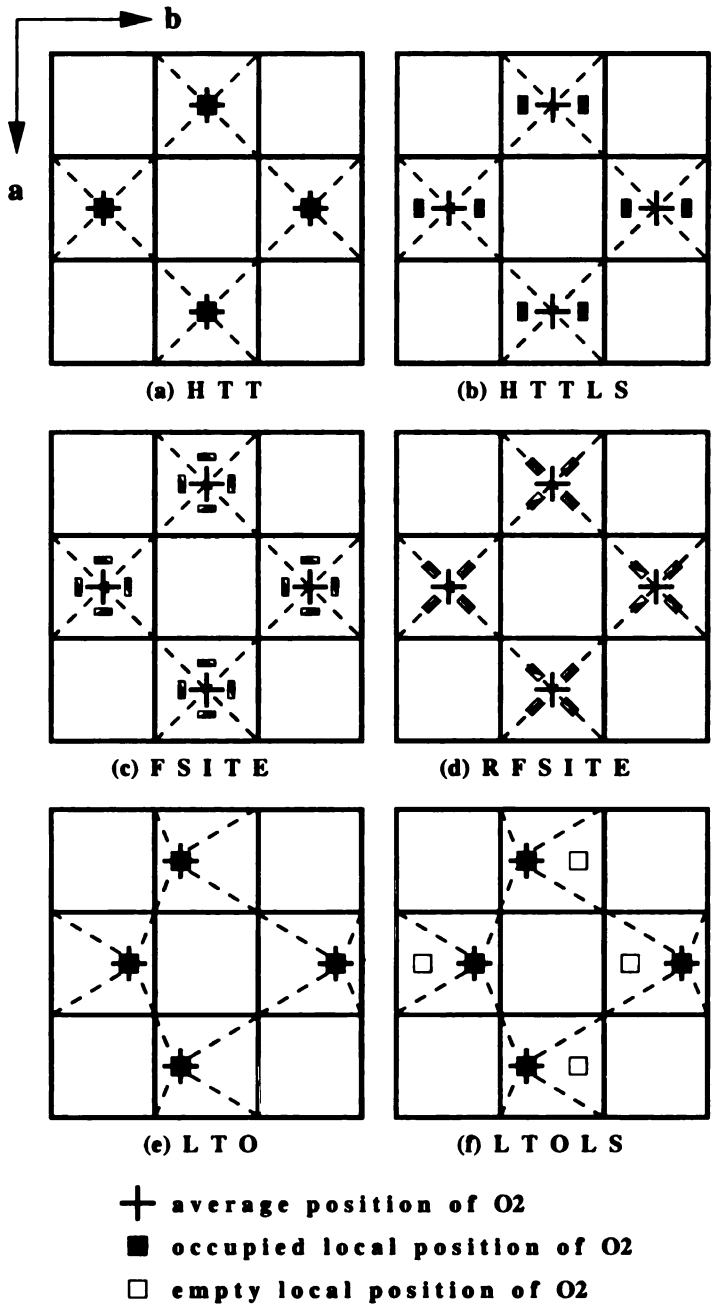

Figure 6.3: Schematic representation of the (a) HTT, (b) HTTLS, (c) FSITE, (d) RFSITE, (e) LTO, and (f) LTOLS models described in the text. Panels give top view of a few neighboring CuO_6 octahedra indicated by the dashed lines. Crosses indicate the average positions of the apical oxygen atoms (O2) obtained crystallographically. Squares indicate the positions of atoms in the local structural models. These displaced sites have partial occupancies ranging from zero to 1 (see text). The size of the O2 displacements are greatly exaggerated.

The HTTLS and LTOLS models are shown schematically in Figure 6.3(b),(f). Two atomic positions, located along the [010] direction, replace each apical oxygen site. The HTTLS model assumes equal occupancies of 0.5 for each displaced site. In the LTOLS model the occupancies are set to zero and 1, recovering the LTO model.

The FSITE model is characterized with four atomic positions that replace each apical oxygen site. The positions are slightly displaced along [100] and [010] directions, and each position is 25 % occupied in the HTT phase. This is presented schematically in Figure 6.3(c). This model features atomic displacements that correspond to the LTO-type tilts.

Within these models the displacements of the planar O atoms are presumably small enough. These atoms were allowed to displace in the LTO fashion in all the models that we considered.

6.4.3 Rotated tilt model

The RFSITE model is also of the "order-disorder" family, and is developed from the FSITE model by rotating each group of four sites representing O2 by 45° about [001] axis, while their occupancies (0.25) are unchanged. Spatial positions are varied in [110] directions in this model, while in the FSITE they are varied along [100] and [010] directions. This model is shown in Figure 6.3(d), where half-filled rectangles present 1/4 occupied atomic sites in the HTT phase. This model features atomic displacements that correspond to the LTT-type tilts.

6.5 Results

6.5.1 Displacive models

Results of the Rietveld refinements of the diffraction patterns for the samples showed that the HTT model provides better agreement above T_t than LTO model, and that

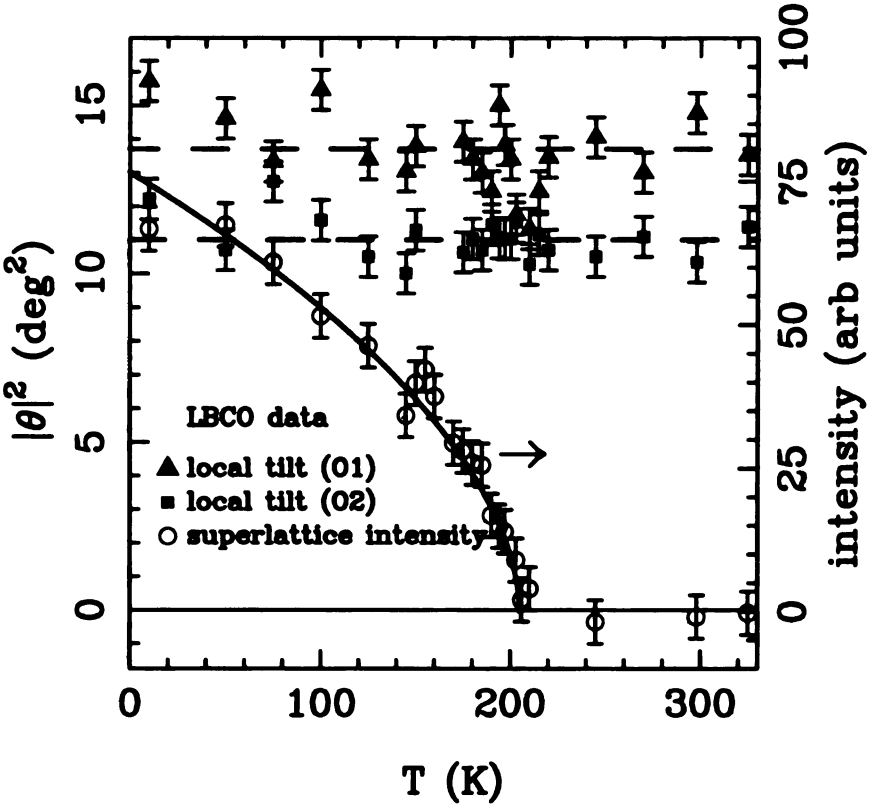

Figure 6.4: Temperature dependence of the square of the octahedral tilt-angle amplitude for LBCO, determined independently from both O1 (triangles) and O2 (squares). This represents the *local* behavior of the octahedra. Temperature dependence of the superlattice peak intensity (open circles) is shown to compare the local with the long-range behavior of the octahedral tilts.

the LTO model provides better agreement than the HTT model below T_t. These results for the *average* structure are in accord with the results that can be found in the literature, and are not presented here in detail.

We have obtained the local octahedral tilt amplitude from the PDF refinements in the same manner as in Chapter 5, using Equations 5.1 and 5.2. In Figures 6.4 and 6.5 we show the temperature dependence of the square of the octahedral tilt-angle magnitudes for LBCO and LSCO respectively, determined independently from both O1 (triangles) and O2 (squares) displacements. It is clear that the local tilt amplitude,

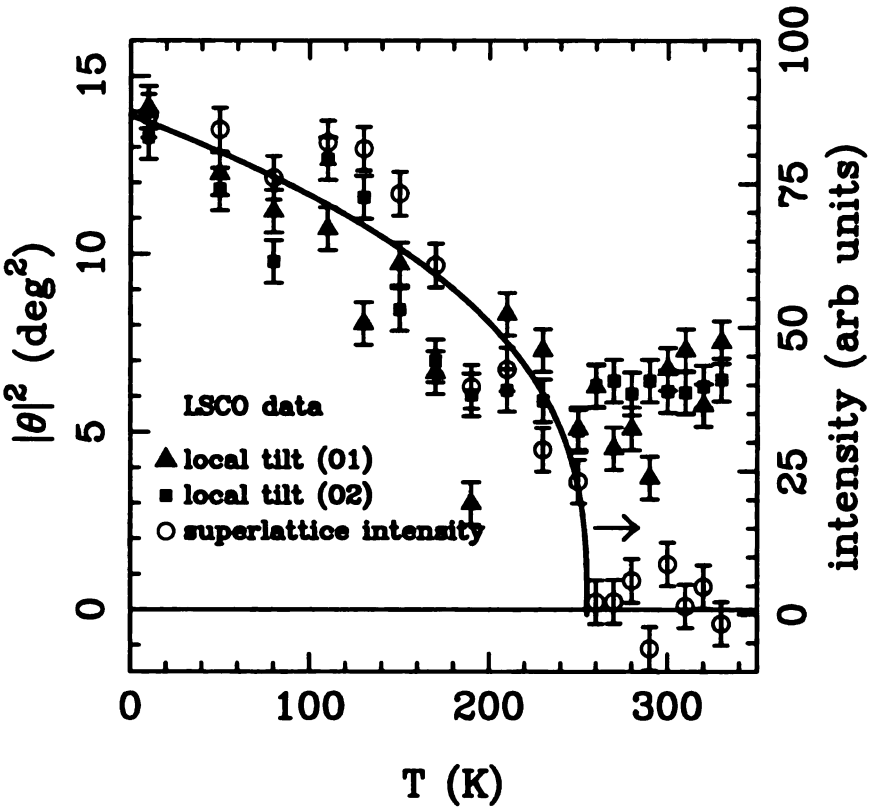

Figure 6.5: Temperature dependence of the square of the octahedral tilt-angle amplitude for LSCO, determined independently from both O1 (triangles) and O2 (squares). This represents the *local* behavior of the octahedra. Temperature dependence of the superlattice peak intensity (open circles) is shown to compare the local with the long-range behavior of the octahedral tilts.

$|\theta|$, is temperature independent in the LBCO sample. In the LSCO sample the local tilt amplitude follows the trend of the canonical behavior at lower temperatures, but some finite residual tilting persists in the high-temperature phase, in agreement with the observations at 10 K in our doping-dependence study presented in Chapter 5.

Temperature dependence of the superlattice peak intensity (open circles) is shown to compare the local with the long-range behavior of the octahedral tilts. In Figure 6.2 the [023] superlattice peak in LBCO data is shown for 10 K data (solid line) and for 325 K data (dashed line) to illustrate this. The peak disappears from the diffraction

Table 6.1: Amplitude of the local and the average octahedral tilts of the CuO_6 octahedra in the LCO at various temperatures. The local (PDF) tilt amplitude is obtained from the fully converged LTO model. The average tilt amplitude is obtained using crystallographic structural parameters reported by Radaelli *et al.* [44]. Labels: *a* denotes HIPD data, *b* denotes GLAD data.

T (K)	O1 tilt (deg)		O2 tilt (deg)	
	PDF	AVERAGE	PDF	AVERAGE
10	4.5(5)[a]	4.65(5)	4.7(5)[a]	5.19(3)
300	4.2(3)[b]	4.23(6)	4.9(1)[b]	4.38(2)
535	4.1(5)[b]	0	4.3(1)[b]	0
565	4.0(1)[b]	0	4.5(2)[b]	0

pattern when the sample goes through the LTO-HTT phase transition. Due to the sparse datasets and wider temperature range studied, the results for the tilt angle magnitude obtained for the undoped sample are shown in Table 6.1. Both the PDF values and the average crystallographic values [44] are presented for comparison. The average tilt angle in the HTT phase is zero due to the symmetry constraints.

The R_w-factor across the temperature range studied suggests that HTT is not the preferred model at any given temperature if the *short* range scale is considered. This is demonstrated in Table 6.2 as obtained from LCO data modeling. Similar behavior of the R_w-factor is observed when LBCO and LSCO data were modeled.

Our result for the local tilt angle magnitude indicates that local octahedral tilts persist in the HTT phase even in the undoped sample. The LCO sample in question, however, showed canonical behavior in the *average* structure, since the [400]/[040] peak splitting was clearly evident in the diffraction patterns when the low temperature and the high temperature data were compared, as shown in Chapter 3.

Table 6.2: R_w-factors for LCO sample at 300 K, 535 K, and 565 K that correspond to fully converged HTT and LTO models.

T (K)	HTT	LTO
300	0.206	0.139
535	0.186	0.148
565	0.193	0.159

The local structure, as obtained from the LTO model, indicates that the local octahedral tilts persist in the HTT phase although in the average crystal structure they disappear. The atomic probability distribution function is not peaked at the untilted position in the HTT phase, but at some displaced position giving a finite octahedral tilt angle which is similar to the amplitude of the fully ordered LTO tilt angle at the lowest temperature. The O2 ion spends more of its time displaced from the untilted position by 0.12-0.18 Å than in the vicinity of the untilted position, even in the HTT phase. Tilts of almost full amplitude are observed in the HTT phase of the LCO and LBCO samples, while smaller but finite tilts exist in the HTT phase of the LSCO samples. Models allowing tilts consistently gave better agreement factors at high temperature than the HTT model clearly indicating that motions of the O2 ions in directions parallel to the CuO_2 planes are anharmonic. The R_w-factors are shown in Tables 6.3 and 6.4 for the LBCO and LSCO samples respectively.

6.5.2 Order-disorder models

The family of "order-disorder" models was considered next for the phase transition, as introduced in Sections 6.4.2 and 6.4.3. The HTTLS model was fit to the LBCO data. This model explains the HTT phase with disordered LTO tilts. This model yielded smaller R_w-factors than HTT at all temperatures above T_t. However, enlarged

Table 6.3: R_w-factors for various structural models used to fit the LBCO data.

T(K)	HTT	LTO	FSITE	RFSITE
10	0.190	0.162	0.168	0.161
50	0.184	0.152	0.158	0.150
75	0.184	0.155	0.156	0.151
100	0.172	0.139	0.146	0.139
125	0.148	0.141	0.143	0.140
150	0.147	0.139	0.141	0.137
175	0.144	0.137	0.135	0.129
200	0.146	0.137	0.132	0.127
215	0.141	0.138	0.133	0.129
245	0.141	0.130	0.125	0.116
270	0.131	0.127	0.123	0.114
298	0.135	0.133	0.128	0.120
325	0.136	0.132	0.123	0.114

anisotropic displacement parameters of O2 were observed along the [100] directions, as shown in Table 6.5 for the case of the optimally doped LBCO sample, indicating possible lateral displacements perpendicular to the LTO-tilt directions. New models were then constructed allowing such displacements, and with tilts in [110] directions, to check whether they could explain the observation. In the case of LBCO models allowing LTT displacements provided better agreement with the data, while for LSCO all of the tilted models provided similar agreement.

Table 6.4: R_w-factors for various structural models used to fit the LSCO data.

T(K)	HTT	LTO	FSITE	RFSITE
10	0.185	0.163	0.167	0.161
50	0.184	0.160	0.162	0.157
80	0.183	0.159	0.156	0.154
110	0.172	0.151	0.151	0.146
150	0.162	0.148	0.142	0.143
210	0.155	0.135	0.131	0.130
250	0.143	0.133	0.128	0.128
280	0.148	0.128	0.129	0.127
300	0.140	0.129	0.126	0.123
310	0.143	0.128	0.132	0.126
320	0.145	0.127	0.132	0.129
330	0.153	0.131	0.133	0.130

Table 6.5: Temperature dependence of the atomic displacement parameters U of the apical oxygen for the LBCO sample as extracted using LTO model. Reported values correspond to the directions parallel and perpendicular to the LTO tilt direction.

T (K)	$U_{\parallel}$ (Å^2)	$U_{\perp}$ (Å^2)
10	0.002862(5)	0.01648(1)
50	0.002751(6)	0.02236(5)
75	0.003177(6)	0.01627(2)
100	0.003123(8)	0.01973(2)
125	0.003407(7)	0.02378(6)
150	0.002726(8)	0.02042(6)
175	0.003961(12)	0.02349(7)
200	0.003706(14)	0.02219(11)
215	0.003451(9)	0.02307(8)
245	0.004171(13)	0.02427(4)
270	0.004819(24)	0.02258(10)
298	0.003498(17)	0.02985(10)
325	0.004337(23)	0.02849(3)

6.6 Discussion

On the basis of these observations we suggest that in the HTT phase of LCO and LBCO finite tilts persist such that the axes of the CuO_6 octahedra possibly precess about the *c*-axis of the crystal. Because the octahedra share corners, this must be a collective precessional mode of low energy. While this represents a distinct possibility for the LCO, in the LBCO the disorder could be more quenched. Although the PDF measurements do not provide information about the dynamics, the PDF results support this picture. This is very similar to the rigid unit modes described by Dove [204] to explain structural phase transitions in tetrahedrally coordinated crystobalite. This kind of picture seems to fit in nicely with the first-principles LDA calculations by Pickett *et al.* in the 214 LBCO system which show that the potential in which the O2 ion lies (Figure 6.6) is a circular trough surrounding the *c*-axis [205]. The trough has deeper wells at the [100] symmetry (LTO-like) displaced positions and slightly deeper still wells at the [110] symmetry (LTT-like) displaced positions. Presumably, at high enough temperature the O2 ion can make its way dynamically around the trough more easily than jumping out of it to execute linear vibrations through the undisplaced average atomic position. The LSCO case is more complicated. The small local octahedral tilt amplitude in the HTT phase limits the sensitivity of the measurement preventing more elaborate conclusions about the nature of the tilts. The fact that the local tilts in LSCO decrease with temperature shows that the transition has a displacive component. However, the results presented in Chapter 5 do suggest that the local tilt pattern of LSCO is complex, possibly composed of the octahedral tilts with directions that are a mixture of LTO and LTT tilt patterns. The possible cause of this apparently different behavior of the LCO and LBCO systems and the LSCO system will be further discussed in light of the bond valence sum analysis results.

In the LTO phase the long-range order indicates the presence of finite average tilts in [100] directions, $\langle\theta\rangle_{[100]}$, which smoothly increase in magnitude on cooling through

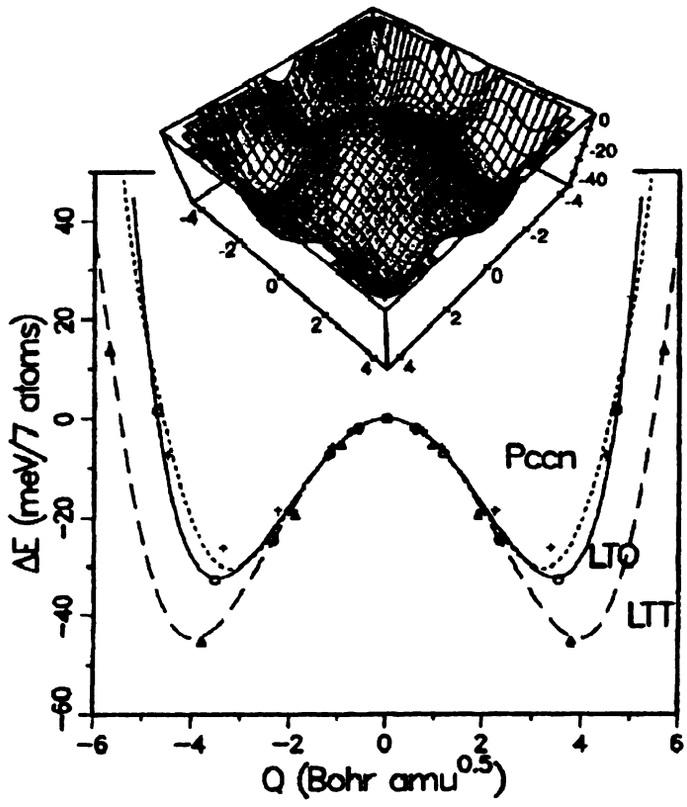

Figure 6.6: Energy difference per primitive cell for different structural phases of LBCO with tilts relative to the HTT structure. Inset shows a surface plot of the octuple-well energy surface for X-point tilts with minimum along the diagonal that corresponds to the LTT phase (after Pickett *et al.*, [205]).

the transition temperature T_t. The long-range ordered tilts with the LTO symmetry and amplitude $\langle\theta\rangle_{[100]}$ provide an order parameter for this phase transition. We have already established that finite local tilts, $|\theta|$ of the full (or almost full) amplitude are already there, though disordered and largely dynamic. The appearance of finite average tilts therefore suggests that, on the average, the local tilts are spending more time in the LTO symmetry positions than elsewhere.

As well as $\langle\theta\rangle_{[100]}$, there is a second order parameter which is orthorhombic strain, $\eta = (a-b)/(a+b)$. Birgeneau *et al.* [202] showed that for this transition the two order parameters are closely coupled. This is consistent with a term in the Landau

theory which couples η to $\langle\theta\rangle^2_{[100]}$ [199]; however, this does not explain microscopically the coupling mechanism. The presumption in the displacive model for this phase transition is that the large amplitude tilts which set in at T_t drive the transition and the relatively small orthorhombic strain is a benign consequence of this coupling term. However, if large amplitude tilts already exist in the structure in the HTT phase, it is not the tilt formation energy which is important, but the energy derived from *ordering* the tilts, which could be considerably smaller. From this point of view, it is likely that the orthorhombic distortion is driving the transition. By breaking the global tetragonal symmetry, it is not surprising that the dynamic tilts spend more time in one direction than the other and a finite *average* tilt emerges. This, however, is not the only possibility. In presence of local charge inhomogeneities (or even local stripes), that prefer the LTT-tilt environment, it is also possible that ordering of the LTT-tilt domains occurs in such manner to give rise to the average LTO-tilt pattern.

6.7 Microscopic origin of the tilts

The Landau theory describes the phenomenology in a self consistent way, but it does not address the microscopic mechanism giving rise to the tilts. This has been addressed by Goodenough [206, 207] who pointed out from simple bond-length arguments that a competition between the Cu-O bonding and the La-O bonding explains the tilting. Using the tables of Shannon and Prewitt [208], the expected bond length for La^{3+} in nine-fold coordination with oxygen (Figure 6.7) is 2.57 Å. The average bond length determined from the crystal structure is 2.67 Å, which suggests that the La site exerts a tensile stress. The site does not contract however because it is held open by the CuO_6 octahedral network. The expected $Cu^{2+}(VI)$-O^{2-}(II) (the roman numerals indicate the atomic coordination number) bond-length is 2.08 Å [208] whereas in the crystal it is 2.06 Å. The copper site is in compression. Goodenough *et*

al. [206, 207] proposed that these two competing bonding requirements would be partially alleviated by introducing buckling into the CuO_2 plane. They also explained the disappearance of the tilting at high temperature by the fact that the La_2O_2 layer has a larger thermal expansion coefficient. At some temperature, the stresses between the lanthanum and copper sites will disappear, at which point the tilts will go away. This simple picture also explains well the disappearance of the tilts on doping. As Sr or Ba are added, the charge state of copper increases from +2 towards +3. The $Cu^{3+}(VI)$-O^{2-}(II) expected bond length is 1.89 Å which is shorter than $Cu^{2+}(VI)$-O^{2-}(II). Thus, at all temperatures the stresses introduced by the mismatch are reduced and the HTT phase is stabilized with respect to the LTO phase, as observed.

This simple picture seems to capture most of the driving force for the tilts. However, based on our local structural observations, the mechanism for the disappearance of the tilts appears to be inadequate since the local tilts still exist at high temperature. We will discuss this in more detail using the language of the bond valence sums [164].

6.7.1 Bond-valence-sum calculations

We address the nature of the local structural distortions using the bond valence method described in detail in Section 2.8. The bond-valences have been calculated for each of the structural models, at low and high temperature (at 75 K and 270 K for the LBCO sample, at 50 K and 300 K for the LSCO sample, and at at 300 K and 565 K for the LCO sample), and these are shown in Table 6.6. The bond valences from crystallographic models are also shown for comparison.

We discuss the results for LSCO at 50 K (obtained from the LTO model), but the qualitative behavior is the same at 300 K. First it is clear that $V_{[La]} = 2.61$ is much smaller than +3 which confirms that this site is in tension, and that $V_{[Cu]} = 2.48$. This is larger than the nominal valence for Cu which should be +2.125 in this material,

Table 6.6: The bond-valence sums, V, in LBCO sample at 75 K and 270 K, in LSCO sample at 50 K and 300 K, and in LCO sample at 300 K and 565 K. Partial bond-valence sums V' are obtained similarly as V, but apical bond is ignored. Labels: *a* calculated based on ref. [197]; *b* taken from [197].

	HTT		LTO		FSITE		RFSITE	
LBCO	75 K	270 K	75 K	270 K	75 K	270 K	75 K	270 K
V [La]	2.556	2.471	2.530	2.461	2.566	2.507	2.555	2.503
V'[La]	1.938	1.931	2.004	1.976	1.992	1.985	1.993	1.998
V [Ba]	3.469	3.354	3.434	3.340	3.482	3.403	3.468	3.397
V'[Ba]	2.630	2.621	2.720	2.682	2.704	2.694	2.705	2.712
V [Cu]	2.450	2.471	2.479	2.502	2.464	2479	2.4711	2.486
LSCO	50 K	300 K	50 K	300 K	50 K	300 K	50 K	300 K
V [La]	2.638	2.539	2.610	2.518	2.603	2.553	2.612	2.544
V'[La]	1.968	1.938	2.024	1.992	2.018	2.009	2.034	2.011
V $[La]_{cryst.}$	-	-	2.670 [a]	-	-	-	-	-
V [Sr]	2.280	2.195	2.255	2.176	2.250	2.206	2.258	2.198
V'[Sr]	1.701	1.675	1.749	1.722	1.744	1.736	1.758	1.738
V [Cu]	2.450	2.464	2.479	2.494	2.479	2.479	2.479	2.479
V $[Cu]_{cryst.}$	-	2.537 [b]	2.544 [b]	-	-	-	-	-
LCO	300 K	565 K	300 K	565 K	300 K	565 K	300 K	565 K
V [La]	2.559	2.474	2.566	2.503	-	-	-	-
V'[La]	1.924	1.872	1.980	1.948	-	-	-	-
V [Cu]	2.518	2.504	2.518	2.458	-	-	-	-

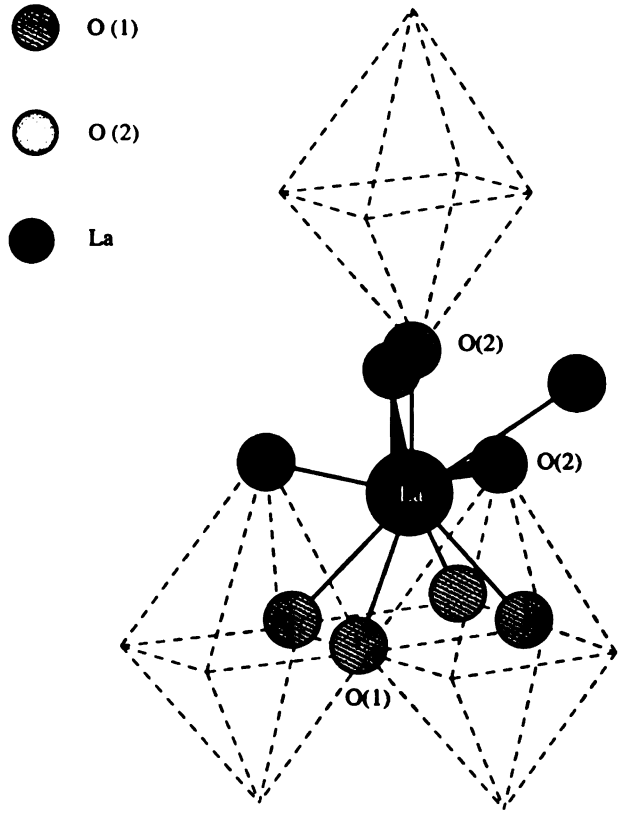

Figure 6.7: The lanthanum coordination cage: La atom surrounded by 9 oxygen atoms, four of O1-type and five of O2-type. Note that out of five La-O2 bonds, there is one very short bond ('apical' with respect to La site), and four longer La-O2 bonds (almost 'planar' with respect to La site).

suggesting that this site is forming the compressive network as discussed above.

There is one very short La-O2 bond which originates from the bond between a neighboring CuO_6 layer and the one below. The bond-valence theory accounts for why this bond is so short. The 8-fold La-O coordination cage (see Figure 6.7), obtained by neglecting this apical bond, is much too large. Without this apical bond, bond valence sum, $V'_{[La]}$, would be an unphysical 2.02. Because the successive CuO_2 layers are not directly bonded octahedron-to-octahedron there is a structural degree of freedom which is to increase or decrease the inter-layer spacing. It is clear that the deficiency in the bond valence sum of La can be rectified by bringing the adjacent

layer as close as possible. It also suggests that, despite this bond being as short as it is, it is apparently not the driving force for the tilting: the La bond valence sum for La can be increased by shortening this bond yet further. Also, as discussed in Section 2.8, the bond valence sum can be increased by lowering the site symmetry. This can be accomplished by the creation of tilts and by displacing La from its central position in the 8-fold coordination cage defined above. Both effects are observed in these materials. The driving force for the tilts is therefore coming from the bonds of the 8-fold cage. We can see which bonds have the largest effect by considering which of the 8-fold cage bonds raise the bond-valence sum the most for any given distortion pattern. For example, considering the LTO pattern, the La-O2 bonds of the 8-fold cage in LSCO increase by 0.063, whereas the increase due to the La-O1 bonds is just 0.007 (as obtained using values given in Table 6.7): the "planar" La-O2 interactions are driving the tilting. In the case of LBCO and LCO samples the corresponding values are (0.056,0.01) and (0.03,0.02) respectively. The most stable tilt pattern will thus be that in which the La-O2 bonds of the 8-fold cage give the greatest bond-valence increase. It is presumed that the short La-O2 bond can respond to the tilts imposed by the cage bonds to then give the greatest stabilization thereafter. The bond valence sum from the 8-fold cage does increase on going from untilted to tilted as expected, though the overall bond valence sum is reduced. This is because the important short La-O2 apical bond gets *longer* at this transition (see Chapter 7). The fact that the O2 ion above the La displaces in the opposite direction to La rather than in the same direction, which would give rise to tilts which were in-phase in successive layers instead of out-of-phase as observed, suggests that the simple bond valence sum model is breaking down in respect to this very short bond and that there is a repulsive interaction between this pair of atoms despite the theory suggesting that the bond should get even shorter. There appears to be a minimum bond-length for this La-O2 bond which is presumably determined by the polarizability of the La and

O ions. The interlayer spacing can be reduced, and $V_{[La]}$ increased, but only until this bond reaches its minimum length. Thereafter tilts appear, lowering the symmetry of the La site to raise $V_{[La]}$. The tilts from one layer to the next arrange themselves to maintain the short La-O2 bond at (or around) its minimum value and in such a way as to minimize the total volume of the unit cell. Typical values of the bondlengths are shown in Table 6.8.

At high temperature, the bond-valence sum of La is still far from being satisfied (indeed thermal expansion of the solid makes it worse) which supports the notion that the tilt distortions which stabilize the La site persist at high temperature, in contrast to the arguments of Goodenough *et al.* [206, 207]. A high temperature phase made up of disordered but finite tilts seems to be well explained within the bond valence model.

In the LTO symmetry tilts the La ion and neighboring O2 ion in the 8-fold cage move towards each other making one short La-O2 bond, one long La-O2 bond, and leaving remaining two La-O2 bonds relatively unchanged. This is in complete accord with the bond valence arguments made above. However, there are four equivalent directions along which this dimerization could to take place. At low temperature, one direction is preferred giving rise to the LTO symmetry tilts. It is interesting to note that at T_t the amplitude of thermal motion of La is 0.08 Å (see Table 6.9 for comparison with LCO). This is comparable to, but slightly larger than the static displacement in the tilted models. Thus, it would be relatively easy for La to switch its dimerization between neighboring O2 ions allowing the tilts to fluctuate dynamically and maintaining the stability of the distorted La site.

6.7.2 Tilt distortions and dopant induced defects

As was discussed above, the La site is underbonded and in tension. In contrast, the Ba and Sr dopants in LBCO and LSCO both have the nominal valence of +2, while

Table 6.7: The bond-valences for La site: in LBCO sample at 75 K, in LSCO sample at 50 K, and in LCO sample at 300 K. Multiplicities of the bonds are as follows: *a* denotes multiplicity 4, *b* denotes multiplicity 2, and *c* denotes multiplicity 1.

	HTT	LTO
LBCO bond at 75 K		
La-O1	0.2748 [a]	0.3145 [b]
	-	0.2401 [b]
La-O2	0.6181 [c]	0.5256 [c]
	-	0.3320 [c]
	0.2097 [a]	0.2154 [b]
	-	0.1324 [c]
LSCO bond at 50 K		
La-O1	0.2823 [a]	0.3145 [b]
	-	0.2466 [b]
La-O2	0.6703 [c]	0.5856 [c]
	-	0.3231 [c]
	0.2097 [a]	0.2213 [b]
	-	0.1361 [c]
LCO bond at 300 K		
La-O1	0.2823 [a]	0.3145 [b]
	-	0.2400 [b]
La-O2	0.6351 [c]	0.5855 [c]
	-	0.3231 [c]
	0.1987 [a]	0.1987 [b]
	-	0.1038 [c]

Table 6.8: The La-O bond-lengths (in units of Å) extracted using LTO model: in LBCO sample at 75 K and 270 K, LSCO sample at 50 K and 300 K, and LCO sample at 300 K and 565 K. Note: (i) *a* denotes data collected at HIPD, *b* denotes data collected at GLAD; (ii) bond-multiplicities in the La-O cage are as follows: *c* denotes multiplicity 2, *d* denotes multiplicity 1.

LBCO bond [a]	at 75 K	at 270 K
La-O2	2.41(1) [d]	2.44(1) [d]
La-O2	2.58(1) [d]	2.60(1) [d]
La-O1	2.60(1) [c]	2.61(1) [c]
La-O1	2.70(1) [c]	2.71(1) [c]
La-O2	2.74(1) [c]	2.73(1) [c]
La-O2	2.91(1) [d]	2.90(1) [d]
LSCO bond [a]	**at 50 K**	**at 300 K**
La-O2	2.38(1) [d]	2.41(1) [d]
La-O2	2.58(1) [d]	2.70(1) [d]
La-O1	2.60(1) [c]	2.58(1) [c]
La-O1	2.69(1) [c]	2.71(1) [c]
La-O2	2.73(1) [c]	2.73(1) [c]
La-O2	2.91(1) [d]	2.81(1) [d]
LCO bond [b]	**at 300 K**	**at 565 K**
La-O2	2.37(1) [d]	2.39(1) [d]
La-O2	2.54(1) [d]	2.55(1) [d]
La-O1	2.60(1) [c]	2.60(1) [c]
La-O1	2.70(1) [c]	2.71(1) [c]
La-O2	2.77(1) [c]	2.79(1) [c]
La-O2	3.01(1) [d]	2.97(1) [d]

Table 6.9: Atomic displacement parameters for LCO sample at 300 K and 565 K as obtained from fully converged HTT and LTO models (in units of $Å^2$).

atom	HTT	LTO
at 300 K		
La	0.0062(9)	0.006(1)
Cu	0.005(1)	0.006(2)
O1	0.010(2)	0.008(2)
O2	0.028(6)	0.011(6)
at 565 K		
La	0.012(3)	0.011(4)
Cu	0.007(3)	0.008(3)
O1	0.013(4)	0.010(5)
O2	0.027(9)	0.017(10)

the observed valences are greater than that. Both the Ba-site and the Sr-site are overbonded and in compression. These sites then tend to maintain as high symmetry as possible and, being too large for their environment, would tend to push out the neighboring atoms to minimize the compressive stress. This should be evident in the structural data. The short "apical" Ba/Sr-O2 bond, for example, is expected to elongate. Indeed, the evolution of the average La/Sr-O2 bondlength with doping at low temperature, as presented in Chapter 7, supports this. We note that in reality the doping is explicit, where some La crystallographic sites are fully occupied by the dopant ions, and others are fully occupied by La. In the modeling procedure used in our study such explicit doping is not assumed. Since the nominal valence of La is +3, while it is +2 for Sr and Ba dopants, the La crystallographic sites then have an effective valence that corresponds to the compositional average. For the samples investigated here (LCO, LBCO with x=0.15, and LSCO with x=0.125) the effective valences of the La sites are +3, +2.925 and +2.9375 respectively. From the results of the bond valence sum analysis presented above it is evident that while both Ba and Sr sites are under compression, the deviation of the observed valence from nominal is much greater for Ba ($\sim$+3.4) than for Sr ($\sim$+2.2). Therefore, the Ba-site in the LBCO system is way too overbonded, and the dopant-induced disorder in LBCO is much greater than in LSCO. It is then not surprising that the local tilts of almost full magnitude persist in the high temperature phase of the LBCO, while the tilts in the LSCO at high temperature remain nonzero but with smaller amplitude. To further support this we show several relevant parameters in Table 6.10. As evident, the mismatch between Ba and La is greater than the mismatch between Sr and La. Due to the opposite characters of the bonding of the sites containing La and the sites containing Ba or Sr, it is expected that competition between these two types of sites takes place, resulting in additional structural disorder.

Motivated by these observations, we propose two models for the dopant ion size-

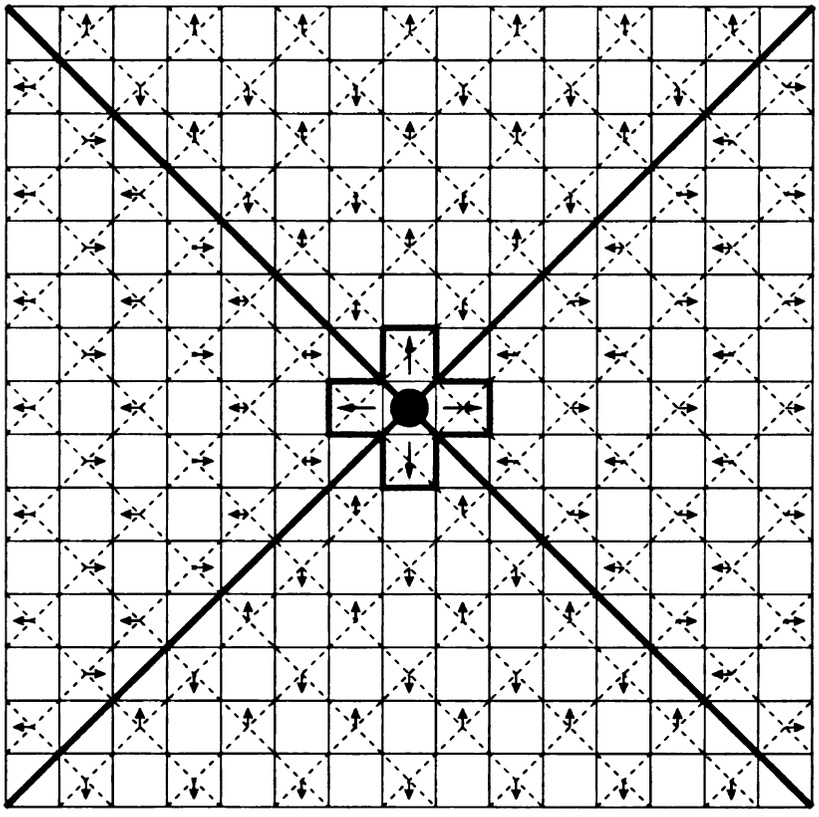

Figure 6.8: Schematic view of the LTO-tilt type size defect (see text). Tilt pattern in the CuO_2 plane is associated with presence of a single defect. Corner shared CuO_6 octahedra are denoted by squares with dashed crosses inside. The displacement of the apical oxygen above the plane due to octahedral tilting is shown with small arrows. In-plane O1 atoms sit at the corners of the octahedra and are displaced up or down by the tilts (not shown). Additonal defects can be placed, but it requires energy to flip the tilts in order to satisfy tilt-symmetry requirements for all the defects embedded.

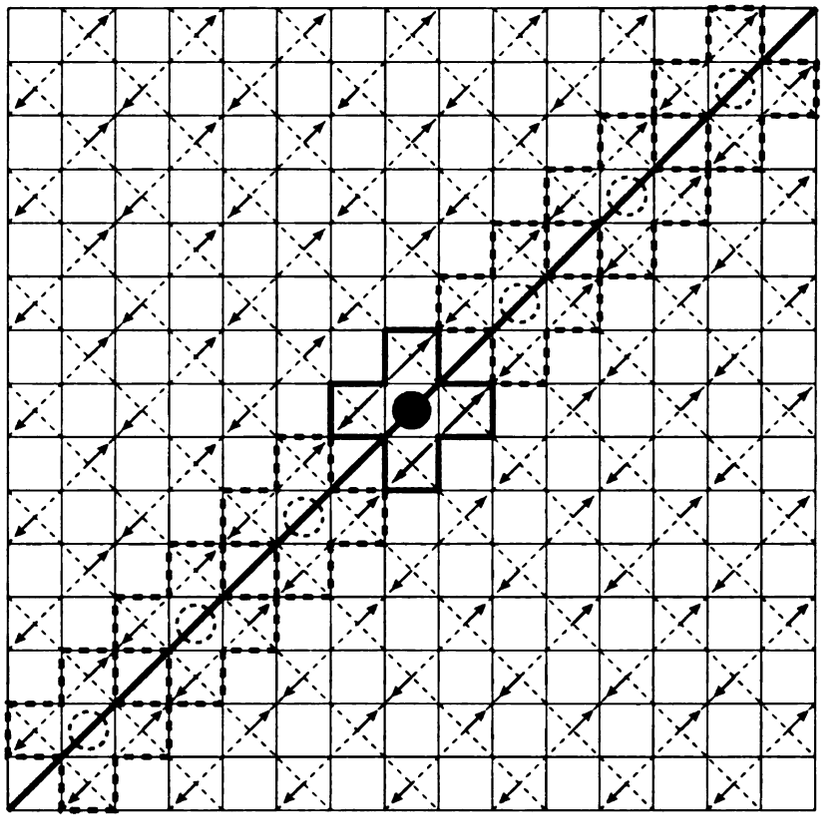

Figure 6.9: Schematic view of the LTT-tilt type size defect (see text). Tilt pattern in the CuO_2 plane is associated with presence of a single defect. Corner shared CuO_6 octahedra are denoted by squares with dashed crosses inside. The displacement of the apical oxygen above the plane due to octahedral tilting is shown with small arrows. In-plane O1 atoms sit at the corners of the octahedra and are displaced up or down by the tilts (not shown). Dashed circles and crosses indicate where additional defects can be placed without additional energy-cost (no tilt-flip is required).

Table 6.10: Several parameters relevant for the bond valence sum and size effect considerations. Covalent (CR) and ionic (IR) radii for several rare earth (RE) elements in 9-fold coordination, the values (after R. D. Shannon) of r_0 parameters for corresponding RE-O bonds, and their deviation from the r_0(La-O) parameter.

RE	CR (Å)	IR (Å)	r_0(RE-O) (Å)	Δr (Å)
Ba^{2+}	1.610	1.470	2.285	+0.113
La^{3+}	1.356	1.216	2.172	0
Sr^{2+}	1.450	1.310	2.118	-0.054

defects based on the tilt-topology considerations. Discussion is carried out with the Ba-dopant in mind. Both models are based on the observation that dopant ions reside on sites that are under compression. These sites, as discussed previously, could relax if the dopant ion remains in a high symmetry position and pushes out neighboring atoms elongating the bonds, yet maintaining the highest symmetry possible. Two distinct possibilities are explored. The first one is an LTO-type defect, shown in Figure 6.8: a single oversized dopant ion, presented as filled circle, forces neighboring CuO_6 octahedra to "tilt out" (as indicated by arrows). The defect is shown as a cross (solid line). This type of defect seeds four different LTO-like tilt domains (domain walls shown as thick solid lines), that exhibit a $\frac{\pi}{2}$ phase shift on crossing the domain-wall boundary. In the second case, Figure 6.9, we considered an LTT-type defect: a single dopant ion in this case forces neighboring CuO_6 octahedra to "tilt out" in an LTT-fashion, creating two LTT-tilt domains (the domain wall is again presented as a thick solid line) that satisfy antiphase domain-wall boundary conditions (π-phase shift across the boundary). This defect is also shown in Figure 6.9 as a solid-line cross with a single oversized dopant ion (solid circle). While the two topological defects are expected to have similar energy requirements for the first defect placed in the

structure, introduction of a second defect in the LTO-defect case is more costly (i.e. formation of the domain walls) than in the LTT case. In the LTO case the defect will again break up one of the LTO domains into four as did the first defect. However, introduction of additional defects in the LTT-defect case is straightforward: additional defects can be introduced, energy-free, if they are placed along the existing domain wall (stripe) created by the seed-defect (presented as dashed circles and crosses in Figure 6.9). In that sense, the LTT-type defect appears to be preferred over the LTO-type defect for further doping. Note that introduction of additional LTT-defects away from the stripe requires additional energy.

This simple reasoning demonstrates how the LTT-tilt pattern, observed in Ba-doped samples as well as in Nd-codoped LSCO samples, may develop on doping. The defects proposed above could be thought of in terms of doped charges as well. Hole doping causes shortening of the in-plane Cu-O bonds. If charges are localized, structural defects would be introduced such that the tilts are removed locally. When an untilted defect (due to hole doping) is placed into a background of LTO tilts, the CuO_2 plane breaks up into rotated domains of LTO order. If the background is made of LTT tilts, the untilted defect results in a line-defect, and further untilted defects can be accommodated without energy cost. There is thus a natural stripe formation tendency for doped holes in the LTT-tilted phase. Indications of the local LTT-tilt pattern were also observed in the doping-dependence study of the Sr-doped samples, as presented in Chapter 5. For higher doping levels dopant induced defects can be accommodated more easily if the tilt symmetry is LTT, rather than if it is LTO. For lower dopings LTO tilt symmetry could be maintained since defects presumably have limited effective range. However, in this scenario, for high enough doping the structure can no longer accommodate the LTO tilt pattern. It has been shown earlier [166] that the average LTO tilt pattern can also be obtained as a linear combination of locally LTT-like tilts, and the mechanism for switching between the

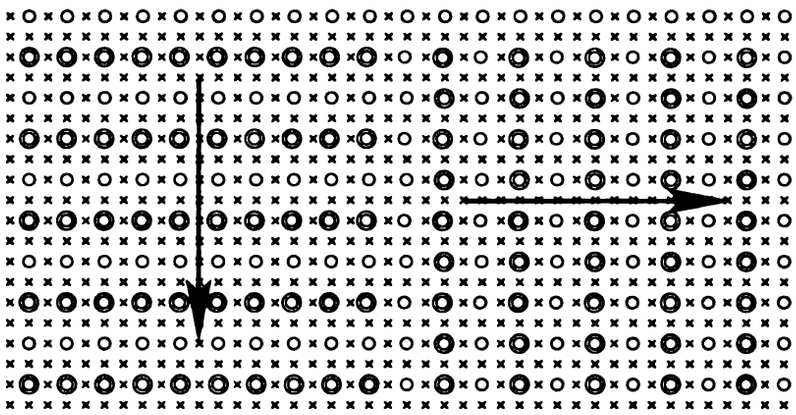

Figure 6.10: Tilt symmetry and the stripe breakup. Concentric circles represent doped sites, and crosses represent sites that are excluded from the strain relaxation. The arrows denote local LTT tilts within different domains resulting from the Cu-O bond shortening on doping.

average LTT and average LTO tilt patterns could then be related to the reorientation of microscopically LTT-like domains.

Finally, we consider the tilt symmetry and its relationship to the charge stripes in 214 systems. Long range ordered charge stripes observed in non-superconducting samples seem to prefer the LTT-symmetry tilts, as mentioned. In superconducting samples stripes, if present, may be dynamic or fluctuating. Stripe breakup in the Sr-doped system has been addressed in a recent study of structural compliance, misfit strain and stripe nanostructures in HTS cuprates [209]. In the presence of charge stripes short highly doped Cu-O bonds become subject to a tensile misfit strain, which is shown to lead to nanoscale microstructures. The stripe breakup scenario has been suggested that is reproduced in Figure 6.10. This structure consists of adjacent domains of stripes that have alternating directions rotated by 90°. It has been suggested that this microstructure is more isotropic and might be favored for minimizing strains between the grains and also minimizing the stripe misfit strain. The structural compliance parameter is defined as $\delta_s = (r_b - r_f)/r_b$, where r_b and

r_s are the Cu-O bondlengths in regions where the CuO_2 planes are buckled and flat respectively. The authors argue that the structural compliance is small in the case of Sr-doped LCO, possibly leading to stripe breakup. On the other hand, structural compliance is argued to be greater in the case of Nd co-doped Sr-doped and Ba-doped LCO, where long range ordered LTT tilts are observed at low temperatures.

We suggest possible tilt patterns in the presence of such broken charge stripes, Figure 6.10. Adopting the tilt symmetry discussed within the topological stripe models in Chapter 5, local octahedral tilts could be considered to have LTT symmetry. If the stripe breakup occurs as suggested in Reference [209], it is readily seen that adjacent domains would contain LTT-tilt patterns rotated by 90° with respect to each other, yielding an LTO-tilt pattern on average. Tilt patterns in the LSCO system could then locally have some LTT-character at low temperature, as suggested from our PDF results presented in Chapter 5. In the Nd co-doped LSCO system, as well as in LBCO, average tilts are LTT at low temperatures.

Chapter 7

Nominal doping and partition of doped holes between planar and apical orbitals in $La_{2-x}Sr_xCuO_4$

"It is a good viewpoint to see the world as a dream. When you have something like a nightmare, you will wake up and tell yourself that it was only a dream. It is said that the world we live in is not a bit different from this." (T. Yamamoto)

7.1 Prelude

By considering both the average structural parameters obtained from Rietveld refinement of neutron powder diffraction data, and the local structural parameters obtained from the atomic PDF, we have tested the recent hypothesis of Perry *et al.* [210] that doping in LSCO system occurs as localized defects of predominantly Cu$d_{3z^2-r^2}$–Op_z character associated with the Sr dopants accompanied by a local destruction of the Jahn-Teller distortion. While the structural parameters behave qualitatively according to the prediction of this model, a quantitative analysis indicates that doped holes

predominantly appear in the planar Cu$d_{x^2-y^2}$–O$p_{x,y}$ band as is normally assumed. However, a small amount of the doped charge does enter the Cu$d_{3z^2-r^2}$–Op_z orbitals and this should be taken into account when theoretical phase diagrams as a function of doping in the planar orbitals are compared to experiment. From the structural parameters we estimate this correction for all values of x using bond-valence methods.

7.2 Introduction

Cuprate high temperature superconductors are doped Mott insulators. The novel superconductivity appears at doping levels just beyond the insulator-metal (IM) transition. The insulating behavior of the undoped endmember is understood to be due to electron correlation effects in the half-filled planar Cu$d_{x^2-y^2}$–Op_α ($\alpha = x, y$) antibonding band. The phase diagram of the cuprates can be interpreted in terms of holes doped into this planar band. For example, in the system $La_{2-x}Sr_xCuO_4$ it is assumed that one hole enters this band per strontium atom. This paradigm for the doping has hardly been questioned and a multitude of papers exist implicitly assuming this behavior. The $La_{2-x}Sr_xCuO_4$ system is archetypal since it is a single layer system which can be straightforwardly doped over a wide range. The resulting phase diagram is thought to exhibit features that are universal to the cuprates.

However, as a result of recent *ab initio* electronic band structure calculations, Perry, Tahir-Kheli and Goddard (PTG) [210] have suggested a new model for the doping in the $La_{2-x}Sr_xCuO_4$ system. In this case the doped holes reside in localized states on the CuO_6 octahedra situated next to the dopant strontium ions. Furthermore, the doped charge resides principally in the Cu$d_{3z^2-r^2}$–Op_z orbitals (i.e., the out-of-plane bonds). The spatial extents of the two types of orbitals are shown in Figure 7.1. Coincidentally a structural distortion occurs such that the local Jahn-Teller (JT) distortion, that results in the long Cu-O apical bond, is destroyed (Figure 7.2).

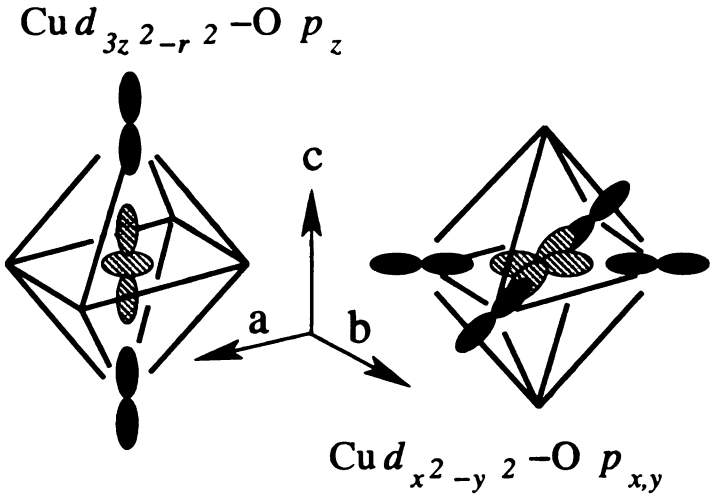

Figure 7.1: Schematic view of the spatial extents of the apical and planar orbitals in CuO_6 octahedra. Note that *a* and *b* crystal axes are rotated 45° about the *c* axis with respect to planar Cu-O distances.

A flat impurity band forms in the gap. The IM transition then occurs on increased doping in a manner similar to doped semiconductors by percolation of the doped impurities. These calculations were originally motivated by XAFS measurements that observed a distorted environment of the CuO_6 octahedra in the vicinity of dopant ions [195]. This new way of understanding the doping, if it is right, clearly will result in a paradigm shift in our understanding of cuprate physics. It is thus of the greatest importance to test the hypothesis experimentally.

A rather direct probe of this doping mechanism is the structure because it involves the local destruction of JT elongated bonds. This anti-Jahn-Teller (A-JT) defect is shown in Figure 7.2. The *average* Cu-O bond length along *z* will shorten with doping and the *width* of the bond-length distribution for this bond will increase reflecting the increased disorder. Despite detailed structural studies of this system [44] the temperature and doping dependence of these parameters has not been reported. In this chapter we investigate whether there is evidence supporting this new doping paradigm in both the average crystal structure, and the local structure as measured

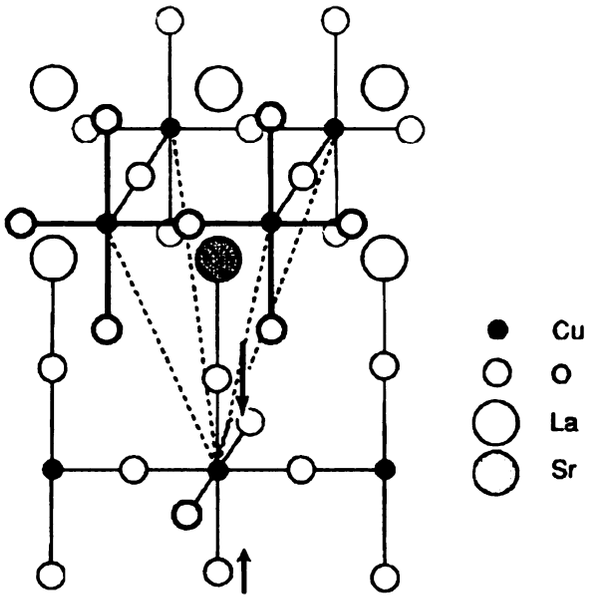

Figure 7.2: Crystal structure around Sr impurity within proposed anti-Jahn-Teller (A-JT) model (after Perry *et al.* [210]). Arrows indicate local destruction of the JT-elongated apical Cu-O bonds.

using the atomic PDF technique [157]. We reexamine the extensive earlier structural data of Radaelli *et al.* to extract the desired parameters. We have also analyzed new neutron powder diffraction data using Rietveld refinement and PDF refinement. We find that the data qualitatively agree with the predictions of Perry *et al.* [210]. However, a more quantitative analysis, including evaluating the bond valences as a function of doping of the in-plane and apical Cu-O bonds, indicates that doped charge is predominantly residing in the planar bonds suggesting the existing paradigm for doping is valid.

7.3 Approach

In this chapter we reexamine the extensive published data of Radaelli *et al.* [44] to extract as a function of doping the interesting parameters of the plane copper to apical oxygen bond length, r_{Cu-O2} and the short lanthanum/strontium to apical oxy-

gen bond length, $r_{La/Sr-O2}$. These parameters were determined from the reported fractional coordinates and lattice parameters. Also important is the doping dependence of the copper to in-plane oxygen bond length, r_{Cu-O1}, which was presented previously [44] but is reexamined here. To check the PTG prediction we also need the anisotropic displacement parameters along the z-axis of copper and the apical oxygen, U_{33}(Cu) and U_{33}(O2) respectively. These were not published in [44] so we have used recently collected neutron powder diffraction data of our own from a less extensive set of samples. Samples were synthesized using solid state methods, as described in Chapter 3, and loose powders of $\sim$ 10 g sealed in vanadium cylinders were measured at 10 K a the GEM diffractometer at the ISIS neutron source. Rietveld refinements were carried out on the data using the program GSAS [211]. The data were also corrected for experimental effects and normalized to obtain the atomic pair distribution function [157] using the program PDFgetN [163], as described in more detail in Chapter 2. Structural models were refined to the PDFs using the program PDFFIT [161]. To check for consistency, the same parameters were varied in the PDF and Rietveld refinements. An example of the measured PDF from the undoped sample is shown in Figure 7.3 with the best fit model-PDF plotted on top.

The PDF allows us to explore models that contain non-periodic defects such as those proposed by PTG, shown in Figure 7.2. The PDF was calculated from a supercell model including doping induced defects discussed by PTG. This was then used as simulated data and fit using the usual long-range orthorhombic (LTO) [44] structural model. In this way it was possible to estimate the size of enlarged displacement factors that would result from the presence of the doping induced disorder described by PTG. In Perry *et al.* [210], for simplicity, no octahedral tilts were considered. In the present case we must compare resulting models with real data and so the doping induced defects described in [210] were superimposed on the background of octahedral tilts observed in the undoped endmember.

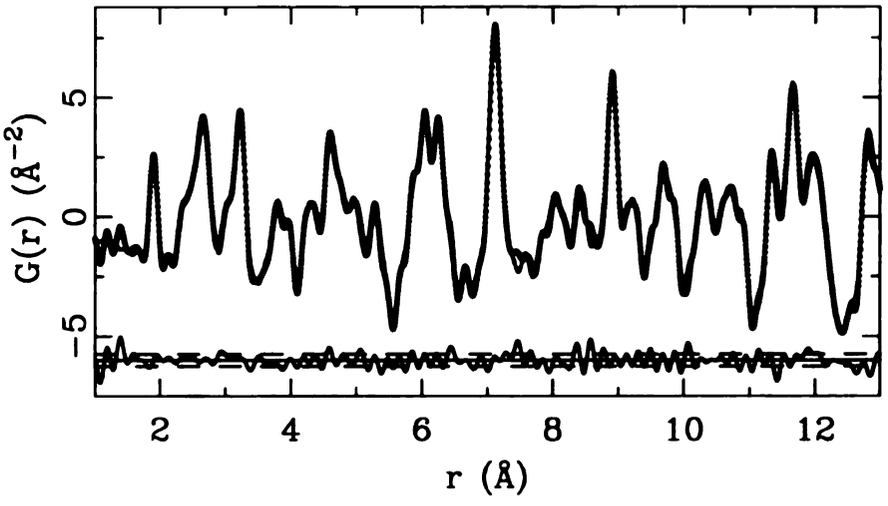

Figure 7.3: Representative full profile PDF fit of standard LTO model to 10 K data for undoped sample. Experimental profile shown as open circles, model profile as solid line. Difference curve is shown below the fit as solid line. Dashed lines denote experimental uncertainties at the 2σ level. PDFs studied in this chapter utilize diffraction information up to $Q_{MAX} = 35$ Å $^{-1}$.

7.4 Results and Discussion

The qualitative predictions for the evolution of the average structure with doping in the scenario of Perry *et al.* [210] are: (1) decrease in the average r_{Cu-O2} due to the local destruction of Jahn-Teller distortions at Cu^{3+} sites; (2) increase in the U_{33}(Cu)+U_{33}(O2) with doping because of the coexistence of Jahn-Teller distorted and non-Jahn-Teller distorted octahedra; (3) increase in the average $r_{La/Sr-O2}$ distance. All these effects are seen qualitatively in the data as shown in Figures 7.4 and 7.5. However, similar effects can be expected even if the doping is taking place in the conventional way: homogeneously into the planar bonds. For example, if the CuO_2 planes are becoming more positively charged with doping the negatively charged apical oxygen would be predicted to come closer to the planes due to simple coulomb attraction. Also, the U_{33} displacement factor of the apical oxygen atom is expected

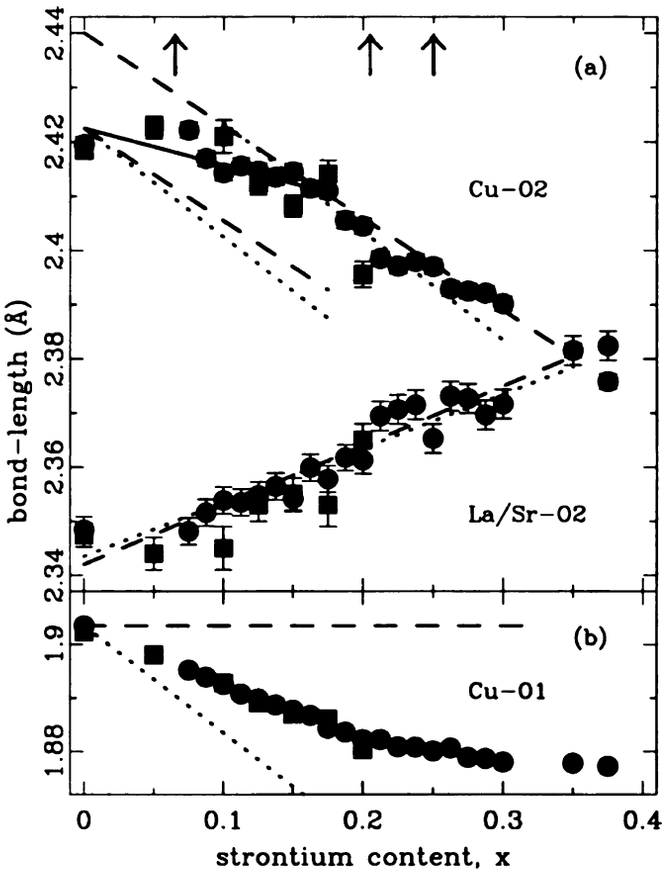

Figure 7.4: Evolution of r_{Cu-O2} and $r_{La/Sr-O2}$ (a), and r_{Cu-O1} (b) average bond lengths with hole doping at 10 K: Rietveld result from [44] (solid circles) and PDF result (solid squares). Dotted lines: slope predicted from simple electrostatics considerations. Dashed lines: slope prediction based on PTG model. Arrows (from left to right): IM transition, structural phase transition, and disappearance of superconductivity.

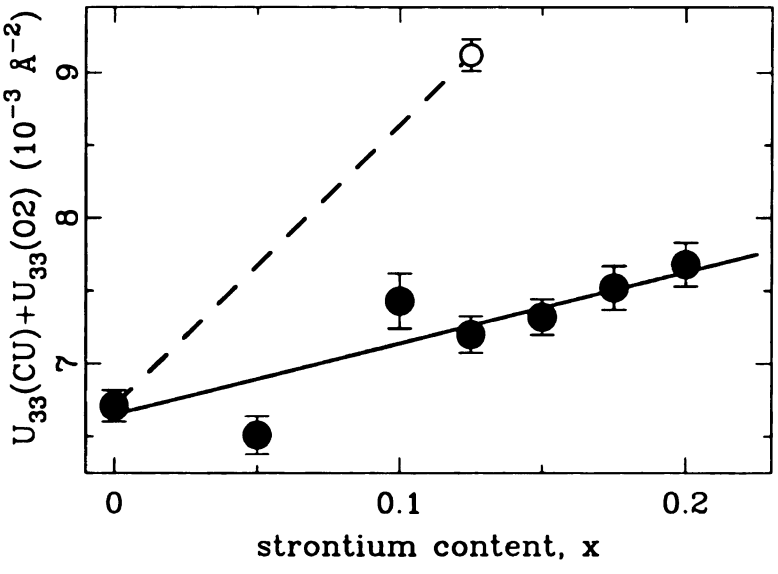

Figure 7.5: Sum of displacement parameters U_{33} for Cu and $O2$ as a function of strontium content at 10 K, from PDF refinements. Solid line is a guide to the eye. Dashed line denotes expected increase in the PDF displacement parameters, estimated from PDF simulation based on PTG model for 1/8 doping (see text).

to increase with doping due to the random doping of larger Sr^{2+} ions. It is therefore important to be more quantitative to distinguish these different possibilities.

The PTG calculations [210] were carried out at special rational doping fractions of 1/8, 1/4 and 1/2 and suggest the appearance of a single distorted CuO_6 octahedron associated with each doped strontium (Figure 7.2). The r_{Cu-O2} bond closest to the strontium is shortened by $\Delta r_{Cu-O2}= -0.24$ Å and that farthest from the Sr on the same octahedron by $\Delta r_{Cu-O2}= -0.10$ Å, the Sr-O2 distance increases by $\Delta r_{La/Sr-O2}= +0.11$ Å , and the in-plane r_{Cu-O1} distances do not change. In the average structure these defects are not seen explicitly; however, the distortions will be apparent as a properly weighted change in the average bond-length and an increase in the respective displacement parameters. If we assume that these defects appear as each strontium is doped and are not a special feature of the rational doping fractions studied, we get the following relations for the strontium doping, x, dependence of the

average bond lengths:

$$\Delta r_{Cu-O2}(x) = -0.17\ x, \quad \Delta r_{La/Sr-O2}(x) = 0.11\ x, \tag{7.1}$$

where x is the doping level. These are shown as the dashed lines in Figure 7.4. The evolution of $r_{La/Sr-O2}$ is in quantitative agreement. The case of r_{Cu-O2} is more complicated. r_{Cu-O2} decreases much more slowly than the prediction initially on doping. However, beyond a doping level of ~ 0.17 the slope of r_{Cu-O2} vs x increases. In this higher doping region the slope of the PTG line agrees rather well with the data. There is no specific prediction from the PTG calculations for the x-dependence of r_{Cu-O1}, although it is expected to be small since the length of r_{Cu-O1} in the defect octahedra does not change and no doping dependent change in lattice parameters has been assumed in their calculations. This reflects the fact that, in the PTG picture the doped charge is almost exclusively located in the apical Cu$d_{3z^2-r^2}$–Op_z orbitals. Therefore, we have drawn a flat dashed line as the PTG prediction for this parameter in Fig. 7.4(b). As is apparent, the data for r_{Cu-O1} slope downward with a slope of $\Delta r_{Cu-O1}/\Delta x \sim -0.105$. This is comparable to, though slightly less than, the observed $\Delta r_{Cu-O2}/\Delta x \sim -0.18$ of the apical bond. This observation will be important later.

The presence of the anti-Jahn-Teller distorted doped CuO_6 octahedra in the PTG calculations will manifest itself in an increased atomic displacement factors for Cu and O2. We concentrate on the c-axis variation of these parameters, U_{33}(Cu)+U_{33}(O2), which should be rather sensitive to the existence of short r_{Cu-O2} distances in the structure. Octahedral tilts, and therefore O2 displacement parameters perpendicular to the Cu-O2 bond, will also be affected but in a less predictable way. Indeed, as is evident in Figure 7.5, U_{33}(Cu)+U_{33}(O2) does increase with increasing doping at constant temperature, a sign that static disorder associated with this bond is increasing with doping. To investigate more quantitatively whether this increase is consistent with the PTG predictions we calculated the PDF of a model structure containing the PTG defects. This simulated PDF was then fit using PDFFIT using

the standard LTO model. This gives us a measure of how much U_{33}(Cu)+U_{33}(O2) would increase in a standard LTO-structure refinement due to the presence of the PTG defects. The PDF was simulated for the $x = 0.125$ composition using an 8x unit cell in the following way. The reference structure used was that of the undoped material with atomic positions taken from [44] and displacement factors taken from our PDF result for the undoped sample. One La in the supercell was then replaced with Sr and the atoms on the CuO_6 octahedron adjacent to the Sr were displaced by the Δ-values from the PTG prediction given above. The displacement parameters in the model retained their values in the $x = 0$ compound. This neglects strain due to the defects that would tend to increase displacement parameters further. The resulting PDFs were refined with the standard LTO unit cell. This resulted in an enlarged value of U_{33}(Cu)+U_{33}(O2)= 9.05×10^{-3} Å^{-2}, plotted on Figure 7.5. This overestimates the observed displacement factors.

Next, using PDF data of 1/8 doped $La_{2-x}Sr_xCuO_4$ at 10 K, *explicit modeling* of the anti-JT (A-JT) model was performed. The outcome is compared to the results of the modeling of the standard LTO model. The modeling employed the program PDFFIT [161]. A large supercell model was generated that incorporates explicit Sr doping, and allows for defining special doping-affected octahedral units, as described above in accord with Ref. [210]. Three distinct variants of the explicit A-JT models were attempted. These variants are distinguished as follows: (1) A model with symmetric A-JT distortion on affected octahedral unit (apical Cu-O distances restricted to have the same length). (2) A model with asymmetric A-JT distortion (relevant apical distances are allowed to vary independently), and (3) A model with asymmetric A-JT distortion this time restricted to have displacements along LTO c-axis only. In all three variants atomic parameters of Sr were decoupled from those of La, except for the displacement factors that were restricted to be the same. In the variant (3) Sr y-coordinate was set to zero and Sr motion was restricted to be along c-axis only.

Table 7.1: Standard LTO model versus A-JT defect models: PDFFIT modeling results summarizing relevant distances. All lengths are in Å. Rw is the weighted PDFFIT agreement factor.

	LTO	A-JT(1)	A-JT(2)	A-JT(3)
Rw	0.127	0.122	0.131	0.127
r(Cu-O2)	2.4179(24)	2.4095(25)	2.4119(22)	2.406(3)
	-	2.460(19)	2.450(20)	2.49(4)
	-	-	2.469(19)	2.51(3)
r(La-O2)	2.346(3)	2.354(3)	2.354(3)	2.361(4)
	-	2.305(20)	2.305(20)	2.27(4)
r(Sr-O2)	2.346(3)	2.27(3)	2.27(3)	2.20(5)

The A-JT models were refined from the same set of initial values as that used for modeling the standard LTO structure. This equality of the starting values was only violated for O2 and Sr fractional y-coordinates in the variant (3), where these were set to zero and fixed.

The results are summarized in Table 7.1, where the weighted PDFFIT agreement factors (Rw) [161] are reported, as well as all relevant distances. Although for all the variants of the A-JT model agreement factor is similar to the one for the LTO model, and for some variants even somewhat more favorable, it is not sufficient to unambiguously favor the distorted model over the standard LTO structure. Moreover, the distortions obtained from such explicit modeling yield relevant distance changes in the direction *opposite* of that originally proposed within the A-JT model of Perry *et al.* [210] (i.e., the Cu-O2 distance of the affected octahedral unit lengthens, while r_{Sr-O2} shortens). However, inspection of the distances for the A-JT model results in the proper weighted average values when compared to corresponding average distances

obtained by employment of the standard LTO model.

We now consider the expected structural changes that would occur based on electrostatic considerations in the conventional doping model. First, we note that the charge of the CuO_2 plane is becoming less negative with doping which could result in the apical O^{2-} moving closer to the plane. A very rough estimate of this behavior is possible neglecting the Jahn-Teller effect and assuming an ionic picture by considering ionic radii $r(O^{2-}) = 1.35$ Å, $r(Cu^{2+}) = 0.73$ Å, $r(Cu^{3+}) = 0.54$ Å, $r(La^{3+}) = 1.16$ Å, and $r(Sr^{2+}) = 1.26$ Å [212]. From this we get $\Delta r_{Cu-O2}= -0.19\ x$ and $\Delta r_{La/Sr-O2}= 0.1\ x$ which appear in Fig. 7.4 as dotted lines. Not surprisingly, these lines are similar to those predicted by PTG that is also a model involving a mixture of Cu^{2+} and Cu^{3+} sites. Uniform doping of charge into the Cu-O planes would not result in an increase in U_{33}(Cu)+U_{33}(O2) on its own; however, the presence of misfitting Sr^{2+} dopant ions would. The fact that the observed increase in U_{33}(Cu)+U_{33}(O2) exists but is smaller than needed to explain the PTG defects may argue in favor of this interpretation.

A more refined empirical framework for studying the distribution of charge between bonds is the bond valence model [164]. In this theory there is a direct relationship established between bond-length, r, and the amount of charge in a bond (the bond-valence, s). The bond valence is defined as

$$s(r) = \exp \frac{(r_0 - r)}{B}, \tag{7.2}$$

where $B = 0.37$ Å is a universal constant and r_0 depends on the chemical identity of the ions in question. Using this approach, within the approximations of the model, it is possible to determine how much of the doped charge is going into the planar vs. the apical bonds from a measurement of their length changes. The theory is successful in unstrained compounds and has recently been applied to mixed valent crystals and crystals containing Jahn-Teller distortions [213]. The nominal valence, V_i, of an ion is then determined by summing the bond-valences over all the bonds

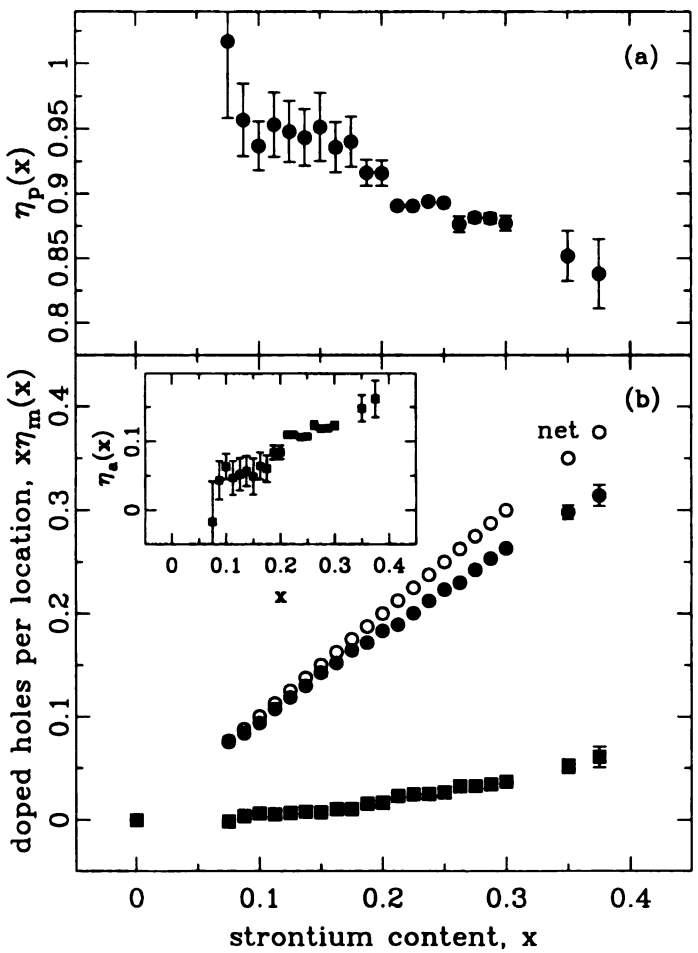

Figure 7.6: (a) Partitioning parameter vs. Sr content. (b) Estimated average distribution of doped charge at 10 K based on bond valence calculations using Rietveld obtained distances: net apical share (solid squares), net planar share (solid circles), total doped charge (open circles). Inset: a measure of the amount of charge doped into the apical orbitals.

in which it participates, $V_i = \sum_j s_{ij}$. In the case of mixed valent crystals some ambiguity exists as to exactly what value to use for r_0. The qualitative results of our analysis, however, do not depend on what value of r_0 is used. The results are shown in Figure 7.6. Here we plot how the total doped charge (assumed to be given by x) distributes itself between the apical and planar orbitals respectively, as determined from the bond-valence sums. The dimensionless variables, η_p (solid circles) and η_a (solid squares) parameterize this partition where $\eta_p + \eta_a = 1$.

Details of these calculations are as follows. First we determine the change in bond-valence of a particular bond due to doping, $\delta s_i(x) = s_i(x) - s_i(0)$. We are interested in the partition of charge between the planar and apical orbitals, therefore we define an orbital-valence $\delta S_m = \sum_i \delta s_i$ where the sum is over the planar bonds for the Cu$d_{x^2-y^2}$–O$p_{x,y}$ orbital, δS_p, and over the apical bonds for the Cu$d_{3z^2-r^2}$–Op_z orbital, δS_a. This is then expressed in dimensionless parameters by dividing by the total *excess* valence of copper determined by the sum over all the orbital-valences, $\eta_m(x) = \delta S_m(x)/V_{Cu}^{ex}$. What is plotted in Figure 7.6 is $x\eta_p$ (solid circles) and $x\eta_a$ (solid squares), that are measures of the amount of charge doped into the planar and apical orbitals, respectively.

As is apparent in Figure 7.4, *both* the apical and in-plane bonds shorten with doping indicating a reduction in charge and doped holes going into both planar and apical bonds. However, one of the key aspects of this theory is the non-linear form of the bond valence, $s(r)$. The exponential form results in a steep slope of $s(r)$ at short bond-length and a shallow slope at long bond-lengths. As a result, the same amount of charge doped into a long-bond shortens it much more than it would a short-bond, and vice versa. At $x = 0$ $r_{Cu-O1} < r_{Cu-O2}$ reflecting the fact that initially the holes that make Cu in the +2-state reside predominantly in the planar orbitals making these the canonical half-filled anti-bonding bands, with the apical bonds being doubly occupied with electrons (i.e., full, no holes). The physics of this is the existence of the Jahn-

Teller distortion; however, this shows that the phenomenological bond-valence model is making the correct prediction for the charge segregation initially. Subsequently, the experimental observation is that *both the planar and the apical bonds shorten at about the same rate* but because the planar bonds are initially shorter, and the fact that there are four of them rather than two, mean that the experimental observations demand that the doped charge is going predominantly into the planar orbitals as is evident in Figure 7.6.

The main result of this analysis is that the simple picture of localized Cu$d_{3z^2-r^2}$–Op_z doped holes associated with Sr sites described by the PTG calculations is not supported by the structural data. To a rather good approximation doped charge is going into the planar Cu$d_{x^2-y^2}$–O$p_{x,y}$ orbitals. This does not rule out localized doped defects if they have sufficient planar character. Such defects have been stabilized in the unrestricted Becke-3-Lee-Yang-Parr density functional calculations [210]. However, the observation that r_{Cu-O2} is getting shorter also requires that some doped charge is appearing in the apical Cu$d_{3z^2-r^2}$–Op_z orbital and a correction should be made to the canonical $p = x$ relationship to account for this, where p is the doped charge in the planar orbitals. The partitioning parameter η_p gives the correction. The number of doped holes in the planar bonds, p, is therefore given by $p = x\eta_p$ (η_p shown in Figure 7.6(a)). This augments spectroscopic measurements that show the partition of charge between copper and oxygen but struggle to differentiate partition between planar and apical bonds [214, 215]. In Figure 7.6(a) we show η_p on an expanded scale. This can be used as a calibration curve for determining the amount of charge in the planar orbitals, p, as a function of Sr doping, x, by multiplying the value of $\eta_p(x)$ by x. Thus, at a strontium content of $x = 0.125$ the doping in the planar orbitals is actually $p = 0.125 \cdot 0.94 = 0.1175$, and conversely, the rational 1/8 filling occurs at $x = 0.134$. Note that, at all dopings, greater than 85% of doped charge goes into the planar orbitals, though increasingly it appears in the apical bonds as doping

increases. Apparent from Figure 7.6 is that as x increases above optimal doping there is a distinct decrease in slope of $x\eta_p(x)$ suggesting that at higher dopings more charge is going into the Cu$d_{3z^2-r^2}$–Op_z orbitals, though over the entire range it is still predominantly going into the planar orbitals. We note that in the higher doped region the octahedral tilting, and therefore mixing of the planar and apical orbital character, is less than in the low-doped region so this cannot explain this behavior.

7.5 Summary

In conclusion of this chapter, we have tested the hypothesis that doping in $La_{2-x}Sr_xCuO_4$ is occurring predominantly in Cu$d_{3z^2-r^2}$–Op_z orbitals [210], rather than the canonical picture of doping into the planar Cu$d_{x^2-y^2}$–O$p_{x,y}$ bands, by studying the evolution of the average and the local structures of $La_{2-x}Sr_xCuO_4$ with doping x. Whilst the average structure evolves *qualitatively* as would be predicted according to Cu$d_{3z^2-r^2}$–Op_z doping picture, more quantitative analysis suggests that the canonical picture of one hole doped into the planar bands per strontium is actually rather close to the true situation. However, a small proportion of the doped charge seems to be going into Cu$d_{3z^2-r^2}$–Op_z orbitals, evidenced by the strong shortening of the r_{Cu-O2} bond with doping and this proportion increases with increasing doping. We present a correction factor quantifying the partition of doped charge between planar and apical bonds.

Chapter 8

Concluding remarks

"In the words of the ancients, one should make his decisions within the space of seven breaths. It is a matter of being determined and having the spirit to break right through to the other side." (T. Yamamoto)

8.1 Summary

A local structural study has been carried out to investigate the nature of the doped-charge distribution within the CuO_2 planes of a series of Sr-doped and Ba-doped La_2CuO_4 samples as a function of doping and temperature. The presence of inhomogeneous doped charge distribution and their striped morphology in these systems could have profound implications on their properties, including the HTS phenomenon. Establishing the nature of the microscopic charge distribution is therefore of great importance. The structural information was obtained from the atomic PDF analysis of neutron powder diffraction data. Evidence was found that supports the presence of temperature dependent atomic scale structural inhomogeneities at low temperature in the underdoped and optimally doped regions of the $La_{2-x}(Sr,Ba)_xCuO_4$ phase diagram, consistent with the presence of an inhomogeneous charge distribution in the CuO_2 planes. The inhomogeneities disappear on crossing into the overdoped re-

gion at low temperature, and also disappear at a temperature which correlates with spin and charge freezing inferred from transport [121], NQR [134], and XANES [135] measurements. The orbital character of doped holes in the LSCO system has been reexamined from the structural perspective using average crystallographic data [44] and less extensive PDF data. The results do support the planar-doping picture in the underdoped and optimally doped regime, but indicate that a small amount of doped charge may have apical character above the optimal doping.

8.2 PDF evidence for inhomogeneous charge distribution

8.2.1 Bondlength disorder

Local structural inhomogeneities in LSCO and LBCO manifest themselves in the PDF as a distribution of the nearest neighbor in-plane Cu-O distances at low temperature. The distribution becomes homogeneous on crossing into the overdoped region, as well as at elevated temperature, as we discussed in detail in Chapter 4. This effect was first observed in the PDFs of $La_{2-x}Sr_xCuO_4$ ($0 \leq x \leq 0.3$) at 10 K. The distribution of the in-plane Cu-O distances appears on doping in the underdoped region, persists up to optimal doping, and abruptly disappears upon further doping. The PDF studies of the temperature dependence in $La_{2-x}Sr_xCuO_4$ ($x = 0.125, 0.150$) and in $La_{1.85}Ba_{0.15}CuO_4$ confirmed the presence of the structural distortion in these samples at low temperature. The inhomogeneous distribution of the nearest neighbor distances has an onset temperature, which was estimated in Chapter 4 from the PDF study.

8.2.2 Nature of the distortion

The observed inhomogeneous distribution of planar Cu-O distances in the local structure is possibly of a bimodal character. While in the undoped endmember all 4 planar Cu-O distances within the CuO_6 octahedron are equal, in the underdoped regime at low temperature short and long planar distances appear and coexist. This PDF observation is consistent with the inhomogeneous doping scenario. According to this, doped holes at low temperature in underdoped and optimally doped regimes are inhomogeneously distributed, such that there is a coexistence of heavily doped and undoped regions. In the heavily doped regions the planar Cu-O bonds are contracted [44], while in the undoped regions the planar bonds are unaltered. The coexistence of a distribution of planar distances broadens the corresponding PDF peak width, as presented in Chapter 4. The dispersion of the planar distances estimated from the PDF study is about 0.025 Å. The onset temperature for the structural inhomogeneities is estimated to be in the vicinity of 100-120 K, as presented in Chapter 4.

8.2.3 Octahedral tilt disorder

Additional PDF evidence supporting the inhomogeneous charge distribution comes from the observation of significant CuO_6 tilt disorder, as we presented in detail in Chapters 4 and 5. In the charge-rich regions the octahedral tilting amplitude is reduced, while in the charge-poor regions the tilting amplitude is unaltered. The PDF results are in agreement with this scenario. Furthermore, evidence of directional tilt-disorder emerged from the PDF study, suggesting the presence of the LTT-type tilts in the local structure of the underdoped LSCO samples.

8.2.4 Implications for charge-stripes

While the PDF cannot directly determine whether observed inhomogeneous charge distribution is striped or not, our results are not inconsistent with the presence of short-range stripe order. The local structure of the LSCO for intermediate doping and at low temperature is well explained as a two-component mixture of undoped and doped material. The structure is seen as a mixture of heavily doped and undoped regions, with heavily tilted and untilted CuO_6 octahedra coexisting. Octahedral tilt directions are locally altered in this view, and include a component of LTT-type tilts. This description of the local structure, however, holds only up to ~8Å, a distance that could be related to the stripe separation. At higher atomic spacings the mixture model breaks up, suggesting a domain-like local structure. The possibility that the symmetry of the local octahedral tilts contains a significant LTT-character is in favor of the striped charge distribution.

8.3 LTO to HTT structural phase transition

Detailed PDF analysis was performed on neutron powder diffraction data for LBCO, LSCO, and LCO samples at various temperatures covering wide temperature ranges of interest through the LTO-HTT structural phase transition, as presented in Chapter 6.

The *local* structure of these systems is found to be different than the *average* structure obtained from crystallography. The amplitude of *local* octahedral tilts of CuO_6 does not disappear in the HTT phase of these materials. In the LCO and LBCO samples local tilts of almost full amplitude were observed in the HTT phase. In the LSCO sample local tilts follow the average behavior, although small residual tilts were evidenced in the HTT phase, in agreement with the results presented in Chapter 5. Reconciliation of the structure on different lengthscales could be achieved for the LCO and LBCO systems if the transition is viewed as "order-disorder" rather

than "displacive" in nature. In contrast, the structural phase transition in the LSCO system appears to have a significant "displacive" component as well. The "order-disorder" model variants account for the enlarged atomic displacement factors in directions perpendicular to the average LTO directions seen by "displacive" models.

The microscopic origin of the octahedral tilts and their local symmetry were addressed in Chapter 6 using the bond valence sum analysis. The tilting seems to be driven by the La-O2 "planar" bonds, while the short "apical" La-O2 bond could possibly be relevant for the symmetry of the tilt patterns of adjacent layers of the CuO_6 octahedra. The La-sites experience tensile stress, while Sr and Ba dopant sites experience compressive stress, and competition between these two different bonding conditions is expected to cause an additional disorder, in particular in the Ba-doped system. However, details of this issue remain unresolved, and models including explicit doping should be considered to draw more elaborate conclusions. Inspired by the experimental observations, two topological models for the substitutional defects were proposed. In this view, the LTT-symmetry of the octahedral tilts is compatible with the stripe-formation tendency.

8.4 Comparison with other probes

The structural inhomogeneities observed in the PDFs of the underdoped samples of the 214 family are naturally explained by the appearance of charge inhomogeneities at low temperature in these samples. Here we compare the PDF results to those of the other local probes.

8.4.1 NMR/NQR results

The nuclear magnetic resonance (NMR) and the nuclear quadrupole resonance (NQR) techniques use the magnetic moments of the nuclei to probe the local environment

of particular atomic species. The experiments involve radio-frequency (RF) radiation that excites the nuclear spins of particular nuclei in the sample, and the sample response is observed. NMR involves an additional external magnetic field, while the NQR is zero-field NMR technique. The NQR measurements detect the interaction of a nuclear quadrupole moment with the electric field gradient produced by the charge distribution in the sample. The quadrupole moments arise due to the non-spherical nuclear charge distribution. Resonance occurs when transition from one spin state to another is excited by the RF oscillations.

Results of early NQR spectroscopic studies on $La_2CuO_{4+\delta}$ [145] indicated that two distinct copper sites coexist within the CuO_2 planes of this material. This was observed by comparing the ^{63}Cu NQR spectra of doped and undoped material, that revealed an additional Cu site from the frequency shift with respect to the Cu response obtained from the undoped La_2CuO_4. The possibility of local structural distortions was considered, but there was no evidence from the structural studies at that time. Further detailed studies [216] of ^{63}Cu NQR spectra of both $La_2CuO_{4+\delta}$ and $La_{2-x}Sr_xCuO_4$ systems suggested that the inhomogeneities are present irrespective of the detailed nature of doping, and the NQR response is the same both when the 214 system is doped by substituting Sr for La and by excess interstitial O. It was concluded that the doped holes are localized in the CuO_2 planes [107]. More recent studies [134, 217] found that the intensity is lost from the ^{63}Cu NQR resonance at temperature coinciding with the charge-order temperature, T_{co}, obtained from diffraction studies. The intensity of the resonance was proposed to be an order parameter for the charge ordering. Since NQR is a local probe, the ^{63}Cu NQR provides information on the local charge order.

8.4.2 XANES results

The XANES, as described in Chapter 2, is a local probe sensitive to changes in the local structure within a cluster of atoms around the photoabsorbing atom. It investigates peak-like features in the spectrum near the absorbtion edge of a given atom. The XANES studies of the underdoped and optimally doped LSCO and LBCO samples [135], found that the peak-intensity ratio involving the peaks corresponding to planar oxygen and La/Sr atoms, exhibits an anomalous increase at characteristic low temperature, which correlates well with T_{co} from neutron diffraction and NQR studies. Furthermore, in XANES experiments on these systems an unusual isotope effect was observed. By replacing ^{16}O with ^{18}O, the characteristic temperature where the intensity increase sets in moves towards much higher temperature. The observed strong isotope effect indicates the importance of the lattice in the stripe formation. [135]

The PDF results are in line with the early NMR/NQR observations of the inhomogeneous doped charge distribution. Also, the temperature scales where the observed PDF structural effects, the NQR intensity-loss, and the XANES peak-intensity ratio sets in correlate rather well.

8.4.3 EXAFS results

The Cu K-edge EXAFS studies of the local structure of 1/8-doped LBCO [218] and optimally doped LSCO [219] samples as a function of temperature found an anomalous increase in the correlated Debye-Waller factor of the in-plane Cu-O pairs, suggesting structural fluctuations in the CuO_2 planes. Further EXAFS studies on optimally doped LSCO samples suggested the formation of a minority phase at low temperature containing two distinct in-plane Cu-O distances [112, 220], the bondlength difference being approximately 0.08 Å. In addition, in the minority phase 0.1 Å shorter apical Cu-O distances were observed, and a local CuO_6 tilt angle of 16(2)° [220]. It was

proposed that the tilts in the minority phase have the LTT-symmetry. This was further interpreted in terms of structural stripes, with the minority phase stripe being approximately 8 Å wide. The temperature at which the minority phase sets in was estimated to be in the range of 100 K [220, 112]. In the same spectra the XANES signal was investigated, observing features similar to those described in the previous section [112]. Similar features were observed from the EXAFS spectra of the multilayer $Bi_2Sr_2CaCu_2O_{8+y}$ [221]. The PDF results are in qualitative agreement with the EXAFS experimental data described above, although there is a disagreement on the interpretation of the data, such as the existance of a very long in-plane Cu-O bond and the enormous local tilts in the minority phase suggested by these experiments. The character of the apical Cu-O bond was not addressed in our PDF study.

In other EXAFS experiments on the LSCO samples, the local structure was studied across the LTO-HTT phase line [194]. The results suggested that the local octahedral tilts persist in the HTT phase. The structural phase transition was proposed to be of mixed "order-disorder" and "displacive" nature if the phase line is crossed along the doping axis, while it was suggested that the transition is purely of "order-disorder" character if the phase line is crossed along the temperature axis. A polarized EXAFS study of 1/8 and optimally doped LBCO samples at 10 K revealed a significant degree of structural disorder caused by the Ba dopant. A distribution of the LTT tilt angles was proposed [179]. The PDF results are consistent with the presence of a small fraction of tilted CuO_6 octahedra within the HTT phase. However, our study suggests that the character of the transition is the same on crossing the phase line along the doping and the temperature axes. Furthermore, recent polarized EXAFS study on Nd co-doped LSCO samples [222], with a Nd concentration of 0.4 and two Sr concentrations of 0.12 and 0.16, observed CuO_6 local directional tilt disorder in the underdoped sample, while in the slightly overdoped sample such disorder was not observed. No changes in tilting were observed on crossing the structural phase tran-

sition line, suggesting "order-disorder" character and the orientational tilt disorder in the higher symmetry structural phases. The PDF results presented in this thesis are in qualitative agreement with this.

8.5 Anomalous behavior of the CuO_6 volume

Volume of the CuO_6 octahedron is defined as a mixed product of the oxygen atomic vectors as

$$V(CuO_6) = \frac{4}{3}(\vec{r}_{P1} \times \vec{r}_{P2}) \cdot \vec{r}_A, \tag{8.1}$$

where the labels P1 and P2 refer to two planar O atoms which do not belong to the same diagonal of the basal CuO_2 plane of the octahedron, and A refers to the apical O of the same octahedron. This definition does not assume a rigid octahedron, and is universal irrespective of the structural phase, giving a geometric perspective of this structural building block. We have used extensive crystallographic data of Radaelli *et al.* [44] on the LSCO system over a wide doping range and at 10 K, 70 K and 300 K temperature, to extract the octahedral volume parameter defined as above. Atomic coordinates have been used to calculate the volume, and not the atomic distances, making this calculation exact rather than approximative. Since the structural parameters used are describing the average crystallographic structure of the LSCO system, the octahedral volume parameter reflects the average behavior.

8.5.1 Observations

In Figures 8.1, 8.2, and 8.3 we show the doping dependence of the CuO_6 volume at various temperatures. Note that the position of the x-axis zero is shifted for clarity in these figures, as indicated by the vertical solid lines. Figure 8.1 shows the volume at 300 K temperature. Vertical dashed line indicates the LTO-HTT structural phase transition at this temperature. Sloped lines are guides to the eye and indicate the

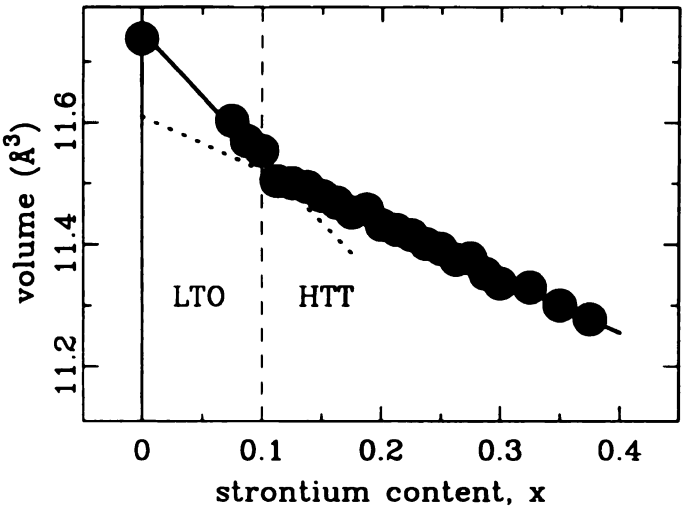

Figure 8.1: CuO_6 octahedral volume at 300 K as a function of doping. The vertical dashed line denotes the LTO-HTT phase transition. Solid and dashed sloping lines are guides to the eye. Note the position of zero on the doping axis.

trends of the data and deviations from such trends in different doping regions. The volume has a decreasing trend as the doping progresses. The break in slope at $x = 0.1$ appears to be the volume response to the LTO-HTT phase transition. In Figure 8.2 the octahedral volume data are shown for 10 K temperature. The decrease in the volume parameter on doping is again evident. The response to the structural phase transition, which at 10 K happens near $x = 0.2$ doping, is evident. However, an anomalous behavior is observed between 0.1 and 0.2 doping, and there appears to be a kink right around optimal doping, as indicated by the arrow. In Figure 8.3 we compare the octahedral volumes at all three temperatures for which the data are available [44]. Crosses indicate 300 K data, solid symbols indicate 70 K data, and open symbols indicate 10 K data. The vertical dashed line indicates the LTO-HTT phase transition in the 70 K data, which coincides with the 10 K case, as the structural phase line is very steep in this region of the phase diagram (see Figure 3.13). The kink feature persists in the 70 K data, and the overall behavior of the CuO_6 volume at 10 K and 70 K appears to be the same. This observation will become important for

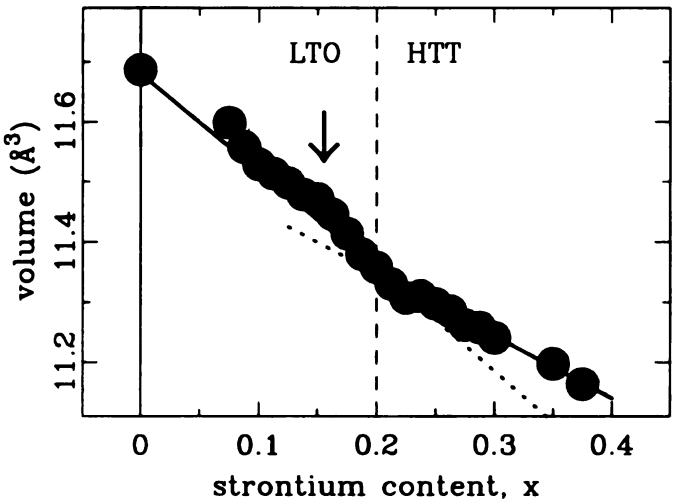

Figure 8.2: CuO_6 octahedral volume at 10 K as a function of doping. Arrow indicates anomalous kink in the volume at optimal doping, where the slope changes. Vertical dashed line denotes the LTO-HTT phase transition. Solid and dashed sloping lines are guides to the eye. Note the position of zero on the doping axis.

the discussion. For now the focus is on the differences in the 10 K and 300 K behavior of the octahedral volume, compared in Figure 8.4. In the figure solid circles represent 10 K data, while open squares denote 300 K data. Vertical dashed lines denote the LTO-HTT structural phase transition at the two temperatures. The sloped lines that run across the entire doping range are guides to the eye, and denote linear trends of the data and deviations from these trends. Ignoring deviations in the undoped endmember, 10 K and 300 K data agree rather well in the undoped region up to optimal doping. Then, after $x = 0.15$, the CuO_6 volume exhibits a sudden and rather dramatic decrease upon increased doping. This decrease is almost perfectly linear, as denoted by the dashed line which is a guide to the eye. At around $x = 0.2$, the slope changes, and the volume decrease slows down and has a slope similar to the one observed in the 300 K data at high doping. The change in slope at $x = 0.2$ of the 10 K data is probably due to the LTO-HTT phase transition. However, the volume behavior between $x = 0.15$ and $x = 0.2$ doping cannot be attributed to the

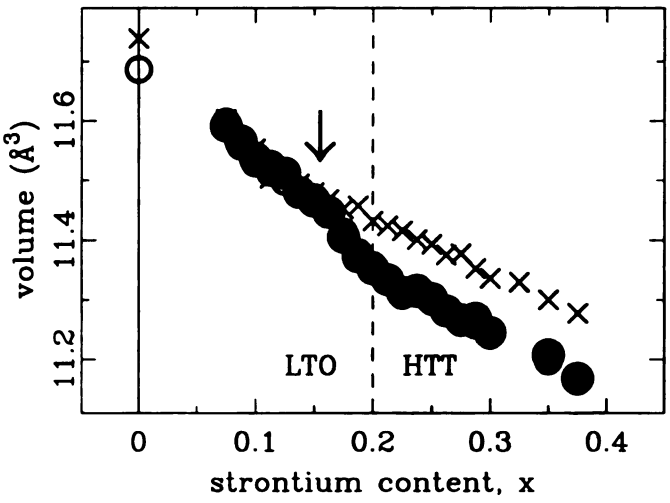

Figure 8.3: CuO_6 octahedral volume at 10 K (open symbols), 70 K (solid symbols), and 300 K (crossed symbols) as a function of doping. Arrow indicates anomalous kink in the volume at optimal doping, where the slope changes in the low temperature data stets. Vertical dashed line denotes the LTO-HTT phase transition at both 10 K and 70 K. Note the position of zero on the doping axis.

phase transition, since this happens at much higher temperatures in these samples. This behavior is anomalous, as we further discuss. The insets in Figure 8.4 show the qualitative evolution of the planar (bottom inset) and apical (top inset) Cu-O distances with doping. Note a significant change in the apical distance after optimal doping, indicated by the arrow in the inset. The doping dependence of the Cu-O distances at 10 K (solid circles) and 300 K (open squares) are shown quantitatively in Figure 8.5: (a) apical distance and (b) planar distance. The apical distance shows the same doping dependence (ignoring $x = 0$ datapoints) at the two temperatures in the underdoped region, up to $x = 0.15$. After optimal doping, the apical bond at 10 K rapidly decreases to $x = 0.2$, and this decrease continues at a changed pace above $x = 0.2$. It is notable that the 10 K and 300 K dependencies appear parallel in the underdoped region and also above $x = 0.2$. This is indicated by the dashed line, which mimics the 10 K trend coming from the overdoped side of the plot, but ignores

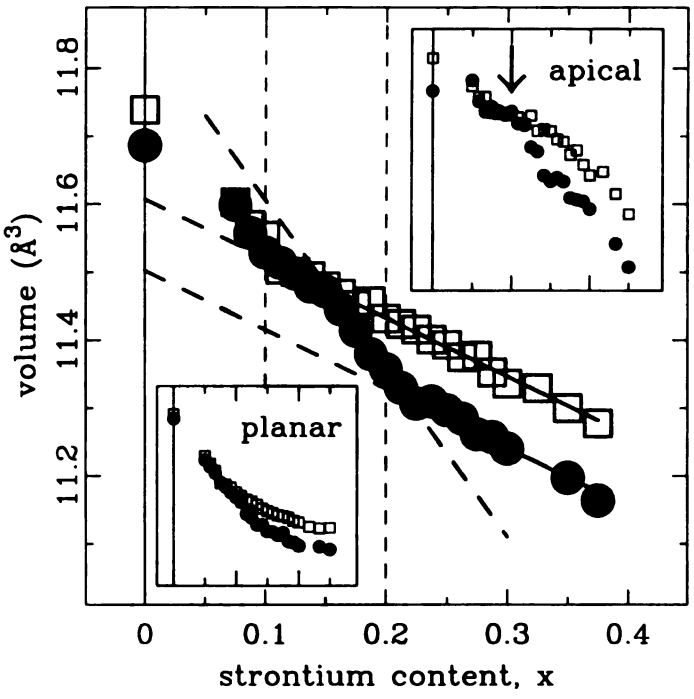

Figure 8.4: CuO_6 octahedral volume at 10 K (solid circles) and 300 K (open squares) as a function of doping. Vertical dashed lines indicate LTO-HTT phase transitions at the two temperatures. Sloping lines are guides to the eye. Top inset: qualitative doping dependence of the apical Cu-O distance at the two temperatures. The arrow indicates optimal doping concentration. Bottom inset: qualitative doping dependence of the planar Cu-O distance at the two temperatures.

the upturn between $x = 0.2$ and $x = 0.15$ doping. The dashed line is obtained by making a constant offset of about -0.1 angstroms to the 300 K data, to overlap the high-doping part with the 10 K data. The inset in Figure 8.5(a) shows the difference in the apical bondlength between the 10 K dataset and such offset 300 K dataset. The horizontal solid lines in the inset are guides to the eye. Inset in Figure 8.5(b) shows the same for the in-plane Cu-O distance. It is interesting to note that the magnitude of the change in the apical bond length is more than twice the change in the planar bond length in the region between $x = 0.15$ and $x = 0.2$ doping.

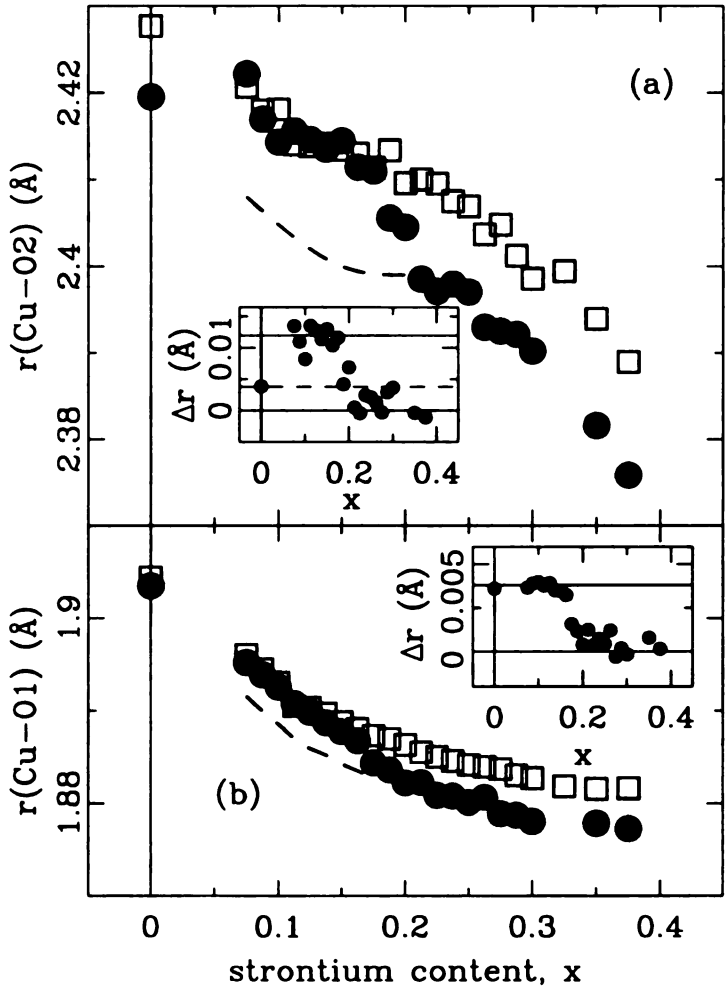

Figure 8.5: Evolution with doping of Cu-O distances at 10 K (solid circles) and 300 K (open squares): (a) apical Cu-O distance, and (b) planar Cu-O distance. Dashed lines are guides to the eye. Explanations of the insets and other details are provided in the text.

8.5.2 Discussion

The origin of the observed CuO_6-volume effect is not understood. In fact, to our knowledge, this is the first observation of this effect in the LSCO system. Here we *speculate* about the possible origin of this anomalous CuO_6-volume doping dependence at low temperature. We propose one possible scenario for this effect, based on circumstantial evidence.

Recently Haskel *et al.* [223] used polarized EXAFS to study the local structure of an optimally doped LSCO sample containing a small concentration of Ni replacing Cu on Cu-sites. Substituting Ni for Cu suppresses superconductivity when the Ni concentration is about 0.03. The EXAFS experiment found a strong contraction of the apical Ni-O bonds of the NiO_6 octahedra relative to the apical Cu-O bonds in the CuO_6 octahedra. The in-plane Ni-O and Cu-O distances were the same within the experimental resolution. The effect was addressed in terms of anti-Jahn-Teller distortions occurring on Ni sites, as Ni^{2+} is a non-JT ion. Comparison of Cu and Ni in the endmember La_2CuO_4 (LCO) and La_2NiO_4 (LNO) materials is helpful for further discussion. As discussed in Section 1.2.4, CuO_6 octahedra in the 214 family are JT distorted. The elongation of the octahedra exists in nickelates as well. However, there is an important difference in the electron configuration of Cu and Ni in these two systems. In LCO, Cu is in the $3d^9$ state with S=1/2, while in LNO Ni is in the $3d^8$ state with S=1. While two split Eg levels of Ni contain one electron each with aligned spins, the corresponding levels of Cu contain 3 electrons, two in the lower energy state and one in the higher energy state, and, in this view, an additional splitting occurs due to the JT effect in cuprate system, making larger elongation of the octahedra in the LCO case as compared to LNO [223]. This would then provide a natural explanation for larger octahedral distortion in LCO compared to that in LNO. When Ni is introduced into the CuO_2 planes of LSCO, due to its non-JT nature, it causes anti-JT distortion of that NiO_6 octahedron. Such local structural distor-

tion induced by substituting Cu with Ni in LSCO was proposed to have important implications in the destruction of superconductivity in Ni co-doped LSCO. In the EXAFS study it was proposed that T_c in this material is completely suppressed when the average distance between Ni dopants in the CuO_2 planes becomes comparable to the in-plane superconducting coherence length, ξ_{ab}, which is about 22.7Å in optimally doped LSCO [224]. Presumably this occurs at a Ni concentration in the range 0.03-0.04, where the average separation between Ni sites, which is proportional to the lattice constant to square root of concentration ratio, is of the order of 19-22 Å [223]. However, this argument may not be fully correct, as we further discuss. There is no evidence at the present time whether local structural distortions would be the same if Zn is used instead of Ni, for example. Both Zn and Ni suppress superconductivity, with Zn achieving it at a faster rate [223].

In the light of the above scenario, we propose for consideration that destruction of superconductivity in the *overdoped* regime of LSCO has the same origin. Significant reduction in the average CuO_6-volume above optimal doping, with particularly large reduction of the average apical Cu-O distance could be a consequence of the anti-JT distortion in the overdoped regime between $x = 0.15$ and $x = 0.2$. This scenario would also imply that the nature of doping changes above optimal doping. The doping character would change from predominantly planar below $x = 0.15$ to significantly apical above $x = 0.15$. In this view, above optimal doping a fraction of doped holes goes into the apical orbitals, creating Ni-like copper sites, possibly with S=1, as hole would reside in the apical branch of the Eg manifold. This would produce local anti-JT distortion on such NiO_6-like CuO_6 octahedra, resulting in the observed anomalous decrease of the average apical distance, and the average CuO_6 volume. It should be noted that planar doping does continue above $x = 0.15$, but at slightly slower rate, since the fraction of holes with apical doping character becomes significant, as compared to the underdoped regime. The destruction of superconductivity may then

have the same nature as the one proposed by Haskel *et al.*, with the excess apical-like hole concentration governing the place on the doping axis of the phase diagram where HTS is completely suppressed. However, the fact that the same structural effects in the CuO_6 volume are observed in the 70 K data argue against the simplistic view proposed by Haskel and collaborators. It rather suggests that this structural effect may be related to the anomalies in the normal state associated with the pseudogap. Further, an important question of why the doping character, as described above, is changed above optimal doping remains unanswered. The interplay between the exchange energy and the JT-distortion energy is expected to play an important role in governing the behavior of the system. In this view, the ab-initio calculation of Perry *et al.* [210] may be an important starting point. The discrepancies discussed in Chapter 7 between the apical-doping model [210] and the structural observations could possibly be reconciled if the constraints of the constant planar bond, assumed tetragonal symmetry, and absence of octahedral tilts are removed.

The LTO-HTT structural phase transition could be relevant for the observed volume effect in the LSCO system. At 10 K, however, the LSCO system undergoes the LTO-HTT phase transition just above $x = 0.2$, while the volume effect sets in at $x = 0.15$. This would then imply that the effect is some kind of precursor for the structural transition, which, although cannot be ruled out completely, is not a very likely scenario. The doping evolution of the CuO_6-volume at 300 K, where the transition happens at $x = 0.1$ doping, further strengthens the view in which the LTO-HTT phase transition is not involved.

If the above view is correct, and if the origin of the volume anomaly is indeed electronic in nature, consequences for the doped charge distribution in the CuO_2 planes could be expected. The sites with the apical hole-character could alter their local environment, and affect the degree of hybridization between the $3d$ and $2p$ planar Cu and O orbitals, for example. This could contribute to the change towards more

homogeneous doped charge distribution in the CuO_2 planes, as inferred from the PDF study where abrupt in-plane bondlength distribution sharpening is observed.

The effect observed in the CuO_6-volume doping dependence at low temperature is an important indicator and should motivate further detailed local structural studies in the vicinity of the boundary between optimally doped and overdoped regimes.

8.6 Future work

Importance of the structure, and its local aspects in particular, for the HTS phenomenon is very significant and still not fully understood. In light of the findings presented in this thesis, several possible avenues for further local structural studies of the HTS systems exploiting the power of the PDF technique can be proposed. For example, a more elaborate study of the LSCO temperature dependence could prove useful, especially in the doping regime between $x = 0.15$ and 0.25. A similar study of the LBCO system over a wide range of doping may nicely complement this. Another possibility is to investigate an electron-doped system with a similar structure, such as $Nd_{2-x}Ce_xCuO_4$, and explore the aspects of the "symmetry" of the electron-hole phase diagrams. When choosing a system for the type of study presented in this thesis, however, caution has to be exercised in light of the number of contributions to the nearest neighbor (planar) Cu-O peak, as well as its separation from the PDF peaks of the neighboring coordination shells.

Further local structural PDF studies of cuprates could also be motivated by interesting observations of coupling between the HTS and structural degrees of freedom. For example, early neutron diffraction study of Braden and collaborators suggested that the tilting of the CuO_6 octahedra is frozen below T_c in $La_{2-x}Sr_xCuO_4$ [203]. This issue was not addressed in any detail in our study, and would require systematic structural analysis with dense temperature points at lower temperatures. More recently,

Chmaissem and collaborators investigated in greater detail the buckling of the CuO_2 planes in $(La_{1-x}Ca_x)(Ba_{1.75-x}La_{0.25+x})CuO_4$, and found that the buckling scales to the T_c in this material, such that a maximum in T_c occurs at a maximum in the buckling. This is in strong contrast to the earlier results suggesting that for fixed chemical composition increased CuO_2 buckling lowers the T_c [189, 203, 225, 226, 227, 228].

Bibliography

[1] J. G. Bednorz and K. A. Müller, Z. Phys. B **64**, 189 (1986).

[2] H. F. Kay and P. C. Bailey, Acta Cryst. **10**, 219 (1957).

[3] H. Shaked, P. M. Keane, J. C. Rodriguez, F. F. Owen, R. L. Hitterman, and J. D. Jorgensen, *Special edition of Physica C: Crystal Structures of the High-T_c Superconducting Copper-Oxides*, Elsevier, Amsterdam, 1994.

[4] J. Bardeen, L. N. Cooper, and J. R. Schrieffer, Phys. Rev. **108**, 1175 (1957).

[5] L. N. Cooper, Phys. Rev. **104**, 1189 (1956).

[6] M. Tinkham, *Introduction to Superconductivity*, McGraw-Hill, New York, 1995.

[7] G. Burns, *High Temperature Superconductivity*, Academic Press, Boston, 1992.

[8] W. H. Little, Science **242**, 1390 (1988).

[9] D. M. Ginsberg, editor, *Physical Properties of High Temperature Superconductors*, World Scientific, Singapore, 1989.

[10] H. Takagi, B. Batlogg, H. L. Kao, J. Kwo, J. R. Cava, J. J. Krajewski, and W. F. Peck, Phys. Rev. Lett. **69**, 2975 (1992).

[11] J. R. Kirtley, C. C. Tsuei, S. I. Park, C. C. Chi, J. Rozen, and M. W. Shafer, Phys. Rev. B **35**, 7216 (1987).

[12] S. Pan, K. W. Ng, A. L. de Lozanne, J. M. Tarascon, and L. H. Greene, Phys. Rev. B **35**, 7220 (1987).

[13] M. E. Hawley, K. E. Gray, D. W. Capone II, and D. G. Hinks, Phys. Rev. B **35**, 7224 (1987).

[14] M. Naito, D. P. E. Smith, M. D. Kirk, B. Oh, M. R. Hahn, K. Char, D. B. Mitzi, J. Z. Sun, D. J. Webb, M. R. Beasley, O. Fischer, T. H. Geballe, R. H. Hammond, A. Kapitulnik, and C. F. Quate, Phys. Rev. B **35**, 7228 (1987).

[15] J. Lynn, editor, *High Temperature Superconductivity*, Springer-Verlag, Berlin, 1990.

[16] S. Uchida, T. Ido, H. Takagi, T. Arima, Y. Tokura, and S. Tajima, Phys. Rev. B **43**, 7942 (1991).

[17] J. Jaklič and P. Prelovšek, Adv. Phys. **49**, 1 (2000).

[18] R. J. Cava, A. Santoro, D. W. Johnson, and W. W. Rhode, Phys. Rev. B **35**, 6716 (1987).

[19] L. F. Mattheiss, Phys. Rev. Lett. **58**, 1028 (1987).

[20] J. B. Torrance, Y. Tokura, A. I. Nazzal, A. Bezinge, T. C. Huang, , and S. S. P. Parkin, Phys. Rev. Lett. **61**, 1127 (1988).

[21] A. W. Sleight, Science **242**, 1519 (1988).

[22] M. Wangbo, D. B. Kang, and C. C. Torado, Physica C **158**, 371 (1989).

[23] R. J. Cava, Science **247**, 656 (1990).

[24] A. Rigamonti, F. Borsa, and A. Carreta, Phys. Rev. Lett. **61**, 1367 (1998).

[25] T. Egami and S. J. L. Billinge, in *Physical properties of high-temperature superconductors V*, edited by D. M. Ginsberg, page 265, Singapore, 1996, World–Scientific.

[26] J. M. Tranquada, B. J. Sternlieb, J. D. Axe, Y. Nakamura, and S. Uchida, Nature **375**, 561 (1995).

[27] J. B. Boyce, F. Bridges, T. Claeson, T. H. Geballe, C. W. Chu, and J. M. Tarascon, Phys. Rev. B **35**, 7203 (1987).

[28] P. Böni, J. D. Axe, G. Shirane, R. J. Birgeneau, D. R. Gabbe, H. P. Jenssen, M. A. Kastner, C. J. Peters, P. J. Picone, , and T. R. Thurston, Phys. Rev. B **38**, 185 (1988).

[29] T. R. Thurston, R. J. Birgeneau, D. R. Gabbe, H. P. Jenssen, M. A. Kastner, P. J. Picone, N. W. Preyer, J. D. Axe, P. Böni, G. Shirane, M. Sato, K. Fukuda, and S. Shamoto, Phys. Rev. B **39**, 4327 (1989).

[30] M. K. Crawford, W. E. Farneth, E. M. McCarron III, R. L. Harlow, and A. H. Moudden, Science **250**, 1390 (1990).

[31] J. M. Tranquada, J. D. Axe, N. Ichikawa, Y. Nakamura, S. Uchida, and B. Nachumi, Phys. Rev. B **54**, 7489 (1996).

[32] H. Y. Hwang, B. Batlogg, H. Takagi, H. L. Kao, J. Kwo, R. J. Cava, J. J. Krajewski, and W. F. Peck, Phys. Rev. Lett. **72**, 2636 (1994).

[33] B. Batlogg, H. Y. Hwang, H. Takagi, R. J. Cava, H. L. Kao, and J. Kwo, Physica C **235-240**, 130 (1994).

[34] B. Batlogg, Physica C **282-287**, XXIV (1997).

[35] B. Keimer, N. Belk, R. J. Birgeneau, A. Cassanho, C. Y. Chen, M. Greven, M. A. Kastner, Y. Endoh, R. W. Erwin, and G. Shirane, Phys. Rev. B **46**, 14034 (1992).

[36] N. F. Mott, *Metal-Insulator Transitions*, Taylor and Francis, London, 1974.

[37] D. Vaknin, S. K. Sinha, D. E. Moncton, D. C. Johnston, J. M. Newsam, C. R. Safinya, and H. E. King, Phys. Rev. Lett. **58**, 2802 (1987).

[38] S. Sugai, S. Shamoto, and M. Sato, Phys. Rev. B **38**, 6436 (1988).

[39] J. H. Cho, F. Borsa, D. C. Johnston, and D. R. Torgeson, Phys. Rev. B **46**, 3179 (1992).

[40] C. Niedermayer, C. Bernhard, T. Blasius, A. Golnik, A. Moodenbaugh, , and J. I. Budnick, Phys. Rev. Lett. **80**, 3843 (1998).

[41] M. Julien, F. Borsa, P. Carretta, M. Horvatic, C. Berthier, and C. T. Lin, Phys. Rev. Lett. **83**, 604 (1999).

[42] J. M. Tranquada and G. Shirane, Neutron News **1**, 35 (1990).

[43] H. Takagi, T. Ido, S. Ishibashi, M. Uota, and S. Uchida, Phys. Rev. Lett. **40**, 2254 (1989).

[44] P. G. Radaelli, D. G. Hinks, A. W. Mitchell, B. A. Hunter, J. L. Wagner, B. Dabrowski, K. G. Vandervoort, H. K. Viswanathan, and J. D. Jorgensen, Phys. Rev. B **49**, 4163 (1994).

[45] A. R. Moodenbaugh, Y. Xu, M. Suenaga, T. J. Folkerts, and R. N. Shelton, Phys. Rev. B **38**, 4596 (1988).

[46] S. Katano, J. A. Fernandez-Baca, S. Funahashi, N. M. and. Y. Ueda, and K. Koga, Physica C **214**, 64 (1993).

[47] J. D. Axe, A. H. Moudden, D. Hohlwein, D. E. Cox, K. M. Mohanty, A. R. Moodenbaugh, and Y. Xu, Phys. Rev. Lett. **62**, 2751 (1989).

[48] K. Yvon and M. Francois, Z. Phys. B **76**, 413 (1989).

[49] J. M. Longo and P. M. Raccah, J. Solid State Chem. **6**, 526 (1973).

[50] M. François, K. Yvon, P. Fischer, and M. Decroux, Solid State Commun. **63**, 35 (1987).

[51] R. M. Fleming, B. Batlogg, R. J. Cava, and E. A. Rietman, Phys. Rev. B **35**, 7191 (1987).

[52] U. Geiser, M. A. Beno, A. J. Schultz, H. H. Wang, T. J. Allen, M. R. Monaghan, and J. M. Williams, Phys. Rev. B **35**, 6721 (1987).

[53] S. C. Moss, K. Forster, J. D. Axe, H. You, D. Hohlwein, D. E. Cox, P. H. Hor, R. L. Meng, and C. W. Chu, Phys. Rev. B **35**, 7195 (1987).

[54] M. K. Crawford, R. L. Harlow, E. M. McCarron, W. E. Farneth, J. D. Axe, H. Chou, and Q. Huang, Phys. Rev. B **44**, 7749 (1991).

[55] B. Büchner, M. Braden, M. Cramm, W. Schlabitz, W. Schnelle, O. Hoffels, W. Braunisch, R. Müller, G. Heger, and D. Wohlleben, Physica C **185-189**, 903 (1991).

[56] Von B. Grande, Hk. Möller-Buschbaum, and M. Schweizer, Z. Anorg. Allg. Chem. **428**, 120 (1977).

[57] P. Fazekas, *Lecture notes on electron correlation and magnetism*, World Scientific, Singapore, 1999.

[58] Y. Nakamura and S. Uchida, Phys. Rev. B **46**, 5841 (1992).

[59] T. Timusk and B. Statt, Rep. Prog. Phys. **62**, 61 (1999).

[60] H. Y. Hwang, B. Batlogg, H. Takagi, H. L. Kao, J. Kwo, J. R. Cava, J. J. Krajewski, and W. F. Peck, Phys. Rev. Lett. **72**, 2636 (1994).

[61] Z. Schlesinger, R. T. Collins, and M. W. Shafer, Phys. Rev. B **35**, 7232 (1987).

[62] A. V. Puchkov, D. N. Basov, and T. Timusk, J. Phys.: Condens. Matter **8**, 10049 (1996).

[63] J. W. Loram, K. A. Mirza, J. R. Cooper, , and J. L. Tallon, Physica C **282-287**, 1405 (1997).

[64] H. J. Tao, F. Lu, and E. J. Wolf, Physica C **282-287**, 1507 (1997).

[65] J. M. Harris, Z. Shen, P. J. White, D. S. Marshall, M. C. Schabel, J. N. Eckstein, and I. Bozovic, Phys. Rev. B **54**, R15665 (1996).

[66] P. J. White, Z. Shen, C. Kim, J. M. Harris, A. G. Loeser, P. Fournier, and A. Kapitulnik, Phys. Rev. B **54**, R15669 (1996).

[67] R. E. Walstedt, R. F. Bell, and D. B. Mitzi, Phys. Rev. B **44**, 7760 (1991).

[68] J. Bobroff, H. Allouh, P. Mendels, V. Viallet, H. F. Marruco, and D. Colson, Phys. Rev. Lett. **78**, 3757 (1997).

[69] M. Julien, P. Carreta, M. Horvatic, C. Bethier, Y. Bethier, P. Segransan, A. Carington, and D. Colson, Phys. Rev. Lett. **76**, 4238 (1996).

[70] J. A. Martindalle and P. C. Hammel, Phil. Mag. B **74**, 573 (1996).

[71] G. Zheng, T. Odaguchi, Y. Kitaoka, K. Asayama, Y. Kodama, K. Mizuhashi, and S. Uchida, Physica C **263**, 367 (1996).

[72] V. J. Emery and S. A. Kivelson, Nature **374**, 4347 (1995).

[73] P. Gopalan, M. W. McElfresh, Z. Kakol, J. Spalek, and J. Honig, Nature **45**, 249 (1992).

[74] Y. Furukawa and S. Wada, J. Phys.: Condens. Matter **6**, 8023 (1994).

[75] V. J. Emery, S. A. Kivelson, and J. M. Tranquada, Proc. Natl. Acad. Sci. USA **96**, 8814 (1999).

[76] J. R. Schrieffer, X.-G. Wen, , and S. Zhang, Phys. Rev. Lett. **60**, 944 (1988).

[77] J. Zaanen and O. Gunnarson, Phys. Rev. B **40**, 7391 (1989).

[78] V. J. Emery and S. A. Kivelson, Physica C **209**, 597 (1993).

[79] P. Prelovšek and X. Zotos, Phys. Rev. B **47**, 5984 (1993).

[80] U. Löw, V. J. Emery, K. Fabricius, and S. A. Kivelson, Phys. Rev. Lett. **72**, 1918 (1994).

[81] H. Tsunetsugu, M. Troyer, and T. M. Rice, Phys. Rev. B **51**, 16456 (1995).

[82] S. Haas, E. Dagotto, A. Nazarenko, and J. Riera, Phys. Rev. B **51**, 5989 (1995).

[83] C. Castellani, C. D. Castro, and M. Grilli, Phys. Rev. Lett. **75**, 4650 (1995).

[84] C. S. Hellberg and E. Manousakis, Phys. Rev. Lett. **78**, 4609 (1997).

[85] A. Bianconi, A. Valletta, A. Perali, and N. L. Siani, Solid State Commun. **102**, 369 (1997).

[86] R. S. Markiewicz, J. Phys. Chem. Solids **58**, 1179 (1997).

[87] S. R. White and D. J. Scalapino, Phys. Rev. Lett. **80**, 1272 (1998).

[88] J. C. Phillips, Philos. Mag. B **79**, 527 (1999).

[89] V. J. Emery, S. A. Kivelson, and O. Zachar, Phys. Rev. B **56**, 6120 (1997).

[90] C. Castellani, C. DiCastro, and M. Grilli, Z. Phys. B **103**, 137 (1997).

[91] A. H. C. Neto and F. Guinea, Phys. Rev. Lett. **80**, 4040 (1998).

[92] T. M. Rice, Physica C **282-287**, XIX (1997).

[93] M. I. Salkola, V. J. Emery, and S. A. Kivelson, Phys. Rev. Lett. **77**, 155 (1996).

[94] Y. Krotov, D. Lee, and A. V. Balatsky, Phys. Rev. B **56**, 8367 (1997).

[95] C. H. Chen, S. Cheong, and A. S. Cooper, Phys. Rev. Lett. **71**, 2461 (1993).

[96] J. M. Tranquada, D. J. Buttrey, V. Sachan, and J. E. Lorenzo, Phys. Rev. Lett. **73**, 1003 (1994).

[97] V. Sachan, D. J. Buttrey, J. M. Tranquada, J. E. Lorenzo, and G. Shirane, Phys. Rev. B **51**, 12742 (1995).

[98] A. Vigliante, M. von Zimmermann, J. R. Schneider, T. Frello, N. H. Andersen, D. J. B. J. Madsen, D. Gibbs, and J. M. Tranquada, Phys. Rev. B **56**, 8248 (1997).

[99] J. M. Tranquada, P. Wochner, and D. J. Buttrey, Phys. Rev. Lett. **79**, 2133 (1997).

[100] S. Lee and S. Cheong, Phys. Rev. Lett. **79**, 2514 (1997).

[101] T. Katsufuji, T. Tanabe, T. Ishikawa, S. Yamanouchi, Y. Tokura, T. Kakeshita, R. Kajimoto, and H. Yoshizawa, Phys. Rev. B **60**, R5097 (1999).

[102] P. Wochner, J. M. Tranquada, D. J. Buttrey, and V. Sachan, Phys. Rev. B **57**, 1066 (1998).

[103] M. von Zimmermann, A. Vigliante, T. Niemöller, N. Ichikawa, T. Frello, J. Madsen, P. Wochner, S. Uchida, N. H. Andersen, J. M. Tranquada, D. Gibbs, and J. R. Schneider, Europhys. Lett. **41**, 629 (1998).

[104] C. H. Chen and S.-W. Cheong, Phys. Rev. Lett. **76**, 4042 (1996).

[105] C. H. Chen, S. Cheong, and H. Y. Hwang, J. Appl. Phys. **81**, 4326 (1997).

[106] A. P. Ramirez, P. Schiffer, S.-W. Cheong, C. H. Chen, W. Bao, T. T. M. Palstra, P. L. Gammel, D. J. Bishop, and B. Zegarski, Phys. Rev. Lett. **76**, 3188 (1996).

[107] P. C. Hammel, B. W. Statt, R. L. Martin, F. C. Chou, D. C. Johnston, and S. Cheong, Phys. Rev. B **57**, R712 (1998).

[108] T. Egami, D. Louca, and R. J. McQueeney, J. Supercond. **10**, 323 (1997).

[109] B. W. Statt, P. C. Hammel, Z. Fisk, S-W. Cheong, F. C. Chou, D. C. Johnston, and J. E. Schirber, Phys. Rev. B **52**, 15 575 (1995).

[110] O. Baberski, A. Lang, O. Maldonado, M. Hücker, B. Büchner, and A. Freimuth, Europhys. Lett. **44**, 335 (1998).

[111] A. P. Kampf, D. J. Scalapino, and S. R. White, Phys. Rev. B **64**, 52509 (2001).

[112] N. L. Saini, A. Lanzara, H. Oyanagi, H. Yamaguchi, K. Oka, T. Ito, and A. Bianconi, Phys. Rev. B **55**, 12759 (1997).

[113] J. Zhou and J. B. Goodenough, Phys. Rev. B **56**, 6288 (1997).

[114] J. M. Tranquada, N. Ichikawa, and S. Uchida, Phys. Rev. B **59**, 14712 (1999).

[115] J. M. Tranquada, J. D. Axe, N. Ichikawa, A. R. Moodenbaugh, Y. Nakamura, and S. Uchida, Phys. Rev. Lett. **78**, 338 (1997).

[116] B. Nachumi et al., Phys. Rev. B **58**, 8760 (1998).

[117] A. R. Moodenbaugh, L. Wu, Y. Zhu, L. H. Lewis, and D. E. Cox, Phys. Rev. B **58**, 9549 (1998).

[118] Y. Lee, R. J. Birgeneau, M. A. Kastner, Y. Endoh, S. Wakimoto, K. Yamada, R. W. Erwin, S. H. Lee, and G. Shirane, Phys. Rev. B **60**, 3643 (1999).

[119] K. Yamada, C. H. Lee, K. Kurahashi, J. Wada, S. Wakimoto, S. Ueki, H. Kimura, Y. Endoh, S. Hosoya, G. Shirane, R. J. Birgeneau, M. Greven, M. A. Kastner, and Y. J. Kim, Phys. Rev. B **57**, 6165 (1998).

[120] A. V. Balatsky and P. Bourges, Phys. Rev. Lett. **82**, 5337 (1999).

[121] N. Ichikawa, S. Uchida, J. M. Tranquada, T. Niemöller, P. M. Gehring, S. Lee, and J. R. Schneider, Phys. Rev. Lett. **85**, 1738 (2000).

[122] A. G. Loeser, Z. X. Shen, D. S. Dessau, D. S. Marshall, C. H. Park, P. Fournier, and A. Kapitulnik, Science **273**, 325 (1996).

[123] C. C. Homes, T. Timusk, R. Liang, D. A. Bonn, and W. N. Hardy, Phys. Rev. Lett. **71**, 1645 (1993).

[124] Ch. Renner, B. Revaz, J.-Y. Genoud, K. Kadowaki, and O. Fischer, Phys. Rev. Lett. **80**, 149 (1998).

[125] J. W. W. Warren et al., Phys. Rev. Lett. **62**, 1193 (1989).

[126] P. Dai, M. Yethiraj, H. A. Mook, T. B. Lindemer, and F. Doğan, Phys. Rev. Lett. **77**, 5425 (1996).

[127] H. A. Mook and F. Doğan, Nature **401**, 145 (1999).

[128] H. J. Schulz, Phys. Rev. Lett. **64**, 1445 (1989).

[129] I. Martin, G. Ortiz, A. V. Balatsky, and A. R. Bishop, Europhys. Lett. **56**, 849 (2001).

[130] T. E. Mason, G. Aeppli, and H. Mook, Phys. Rev. Lett. **68**, 1414 (1992).

[131] T. R. Thurston, P. M. Gehring, G. Shirane, R. J. Birgeneau, M. A. Kastner, Y. Endoh, M. Matsuda, K. Yamada, H. Kojima, and I. Tanaka, Phys. Rev. B **46**, 9128 (1992).

[132] S. Wakimoto, G. Shirane, Y. Endoh, K. Hirota, S. Ueki, K. Yamada, R. J. Birgeneau, M. A. Kastner, Y. S. Lee, P. M. Gehring, and S. H. Lee, Phys. Rev. B **60**, R769 (1999).

[133] H. A. Mook, P. Dai, F. Doğan, and R. D. Hunt, Nature **404**, 729 (2000).

[134] A. W. Hunt, P. M. Singer, K. R. Thurber, and T. Imai, Phys. Rev. Lett. **82**, 4300 (1999).

[135] A. Lanzara, G. M. Zhao, N. L. Saini, A. Bianconi, K. Conder, H. Keller, and K. A. Müller, J. Phys: Condens. Matter **11**, L541 (1999).

[136] T. Egami, J. H. Chung, R. J. McQueeney, M. Yethiraj, H. A. Mook, C. Frost, Y. Petrov, F. Doğan, Y. Inamura, M. Arai, S. Tajima, and Y. Endoh, Physica B **316**, 62 (2002).

[137] T. Egami and S. J. L. Billinge, Prog. Mater. Sci. **38**, 359 (1994).

[138] E. Salje, A. S. Alexandrov, and W. Y. Liang, editors, *Polarons and Bipolarons in High-*T_c *Superconductors and Related Materials*, Cambridge University Press, Cambridge, 1995.

[139] K. A. Müller and G. Benedek, editors, *Phase Separation in Cuprate Superconductors*, World Scientific, Singapore, 1993.

[140] E. Sigmund and K. A. Müller, editors, *Phase Separation in Cuprate Superconductors*, Springer-Verlag, New York, 1994.

[141] Y. Bar-Yam, T. Egami, J. Mustre-de Leon, and A. R. Bishop, editors, *Lattice Effects in High-Temperature Superconductors*, World Scientific, Singapore, 1992.

[142] B. E. Warren, *X-ray Diffraction*, Dover, New York, 1990.

[143] T. Egami, Mater. Trans. **31**, 163 (1990).

[144] S. J. L. Billinge, in *Local Structure from Diffraction*, edited by S. J. L. Billinge and M. F. Thorpe, page 137, New York, 1998, Plenum.

[145] P. C. Hammel, A. P. Reyes, S.-W. Cheong, Z. Fisk, and J. E. Schirber, Phys. Rev. Lett. **71**, 440 (1993).

[146] B. Grevin, Y. Berthier, P. Mendels, and G. Collin, Phys. Rev. B **61**, 4334 (2000).

[147] M. F. F. C. Ladd and R. A. Palmer, *Structure determination by x-ray crystallography*, Kluwer Academic, New York, 1994.

[148] C. N. J. Wagner, J. Non-Cryst. Solids **31**, 1 (1978).

[149] B. E. Warren, *X-ray diffraction*, Dover, New York, 1990.

[150] J. I. Langford and D. Louër, Rep. Prog. Phys. **59**, 131 (1996).

[151] H. M. Rietveld, J. Appl. Cryst. **2**, 65 (1969).

[152] F. Frey, Z. Kristallog. **212**, 257 (1997).

[153] G. E. Ice and C. J. Sparks, Annu. Rev. Mater. Sci. **29**, 25 (1999).

[154] E. A. Stern, D. E. Sayers, and F. W. Lytle, Phys. Rev. B **11**, 4836 (1975).

[155] B. K. Teo, in *EXAFS spectroscopy: techniques and applications*, edited by B. K. Teo and D. C. Joy, page 13, New York, 1980, Plenum.

[156] R. Prinz and D. Koningsberger, *X-ray absorption: principles, applications techniques of EXAFS, SEXAFS and XANES*, J. Wiley and Sons, New York, 1988.

[157] T. Egami and S. J. L. Billinge, *Underneath the Bragg Peaks: Structural analysis of complex materials*, Pergamon, Oxford, 2003.

[158] C. G. Windsor, *Pulsed neutron scattering*, Taylor and Francis, London, 1981.

[159] Y. Waseda, *The structure of non-crystalline materials*, McGraw-Hill, New York, 1980.

[160] J. M. F. Gunn, in *Neutron scattering at a pulsed source*, edited by R. J. Newport, B. D. Rainford, and R. Cywinski, page 1, Bristol, 1988, Adam Hilger.

[161] Th. Proffen and S. J. L. Billinge, J. Appl. Crystallogr. **32**, 572 (1999).

[162] I. Jeong, J. Thompson, A. M. P. Turner, and S. J. L. Billinge, J. Appl. Cryst. **34**, 536 (2001).

[163] P. F. Peterson, M. Gutmann, Th. Proffen, and S. J. L. Billinge, J. Appl. Cryst. **33**, 1192 (2000).

[164] I. D. Brown and D. Altermatt, Acta Cryst. B **41**, 244 (1985).

[165] M. Breuer, B. Büchner, R. Müller, M. Cramm, D. Maldonado, A. Freimuth, B. Rodan, R. Borowski, B. Heymer, and D. Wohlleben, Physica C **208**, 217 (1993).

[166] S. J. L. Billinge, G. H. Kwei, A. C. Lawson, J. D. Thompson, and H. Takagi, Phys. Rev. Lett. **71**, 1903 (1993).

[167] J. Rodriguez-Cavajal, in *Abstract of the Satellite Meeting on Powder Diffraction of the XV Congress of the UICr*, page 127, Toulouse, France, 1990.

[168] J. Rodriguez-Cavajal, Physica B **192**, 55 (1993).

[169] A. I. Nazal, V. Y. Lee, E. M. Engler, R. D. Jacowitz, Y. Tokura, and J. B. Torrance, Physica C **153-155**, 1367 (1988).

[170] Y. Maeno, H. Teraoka, K. Matsukuma, K. Yoshida, K. Sugiyama, F. Nakamura, and T. Fujita, Physica C **185-189**, 587 (1991).

[171] W. M. Chen, C. C. Lam, J. F. Geng, L. Y. Li, K. C. Hung, and X. Jin, Physica C **270**, 155 (1996).

[172] W. M. Chen, J. Chen, and X. Jin, Physica C **276**, 132 (1997).

[173] Z. S. Teweldemedhin, R. L. Fuller, and M. Greenblatt, J. Chem. Ed. **73**, 906 (1996).

[174] M. Gutmann, *PhD Thesis*, ETH Zurich, 1999.

[175] M. Gutmann, private communication, 2001.

[176] J. B. Goodenough, Ferroelectrics **130**, 77 (1992).

[177] V. Petkov, I-K. Jeong, J. S. Chung, M. F. Thorpe, S. Kycia, and S. J. L. Billinge, Phys. Rev. Lett. **83**, 4089 (1999).

[178] E. S. Božin, S. J. L. Billinge, G. H. Kwei, and H. Takagi, Phys. Rev. B **59**, 4445 (1999).

[179] D. Haskel, E. A. Stern, F. Dogan, and A. R. Moodenbaugh, Phys. Rev. B **61**, 7055 (2000).

[180] E. S. Božin, S. J. L. Billinge, and G. H. Kwei, Physica B **241-243**, 795 (1998).

[181] H. Takagi, R. J. Cava, M. Marezio, B. Batlogg, J. J. Krajewski, W. F. Peck Jr., P. Bordet, and D. E. Cox, Phys. Rev. Lett. **68**, 3777 (1992).

[182] T. Egami, in *Local Structure from Diffraction*, edited by S. J. L. Billinge and M. F. Thorpe, page 1, Plenum, New York, 1998.

[183] E. S. Božin, S. J. L. Billinge, H. Takagi, and G. H. Kwei, Phys. Rev. Lett. **84**, 5856 (2000).

[184] S. J. L. Billinge and T. Egami, Phys. Rev. B **47**, 14386 (1993).

[185] E. Sevillano, H. Meuth, and J. J. Rehr, Phys. Rev. B **20**, 4908 (1979).

[186] A. Lanzara, N. L. Saini, M. Brunelli, F. Natali, A. Bianconi, P. G. Radaelli, and S. Cheong, Phys. Rev. Lett. **81**, 878 (1998).

[187] T. Niemöller, B. Büchner, M. Cramm, C. Hunt, L. Tröger, and M. Tischer, Physica C **299**, 191 (1998).

[188] B. Büchner, M. Breuer, W. Schlabitz, A. Viack, W. Schäfer, A. Freimuth, and A. P. Kampf, Physica C **235-240**, 281 (1994).

[189] B. Büchner, M. Breuer, A. Freimuth, and A. P. Kampf, Phys. Rev. Lett. **73**, 1841 (1994).

[190] D. E. Cox et al., Mater. Res. Soc. Symp. Proc. **156**, 141 (1989).

[191] S. J. L. Billinge, G. H. Kwei, and H. Takagi, Phys. Rev. Lett. **72**, 2282 (1994).

[192] T. Egami, W. Dmowski, J. D. Jorgensen, D. G. Hinks, D. W. Capone II, C. U. Segre, and K. Zhang, Rev. Solid State Sci. **1**, 247 (1987).

[193] S. J. L. Billinge and G. H. Kwei, J. Phys. Chem. Solids **57**, 1457 (1996).

[194] D. Haskel, E. A. Stern, D. G. Hinks, A. W. Mitchell, J. D. Jorgensen, and J. I. Budnick, Phys. Rev. Lett. **76**, 439 (1996).

[195] D. Haskel, E. A. Stern, D. G. Hinks, A. W. Mitchell, and J. D. Jorgensen, Phys. Rev. B **56**, R521 (1997).

[196] The agreement factor, which is similar to the profile-weighted residuals function in Rietveld refinement, equals 0.18896 for the LTO model and 0.18473 for the HTT model for the $x = 0.25$ data set, where the LTO model has 13 independent variables and the HTT model has 11 independent variables.

[197] M. Braden, P. Schweiss, G. Heger, W. Reichardt, Z. Fisk, K. Gamayunov, I. Tanaka, and H. Kojima, Physica C **223**, 396 (1994).

[198] F. C. Zhang and T. M. Rice, Phys. Rev. B **37**, 3759 (1988).

[199] J. D. Axe, in *Proc. Conf. Lattice Effects in High* T_c *Superconductors*, edited by Y. Bar-Yam, T. Egami, J. Mustre-de Leon, and A. R. Bishop, Singapore, 1992, World Scientific.

[200] J. L. Sarrao, D. Mandrus, A. Migliori, Z. Fisk, I. Tanaka, H. Kojima, P. C. Canfield, and P. D. Kodali, Phys. Rev. B **50**, 13125 (1994).

[201] C. Friedrich, B. Büchner, M. M. Abd-Elmeguid, and H. Micklitz, Phys. Rev. B **54**, R800 (1996).

[202] R. J. Birgenau, C. Y. Chen, D. R. Gabbe, H. P. Jenssen, M. A. Kastner, C. J. Peters, P. J. Picone, T. Thio, T. R. Thurston, and H. L. Tuller, Phys. Rev. Lett. **59**, 1329 (1987).

[203] M. Braden, O. Hoffels, W. Schnelle, B. Büchner, G. Heger, B. Hennion, I. Tanaka, and H. Kojima, Phys. Rev. B **47**, 12288 (1993).

[204] M. T. Dove, V. Heine, K. D. Hammonds, M. Gambhir, and A. K. A. Pryde, in *Local Structure from Diffraction*, edited by S. J. L. Billinge and M. F. Thorpe, page 253, New York, 1998, Plenum.

[205] W. E. Pickett, R. E. Cohen, and H. Krakauer, Phys. Rev. Lett. **67**, 228 (1991).

[206] A. Manthiram and J. B. Goodenough, J. Solid State Chem. **87**, 402 (1991).

[207] A. Manthiram and J. B. Goodenough, J. Solid State Chem. **92**, 231 (1991).

[208] R. D. Shannon, Acta Cryst. A. **32**, 751 (1976).

[209] S. J. L. Billinge and P. M. Duxbury, Int. J. Mod. Phys. B **16**, 1697 (2002).

[210] J. K. Perry, J. Tahir-Kheli, and W. A. Goddard III, Phys. Rev. B **65**, 144501 (2002).

[211] A. C. Larson and R. B. Von Dreele, *GSAS-General Structure Analysis System*, Report LA-UR-86-748, Los Alamos National Laboratory, 1987.

[212] R. D. Shannon and C. T. Prewitt, Acta Cryst. B **25**, 925 (1969).

[213] I. D. Brown, J. Solid State Chem. **82**, 122 (1989).

[214] C. T. Chen, F. Sette, Y. Ma, M. S. Hybertsen, E. B. Stechel, W. M. C. Foulkes, M. Schluter, S-W. Cheong, A. S. Cooper, L. W. Rupp Jr., B. Batlogg, Y. L. Soo, Z. H. Ming, A. Krol, and Y. H. Kao, Phys. Rev. Lett. **66**, 104 (1991).

[215] C. T. Chen, L. H. Tjeng, J. Kwo, H. L. Kao, P. Rudolf, F. Sette, and R. M. Fleming, Phys. Rev. Lett. **68**, 2543 (1992).

[216] P. C. Hammel and D. J. Scalapino, Phil. Mag. B **74**, 523 (1996).

[217] A. W. Hunt, P. M. Singer, A. F. Cederström, and T. Imai, Phys. Rev. B **64**, 134525 (2001).

[218] A. Lanzara, N. L. Saini, T. Rosetti, A. Bianconi, H. Oyanagi, H. Yamaguchi, and Y. Maeno, Solid State Commun. **97**, 93 (1996).

[219] N. L. Saini, A. Lanzara, A. Bianconi, H. Oyanagi, H. Yamaguchi, K. Oka, and T. Ito, Physica C **268**, 121 (1996).

[220] A. Bianconi, N. L. Saini, A. Lanzara, M. Missori, T. Rossetti, H. Oyanagi, H. Yamaguchi, K. Oka, and T. Ito, Phys. Rev. Lett. **76**, 3412 (1996).

[221] A. Bianconi, M. Lusignoli, N. L. Saini, P. Bordet, A. Kvick, and P. G. Radaelli, Phys. Rev. B **54**, 4310 (1996).

[222] S. Han, E. A. Stern, D. Haskel, and A. R. Moodenbaugh, Phys. Rev. B **66**, 094101 (2002).

[223] D. Haskel, E. A. Stern, V. Polinger, and F. Dogan, Phys. Rev. B **64**, 104510 (2001).

[224] M. E. Nachumi, A. Keren, K. Kojima, M. Larkin, G. M. Luke, J. Merrin, O. Tchernyshöv, Y. J. Uemura, N. Ichikawa, M. Goto, and S. Uchida, Phys. Rev. Lett. **77**, 5421 (1996).

[225] Y. Yamada and M. Ido, Physica C **203**, 240 (1992).

[226] H. Takahashi, H. Shaked, B. A. Hunter, P. G. Radaelli, R. L. Hitterman, D. G. Hinks, and J. D. Jorgensen, Phys. Rev. B **50**, 3221 (1994).

[227] B. Dabrowski, Z. Wang, K. Rogacki, J. D. Jorgensen, R. L. Hitterman, J. L. Wagner, B. A. Hunter, P. G. Radaelli, and D. G. Hinks, Phys. Rev. Lett. **76**, 1348 (1996).

[228] E. Kaldis, J. Röhler, E. Liarokapis, N. Poulakis, K. Conder, and P. W. Loeffen, Phys. Rev. Lett. **79**, 4894 (1997).